FINITE-ELEMENT MODELING OF A DAMAGED PRESTRESSED

CONCRETE BRIDGE

Except where reference is made to the work of others, the work described in this thesis is my own or was done in collaboration with my advisory committee. This thesis does not include proprietary or classified information.

_____
Kelli Ann Shapiro

Certificate of Approval:

_____
Mary L. Hughes
Assistant Professor
Civil Engineering

_____
Robert W. Barnes, Chair
Associate Professor
Civil Engineering

_____
Anton K. Schindler
Assistant Professor
Civil Engineering

_____
Joe F. Pittman
Interim Dean
Graduate School

FINITE-ELEMENT MODELING OF A DAMAGED PRESTRESSED

CONCRETE BRIDGE

Kelli Ann Shapiro

A Thesis

Submitted to

the Graduate Faculty of

Auburn University

in Partial Fulfillment of the

Requirements for the

Degree of

Master of Science

Auburn, Alabama
May 10, 2007

FINITE-ELEMENT MODELING OF A DAMAGED PRESTRESSED

CONCRETE BRIDGE

Kelli Ann Shapiro

_____
Signature of Author

_____
Date of Graduation

VITA

Kelli Ann Shapiro, daughter of Bruce and Mischell Shapiro, was born on February 3, 1981, in Salt Lake City, Utah. In June of 1999, she graduated with honors as Valedictorian from Ansbach American Middle/High School in Ansbach, Germany. She began school at Brigham Young University in September 1999 on academic scholarship and received a Bachelor of Science in April 2004. She entered graduate school at Auburn University in August 2004 and completed a Master of Science degree in Civil Engineering with an emphasis in Structural Engineering in May 2007. After completing graduate school, she began work as a stress analyst at Marshall Space Flight Center in Huntsville, Alabama.

THESIS ABSTRACT

FINITE-ELEMENT MODELING OF A DAMAGED PRESTRESSED

CONCRETE BRIDGE

Kelli Ann Shapiro

Master of Science, May 10, 2007
(B.S., Brigham Young University, 2004)

258 Typed Pages

Directed by Robert W. Barnes

Spans 10 and 11 of the Interstate Highway 565 bridge structure in Huntsville, Alabama were noticed to be cracked shortly after their construction. Alabama Department of Transportation (ALDOT) employees investigated and concluded that the probable cause of the cracking was stress at the continuous support due to the temperature differential between the bridge deck and the bulb-tee girders. Further investigation to determine the cause of the cracking, the results of the cracking, and the possible repair methods was conducted by ALDOT in cooperation with Auburn University personnel. It was concluded that fiber-reinforced polymer (FRP) repair was feasible, and a repair procedure was devised. In order to measure the effect of the repair, load tests were planned to occur both before and after the repair. On June 1 and 2, 2005, the pre-repair load tests were conducted.

A finite-element model (FEM) was created to provide a basis for an analytical comparison to measured data and observed bridge behavior. The model was designed to simulate the current behavior of the bridge and to predict the change in behavior due to the repair work. Modeling results supported the hypothesis that rather than behaving as a continuous two-span beam, the bridge displayed behavior consistent with a continuous beam including a hinge located in the cracked region. An additional goal of the analytical modeling was to determine which of the strain gauges used in the pre-repair bridge tests should be reassigned to other locations of the bridge for the post-repair tests. It was determined that eight gauges should be relocated from the face of the girder near the top pf the web to the base of the FRP reinforcement.

Results of the analytical modeling warranted the prediction that the FRP repair would return the bridge to near fully continuous behavior. Further analysis will be necessary after the repair is complete and the post-repair test has been conducted to determine the results of the repair on the behavior of the bridge.

ACKNOWLEDGEMENTS

Style manual used   Kate L. Turabian A Manual for Writers of Term Papers, Theses,

and Disserations. 6th ed.

Computer software used   Microsoft Word, Microsoft Excel, ABAQUS CAE 6.5-1,

ABAQUS CAE 6.6-1, Microsoft Paint

TABLE OF CONTENTS

LIST OF TABLES

LIST OF FIGURES

CHAPTER 1: INTRODUCTION

1.1 BACKGROUND

In 1992, large and unexpected cracks were discovered in prestressed concrete girders of several recently-constructed bridge spans of I-565 in Huntsville, Alabama. Once restrained thermal deformations of the superstructure were determined to be the cause, several attempts were made to alleviate the problem over the course of the next few years. Since they were discovered, the progression of the cracks has been closely tracked by Alabama Department of Transportation (ALDOT) employees. Swenson (2003) proposed a repair using externally bonded, fiber-reinforced polymer (FRP) reinforcement. To fully assess the efficacy of this repair system, load tests were required before and after the repair.

   This thesis describes the development of a finite-element model (FEM) of a two-span portion of I-565. Simulations were conducted for conditions both before and after installation of the FRP reinforcement. Analytical results generated from these models shed light on the structural behavior of the damaged bridge. In addition, the model of the post-repair bridge has been used to predict changes in behavior that should be measured when the repaired structure is load tested.

1.2 OBJECTIVES

The purpose of the investigation reported herein was threefold:

1. Use finite-element modeling to accurately simulate the behavior of a damaged, two-span unit of the I-565 superstructure.

2. Use data collected in a load test to verify the accuracy of the model and refine it as necessary.

3. Use the model to predict the performance of the two-span unit after installation of the fiber-reinforced polymer repair.

1.3 RESEARCH APPROACH

ABAQUS/CAE was used to create a finite-element model of the two-span superstructure unit under investigation. Data collected from the pre-repair load test was used to validate the model's response. Once a model was developed that described the current behavior of the bridge with reasonable accuracy, the simulated FRP repair was added to the model, and the results were analyzed for prediction of post-repair behavior.

1.4 THESIS OUTLINE

A brief summary of previous studies conducted using finite-element modeling of multigirder bridges is presented in Chapter 2. Chapter 3 presents a historical overview of the I-565 bridge construction and condition, along with details of the bridge structure. Load testing of the damaged structure is described in Chapter 4. Results of this testing were used to refine the FEM bridge model. Details of the ABAQUS models are described in Chapter 5. Results of the load tests and the finite-element bridge models are presented in Chapter 6. Chapter 7 includes a discussion of the significance of these results and a forecast of the performance of the repaired structure based on the

analytical results. Finally, Chapter 8 consists of a summary of the study as well as the

resulting conclusions and recommendations.

CHAPTER 2: FINITE-ELEMENT MODELING OF MULTIGIRDER BRIDGES

2.1 INTRODUCTION

As the bulk of the investigation reported herein involves finite-element modeling

(FEM) of a bridge deck supported by multiple longitudinal girders, it is important to

first briefly explore the work which has already been conducted on this subject. There

are myriad options from which to choose when selecting both the components and the

construction approach for the model. From the very basic question of which structural

elements to include to the more advanced question of mesh size, many issues need to be

considered before beginning. It is best to learn from the experiences of others as much

as possible. This chapter consists of a review of previous research that involved FEM

of multigirder bridges, including comparisons with load-test results.

2.2 AASHTO LRFD REQUIREMENTS

Section 4.6.3 of the *AASHTO LRFD Bridge Design Specifications* (American

Association of State Highway and Transportation Officials 2004) provides minimum

requirements for using refined methods of analysis. First, consideration is given to

aspect ratios of elements, positioning and number of nodes, and other topological

features which might affect the accuracy of the solution. Though normally neglected, a

continuous railing, barrier, or median may be considered structurally active if full

composite behavior is certain.

For the deck, flexural and torsional deformation must be considered, but vertical shear deformation need not be. The wheel loads on the deck should be modeled as patch loads distributed over an area approximating the wheel contact surface. For the material properties of the deck elements, if a bridge deck is solid with uniform or near-uniform depth and the stiffness is approximately equal in every in-plane direction, it can be considered isotropic (AASHTO 2004).

The maximum acceptable aspect ratio of finite elements is 5.0. Sudden changes in either size or shape of finite elements should be avoided. The nodal loads need to be statically equivalent to the physical loads applied. At least five nodes per beam should be employed, though nine is preferable. For finite-element analyses which involve plate or beam elements, it is best to maintain the relative vertical distances between elements. If this is impractical, longitudinal and transverse elements may be placed at the midthickness of the plate-bending elements if the eccentricities are accounted for in the equivalent properties of the composite sections (AASHTO 2004).

Inelastic behavior must be restricted to the flexure of beams or girders. Inelastic behavior resulting from shear and/or uncontrolled buckling is not allowed (AASHTO 2004).

2.3 FINITE-ELEMENT MODELING OF BRIDGES WITHOUT LOAD TESTING VERIFICATION

Tedesco, Stallings, and Tow (1995) used dynamic FEM analysis in ADINA™ to investigate a single-span, multigirder steel bridge with no skew. The three structural components that they included in their model were the reinforced-concrete bridge deck, the steel girders, and the steel diaphragms. For the deck slab, four-node shell elements

5

with five degrees-of-freedom (DOF) per node were chosen. These were determined to accurately reflect the membrane stresses caused by the primary flexure of the bridge while permitting the slab to experience out-of-plane flexure. In order to sufficiently represent the cracking which the bridge deck had already experienced, two approaches were utilized: the modulus of elasticity was altered to represent the effective stiffness of the slab, and the deck slab elements were defined as an orthotropic material. The report does not specify the manner used to determine the effective stiffness of the slab.

Because the effects of the diaphragms were under investigation in this study, it was important for those effects to be readily available for analysis. Also, it was important that those effects be accurately reflected. This meant that the out-of-plane flexure that the girders experienced as a result of the presence of the diaphragms needed to be considered. For this reason, the girder web and flanges were modeled independently of one another. The stresses in the web were judged to not greatly affect the total girder bending moment, so three-node plate bending elements were used for the web. Because of the sensitivity of the bending moment to flange stresses, the flanges were modeled with the same shell elements that were used for the deck. This allowed for the in-plane stress as well as the slight torsional and flexural stiffness of the flanges to be accounted for by the model. The ratio of element length to girder length was approximately 1:60.

The diaphragms were modeled with two-node beam elements. One line of elements was created at the mid-height of the diaphragm, and a rigid link, illustrated in Figure 2.1, was used to create nodes on the ends that were representative of both the top and the bottom of the actual diaphragm. This allowed for the total height of the diaphragms to be considered. These nodes were then attached to the girder by truss elements. The

element stiffness was determined by considering the stiffness of the connection plate in the bridge.
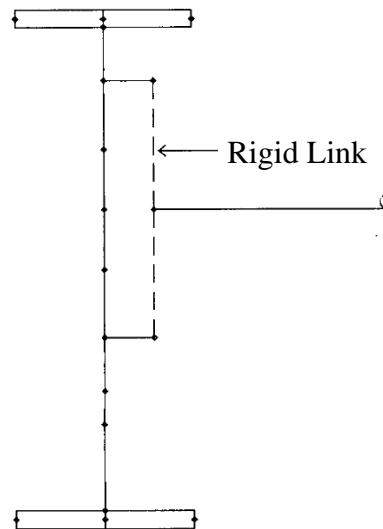
Figure 2.1 Diaphragm-to-Girder Connection Detail Using a Rigid Link (Tedesco, Stallings, and Tow 1995)

The type of rigid links that were used in the diaphragm was employed elsewhere in the model as well. These links were used to bridge the physical gap between elements to establish composite behavior in the model. This purpose was served by connecting the web to the flanges of the girders and the flanges to the deck.

Dynamic analyses were conducted modeling the truck wheel loads as concentrated loads acting at the nodes of the deck slab elements. The results indicated that the removal of diaphragms would not have a significant effect on the bridge response. Increases in flexural stress and vertical deflection for the model without diaphragms over those for the model with diaphragms were found to be 8 and 9 percent, respectively, for the most highly stressed girders. Maximum positive deck slab bending moment increased by only 14 percent, and maximum negative deck slab bending moment decreased by almost one-half.

7

Zokaie (2000) presented a report on the development of live load distribution formulas for the *AASHTO LRFD Bridge Design Specifications*. Finite-element analyses of typical bridges were used to investigate the sensitivity of live load distribution to specific parameters such as girder spacing, span length, girder thickness, and slab thickness. Diaphragm effects were neglected. The deck slab was modeled using plate elements, and Zokaie states that the model also accounted for the eccentricity of the girders. New distribution formulas were generated based on the results of the sensitivity analyses. Accuracy of the generated formulas was evaluated by comparison with the results of finite-element models of representative bridges, but no experimental verification was reported by Zokaie (2000).

Huo, Wasserman, and Zhu (2004) also used FEM to explore live load distribution of girder bending moment for a variety of bridge structures. Modeled using ANSYS™ 5.7, all superstructures were analyzed in the linearly elastic range. Four-node shell elements that had six DOF per node were used to model the bridge deck slab. These were selected to incorporate both membrane and bending stiffnesses and in- and out-of-plane bending. The precast concrete girders were modeled using three-dimensional, two-node beam elements with six DOF per node. The girder elements and the slab elements were "integrated" to reflect composite behavior. Hinges and rollers modeled the bridge supports.

The finite-element results thus obtained were used as a baseline in determining whether a simplified method of calculating live load distribution factors in bridges was sufficiently accurate. The procedure, known as Henry's method, compared favorably

with the AASHTO LRFD and the AASHTO standard methods as well as with the FEM results (Huo, Wasserman, and Zhu 2004).

Green, Yazdani, and Spainhour (1994) created ANSYS™ FEMs to study the effects of intermediate diaphragms, temperature variability, bearing stiffness, and girder skewness on precast, prestressed bridge girders. The element they selected to model the bridge girders, deck slab, and diaphragms was a three-dimensional reinforced concrete element. Though this element was capable of simulating concrete cracking and crushing, plastic deformation, and creep, these properties were not utilized because the girder behavior under the assumed service load fell well within the elastic region of the members. The connection between the girders and the diaphragms was assumed to be rigid as a result of monolithically placed concrete.

Unlike the study conducted by Tedesco, Stallings, and Tow (1995), this study showed that for *straight* bridges, intermediate diaphragms helped to stiffen the girders and reduce maximum deflection by about 18–19 percent. While the diaphragms helped to stiffen girders in bridges with increased skew angles as well, the reduction in deflection decreased with increased skew angles (Green, Yazdani, and Spainhour 2004).

2.4 FINITE-ELEMENT MODELING OF BRIDGES WITH LOAD TESTING VERIFICATION

Mabsout et al. (1997) published a comparison of four different FEM techniques used to calculate wheel load distribution factors. Using SAP90™ and ICES-STRUDL II™, they created four models of a bridge made with steel girders and a concrete slab deck. The ratio of element length to girder length was approximately 1:16, which represents a significantly coarser mesh than that employed by Tedesco, Stallings, and Tow (1995).

For the first three models, the bridge deck was modeled using quadrilateral shell elements with five DOF per node (Mabsout et al. 1997). The first two models employed a space-frame member with six DOF per node to model the steel girders. In the first model, the centroid of the girder coincided with the centroid of the concrete slab, but in the second model an eccentricity between those centroids was imposed using a rigid link. The third model used a quadrilateral shell element for the girder web and a space-frame element for the girder flange, and once again a rigid link was used to model the eccentricity between the flange and bridge deck. Their fourth FEM used isotropic eight-node brick elements for the deck slab and quadrilateral shell elements for the girders.

The models employed gave an error of approximately 5 percent when compared to the total bending moment expected at the critical section of the bridge. Expected bending moments were calculated using both strain and deflection readings from numerous load tests. From the four models employed, Mabsout et al. concluded that when investigating the load-carrying capacity of noncomplex, straight steel girder bridges, quadrilateral shell elements are sufficiently accurate for the concrete slab deck and concentric space frame elements for the girders. The other cases could be employed to accurately realize the actual boundary conditions.

Barr, Eberhard, and Stanton (2001) reported on SAP2000™ finite-element models that they created to evaluate the procedures for computing flexural live-load distribution factors found in AASHTO-LRFD, AASHTO Standard, and the Ontario Highway Bridge Design Code (OHBDC). For their initial model, they paid special attention to the mesh size. The need to simulate the loading with a variety of loading conditions

and bridge skew angles dictated the need for a fine element mesh in the deck. They therefore selected a node spacing of roughly 2 ft in the transverse direction and 1 ft in the longitudinal direction. These correspond to a ratio of element length to girder length of approximately 1:80 for two of the spans and 1:137 for one of the spans. This represents a finer mesh than those used by either Tedesco, Stallings, and Tow (1995) or Mabsout et al. (1997).

A series of shell elements was used to represent the bridge deck, and rigid links connected the deck to the frame elements used to model the prestressed concrete girders. Rather than explicitly modeling the prestressing strands in the girders, the values of the modulus of elasticity for the various components of the finite-element model were measured from material tests. The intermediate diaphragms and the pier diaphragms were modeled using shell elements. The pier diaphragms were then connected, with rigid constraints, to the pier caps, which were modeled with 1-foot-long frame elements—as were the columns. The elastomeric bearings were represented by releasing horizontal displacements.

In conducting their investigation, Barr, Eberhard, and Stanton created a series of progressively more detailed models. Their original model, which was very similar to the model used to develop the AASHTO LRFD Specifications, did not include lifts (deck build-up over the girders), intermediate diaphragms, end diaphragms, or span continuity. Each ensuing model then added one of these elements. Model 2 included lifts. Model 3 built on Model 2 and added intermediate diaphragms. Model 4 then included end diaphragms. Finally, in Model 5, two adjacent spans were added, and the three spans were made continuous.

From the progression of the model, the authors were able to study the effects of lifts, intermediate diaphragms, end diaphragms, and span continuity. They concluded that incorporating the lift slightly increased the composite girder stiffness by increasing the effective thickness of the deck, which therefore increased the transverse bending stiffness relative to the longitudinal stiffness. The inclusion of the intermediate diaphragms had less impact than any of the other three variables, though at high skew angles, they were found to be slightly beneficial to the exterior girders. The end diaphragms were found to reduce the positive midspan moment, especially with a high skew angle and a torsionally stiff end diaphragm. Finally, the study found that continuity increased the longitudinal stiffness but did not affect the transverse stiffness (Barr, Eberhard, and Stanton 2001).

The distribution factors calculated from Model 1 were found to be, on average, 6 percent lower than those calculated using the AASHTO LRFD Specification. This is not unexpected as the code was based on a single-span model similar to Model 1. Those calculated from Model 5, on the other hand, were approximately 28 percent lower than those calculated using the LRFD code. Similarly, the distribution factors calculated using the AASHTO Standard Specification were closer to those calculated from Model 1 than Model 5. This is also due to the fact that the AASHTO Standard Specifications do not account for the effect of skew (Barr, Eberhard, and Stanton 2001).

The final model, Model 5, was judged to be most closely representative of the physical structure being modeled. In comparing moments calculated from Model 5 and those calculated from measured strains, for two of the bridge girders the magnitude of error between measured and computed moments was about the same as the discrepancy

between individual strain gauge readings. The largest difference was less than 6 percent, which provided strong evidence that the finite-element model "reflected well the behavior of the prototype bridge" being studied (Barr, Eberhard, and Stanton 2001).

Eamon and Nowak (2002) used ANSYS™ to study the effects of multiple secondary elements, including diaphragms, on load distribution in both the elastic and inelastic ranges. They studied the effects of diaphragms for both composite steel girder bridges and prestressed concrete girder bridges. Two types of FEMs were created for their study: a simplified model, which was utilized to analyze maximum girder moments and deflections, and a more detailed model, which was used to analyze deck behavior.

The simplified concrete models used three-dimensional line elements with six DOF per node to simulate the bridge girders and diaphragms. These were attached directly to the bottom of the deck, which—like the sidewalk and barriers—was modeled using solid elements. The solid elements used to model the deck were eight-node brick elements with three DOF per node. The reinforcing steel was not found to have a significant effect on the deck stiffness, so it was not explicitly included in the elastic analysis. The model allowed no slip between the deck and the girders. All elements in the detailed concrete models were brick elements with a mesh density that was finer than that of the simplified models. The FEM results matched field-measured deflections and strains within 5 percent.

The study results indicate that diaphragms are more effective at wider girder spacings and longer spans, and an increased number of diaphragms has no significant effect. The diaphragms were found to reduce the maximum girder moment by up to 13 percent—4 percent on average. The diaphragms were found to "pull down exterior girders and

raise interior girders," which evens girder deflections (Eamon and Nowak 2002). The study concluded that the presence of secondary elements is significant to the bridge behavior.

Fu and Lu (2003) reported on a nonlinear analysis using FORTRAN™ and RESIDU™. The authors explain that although the steel girders in the bridge that they investigated remained within their elastic range, the concrete deck could not be adequately represented by a linearly elastic model, because concrete is a material that exhibits nonlinear behavior with a very small tensile strength. The flanges of the rolled steel I-girders were modeled with plate elements while the web was modeled with plane-stress elements. Both of these were eight-node, isoparametric, quadrilateral elements.

The deck was also modeled using isoparametric quadrilateral elements. Effects of deck cracks that were predicted through stress analysis of Gauss points were distributed homogeneously throughout the entire element by modeling the element as weaker than the surrounding, uncracked elements. This weakness was modeled by setting the modulus of elasticity of the cracked element, and the stress at the affected Gauss points, to zero.

The reinforcement of the deck was also explicitly modeled. Each set of reinforcement was represented by a smeared two-dimensional membrane layer with equivalent thickness, which was modeled using an isoparametric plane-stress element. This embedded membrane layer then acted "as an integral part of the element."

The results of the study show that while the deflection results of the finite-element method are close to those measured experimentally, the results from the transformed

area method, which is the traditional AASHTO Standard design method, are not. The

authors did not report any comparisons that showed that a linear elastic model was

deficient, and the results of the nonlinear analysis are not compared to results from a

linear analysis of the same model.

Zhou, Rizos and Petrou (2003) presented the results of an investigation into the

effects of various structural components: (a) composite action, (b) girder spacing to slab

thickness ratio, and (c) presence of diaphragms. They also noted the limitation of

previous studies regarding the nonlinearity of concrete. To correct this oversight, they

constructed models in ANSYS™, which was readily available.

The ANSYS™ *Solid 65* element used to model the concrete deck "accommodates

cracking and crushing of concrete and yielding of the reinforcement, among other non-

linear characteristics." It is limited, however, in that the reinforcement is "smeared

throughout the element" and "full bond is assumed between reinforcement and

concrete." Shell elements and rigid links were used to model the steel girders and steel

diaphragms, respectively.

The results of the study of the effects of composite action and girder spacing to slab

thickness ratio do not differ significantly from previous, linear studies. In contrast, the

nonlinear behavior of the concrete does affect the results of the diaphragm analysis as

compared to that found in the literature Zhou, Rizos and Petrou (2003) reviewed. This

effect is only noted, however, at significantly large girder loads.

Wan et al. (2004) used ANSYS™ to investigate four parameters for service load

conditions, including the effect of diaphragms. Eight-node shell elements were used to

model the glass fiber-reinforced polymer (GFRP) deck flanges and webs and the steel

15

girders. A link element was used to model the steel diaphragms. The authors

concluded that the diaphragms prevent girder rotation, increase stiffness of the entire

structure, and assist slightly in the transverse load distribution through the deck. They

noted, however—as did Zhou, Rizos, and Petrou (2003)—that the presence of

diaphragms has minimal effect on the net deflection when the load is small.

Xia and Brownjohn (2004) published a technique for model updating that "can

produce a systematically validated FE model by correcting uncertainties from modeling,

geometry, physical parameters, and analysis." One important aspect of this technique is

to accurately model uncertainties in a structure. One approach that they propose is to

model damaged zones with "weak" elements which cover the area of the damage and

are refined, using the measured data, to quantify the residual stiffness and load-carrying

capacity.

For finding the effective modulus of elasticity and other material properties for the

structure in the undamaged state, a two-step approach was presented. First, prior to

loading, a model for the uncracked structure was validated using experimental results.

This provided a reasonable baseline from which to identify damage. Second, after

loading, the dynamically measured data was used to post-validate the model. The

authors cautioned that "if the FE model validating goes straight to the damaged case,

then the identified damage may reflect uncertain structural parameters not associated

with damage; furthermore, the updating may not converge because of too large

differences between the modal properties generated by the FE model and those

measured" (Xia and Brownjohn 2004). The load-carrying capacity of the bridge can

then be systematically validated using dynamics-based model updating techniques.

Chung, Liu, and Sotelino (2006) utilized ABAQUS™ to investigate the effects of

secondary elements on the lateral load distribution of steel girder bridges and, through

nonlinear analysis, to explore the effects of deck cracking on load distribution. The

concrete deck was modeled using eight-node shell elements. The steel girders and

diaphragms were modeled using three-node beam elements. The connections between

the deck and the girders—as well as between the girders and the diaphragms—were

established through rigid links. The maximum difference between the predicted and the

experimentally measured deflections was 9 percent at midspan of the exterior girder.

The maximum difference between the calculated and measured strains was less than 7

percent.

The study found that modeling the diaphragms resulted in a load distribution factor

that was as much as 12 percent less than the load distribution factor determined

according to the AASHTO LRFD specifications. Like Eamon and Nowak (2002), the

authors concluded that the presence of secondary elements significantly helps the

transverse load distribution of girder bridges. In addition, they observed that transverse

deck cracking reduces the stiffness of the bridge but does not significantly affect

transverse distribution of moments to girders (Chung, Liu, and Sotelino 2006).

2.5 SUMMARY OF THE FINDINGS

When creating a finite-element model to study the live load effects on various bridge

components, there are certain minimum requirements which must be met. These

minimum requirements are well-summarized in the *AASHTO LRFD Bridge Design

Specifications.* When selecting elements, the main concern is that the element

configuration selected has a sufficiently fine mesh and sufficient degrees of freedom to

account for the movement of the girders or the bridge deck under the loading. The

selection of element type, such as beam element or plate-bending element, is not as

critical as the effects allowed for by the element selected. The studies conflict as to the

significance of the inclusion of secondary elements such as diaphragms on the bridge

response, and there is insufficient information to conclude that the nonlinearity of the

concrete deck needs to be accounted for in order to achieve an accurate model.

CHAPTER 3: BRIDGE DESCRIPTION AND HISTORY

3.1 INTRODUCTION

The prestressed concrete girder bridge that was studied is located in Huntsville, Alabama along northbound bridge Spans 10 and 11 of I-565. This chapter summarizes the history of the structure, its current conditions, and the proposed fiber-reinforced polymer repair system.

3.2 HISTORICAL OVERVIEW

Construction of the elevated Interstate Highway 565 bridge structures began in January 1988 and was completed in March 1991 (ALDOT 1994). Single span and multispan continuous units were erected for both the northbound and southbound lanes. Bridges consist of either steel or prestressed concrete girders supporting a cast-in-place composite reinforced concrete (RC) deck. Most of the prestressed concrete girders are bulb-tee girders, either AASHTO-PCI BT54 or BT63, which were made continuous for live load by means of the cast-in-place deck and diaphragms. The other prestressed concrete girders are standard AASHTO girders (Swenson 2003).

During a routine bridge inspection in 1992, hairline cracks were discovered in some of the bulb-tee girders. Because hairline cracks often form at early ages in prestressed concrete girders, this did not necessarily indicate a serious problem. Eighteen months later, another inspection was conducted in March and April of 1994. Inspectors discovered that many of the earlier cracks had propagated and widened (ALDOT 1994).

19

Typical crack widths ranged from 0.002 in. to 0.25 in. Figure 3.1 presents the pattern of

cracking found in 1994 in one 54-in. girder of Span 5 (Barnes et al. 2006). Many of the

cracks were inclined and as a result intersected transverse reinforcing bars. These

inclined cracks were limited to a width of approximately 0.06 in. In the bottom flange,

however, the cracks were vertical and therefore crossed only the longitudinal

prestressing strands. These larger cracks (widths up to 0.25 in.), such as those found on

the girders shown in Figure 3.2, were visible from the ground (Barnes et al. 2006).
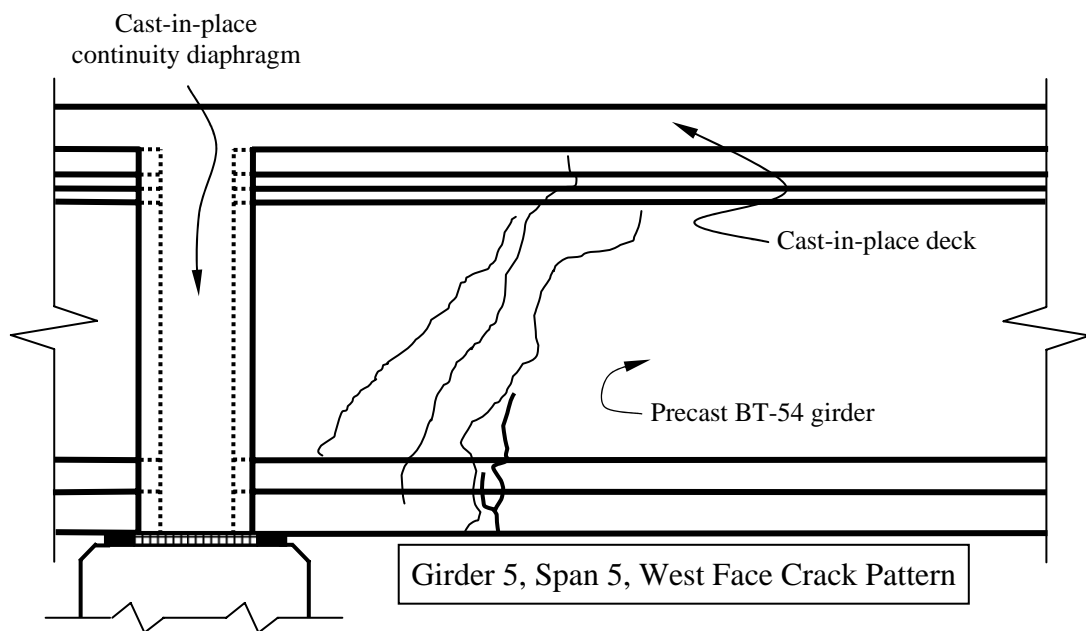
**Figure 3.1 Typical Pattern of Cracking in End Region of Precast Girder
(Barnes et al. 2006) Note: The bolder line on the bottom-flange cracks indicates a
greater crack width.**

Monitoring to determine the cause of the cracks commenced. After several weeks of

load testing, ALDOT personnel concluded that traffic and wind loads were not the most

likely causes of the cracks. Traffic loading was an unlikely cause because the largest

cracks formed where service live loads would be expected to induce compression

(Barnes et al. 2006). The temperature gradient between the bridge deck and the

underside of the superstructure was the suspected cause. The temperature gradient

caused an upward deflection of the superstructure which was restrained at interior

supports. This resulted in positive moments at the continuous girder ends which

ultimately caused the cracks (Swenson 2003).

To prevent a total collapse of the structure in the event that the girders failed,

temporary, or false, supports were installed under all spans which contained cracked

girders (Barnes et al. 2006). The supports were installed within 10 ft of the support bent

(Swenson 2003). A small space was left between the top of the false supports and the

bottom of the girders to allow for the deflection of the girders (Gao 2003).

Two measures were also attempted to alleviate the problem. As shown in Figure 3.3,

the cracks were injected with epoxy. Unfortunately, this proved to be relatively

ineffective as new cracks later formed near some of the epoxy-injected cracks (Gao

2003). The new cracks had widths of 0.002 in. to 0.030 in. These new cracks

discouraged ALDOT personnel from considering epoxy injection as a feasible final

solution.

The second measure to be attempted was to release some of the prestressed girders

from the continuity diaphragm. To do this, the continuity diaphragm was sawed around

the girder, thus allowing the girder to move independently of the diaphragm and

effectively changing it from a continuous to a simply supported beam. This was

performed at Bent 11, which supports the continuity diaphragm for the two-span unit

modeled in the current study. The sawing technique proved too difficult and was

abandoned after cutting portions of the diaphragm at only a few girder ends (Swenson

2003).

21
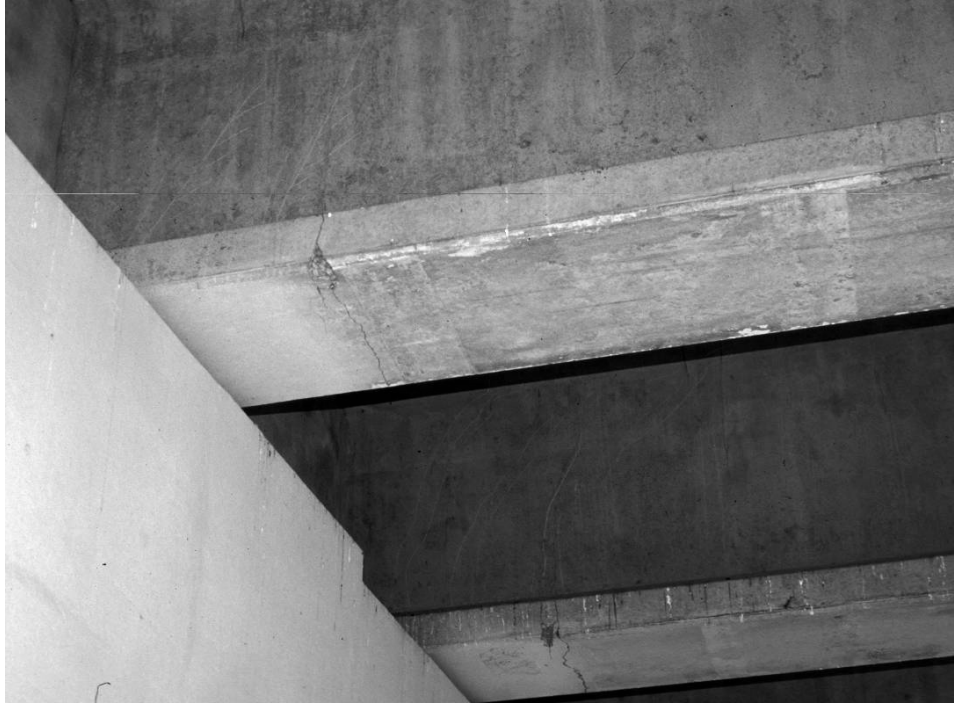
Figure 3.2 Cracked Pretensioned Bulb-Tee Girders (Barnes et al. 2006)

Figure 3.3 Epoxy-Injected Cracks

Swenson (2003) proposed a fiber-reinforced polymer (FRP) repair technique to restore structural capacity. To determine the efficacy of the repair technique, load tests needed to be conducted before and after installation of the FRP. The pre-repair load tests occurred on June 1 and 2, 2005. The FRP repair system has been designed, but ALDOT has not yet accepted bids for the installation contract.

Structural details of the I-565 bridge structure are presented in Section 3.3. Section 3.4 includes a brief summary of research that was conducted to determine the cause of the cracking and its potential ramifications with respect to the structural integrity of the bridge.

3.3 DETAILS OF THE CRACKED I-565 BRIDGE STRUCTURE

3.3.1 Bridge Geometry

The bridge section investigated for this report consists of a two-span bridge portion composed of nine prestressed concrete bridge girders made continuous for live load and a cast-in-place reinforced concrete (RC) bridge deck.

Figure 3.4 presents a cross-sectional view of the bridge. The bridge deck is 70.75-feet wide with a thickness of 6.5 in., not including the variable-depth build-up over each girder. The bridge deck was designed to act compositely with the girders. This composite action was accomplished by extending the girder stirrups into the deck slab and by roughening of the top surface of the girders (Swenson 2003). The nine girders are spaced 96 in. center-to-center. Figure 3.5 shows the dimensions of the BT54 girder used. A cast-in-place traffic barrier rail runs the length of the bridge on both edges of the deck (ALDOT 1987).

23

Cast-in-place
concrete barrier

6.5"

AASHTO BT54
girders

3' - 4½" 8' – 0"

64' – 0"

70' – 9"
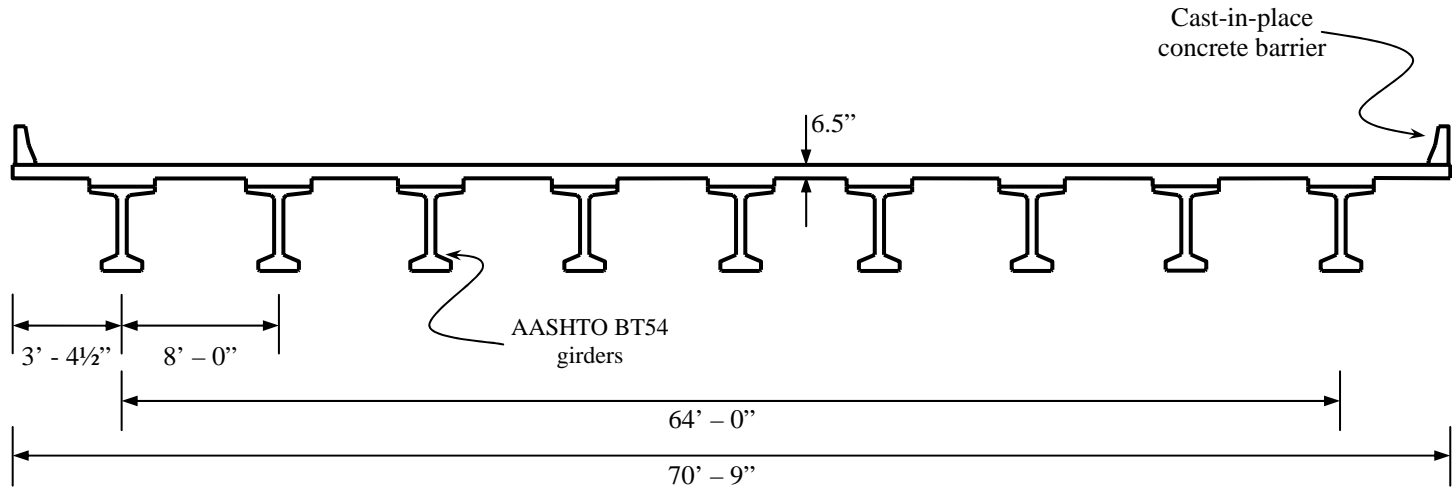
Figure 3.4 Bridge Cross Section (Swenson 2003)
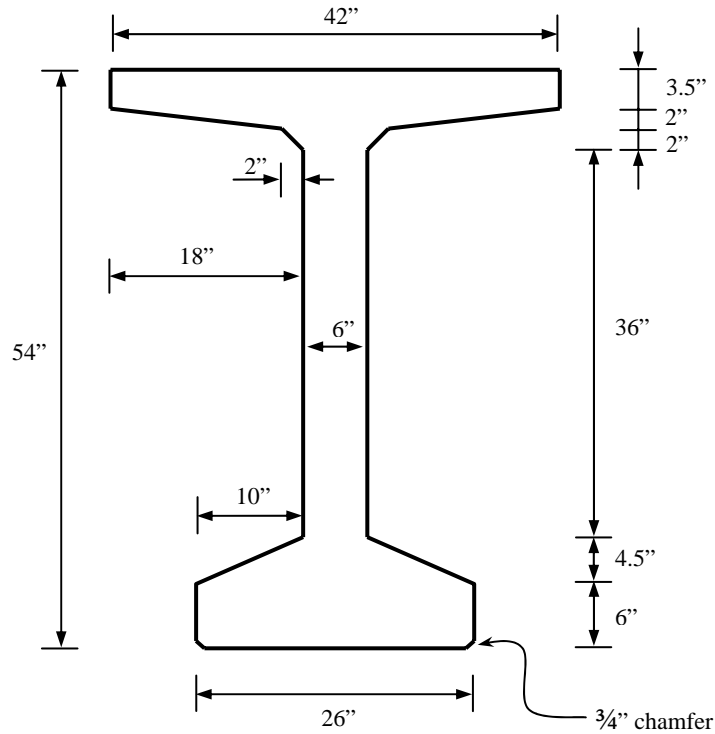
Figure 3.5 BT54 Cross Section Dimensions (Swenson 2003)

Figures 3.6 and 3.7 depict the plan view of the portion under investigation. The total

length of the two-span continuous unit is 200 ft. Figure 3.8 presents an elevation view

of the two-span continuous unit. The bridge girders are BT54s with both straight and

draped prestressing strands. See Figures 3.9 and 3.10 for bonding configurations and

strand placement at the girder end and the girder midspan, respectively. As depicted in

Figure 3.11, the bridge girders are numbered one through nine, proceeding from the

west side to the east side of the bridge.

Continuity was created along a girder line by casting a continuity diaphragm which

restrained the rotation of the adjacent girder ends. A portion of the deck slab was cast

simultaneously with the continuity diaphragms. The vertical reinforcement present in

the continuity diaphragms consists of No. 4 and No. 6 mild steel reinforcing bars.

Figure 3.12 depicts bent No. 6 reinforcing bars—which were intended to provide

positive moment continuity—extending from the ends of the prestressed concrete bulb-

tee girders. Eight bars extend from 41 in. into each girder end to 8 in. into the

continuity diaphragm. A vertical leg located in the continuity diaphragm is 12 in. long

(Swenson 2003).

3.3.2 Crack Locations

In April 2004, a team from Auburn University conducted a thorough study of the

current conditions of the two-span continuous bridge unit. This study included

determination of the locations of the cracks on both faces and both spans of all nine

girders. For illustrations of the locations of the cracks, see Figures 3.13-3.21 (Fason

and Barnes 2004). The figures differentiate between cracks that have been sealed with

epoxy and those that have not.
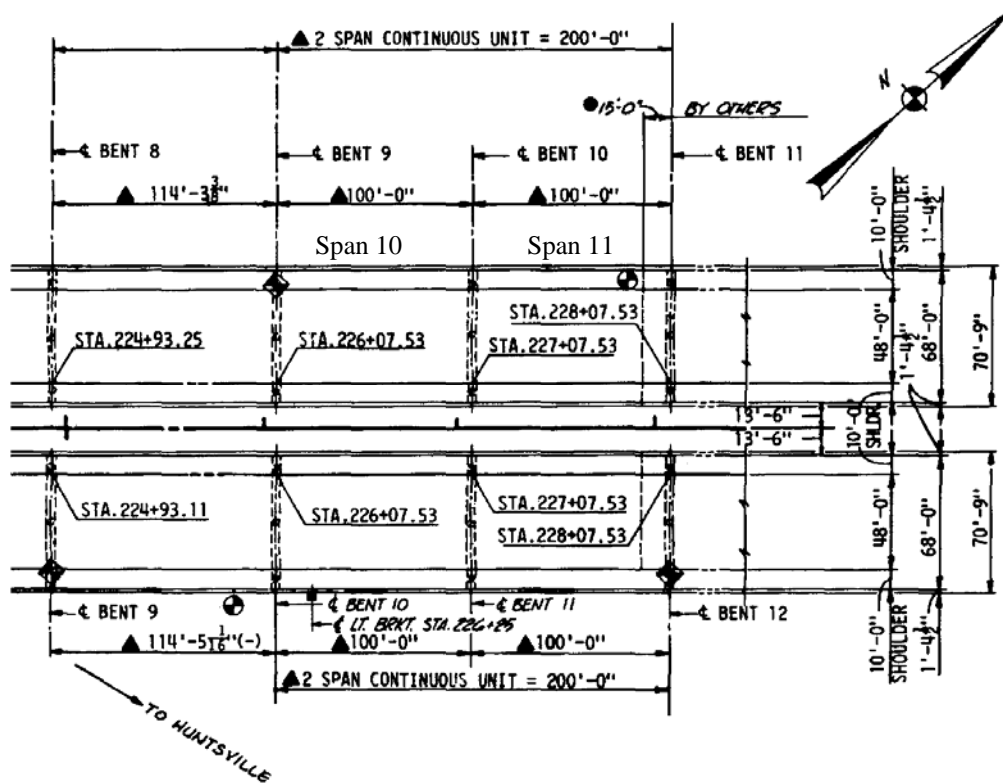
Figure 3.6 Plan View of the Two-Span Continuous Unit (ALDOT 1987)

Figure 3.7 Detailed Plan View of the Two-Span Continuous Unit (ALDOT 1987)
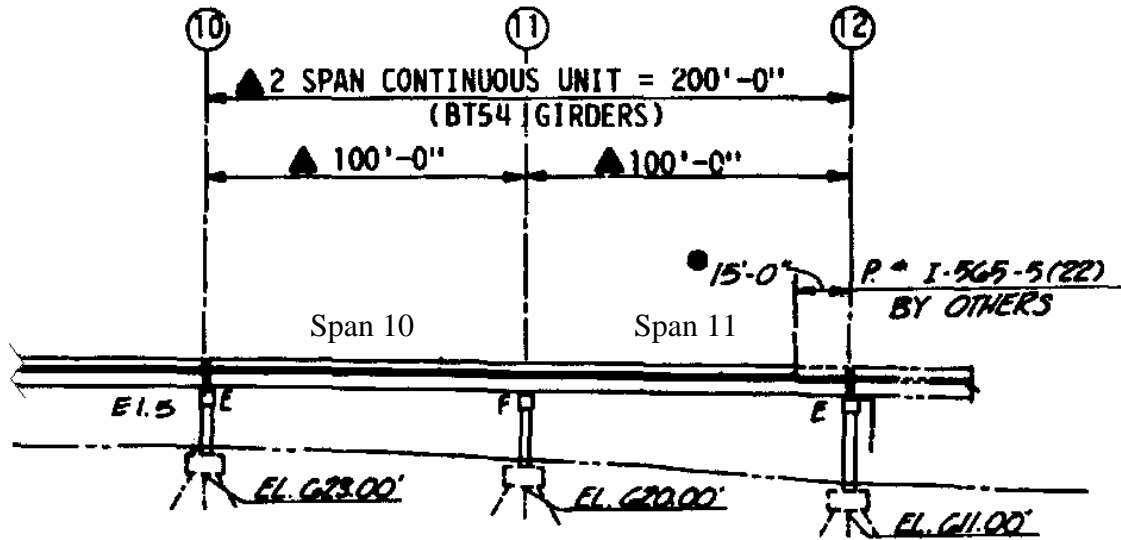
Figure 3.8 Elevation View of the Two-Span Continuous Unit (ALDOT 1987)

- ● Fully bonded tendon (0.5" Special)
- ○ Debonded tendon (48" debond length, 0.5" Special)
- □ Debonded tendon (168" debond length, 0.5" Special)
- ● Fully bonded tendon (7/16")
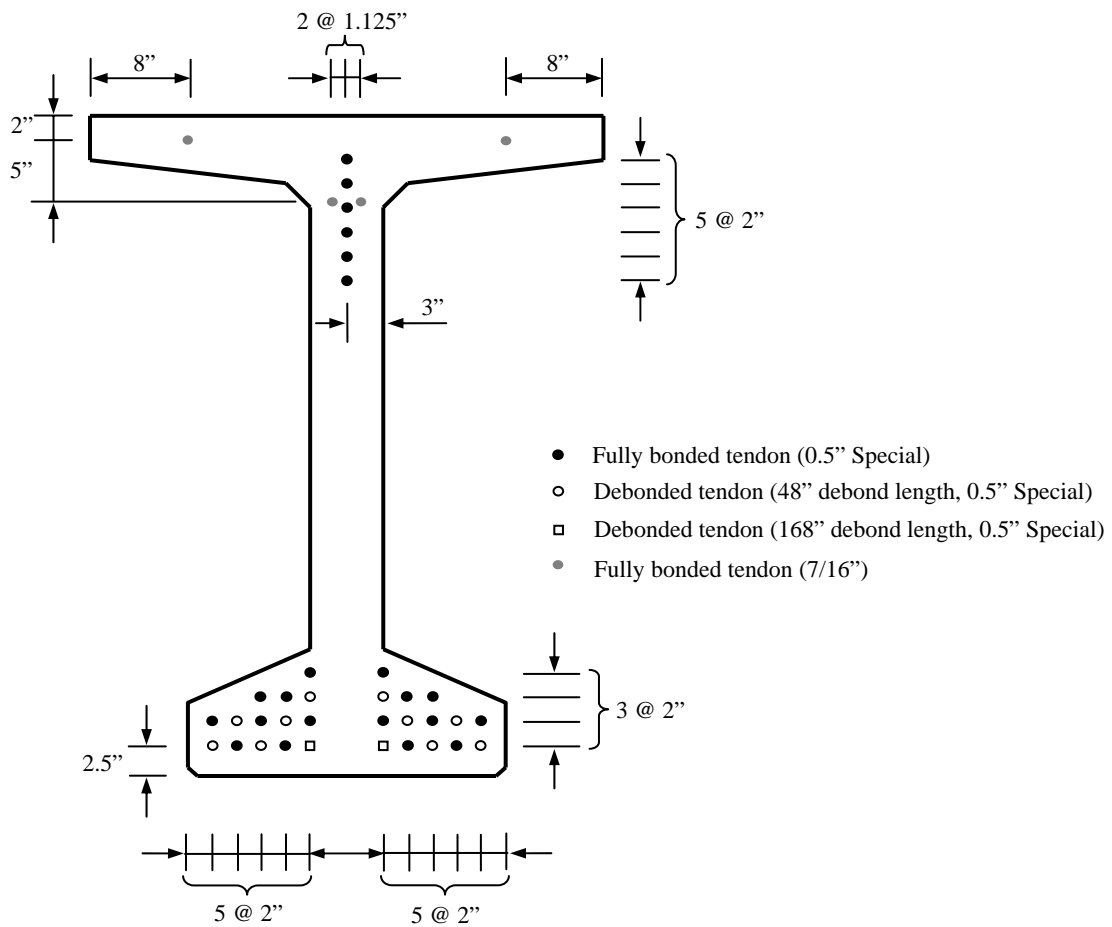
Figure 3.9 Girder End Strand Pattern (Swenson 2003)

28
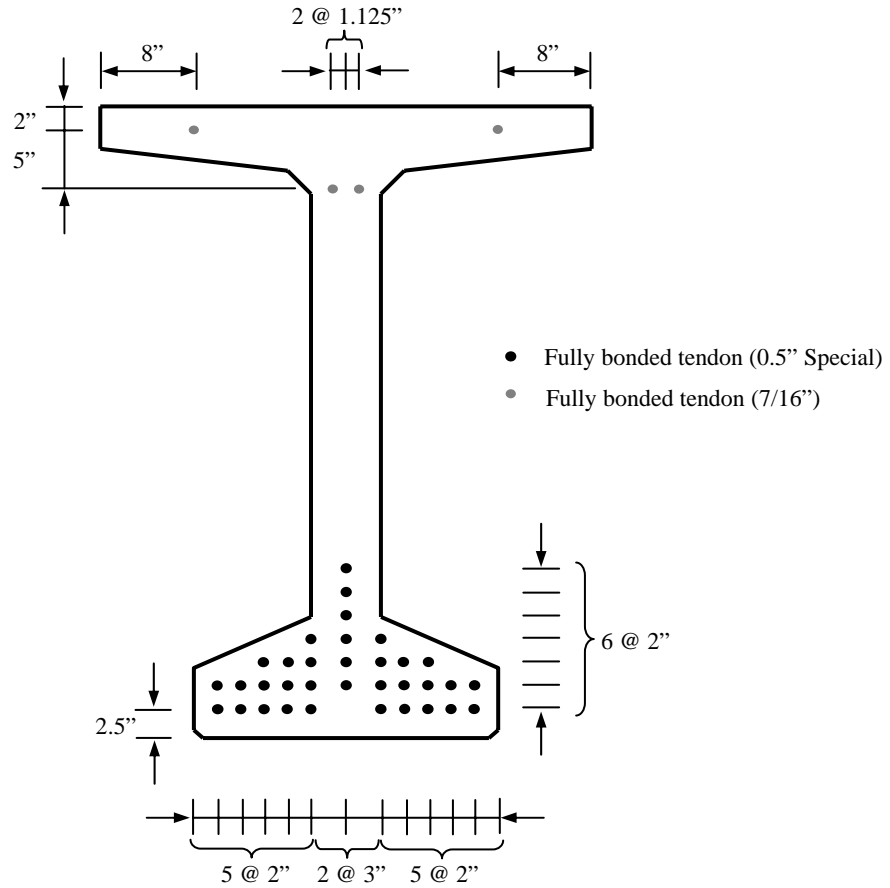
Figure 3.10 Girder Midspan Strand Pattern (Swenson 2003)

- Fully bonded tendon (0.5" Special)
- Fully bonded tendon (7/16")

2 @ 1.125"

8"   8"

2"
5"

6 @ 2"

2.5"

5 @ 2"   2 @ 3"   5 @ 2"

N

Bent 10   Bent 11   Bent 12

Span 10   Span 11

1
2
3
4
5
6
7
8
9

Girder End

Continuity Diaphragm

Area Being Inspected
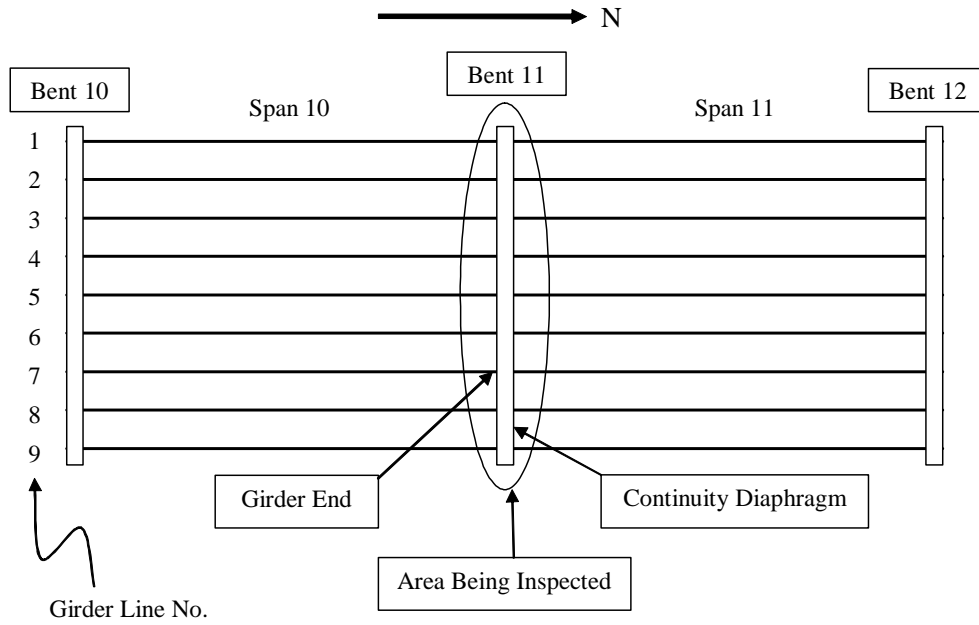
Girder Line No.

Figure 3.11 Girder Numbering System (Fason and Barnes 2004)

Figure 3.12 Bent Bar Detail at Continuity Diaphragm (Swenson 2003)

Labels within figure:

℄

8"

3"

MK-651 bent bar (8 per girder end made continuous)

Black – 9" x 24.5" x ¾" Elastomeric Bearing Pad
Checked – ¾" Premolded Bituminous Filler

¾" diameter dowel, 21" long

MK-651 bent bar detail

12"

49"

Girder 1 - Span 10 - East Face

10' 9' 8' 7' 6' 5' 4' 3' 2' 1'

Girder 1 - Span 11 - East Face

1' 2' 3' 4' 5' 6' 7' 8' 9' 10'

Girder 1 - Span 11 - West Face

10' 9' 8' 7' 6' 5' 4' 3' 2' 1'

Bolt

Girder 1 - Span 10 - West Face

1' 2' 3' 4' 5' 6' 7' 8' 9' 10'

- - - - - = sealed   ——— = unsealed
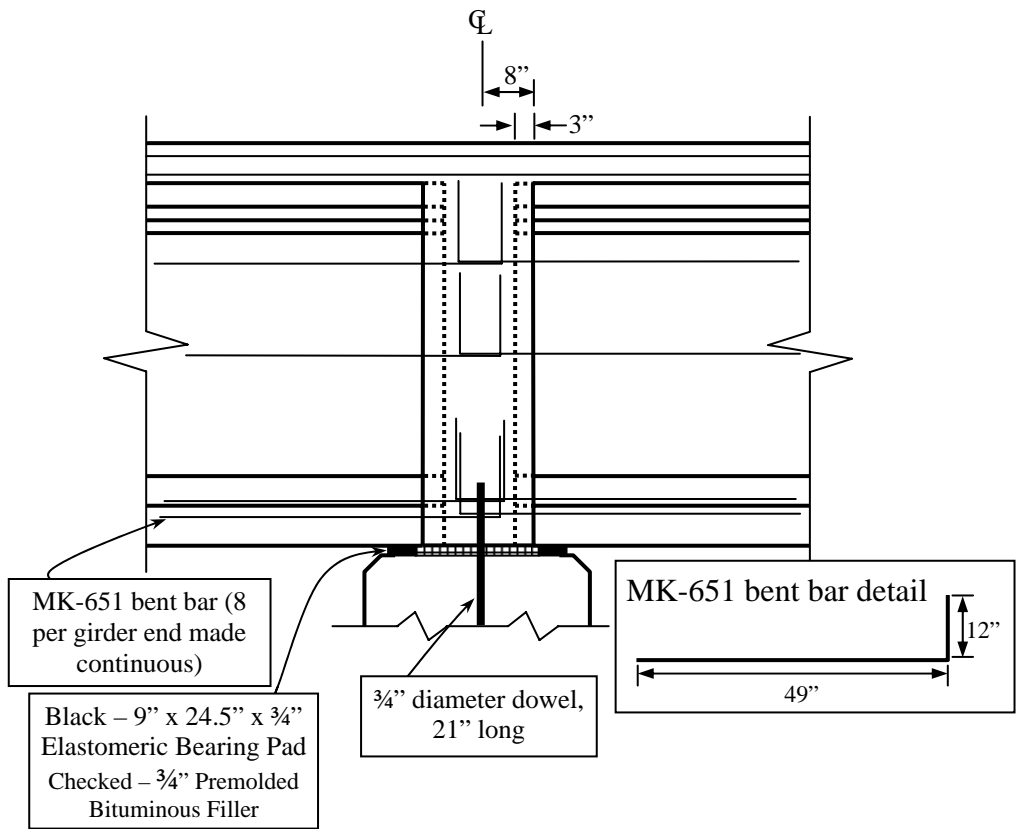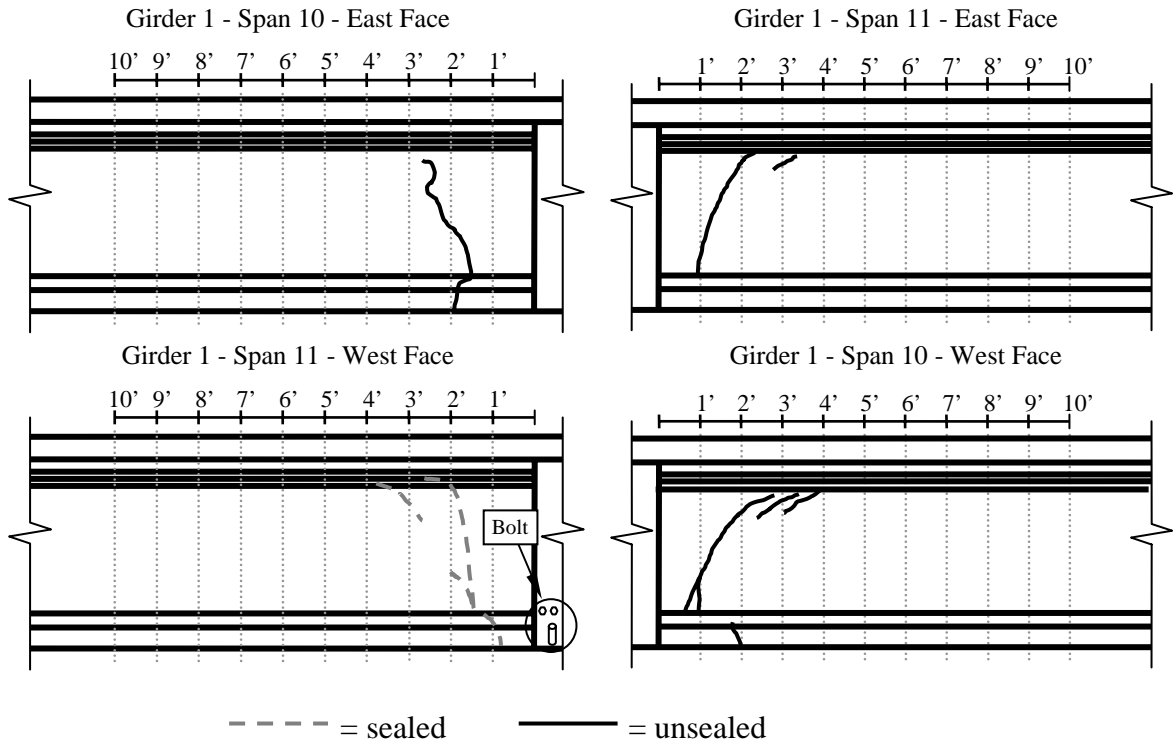
Figure 3.13 Girder Line 1 Cracking (Fason and Barnes 2004)

Girder 2 - Span 10 - East Face

10' 9' 8' 7' 6' 5' 4' 3' 2' 1'

No cracking

Girder 2 - Span 11 - East Face

1' 2' 3' 4' 5' 6' 7' 8' 9' 10'

No cracking

Girder 2 - Span 11 - West Face

10' 9' 8' 7' 6' 5' 4' 3' 2' 1'

No cracking

Girder 2 - Span 10 - West Face

1' 2' 3' 4' 5' 6' 7' 8' 9' 10'

No cracking

- - - - - = sealed   ——— = unsealed
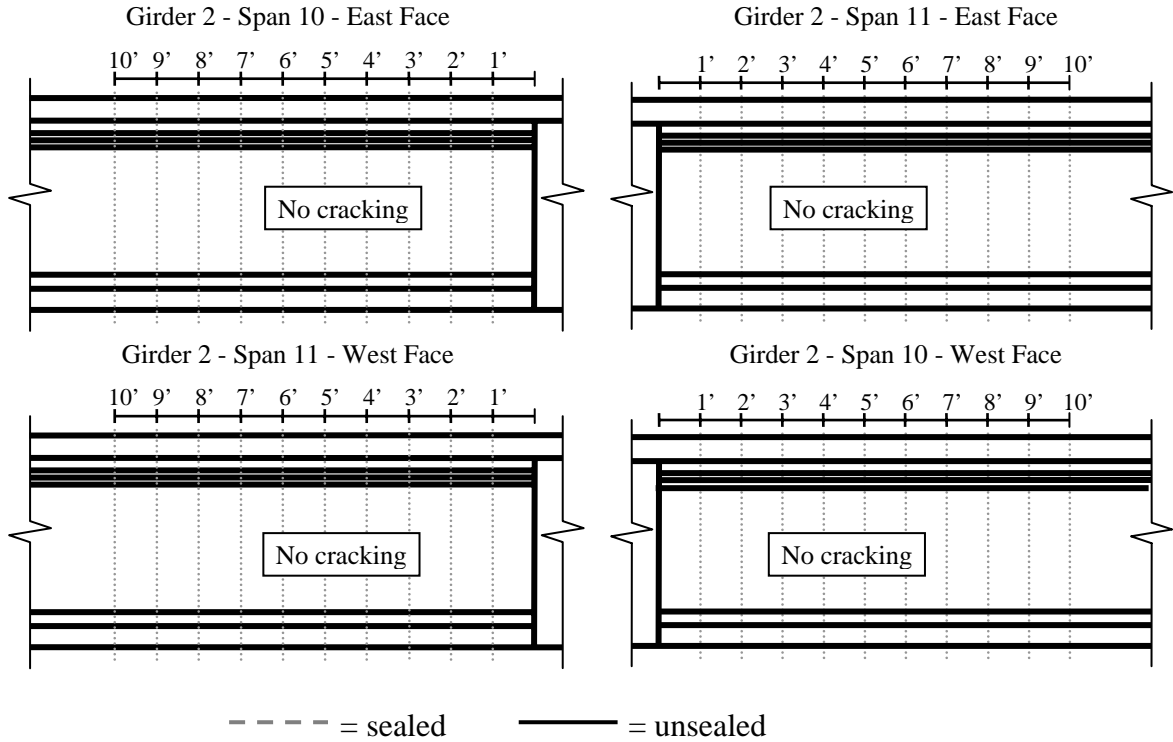
Figure 3.14 Girder Line 2 Cracking (Fason and Barnes 2004)

31

Girder 3 - Span 10 - East Face

10' 9' 8' 7' 6' 5' 4' 3' 2' 1'

Girder 3 - Span 11 - East Face

1' 2' 3' 4' 5' 6' 7' 8' 9' 10'

Girder 3 - Span 11 - West Face

10' 9' 8' 7' 6' 5' 4' 3' 2' 1'

Girder 3 - Span 10 - West Face

1' 2' 3' 4' 5' 6' 7' 8' 9' 10'

- - - - - = sealed   ———— = unsealed
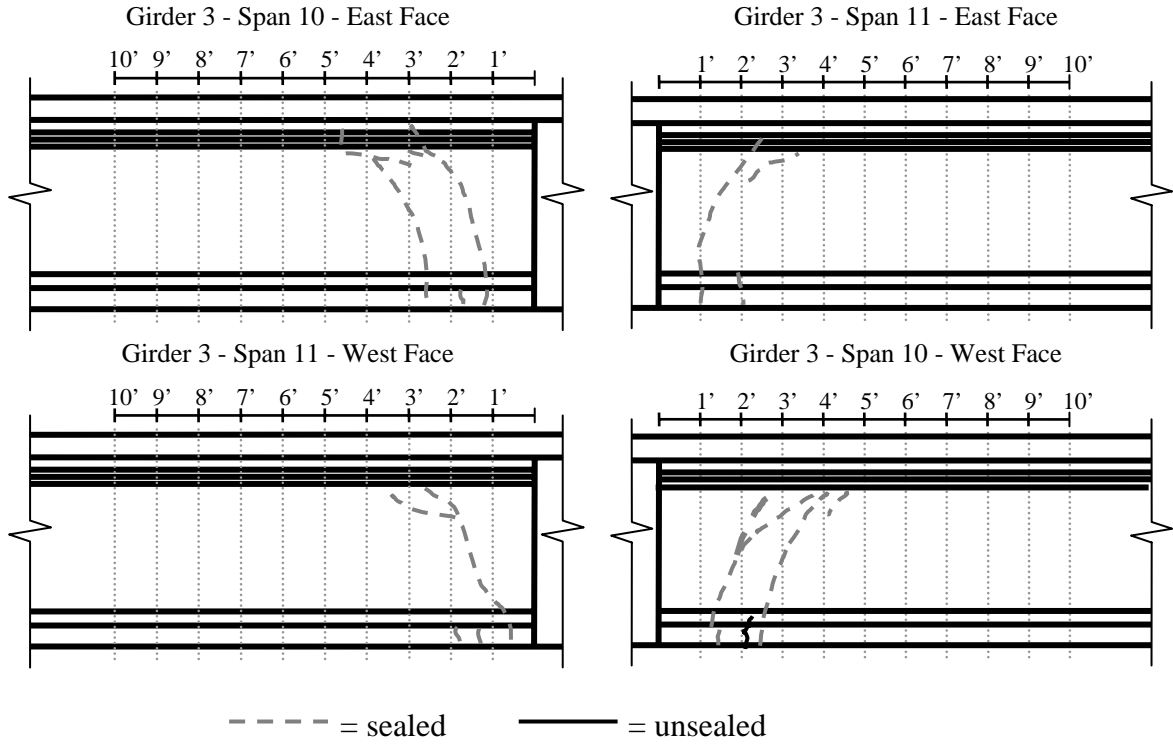
Figure 3.15 Girder Line 3 Cracking (Fason and Barnes 2004)

Girder 4 - Span 10 - East Face

10' 9' 8' 7' 6' 5' 4' 3' 2' 1'

Girder 4 - Span 11 - East Face

1' 2' 3' 4' 5' 6' 7' 8' 9' 10'

Girder 4 - Span 11 - West Face

10' 9' 8' 7' 6' 5' 4' 3' 2' 1'

Girder 4 - Span 10 - West Face

1' 2' 3' 4' 5' 6' 7' 8' 9' 10'

- - - - - = sealed   ———— = unsealed
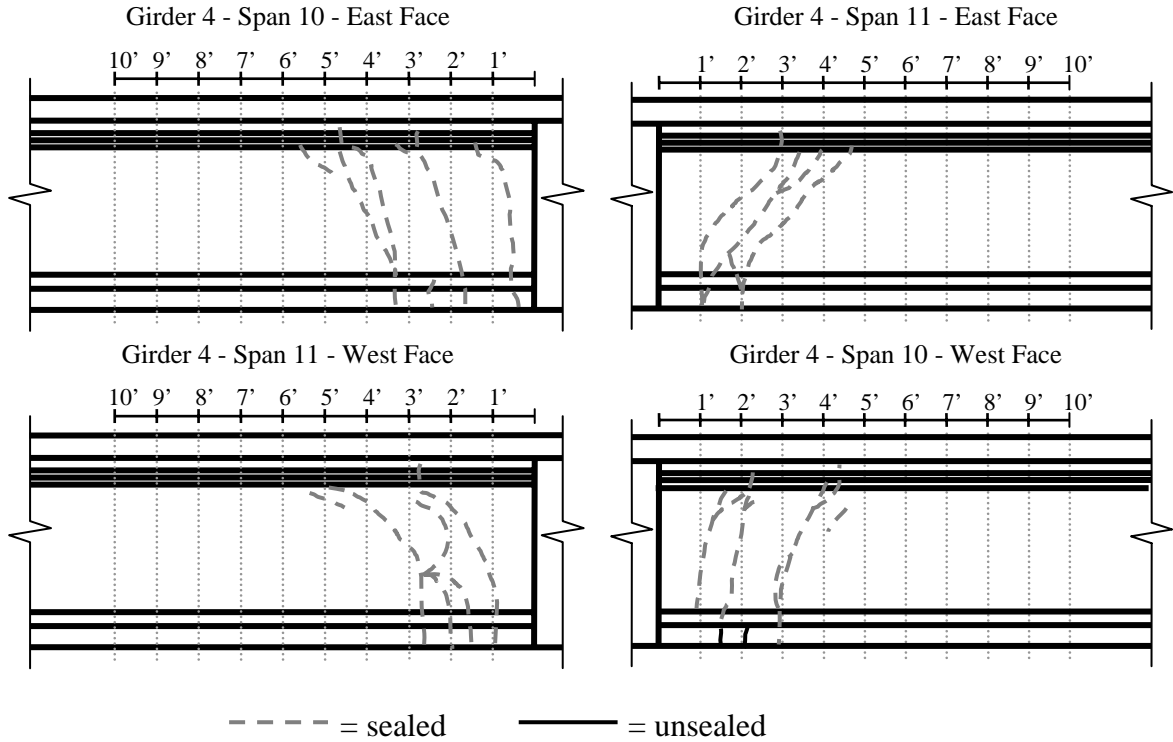
Figure 3.16 Girder Line 4 Cracking (Fason and Barnes 2004)

Girder 5 - Span 10 - East Face

10' 9' 8' 7' 6' 5' 4' 3' 2' 1'

Girder 5 - Span 11 - East Face

1' 2' 3' 4' 5' 6' 7' 8' 9' 10'

Girder 5 - Span 11 - West Face

10' 9' 8' 7' 6' 5' 4' 3' 2' 1'

Girder 5 - Span 10 - West Face

1' 2' 3' 4' 5' 6' 7' 8' 9' 10'

- - - - = sealed   ———— = unsealed
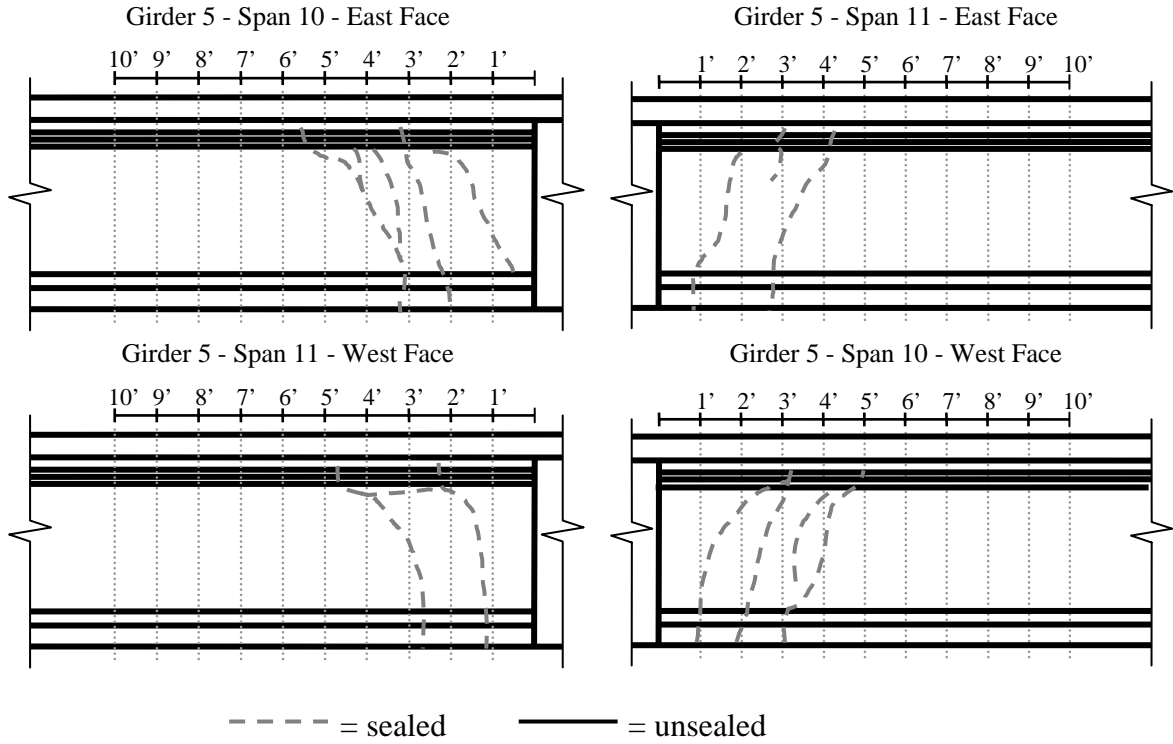
Figure 3.17 Girder Line 5 Cracking (Fason and Barnes 2004)

Girder 6 - Span 10 - East Face

10' 9' 8' 7' 6' 5' 4' 3' 2' 1'

Girder 6 - Span 11 - East Face

1' 2' 3' 4' 5' 6' 7' 8' 9' 10'

Girder 6 - Span 11 - West Face

10' 9' 8' 7' 6' 5' 4' 3' 2' 1'

Girder 6 - Span 10 - West Face

1' 2' 3' 4' 5' 6' 7' 8' 9' 10'

- - - - = sealed   ———— = unsealed
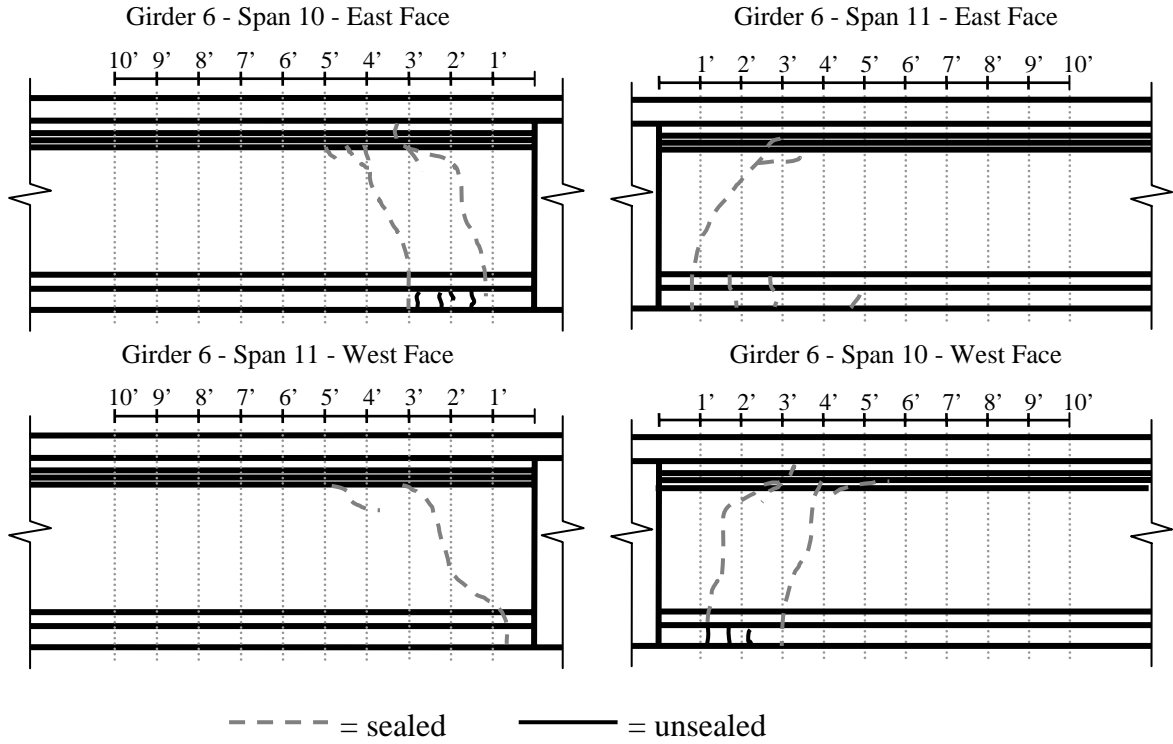
Figure 3.18 Girder Line 6 Cracking (Fason and Barnes 2004)

33

Girder 7 - Span 10 - East Face

10' 9' 8' 7' 6' 5' 4' 3' 2' 1'

cracked
through
seal

Girder 7 - Span 11 - East Face

1' 2' 3' 4' 5' 6' 7' 8' 9' 10'

Girder 7 - Span 11 - West Face

10' 9' 8' 7' 6' 5' 4' 3' 2' 1'

Girder 7 - Span 10 - West Face

1' 2' 3' 4' 5' 6' 7' 8' 9' 10'

cracked
through
seal

- - - - - = sealed   ———— = unsealed
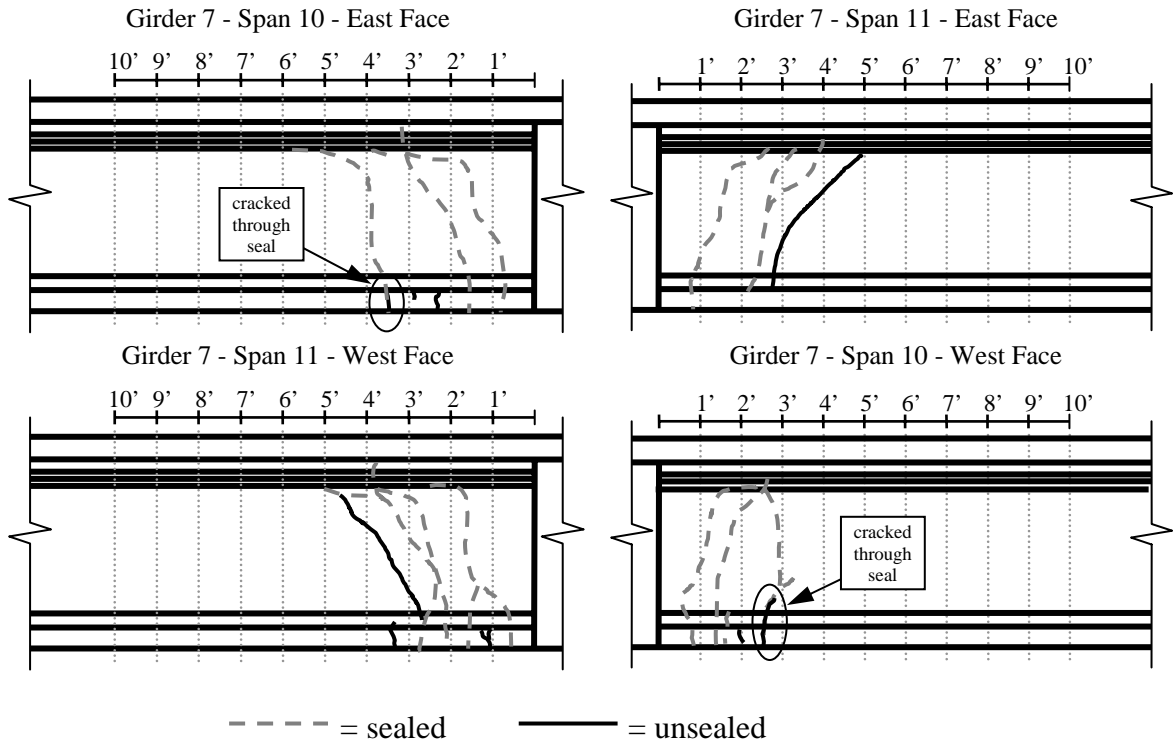
Figure 3.19 Girder Line 7 Cracking (Fason and Barnes 2004)

Girder 8 - Span 10 - East Face

10' 9' 8' 7' 6' 5' 4' 3' 2' 1'

Girder 8 - Span 11 - East Face

1' 2' 3' 4' 5' 6' 7' 8' 9' 10'

Girder 8 - Span 11 - West Face

10' 9' 8' 7' 6' 5' 4' 3' 2' 1'

Girder 8 - Span 10 - West Face

1' 2' 3' 4' 5' 6' 7' 8' 9' 10'

cracked
through
seal

- - - - - = sealed   ———— = unsealed
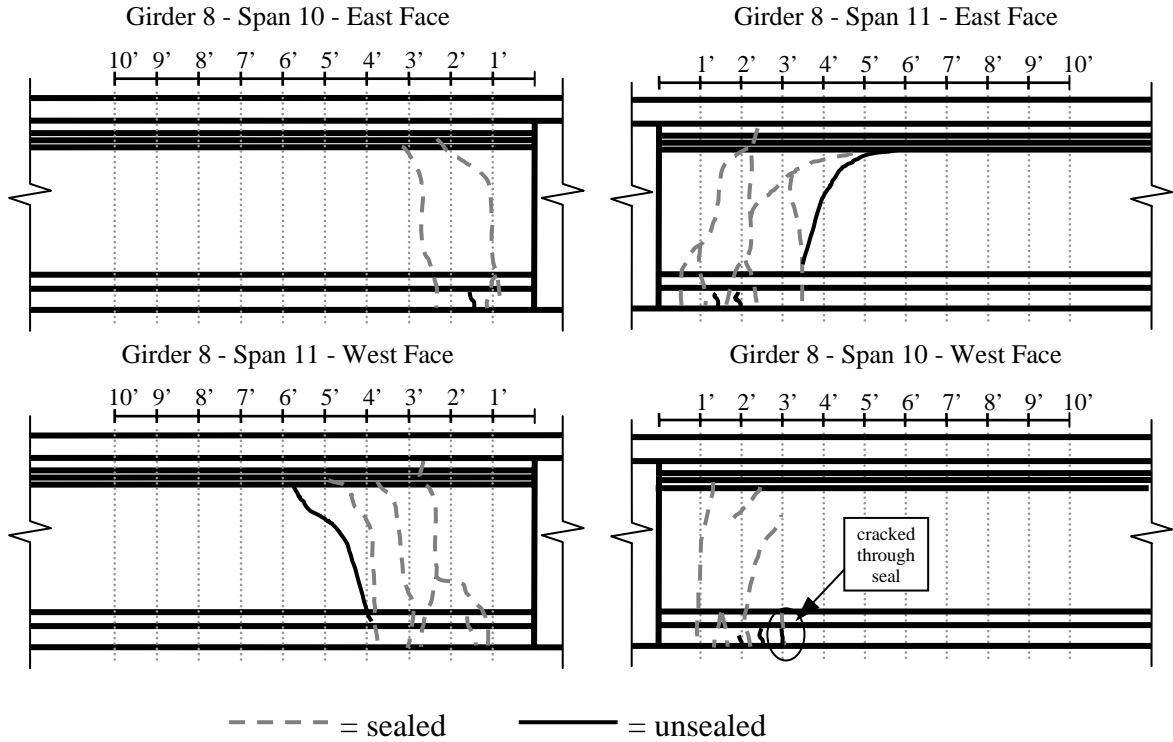
Figure 3.20 Girder Line 8 Cracking (Fason and Barnes 2004)

34

Girder 9 - Span 10 - East Face

Girder 9 - Span 11 - East Face

Girder 9 - Span 11 - West Face

Girder 9 - Span 10 - West Face

- - - - - = sealed   ———— = unsealed

Figure 3.21 Girder Line 9 Cracking (Fason and Barnes 2004)

3.4 PREVIOUS INVESTIGATIONS OF GIRDER CRACKING

3.4.1 Cause of Cracking

At first, it was hypothesized that the cracks were due to restraint of time-dependent or

temperature-induced deformations. Load testing and monitoring of the cracked girders

indicated that the magnitude of deformations due to daily temperature changes regularly

exceeded that caused by representative truck loading. Therefore, ALDOT officials

concluded that temperature-induced effects were responsible for the cracking (Barnes et

al. 2006).

Since then, Auburn University researchers have more thoroughly investigated the

cracking and its potential causes (Gao 2003). Time-dependent and temperature-

dependent influences were modeled analytically. During the course of this

35

investigation, it was discovered that the staged casting of the bridge deck and diaphragms was performed in an order different from that originally specified in the contract documents. Because previous research (Ma et al. 1998) has shown that construction sequence can significantly affect the behavior of this type of bridge system, the potential effects of this change were also evaluated (Barnes et al. 2006).

Time-dependent, structural analysis of a typical girder line through the complete construction sequence of a two-span continuous unit of the bridge was conducted. At the time the bridges were designed, the relevant design standards supplied little information on temperature gradients. More recent U.S. bridge design standards (AASHTO 2004) prescribe consideration of a temperature gradient of only 41.4˚F for this region. A single day of testing measured a temperature difference of 43.7˚F. Test notes indicate that it was not a very sunny day, so it is likely that actual temperature gradients might regularly be even higher than those measured. The site-specific values measured by ALDOT were used in the analysis (Barnes et al. 2006).

Analysis indicated that creep and shrinkage alone would not have resulted in cracking of the bridge superstructure within the first 10 years of service life. When the specified deck and diaphragm casting sequence was compared to the actual casting sequence, only small differences—on the order of 50 psi or less—in the relevant stresses were observed. As expected, the analysis of temperature-induced stresses yielded more noteworthy results. Daily temperature-induced stress cycles of the magnitude predicted in the end regions of the prestressed girders—between 700 and 1000 psi bottom-flange tensile stresses—could easily induce cracking in regions with little or no precompression. Based on the time-dependent analysis results, this would have been

the case for the end regions of the I-565 bridges at a relatively young age (Barnes et al. 2006).

The question which then remains is: why did the cracking occur within the girder itself rather than at the joint between the girder and the diaphragm where the largest tensile stresses occur? The answer is a twofold contribution from the reinforcement details, which are shown in Figure 3.22. First is that of the reinforcing bars used to establish continuity. There is both a relatively weak plane at the end of the continuity bars and a stress concentration at such a discrete transition point. The second contribution is from the debonding of the prestressing strands which occurs shortly past the end of the reinforcing bars for continuity. The increased tension found just behind these debonding points combined with the increased stress resulting from the reinforcement bars for continuity to produce cracked girders rather than separation of the girder from the diaphragm. Careful attention to reinforcing details can prevent such cracking from occurring (Barnes et al. 2006).

No. 6 reinforcing bars for continuity (8 in each girder end)

10 of 28 bottom-flange prestressing strands are debonded from end of girder to this section.
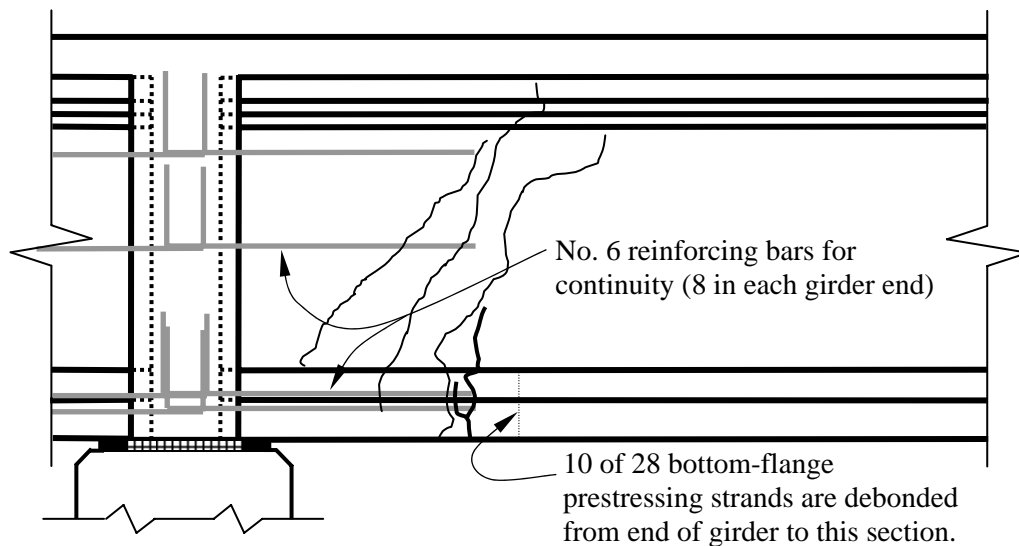
Figure 3.22 Cracked Girder with Continuity Reinforcement Details (Barnes et al. 2006)

37

3.4.2 Effects of Cracking on Bridge Capacity

A further study was conducted to determine the residual strength of the damaged
bridges. While it is possible that the effect on strength limit state performance is
minimal, the amount of remaining prestressed force in the end regions is vital to the
shear strength of the structure. Given the cracking pattern, it was assumed that (1) the
prestress force is ineffective between the end of the girder and the cracked sections, and
(2) the effective prestress force only begins to develop after the cracked section. Based
on the large slip evidenced, it is also doubtful that the affected strands are capable of
developing tensile resistance when subjected to significant flexural demand (Barnes et
al. 2006).

There are three possible behaviors of the bridge resulting from the cracks in the
girders (Swenson 2003). Ideally, it is behaving as a two-span continuous structure as
designed. Alternatively, it could have lost continuity completely and as a result could
be acting as two independent simply-supported spans. A third possibility is that the
girders act continuously but with an internal hinge at the crack locations. Each of these
possible behaviors was investigated. It was concluded that the spans with girder
cracking are only structurally adequate for the strength limit state if they behave as
completely continuous under the influence of live loads (Barnes et al. 2006).

When the structure is analyzed using either the second or third of the latter
possibilities, two shortcomings are apparent in the capacity of the structure: positive
bending resistance and shear resistance in the cracked end regions of the girders. Lack
of continuity and the suspected lack of development of the tensile reinforcement support
the conclusion that positive moments cannot be reliably resisted in these end regions.

Referring to Figure 3.23, the loss of shear resistance is less straightforward. Though the lack of effective prestress force in the end regions results in a decrease of the concrete contribution to web-shear cracking resistance, there is still sufficient transverse reinforcement in these regions to compensate. This is likely attributable to the conservative standard reinforcing details employed in the girder design. However, the bottom flange tensile reinforcement is inadequate to effectively resist the longitudinal component of the diagonal tension, T, resulting from shear-critical loading (Barnes et al. 2006).
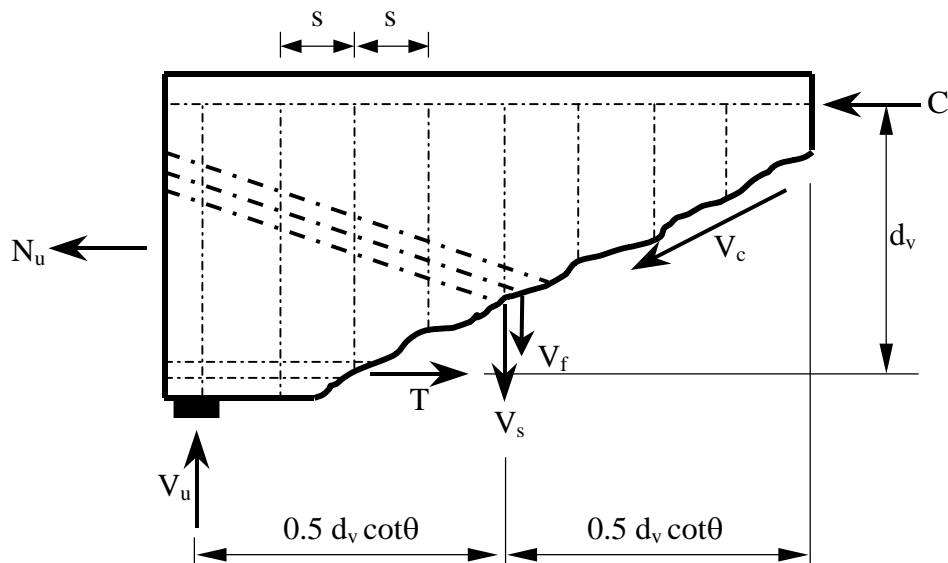
Figure 3.23 Influence of Shear on Required Bottom-Flange Tensile Resistance (Barnes et al. 2006)

3.5 PROPOSED REPAIR SYSTEM

For a damaged bridge, there are a number of possible repair options. One which has proven effective is mechanical attachment of steel plates to the tension face of the deficient member (Tedesco, Stallings, and El-Mihilmy 1999). There are several reasons, however, why steel plates, though effective, are undesirable. These include

"corrosion, difficulty in handling plates, deterioration of the bond at the steel-concrete interface and the requirement of massive scaffolding during installation." As an alternative repair method, FRP plates have an advantage over steel plates due to their ease in handling, corrosion resistance, light weight, and high strength.

Swenson (2003) presented possible repair scenarios with a recommendation for which would be most effective. The repair scenario he recommended was a 4-ply FRP system. The longitudinal and cross-sectional configurations of the 4-ply FRP strengthening system are shown in Figures 3.24 through 3.26. Note in Figure 3.24 that the bottom ply runs 130 in. from the face of the continuity diaphragm. Each ensuing ply is then 6 in. shorter. The system is designed to accomplish three complementary objectives: (1) provide adequate positive bending resistance regardless of continuity conditions, (2) provide adequate shear resistance regardless of continuity conditions, and (3) shift future cracking due to restrained time- and temperature-dependent deformations to a more benign location within or at the face of the diaphragm.

The FRP product chosen for the repair discussed in this investigation is the Tyfo SCH-41 composite manufactured by Fyfe Co. This product is a "wet lay-up system comprised of Tyfo SCH-41 reinforcing fabric and Tyfo S epoxy" (Swenson 2003). The reinforcing fabric is comprised of unidirectional carbon fibers backed with a glass veil to increase and support fabric stability during installation. The epoxy is a "two-part adhesive used to both saturate the composite fabric and bond the fabric to the concrete." Installation of the FRP repair system is expected in early 2007. Load testing to assess the behavior of the repaired spans will follow the FRP installation (Barnes et al. 2006).

40
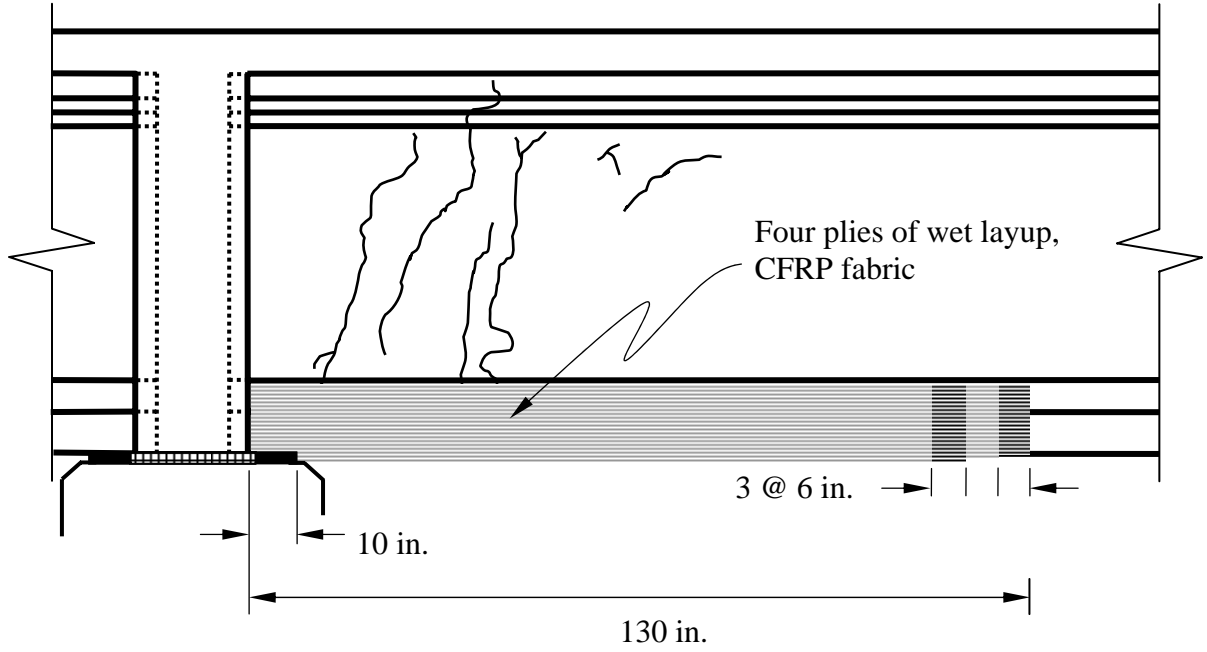
Figure 3.24 Longitudinal Configuration Profile for FRP (Barnes et al. 2006)

Four plies of wet layup, CFRP fabric

3 @ 6 in.

10 in.

130 in.

6.5"

Total effective width of
FRP reinforcement
bonded to girder = 30 in.

A

A

Inside face of
bearing pad

Bearing pad

Section A

Face of continuity
diaphragm
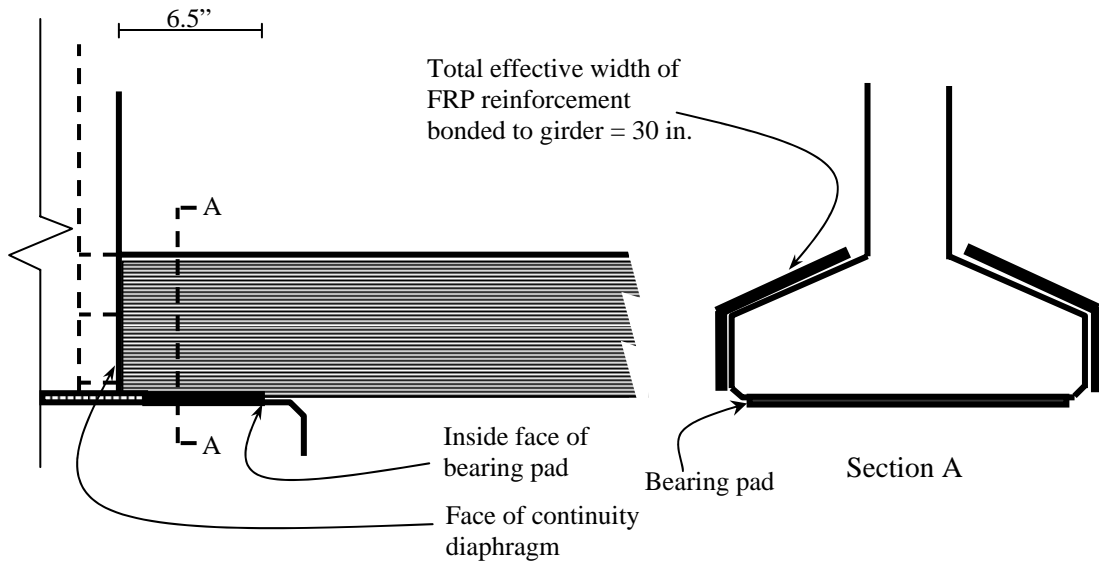
**Figure 3.25 Cross-Sectional Configuration for FRP near the Continuity
Diaphragm (Swenson 2003)**

41

6.5"

Total effective width of
FRP reinforcement
bonded to girder = 58 in.

B

B

Inside face of
bearing pad

Face of continuity
diaphragm
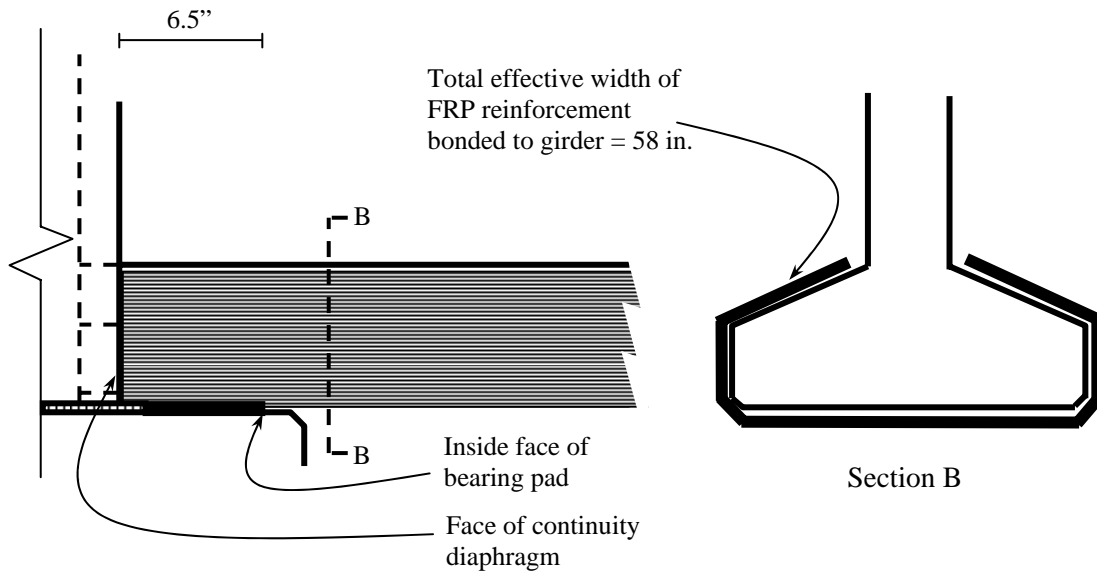
Section B

Figure 3.26 Cross-Sectional Configuration for FRP away from the Continuity Diaphragm (Swenson 2003)

CHAPTER 4: LOAD TESTING PROCEDURE

4.1 INTRODUCTION

In order to test the efficacy of FRP repair, tests before and after FRP application were deemed necessary. The pre-FRP load testing occurred on the mornings of June 1 and 2, 2005. There were nine longitudinal stop positions and three distinct patterns of transverse positions, creating a total of twenty-seven different load positions.

Load testing occurred over the course of two nights; however, the first day's loadings were dedicated to acoustic emissions (AE) testing, which is not within the scope of this particular investigation. Therefore, this summary will focus on the second day of testing, which occurred on the morning of June 2.

4.2 APPLIED LOADS

4.2.1 Load-Testing Vehicles

Test loads were applied using two different test trucks (ALDOT ST-6400 and ST-6902) simultaneously. Because the trucks had different frames, they had slightly different weight distributions and arrangements of wheel groups. The weight distribution chosen corresponds to an ALDOT LC-6 standard load truck configuration. This configuration was selected in order to induce load effects slightly larger than values corresponding to the full service-level live load for which the bridge was designed. Figures 4.1 and 4.2 indicate the relative positions of the wheel groups for the two trucks. Figures 4.3 and 4.4 show the trucks with the load configurations used for the load tests. There is a

raised axle visible on the ST-6400 Load Truck that was not used during load testing.

Table 4.1 reports the individual loads for each wheel group as measured using

ALDOT's portable scales approximately one week after the I-565 tests.

Table 4.1 Test Truck Wheel Group Loads

Axle	Wheel Group	Loading (lbs)	
		ST-6400	ST-6902
Front	Left	10,750	7,850
	Right	10,900	7,450
Rear 1	Left	18,900	19,350
	Right	18,350	18,750
Rear 2	Left	17,200	18,600
	Right	17,500	19,250
Total		93,600	91,250

4.2.2 Load Positions

Figures 4.5 through 4.7 indicate the three transverse truck positions used for testing—A,

B, and C. As Girders 7 and 8 exhibited some of the most severe damage, these

positions were chosen to maximize the influence on these two girders.

   Figure 4.8 illustrates the nine longitudinal stop positions used in the load testing.

Table 4.2 describes each of these stop positions. The stop positions are defined by the

middle axle of the trucks being centered on the location. Five stop positions are located

on Span 10, and four stop positions are located on Span 11. They range from midspan

of Span 10 to midspan of Span 11.
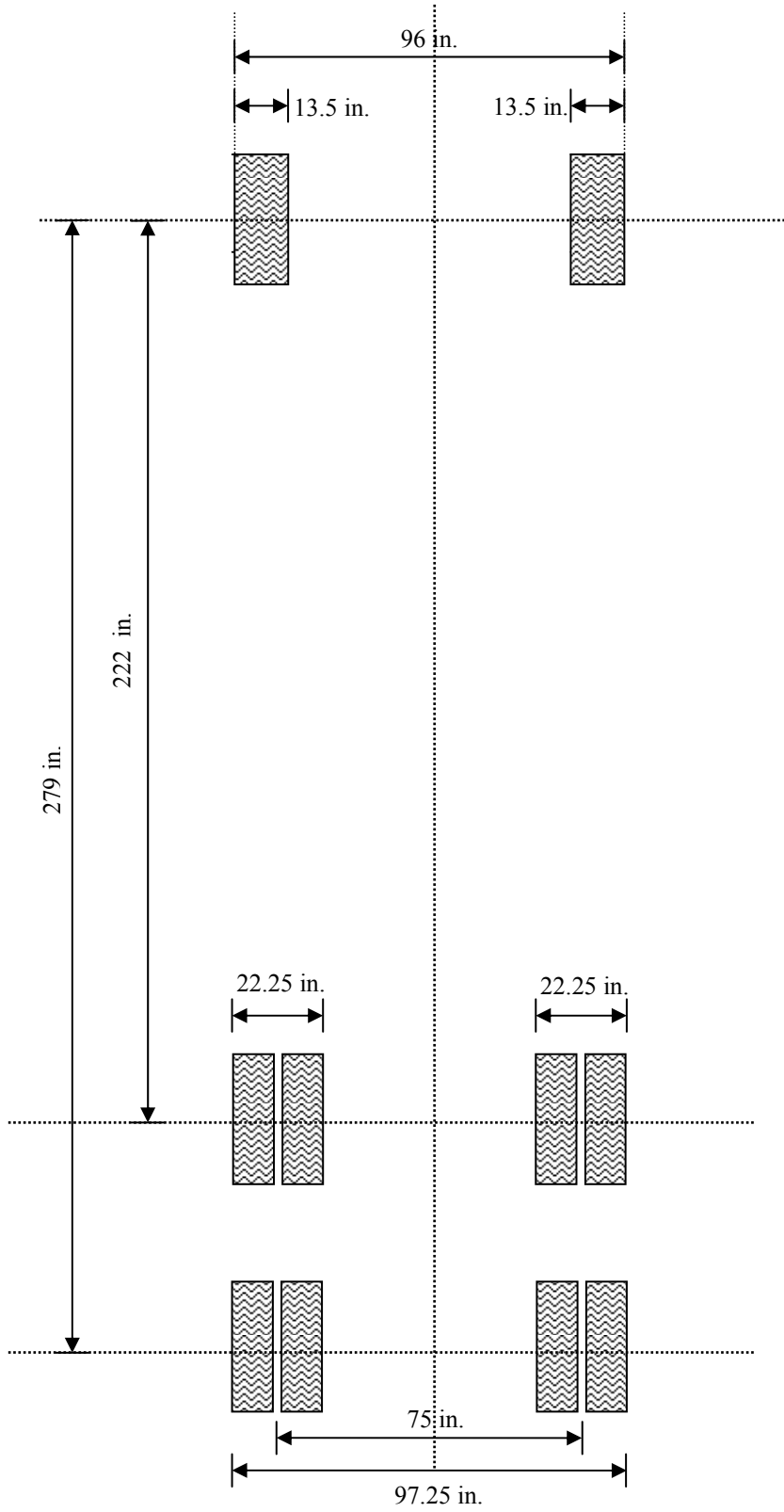
Figure 4.1 ST-6400 Wheel Group Configuration
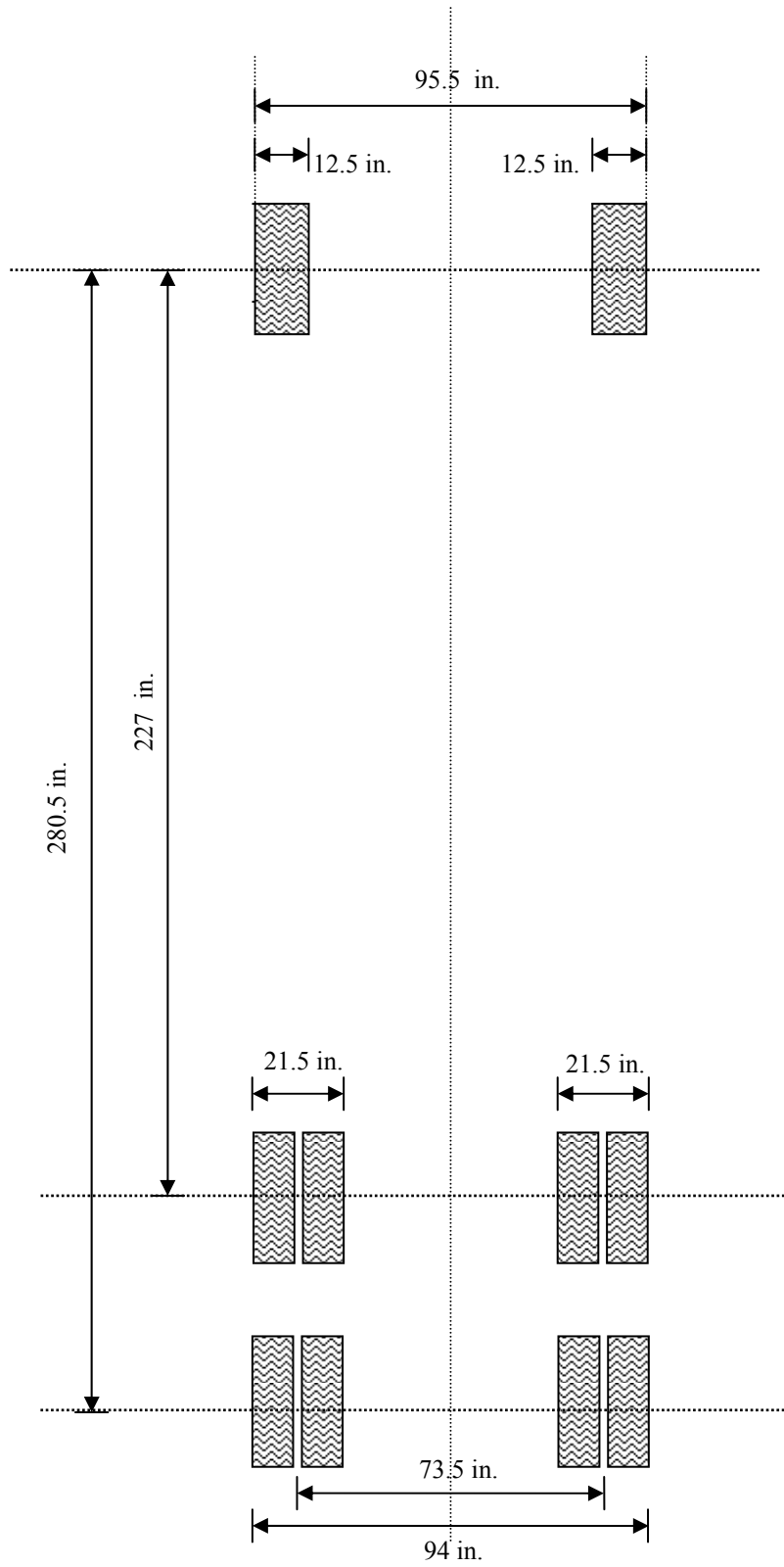
Figure 4.2 ST-6902 Wheel Group Configuration

Figure 4.3 ST-6400 Load Truck

Figure 4.4 ST-6902 Load Truck

ST-6902   ST-6400

73.5"   49"   75"

6.5"

Cast-in-place
concrete barrier

AASHTO BT54
girders

Girder 7   Girder 8

3' - 4 ½"   8' – 0"

64' – 0"

70' – 9"
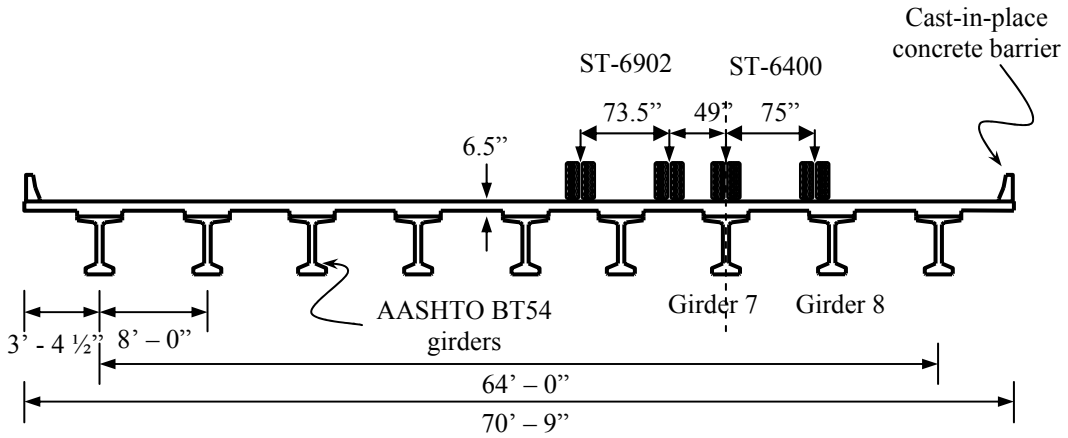
Figure 4.5 Transverse Truck Position A

ST-6902   ST-6400

73.5"   49"   75"

6.5"

Cast-in-place
concrete barrier

AASHTO BT54
girders

Girder 7   Girder 8

3' - 4 ½"   8' – 0"

64' – 0"

70' – 9"
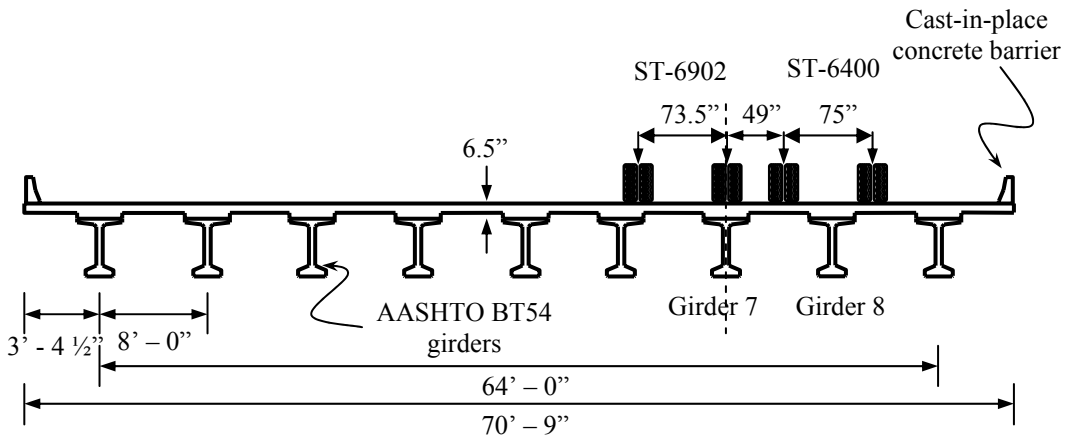
Figure 4.6 Transverse Truck Position B

ST-6902   ST-6400

73.5"   49"   75"

6.5"

Cast-in-place
concrete barrier

AASHTO BT54
girders

Girder 7   Girder 8

3' - 4 ½"   8' – 0"

64' – 0"

70' – 9"
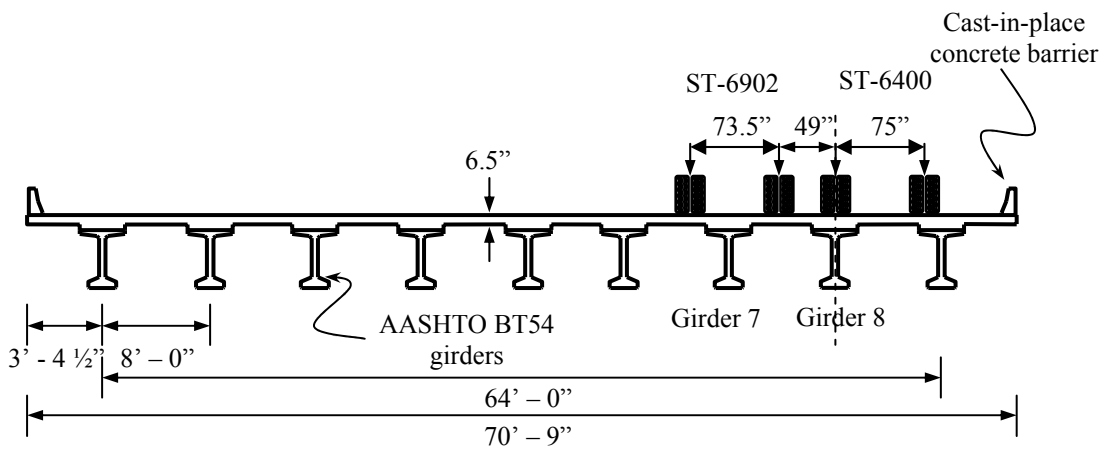
Figure 4.7 Transverse Truck Position C

48

**Centerline
of
Continuity
Diaphragm
on Bent 11**

Span 10

Span 11

Stop
Line
4
70"

Stop
Line
6
70"

Stop
Line
1
600"

Stop
Line
2
291"

Stop
Line
3
151"

Stop
Line
5
12"

Stop
Line
7
128"

Stop
Line
8
300"

Stop
Line
9
600"

1200"
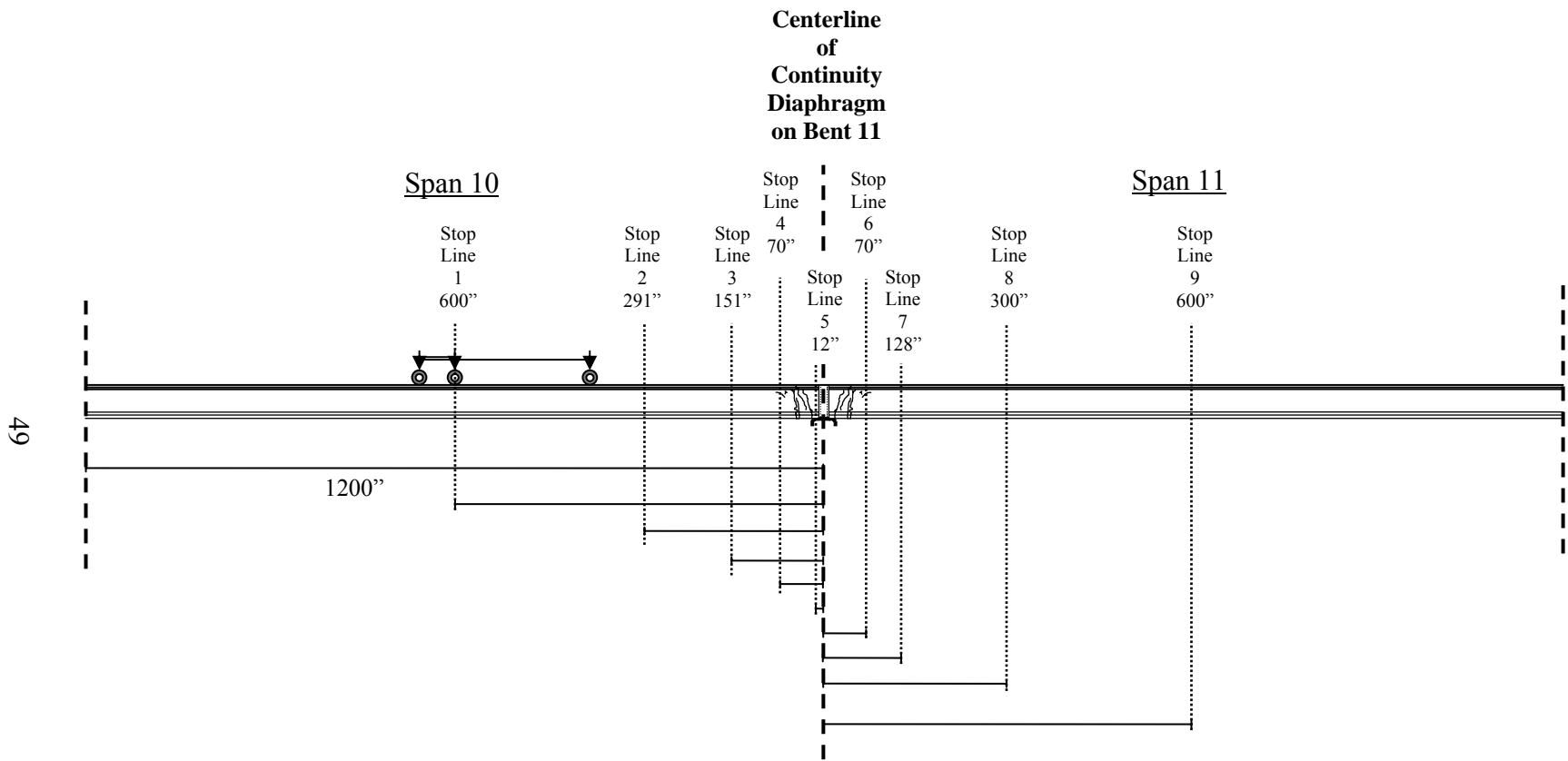
Figure 4.8 Longitudinal Stop Positions for Test Trucks

During the testing, the two trucks were placed side-by-side driving northbound. Two north-south lines were painted on the deck to define each transverse position—one for each truck. An east-west line was painted to mark each stop position. Figure 4.9 shows a truck properly aligned and in position. The trucks traveled slowly north along the north-south lines; they stopped at each of the nine stop positions long enough for braking effects to dissipate and then for data collection over a period of at least three seconds.

Figure 4.9 Load Truck in Stopped Position

The identification used for each of the 27 load positions comes from the transverse lane and the longitudinal stop position—with the transverse position coming first. For example, the load positions along Transverse Position A are A1, A2, and so forth

through A9. The load positions along Transverse Position B are B1, B2, etc. And the

load positions for Transverse Position C are C1, C2, etc.

Table 4.2 Locations of the Nine Longitudinal Stop Positions

Stop Position[a] No.	Position Description	Distance from Center of Continuity Diaphragm (in.)
1	Middle tire over the midspan of Span 10	-600
2	Front tire over Cross Section 1[b]	-291
3	Front tire over Cross Section 4	-151
4	Middle tire over Cross Section 1	-70
5	Rear tire over Cross Section 1	-12
6	Middle tire over Cross Section 4	70
7	Rear tire over Cross Section 4	128
8	Middle tire over the quarter-span of Span 11	300
9	Middle tire over the midspan of Span 11	600

[a] Trucks were stopped when the middle axles were located the specified distance from the center of the continuity diaphragm

[b] The convention for the numbering of the cross sections is given in Section 4.3.4.1

4.2.3 Testing Sequence

One repetition of static loading consisted of the two trucks driving along the bridge in

one transverse position and stopping long enough for data to be collected at each of the

nine stop positions. The following step-by-step procedure details how this maneuver

was accomplished.

1. Paint all necessary lines on bridge deck (truck positions A, B, and C and stopping

    positions 1–9).

2. Align both trucks to Transverse Position A.

3. Balance data acquisition device with trucks not on continuous spans.

51

4. Drive trucks to Position 1 and record data for three seconds.

5. Repeat Step 4 for Positions 2–9.

6. Drive trucks off span and record data without load.

7. Drive trucks back to starting position and align for Transverse Position B.

8. Repeat Steps 3–6.

9. Drive trucks back to starting position and align for Transverse Position C.

10. Repeat Steps 3–6.

4.3 INSTRUMENTATION

Several types of measurements were collected during the pre-FRP repair load testing. However, only longitudinal strain and vertical deflection measurements are relevant to the analysis reported in this thesis.

4.3.1 Concrete Strains

For this load testing, concrete surface strains were measured using electrical-resistance strain gauges (ERSGs) bonded with epoxy directly to the surface of the concrete as depicted in Figure 4.10. Because concrete is not a homogeneous material, a gauge length several times as large as the coarse aggregate size was selected to prevent accidental measurement of strain values not representative of the concrete material as a whole. The ERSGs used in this test were 60-mm, quarter-bridge strain gauges with a resistance of 350 Ω and temperature compensation appropriate for concrete or steel (Texas Measurements MFLA-60•350-1L). Installation of the strain gauges is explained in Section 4.3.3.1.
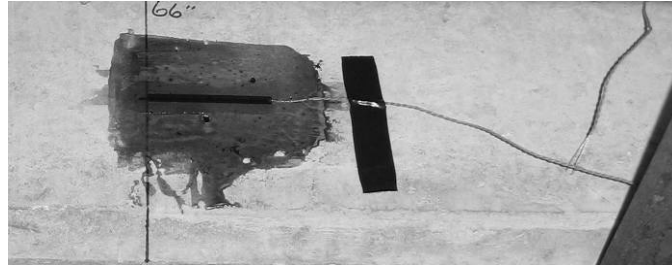
Figure 4.10 Installed ERSG

4.3.2 Girder Deflections

Deflectometers were used to measure the amount of vertical movement that the bridge experienced under loads. These measurements were useful in determining the general behavior of the bridge. The deflectometers used were relatively elementary devices. An installed deflectometer is depicted in Figure 4.11. They were constructed primarily of a cantilevered aluminum beam with a longitudinal, quarter-bridge strain gauge attached to the underside of the beam. The beam was attached to a base that firmly supported it on the ground. An eye bolt was attached to the end of the beam, and a taut wire was attached to the underside of a bridge girder and connected to the eye bolt on the deflectometer.
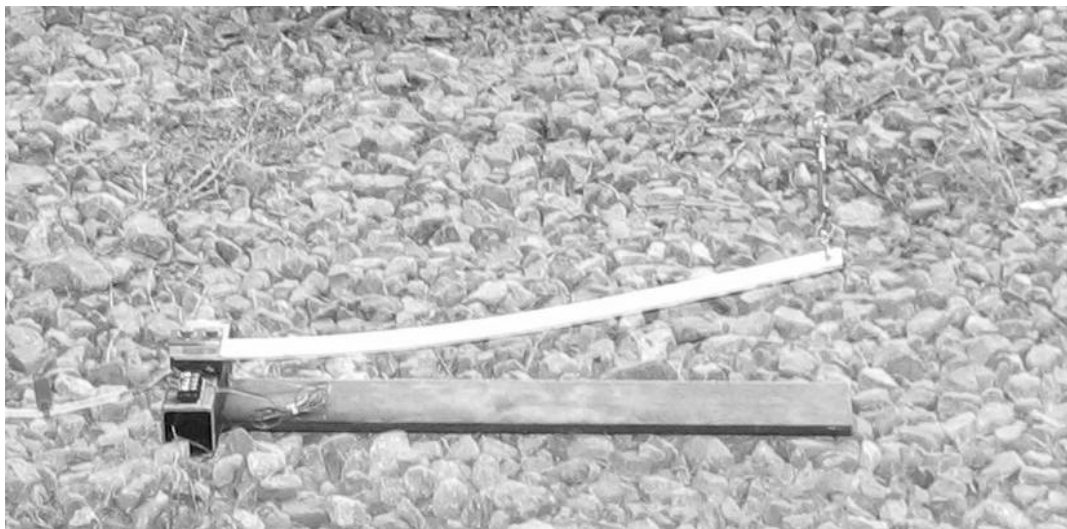
Figure 4.11 Installed Deflectometer

In order to keep the wire taut and acquire useful data when the girder deformed, the aluminum beam was pre-bent approximately three or four inches. This was done by tightening the turnbuckle attached to the wire. Once the beam was bent and the wire was in tension, the strain gauge was capable of measuring both upward and downward deflections of the bridge girder within the expected range. Installation of the deflectometers is further explained in Section 4.3.3.2. Deflectometer positions are described in Section 4.3.4.2.

The deflectometers also needed to be calibrated. This was accomplished by taking a base reading of the strain gauge when the aluminum beam was in position and then taking a series of readings as the beam was carefully moved through a range of precisely measured distances. A linear relationship was established between the gauge output and the tip deflection of the aluminum beam through the entire range encountered during the actual bridge test. This relationship was then used to compute the measured girder deflection for the strain measured for each load position.

4.3.3 Sensor Installation

4.3.3.1 Strain Gauges

Because concrete is a porous material, water may penetrate to the strain gauge if the surface is not sealed against moisture. Surface preparation was conducted according to the gauge manufacturer's recommendations.

The application of the gauges was performed according to the manufacturer's instructions. To prepare the gauges, each gauge was removed from its package and taped to a clean glass plate. The tape was kept smooth and free of air bubbles during this transfer. When the concrete surface was ready, the tape with the attached strain

gauge was carefully removed and attached to the desired location on the girder. When that was finished, the tape was carefully peeled back to reveal the underside of the strain gauge. To attach the strain gauge, a standard 5-minute epoxy was then applied to both the strain gauge and the concrete, and the strain gauge was held in place until the gauge was attached sufficiently. After the epoxy hardened, the tape was removed completely and a layer of Dow Corning® 3145 RTV silicone rubber was applied over the entire strain gauge to provide protection against moisture and wear.

4.3.3.2 Deflectometers

The installation of the deflectometers was relatively simple when compared to that of the strain gauges. After the installation location was identified, a bracket was glued into place on the girder using 5-minute epoxy. After the epoxy was set, a wire was attached to the bracket with a turnbuckle at the end of the wire. Once the deflectometer was placed securely in position on the ground, the turnbuckle was attached to the eyebolt, and the aluminum beam was pre-bent approximately 4 inches. The deflectometer strain gauge was then connected to the data acquisition system.

4.3.4 Sensor Positions

Because of practical limitations, a choice had to be made between lightly instrumenting all of the girders or heavily instrumenting only some of them. It was decided to heavily instrument only two of them, and Girders 7 and 8 were selected as being representative of the occurrences of cracking. These are the first two interior girders on the east side of the bridge. Figures 4.12 through 4.19 depict the end regions of Spans 10 and 11 of Girders 7 and 8.

Figure 4.12 Girder 7 Span 10 East Face

Figure 4.13 Girder 7 Span 10 West Face

Figure 4.14 Girder 7 Span 11 East Face

Figure 4.15 Girder 7 Span 11 West Face

Figure 4.16 Girder 8 Span 10 East Face

Figure 4.17 Girder 8 Span 10 West Face

58

Figure 4.18 Girder 8 Span 11 East Face

Figure 4.19 Girder 8 Span 11 West Face

4.3.4.1 Strain Gauges

Longitudinal strain data were collected at twenty-eight positions along each of the two bridge girders. Because the cracked area is of greatest concern, the bulk of the strain gauges were located close to the girder ends where the cracking had occurred. Because Span 11 was chosen to be the primary span, it had six cross sections that were instrumented with strain gauges while Span 10 had only two instrumented cross sections.

The locations of Cross Sections 1 through 4 are indicated in Figure 4.20. On Span 10, Cross Section 1 is located 75.25 in. from the center of the continuity diaphragm, and Cross Section 2 is located 12.75 in. from the center of the continuity diaphragm. On Span 11, Cross Section 3 is located 12.75 in. from the center of the continuity diaphragm, and Cross Section 4 is located 75.25 in. from the center of the continuity diaphragm. Cross Sections 5 through 8 are located on Span 11 104 inches, 272 inches, 440 inches, and 608 inches from the center of the continuity diaphragm, respectively.

In order to get more comprehensive data in the cracked region, Cross Sections 1–4 each had six strain gauges as depicted in Figures 4.21 and 4.22. Cross Sections 5–8 only had gauges located on the bottom of the girder. The primary purpose of the gauges along the bottom of the girder was to better determine the overall behavior of the girders, particularly the manner in which the damaged regions affected the distribution of bending moments within the structure.
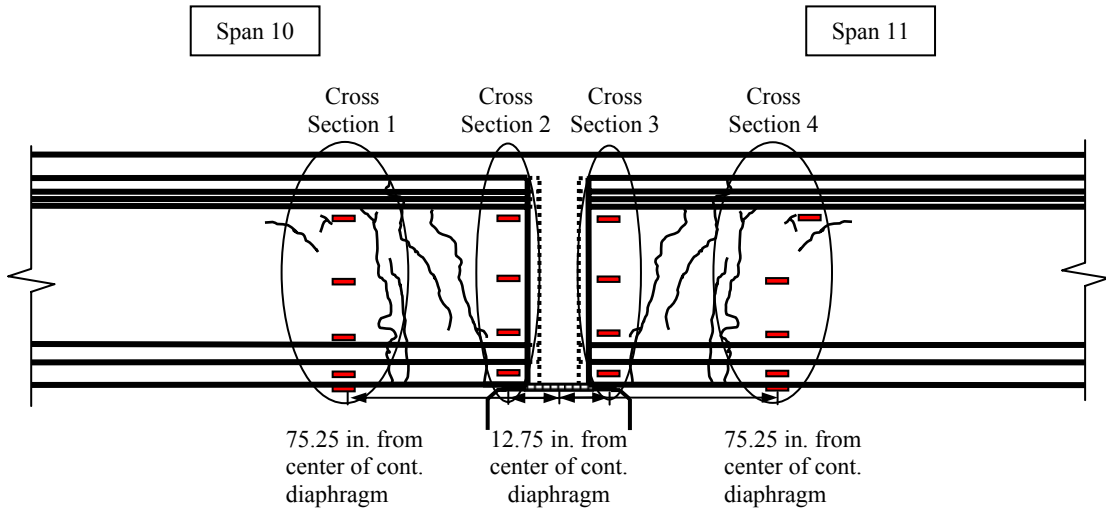
Figure 4.20 Approximate Locations for Cross Sections 1 through 4
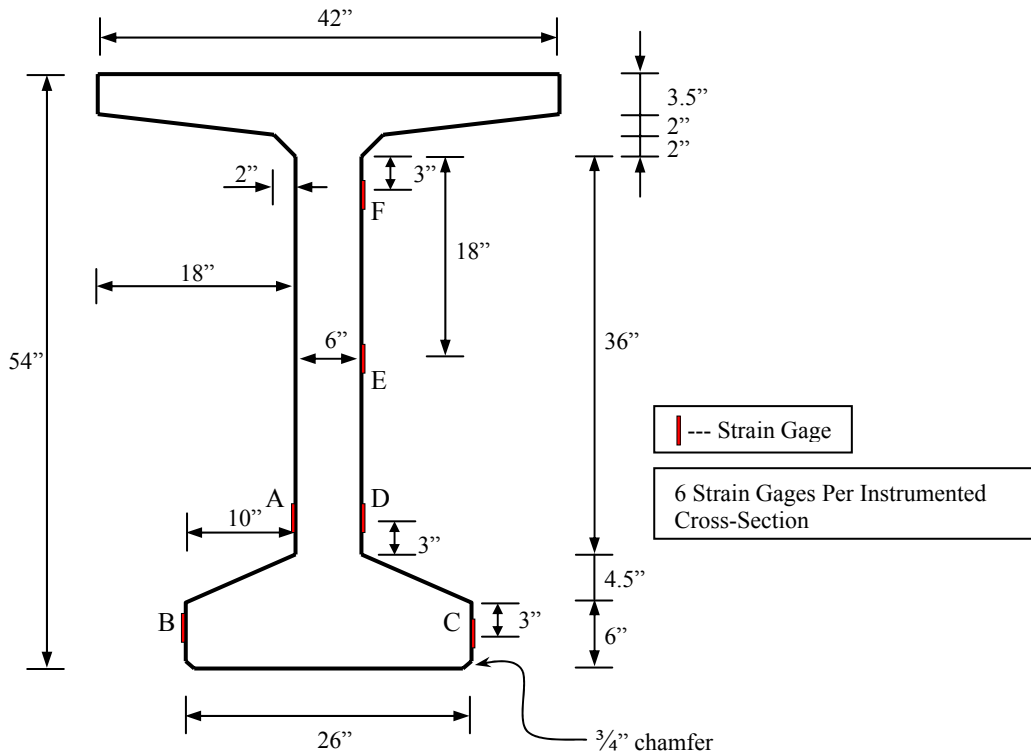
Figure 4.21 Strain Gauge Instrumentation at Cross Sections 2 and 3

61
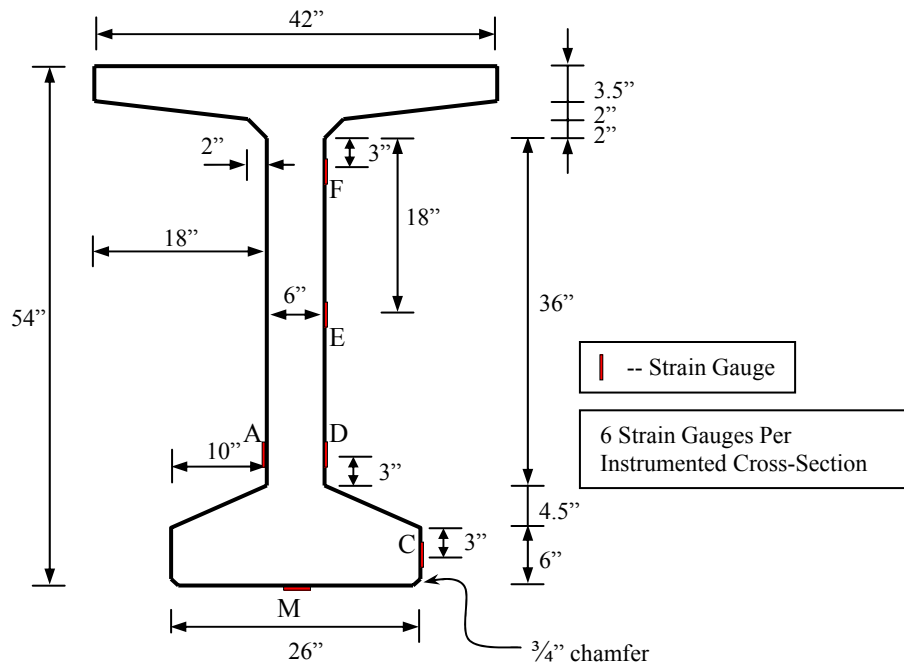
Figure 4.22 Strain Gauge Instrumentation at Cross Sections 1 and 4

4.3.4.2 Deflectometers

There were twelve deflectometers used in the load testing. These were placed at six

different locations on each of the two girders as depicted in Figure 4.23. Because Span

11 was the primary span, it had four deflectometers per girder while Span 10 had only

two. For Span 11, the deflectometers were located 150 in., 300 in., 450 in., and 600 in.

from the center of the continuity diaphragm. These distances represent 1/8, 1/4, 3/8,

and 1/2 of the span length, respectively. For Span 10, the deflectometers were located

300 in. and 600 in. from the center of the continuity diaphragm. Figure 4.24 shows

several installed deflectometers.

Midspan

Span 10

Span 11

Midspan

D-1

300"

D-2

300"

150"

D-3

150"

D-4

150"

D-5

150"

D-6

Bent 11
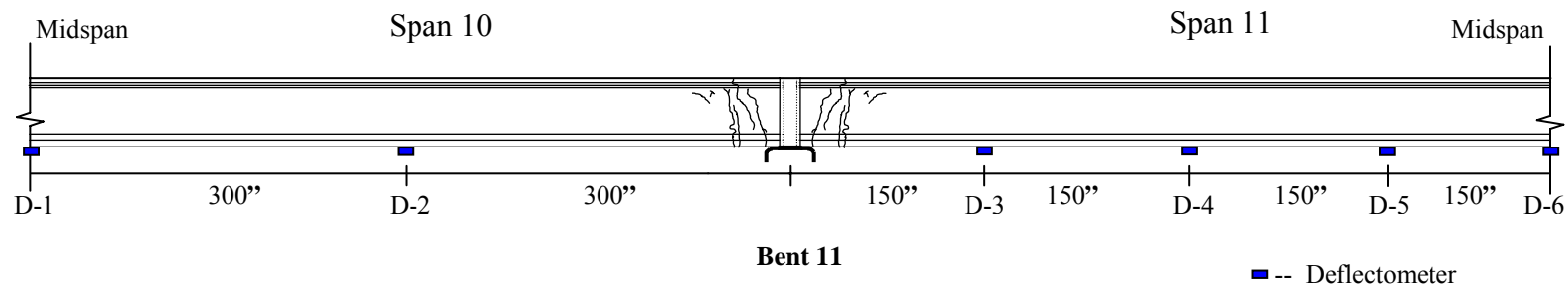
■ -- Deflectometer

Figure 4.23 Installed Deflectometer Locations

Figure 4.24 Installed Deflectometers

4.4 DATA ACQUISITION AND PROCESSING

4.4.1 Data Acquisition System

An Optim MEGADAC data acquisition system was used to record the test data. For

each truck position, sensor readings were recorded at a rate of 240 scans per second for

at least 3 seconds. The entire positioning sequence was repeated three times. Figure

4.25 is a picture of the complete van setup during the load test.

4.4.2 Averaging Process

There were at least 720 readings recorded for each repetition of each static load

position. These 720 (or more) readings were averaged to eliminate variation due to

electronic noise, resulting in a single measured deformation (strain or deflection) for

each position repetition. If one of these three resulting values for a single position

differed significantly from the other two values, the outlier was discarded and the two

remaining values were averaged to determine a single deformation measurement for

each load position. Usually there was no apparent outlier, and the deformation value

was determined as the average of all three repetition results.

4.5 DATA USED TO EVALUATE AND REFINE FINITE-ELEMENT MODELS

Results from only four of the load positions—A7, A9, C7, and C9—were used to

evaluate the accuracy of the model and investigate the effectiveness of various

modeling options. Transverse Positions A and C were selected because these positions

primarily load Girders 7 and 8, respectively, and produce a more distinct response than

Transverse Position B.

   Longitudinal Positions 7 and 9 were selected to give behavior representative of

maximum load effects near the damaged regions. Position 7 had the truck wheels in a

position that could be expected to induce the largest shear forces near the cracked sections. Position 9 could be expected to induce the largest bending moments in the cracked regions. Positions 7 and 9 were chosen over the corresponding locations on Span 10 because Span 11 was more heavily instrumented than Span 10 and as a result had the most data for comparisons.

Measured bottom-fiber strains were employed as the primary means of assessing the accuracy of various modeling options with respect to the overall behavior of the bridge superstructure. Complete results for all twenty-seven load positions for the pre-repair load testing conducted on June 2, 2005 are reported in Appendix H

Figure 4.25 Van Setup during Testing

CHAPTER 5: FEM DEVELOPMENT AND VERIFICATION

5.1 INTRODUCTION

In creating the finite-element model for the bridge using ABAQUS, there were many

aspects of the geometry and material properties that needed to be considered. For the

practical purposes of this model, it was permissible for some assumptions and

simplifications to be used. For example, a slightly simplified girder cross section was

used for ease in meshing, and as explained in Section 5.10, the cracks were modeled as

a group rather than by discretizing each crack location. In addition, average material

properties of concrete and prestressing steel were employed. This chapter presents the

details of those and other components of the model definition.

5.2 GIRDER CROSS SECTION

The first step in defining the model was to determine what the cross-sectional shape of

the girders would be. The dimensions of a BT54, the girder section used in the I-565

bridge (ALDOT 1987), are shown in Figure 5.1a, but for the purposes of the model and

for ease in meshing, it was decided to simplify these dimensions slightly. In order to

verify the accuracy of the simplified section, section properties were computed for the

simplified section shown in Figure 5.1b and on the same section with a ¾"chamfer on

each outer corner of the bottom flange.
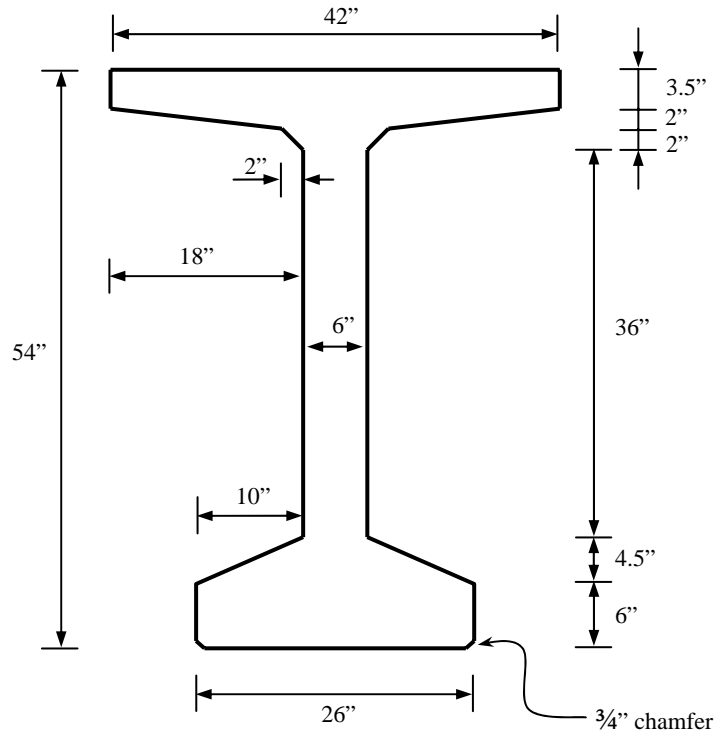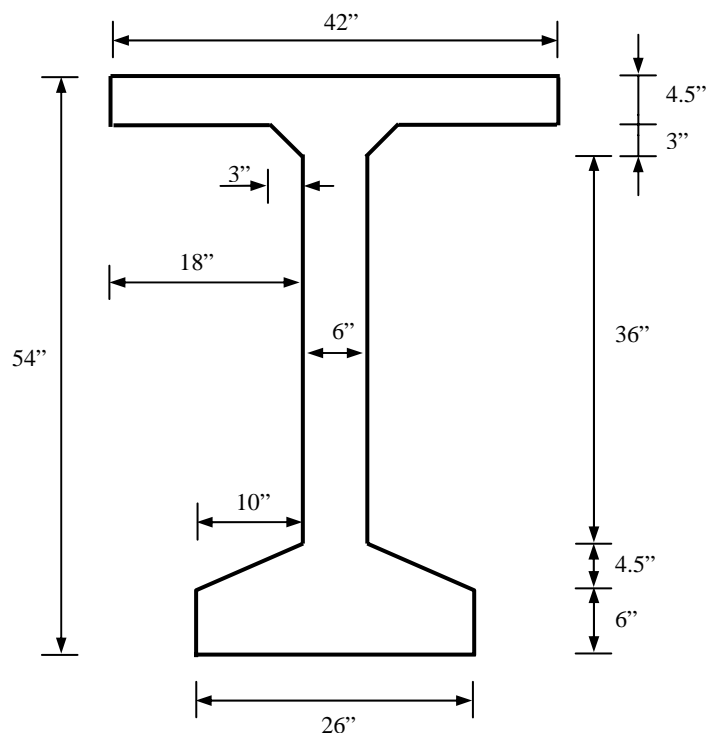
Figure 5.1 Cross-Sectional Dimensions for (a) BT54 and (b) Simplified BT54

The cross-sectional properties that were compared include area (A), moment of inertia (I), height (h), distance from neutral axis to top of the flange (y_t), section modulus of the area above the neutral axis (S_t), section modulus of the area below the neutral axis (S_b), and radius of gyration (r^2). A comparison of the computed values to the section properties of the actual BT54 is shown in Table 5.1. Percent errors were calculated by dividing the difference between the two values—the cross-sectional property value for the BT54 versus the modified shape—by the value for the BT54. As can be seen in the table, the errors associated with the simplified shape without chamfers range up to approximately three times as great as the corresponding errors associated with the simplified shape with the chamfers; however, all errors are less than one percent. This level of error was considered acceptable, and the simplified cross section without chamfer was employed for the FEM. This cross-sectional shape was then extruded 200 feet to produce a continuous girder.

Table 5.1 Section Properties of Simplified BT54 Cross Section

Cross-Sectional Property	BT54	Modified Shape (without chamfer)	Modified Shape (with chamfer)	Percent Errors	
				Modified Shape (without chamfer)	Modified Shape (with chamfer)
A (in^2)	659	660	659	0.15	0.07
I (in^4)	268100	269600	269200	0.57	0.42
h (in)	54	54	54	0	0
y_t (in)	26.37	26.31	26.29	0.23	0.30
S_t (in^3)	10170	10250	10240	0.80	0.72
S_b (in^3)	9702	9737	9715	0.35	0.13
r^2 (in^2)	406.8	408.5	408.2	0.42	0.35

5.3 REINFORCED CONCRETE DECK

The reinforced concrete (RC) deck was modeled by an 849 in. by 6.5 in. rectangular cross section extruded 200 ft. This represents a slight simplification of the actual deck cross section which is depicted in Figure 5.2. That figure shows a slight, variable build-up present over the girders. It was reasoned that because the load tests measured *change* in strain, the rectangular approximation would sufficiently represent the deck-girder composite behavior.
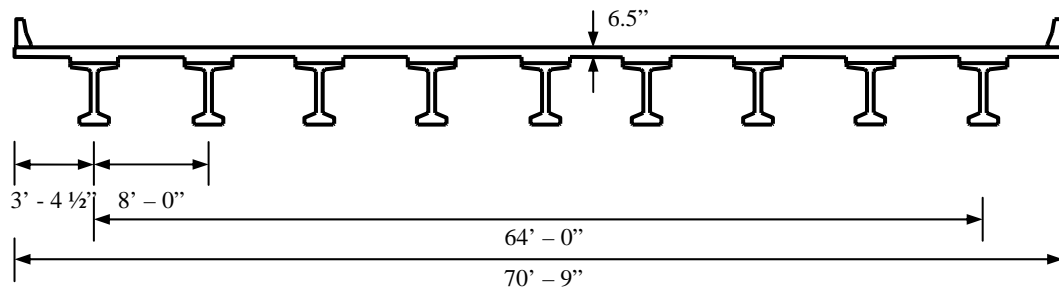
Figure 5.2 Bridge Cross Section

5.4 MESH SIZE

The next issue to be addressed was the mesh size of the model. In order to select a mesh size, several analyses of the same basic model were run with different mesh sizes. This basic model had no diaphragms or barrier rails; it consisted solely of the deck, nine continuous girders, and a central bent—which was approximated by the continuity diaphragms as explained in Section 5.5. It was loaded with a pressure load of 1 psi on the entire deck.

The four mesh sizes compared divided the length of the bridge into elements that were 6 in., 9 in., 12 in., and 15 in. long along the length of the bridge. In determining these four options, the AASHTO LRFD (2004) requirements regarding aspect ratio were considered: "the aspect ratio of finite elements and grid panels should not exceed

70

5.0." Each of these mesh sizes conforms to the 5.0 aspect-ratio limit. The least number

of elements per girder span that satisfies the AASHTO LRFD limit is ten elements. Ten

elements per span results in an aspect ratio of 4.6 for the elements in the bottom flange.

This is an acceptable minimum number of elements only if each element encompasses

the full width of the cross section and the top and bottom flanges are each approximated

as rectangles, as shown in Figure 5.3. In order to achieve more refined analysis results,

at least two elements were used across the width of the cross section for all mesh sizes

investigated. An example of this—the cross section for the 9-in. mesh—is shown in

Figure 5.4. The coarsest (15-in.) mesh of the four mesh sizes investigated had at least 8

times the minimum number of elements along the span recommended by AASHTO

LRFD.
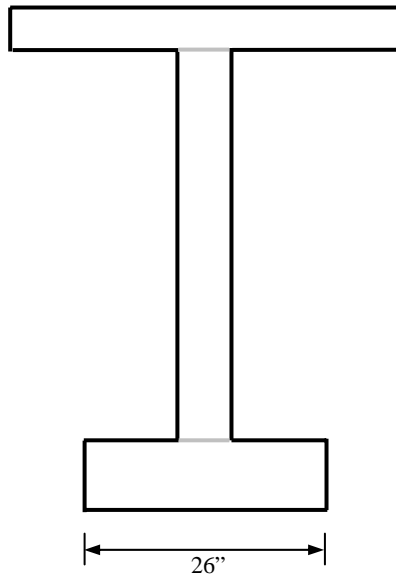
Figure 5.3 Cross Section of Coarsest Mesh
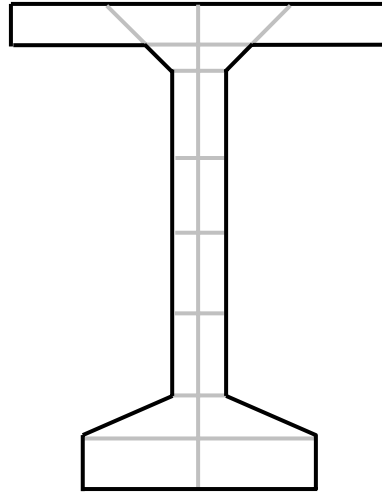
Figure 5.4 Cross Section of 9-in. Mesh

As can be seen in Figure 5.5, all of the longitudinal stress values approach one another as the distance from the bent cap (modeled as a pinned support at the bottom of each of the nine continuous girders) increases. Closer to the pinned connection, it can be seen that the stress pattern changes noticeably between that for the 15 in. mesh and that for the 12 in. mesh, also between that for the 12 in. mesh compared to that for the 9 in. mesh. The difference between the stress patterns shown for the 9-in. and 6-in. mesh values, however, is not so drastic.

The other component considered in selecting the mesh size was the computational burden. Figure 5.6 depicts the run-times of each of the four models. It can be seen that as the mesh size decreased, the computer time required for the additional calculations increased significantly. The computer time for a 6-in. model was more than twice that of the 9-in. model, but the increase in accuracy was not significant enough to warrant the necessary commensurate increase in computational burden, particularly for the nonlinear aspects of the analysis that were anticipated. As a result, the 9-in. mesh as depicted in Figure 5.7 was selected for the ABAQUS model. This 9-in. mesh results in

a ratio of element length to girder length of approximately 1:133, which is close to that of 1:137 used by Barr, Eberhard, and Stanton (2001).
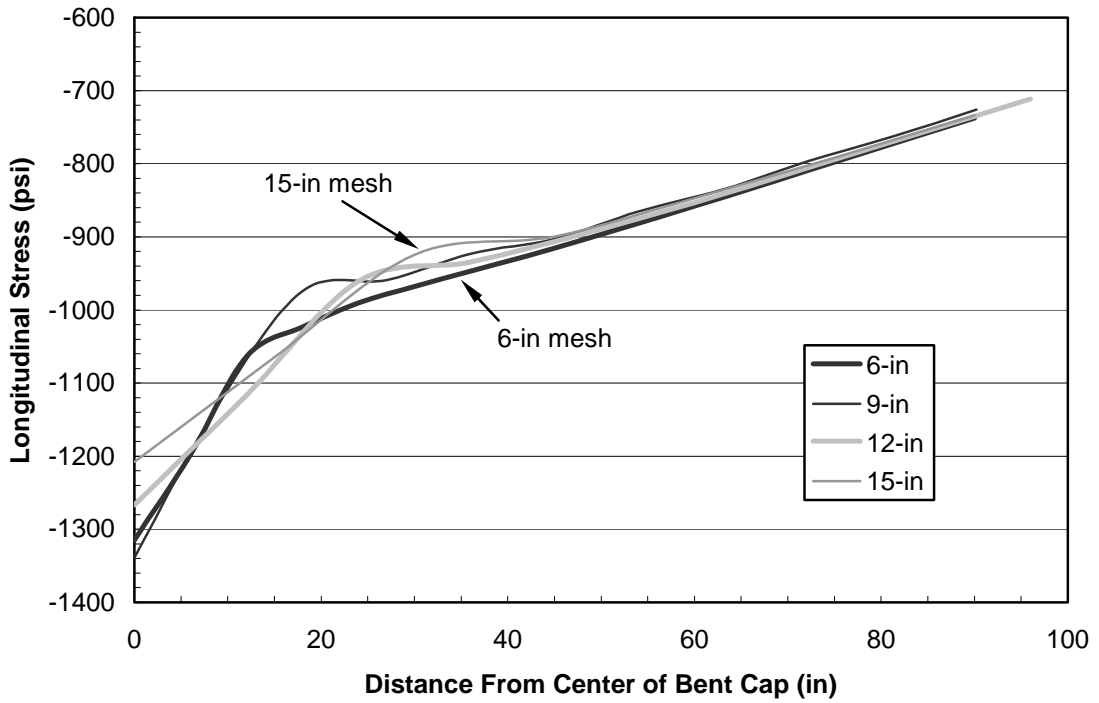
Figure 5.5 Mesh Size Stress Comparisons
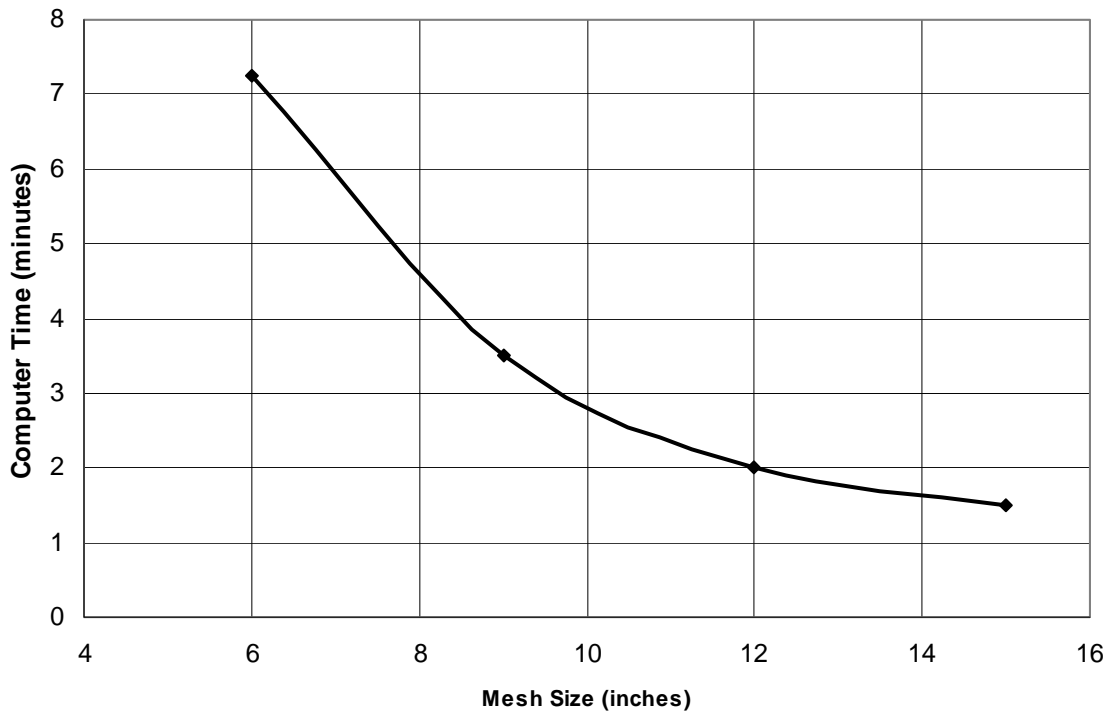
Figure 5.6 Mesh Size vs. Computer Time

73
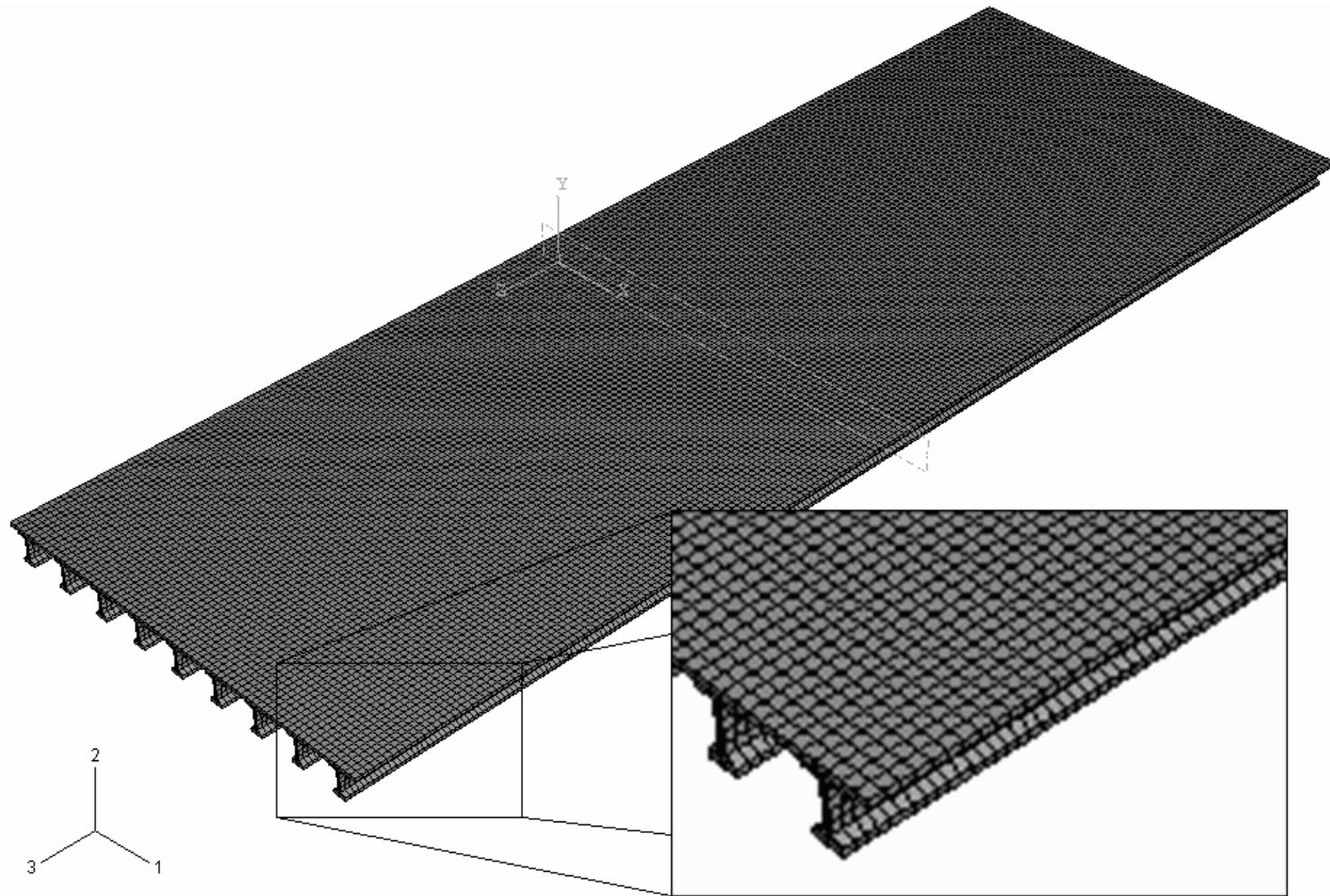
Figure 5.7 ABAQUS Bridge Model Depicting a 9-in. Mesh

5.5 DIAPHRAGMS

The next step was to take the very basic model and add the continuity and midspan diaphragms as depicted in Figures 5.8 and 5.9, respectively. The midspan diaphragms and the diaphragms at the discontinuous far ends of each span have the same cross-sectional shape. FEM model diaphragms are shown in Figure 5.10. The girders were modeled as continuous girders rather than as two simply supported girders joined at the continuity diaphragm. To accomplish this, the girders were extruded 200 ft—the length of both spans—and connected at the bent with continuity diaphragms between adjacent girders. This connection was achieved using a tie constraint—which is explained in Section 5.12.
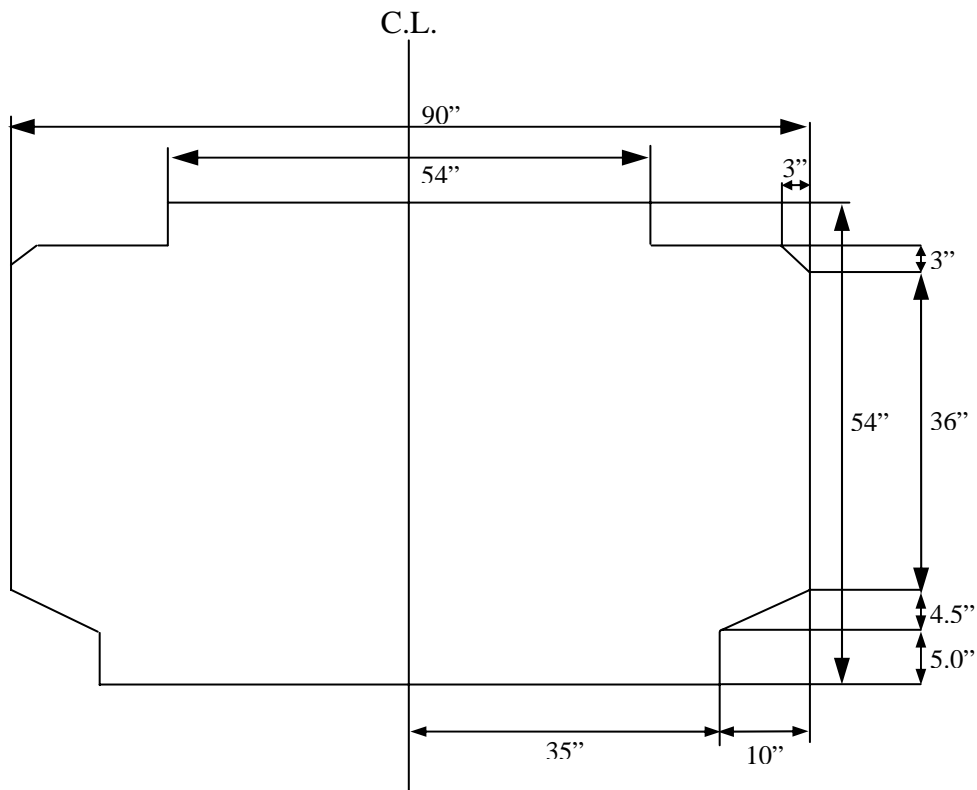
Figure 5.8 Cross Section of Continuity Diaphragm, Thickness = 16"
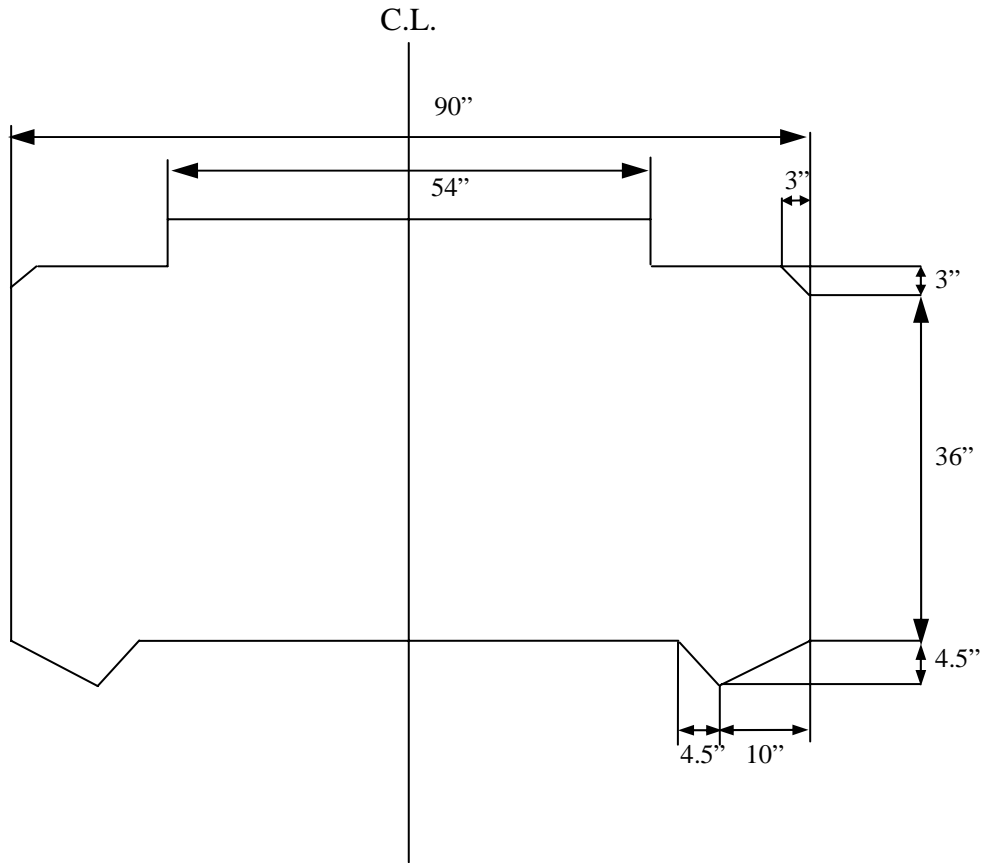
Figure 5.9 Cross Section of Midspan Diaphragm, Thickness = 8"
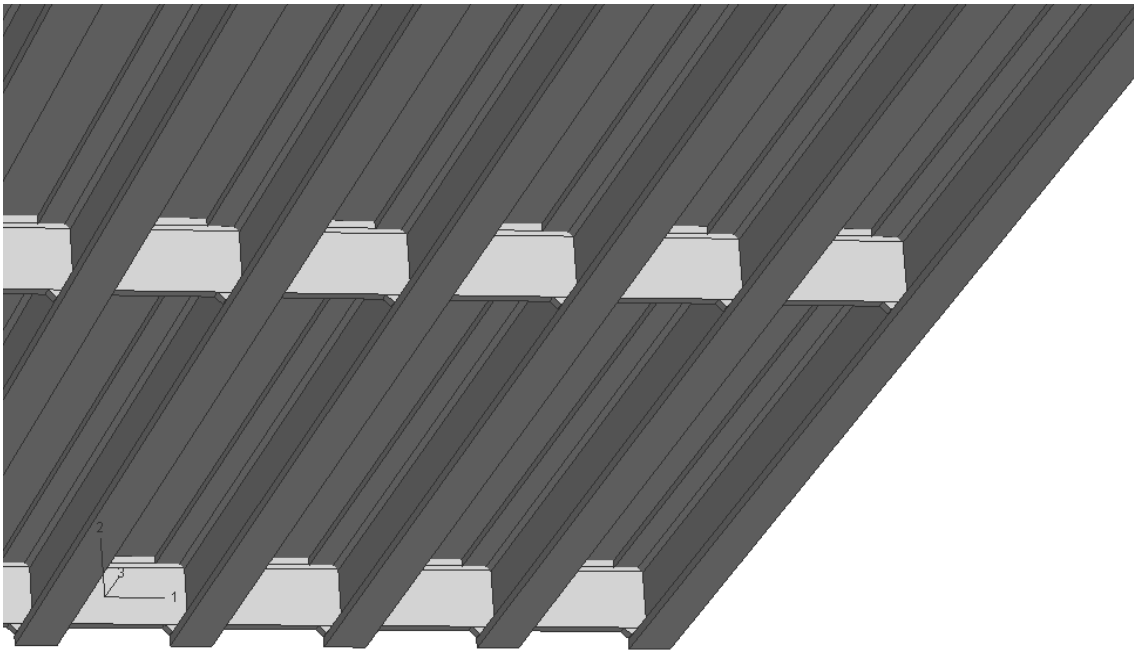
Figure 5.10 Model Simulation of Installed Midspan Diaphragms

5.6 BARRIER RAILS

According to the AASHTO LRFD specifications, though normally neglected, a

continuous barrier may be considered structurally active if full composite behavior is

certain (AASHTO 2004). In placing the barrier rails on the bridge model, a simple

extrusion of the cross-sectional shape shown in Figure 5.11 was made for the entire

200-ft. span of the bridge spans being modeled. In the actual bridge, there are

transverse saw-cut joints through the rail at a few positions along the length of the

bridge, so this approximation may add a slight measure of stiffness that is not actually

present. An ABAQUS image showing a barrier rail is given in Figure 5.12.
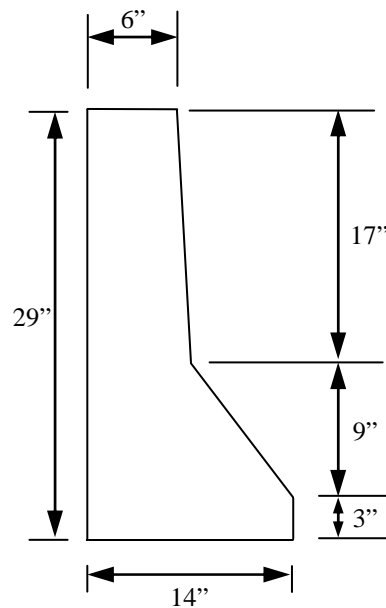
Figure 5.11 Barrier Rail Cross Section
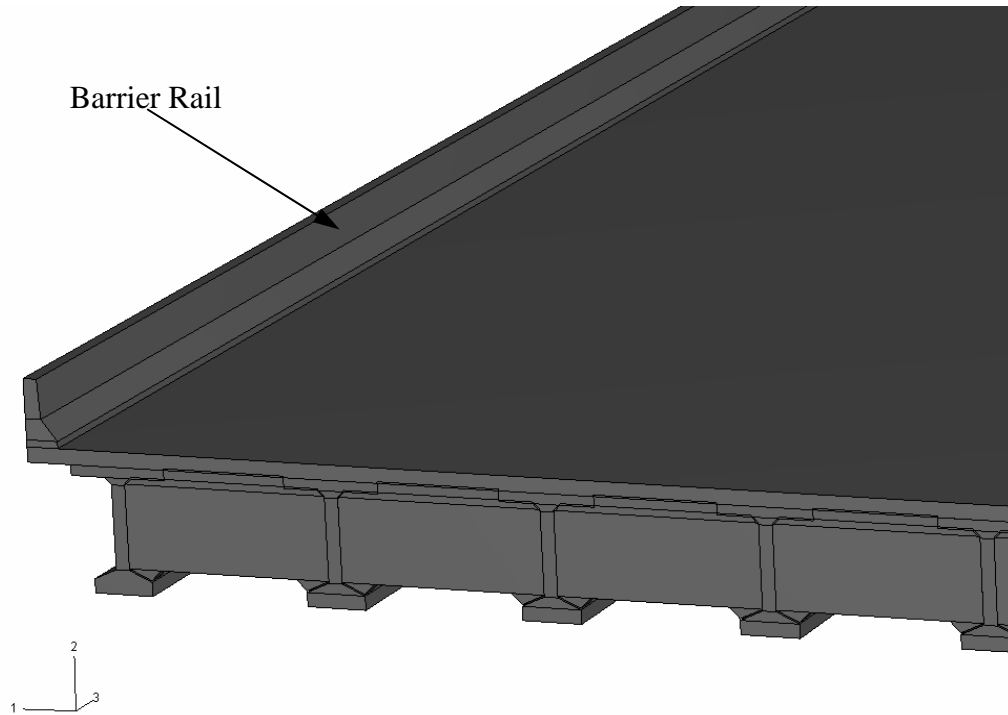
Figure 5.12 Bridge End View Showing Barrier Rail

5.7 BEARING PADS

For simplicity, one long bearing pad was used to represent the nine individual pads that

support the girders at each end of each span. The geometry of the bearing pads was

defined by an extrusion of a 7-in. by 0.75-in. rectangular cross section. The shape was

extruded 794 in.—the distance between the exterior edges of the bottom flanges of the

exterior girders. The centers of the bearing pads at the continuity diaphragm were

placed 10 in. away from the centerline of the diaphragm, and the bearing pads at the far

ends of the spans were placed such that the center-to-center distance between the

bearing pads on each span was 1182 in. The mesh size for the bearing pads is 9 inches.

The bearing pad at the far end of Span 10 is depicted in Figure 5.13. See Section 5.13

for more information about the support conditions.

78

The elastomeric bearing pads were assigned a conservative modulus of elasticity of 450 psi—based on the design values for rubber. Poisson's ratio for the elastomeric bearing pads was modeled as 0.5.
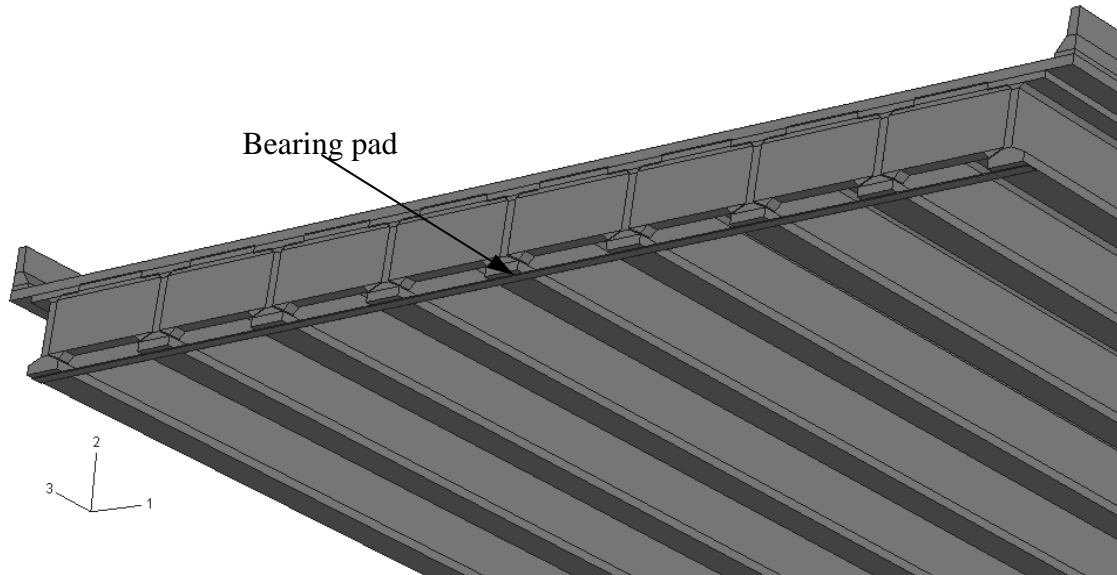
Figure 5.13 Bridge End View Showing Bearing Pad

5.8 ELEMENT SELECTION

There are many options for element types when constructing a finite-element model. For this model, three different types of elements were used.

5.8.1 Brick Elements

The element selected for most of the components in the model was an 8-node linear brick such as that shown in Figure 5.14a. The default element in ABAQUS for such an element is C3D8R, which incorporates reduced integration and hourglass control as well as translational degrees of freedom in the three global directions at each node.

Hourglass control relates to one of the problems associated with "first-order, reduced-integration elements… in stress/displacement analyses. Since the elements have only one integration point, it is possible for them to distort in such a way that the

strains calculated at the integration point are all zero, which, in turn, leads to uncontrolled distortion of the mesh" (ABAQUS 2006). Hourglass control helps prevent this.

Reduced integration "uses a lower-order integration [than full integration does] to form the element stiffness… [It therefore] reduces running time, especially in three dimensions" (ABAQUS 2006). See Section 5.8.4 for a more complete explanation of reduced versus full integration.

5.8.2 Shell Elements

Another type of element used in the model is a shell element such as that depicted in Figure 5.14b. Shell elements are used for the steel reinforcement, the load application, and the FRP—as explained in Section 5.11, Section 5.14, and Section 5.16, respectively. "Shell elements are used to model structures in which one dimension, the thickness, is significantly smaller than the other dimensions" (ABAQUS 2006). A shell element has geometry-defined length and width, but the thickness is defined as a section property rather than a property of the geometry. The shell elements used in this model are 4-node elements with translational and rotational degrees of freedom at each node. The elements selected to model steel reinforcement and truck loadings employ reduced integration. For reasons explained in Section 5.8.4, the FRP elements utilize full integration. The name used in ABAQUS for the steel and load application elements is S4R. The FRP elements are S4 elements.

5.8.3 Tetrahedral Elements

One other type of element used in the model is a tetrahedral element (C3D4). A tetrahedral element has 4 nodes and 4 sides, as shown in Figure 5.14c. According to the

ABAQUS Analysis User's Manual (2006), "C3D4 is recommended only for filling in regions of low stress gradient in meshes of C3D8 or C3D8R elements, when the geometry precludes the use of C3D8 or C3D8R elements throughout the model." This is exactly the use to which these elements were put in this model. There is a location at the base of the midspan diaphragms—identified in Figure 5.15—where the geometry makes meshing with brick elements awkward, and this is where the tetrahedral elements were used.
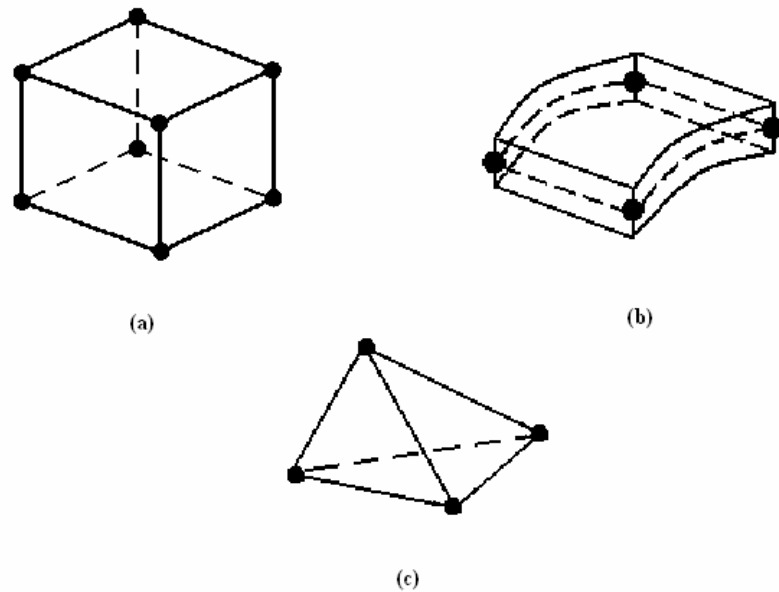
Figure 5.14 Examples of (a) an 8-Node Brick Element, (b) a 4-Node Shell Element, and (c) a 4-Node Tetrahedral Element (adapted from ABAQUS 2006)

tetrahedral elements
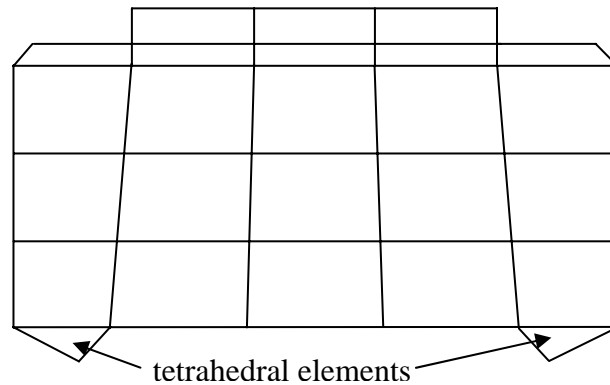
Figure 5.15 Mesh of Midspan Diaphragm

5.8.4 Element Integration Options

For many of the elements in ABAQUS, the option exists to use either full or reduced integration. With reduced integration, "the mass matrix and distributed loadings are still integrated exactly. Reduced integration usually provides more accurate results (provided the elements are not distorted or loaded in in-plane bending) and significantly reduces running time, especially in three dimensions" (ABAQUS 2006).

When analyzing the strain results of the FRP, it was apparent that the shell elements with reduced integration were insufficient for the task. These elements did not have enough integration points to adequately reflect the buildup of FRP stresses in the transition regions near where the FRP crosses the concrete cracks. This was evident because rather than reporting one strain value, as at other nodes, ABAQUS reported *four* strain values for the nodes on either side of the cracked region. These represented the strain values in each of the four adjoining elements, and the values varied widely. To avoid this, it was determined to use full integration for the FRP shell elements.

5.9 MODULUS OF ELASTICITY

In creating the model, a stiffer modulus of elasticity (E_c) was assigned to the prestressed girders than to the other concrete elements. The girder concrete was designed to be stronger in order to resist prestress forces at an early age. Based on previous research into the material properties of prestressed concrete, a value of 6,000,000 psi was selected as being representative of typical precast, prestressed concrete girders in the region (Roberts 2005).

For the deck, the modulus of elasticity was selected by computing a value that would reflect the approximate stiffness of the composite reinforced-concrete section when

modeled as a single isotropic material. Based on an assumed compressive strength of 4,000 psi—which, from ACI 318 Section 8.5.1, results in a modulus of elasticity of 3,605,000 psi—and an average modulus of elasticity for reinforcing steel of 29,000,000 psi (Gere 2001), an effective E_c value of 4,000,000 psi was used. This value was also used for the barrier rails despite their lighter reinforcement because they were assumed to have slightly stiffer concrete based on the low-slump mixture used to cast the rails. For the diaphragms, a modulus of elasticity of 3,605,000 psi was used.

When steel reinforcement was explicitly modeled, a modulus of elasticity of 29,000,000 psi was used. The modulus of elasticity for the bearing pads is explained in Section 5.7. The modulus of elasticity for the fiber-reinforced polymer is discussed in Section 5.16.

5.10 SEAMS

To approximate the behavior of a crack in a girder, a Seam was used in the FEM. This is a feature in ABAQUS which "defines an edge or a face in [the] model that is originally closed but can open during an analysis" (ABAQUS 2004). Figure 5.16 depicts a Seam which has opened due to loading. ABAQUS/CAE "places overlapping duplicate nodes along a [Seam] when the mesh is generated." Typically this feature is used in fracture mechanics to investigate crack growth using contour integral analysis. As the purpose of this investigation was to model the effects of the cracks rather than to study their propagation, the Seam approximation was considered sufficient.

The Seam feature allows the sides of the "crack" to either separate or close without establishing contact with each other. This was acceptable because in the actual structure a space was already physically present between the two faces of the crack, and

as such, some movement in either direction was possible. However, no initial condition in the model established a specific pre-existing gap. The effects of this are discussed in Section 7.5.
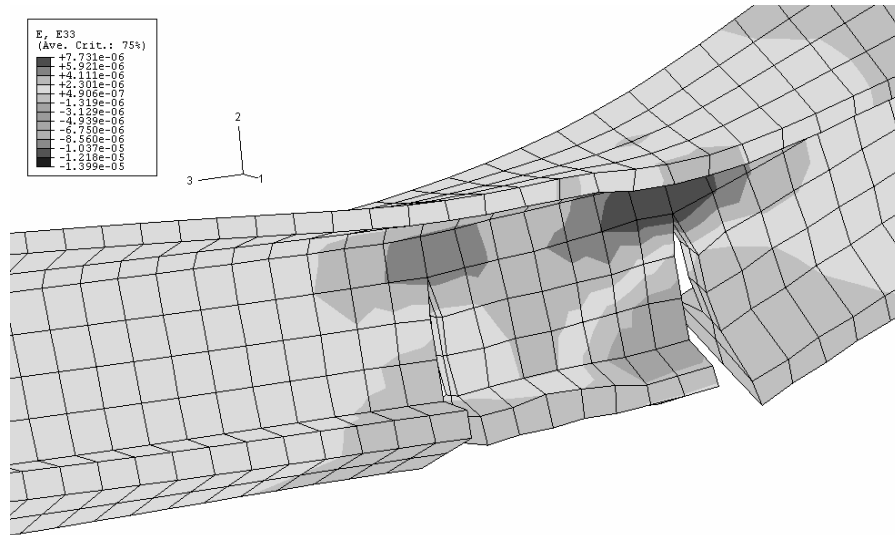
Figure 5.16 Cracked Girder with Seams Open Due to Loading

The locations of the Seams along the girders were determined from the drawings of the crack locations found in Figures 3.13 through 3.21. A summary of the locations of the Seams used in the *Pre-Repair* and *Post-Repair* FEMs is presented in Table 5.2. The locations of the seams are compared in Figures 5.17 and 5.18 to the locations of the actual cracks in Girders 7 and 8—the instrumented girders.

In addition to cracks in the girders, however, cracks are present in the faces of some of the continuity diaphragms near the girder connection. These were approximated with Seams in the girder located at the face of the diaphragm. Girder 2 is an example of a girder which has a seam defined only at the face of the continuity diaphragm. As shown in Figure 3.14, there are no cracks in the girder. But there is a crack in the continuity diaphragm adjacent to the girder, and this is why there is a seam at the face of the continuity diaphragm.

84

Table 5.2 Summary of Seam Locations for Pre-Repair and Post-Repair FEMs

Girder No.	Span 10		Span 11	
	Distance From Diaphragm Face (in.)	Distance up the girder (in.)	Distance From Diaphragm Face (in.)	Distance up the girder (in.)
1	24	up to top flange	18	up to top flange
	0[a]	up to top flange	0[a]	up to top flange
2	0[a]	45	none	n/a
3	24	6	all sealed	n/a
4	0[a]	27	0[a]	27
	21	6		
5	0[a]	27	0[a]	27
6	24	6	0[a]	up to top flange
7	36	18	36	up to top flange
8	36	6	48	up to top flange
9	18	up to top flange	none	n/a

[a] As explained in Section 5.15.4, seams at the face of the continuity diaphragms were not modeled in the *Uncracked*, *Cracked*, and *Cracked-with-Reinforcement* models

Each girder has a maximum of four Seams. One Seam could be located along the face of the continuity diaphragm to represent the cracking of the continuity diaphragm. This Seam could be located on either one or both spans. In addition to that, there could be one Seam located between 18 to 48 inches from the face of the continuity diaphragm on one or both spans to represent the cracking in the girder. Because each cracked girder end contains only one major crack, only one Seam was inserted at a location that was central to the location of the cracks present on each face of the girder.

Girder 7 - Span 10 - East Face

Girder 7 - Span 11 - East Face

Girder 7 - Span 11 - West Face

Girder 7 - Span 10 - West Face

———— = seam in FEM   ·············· = crack in girder
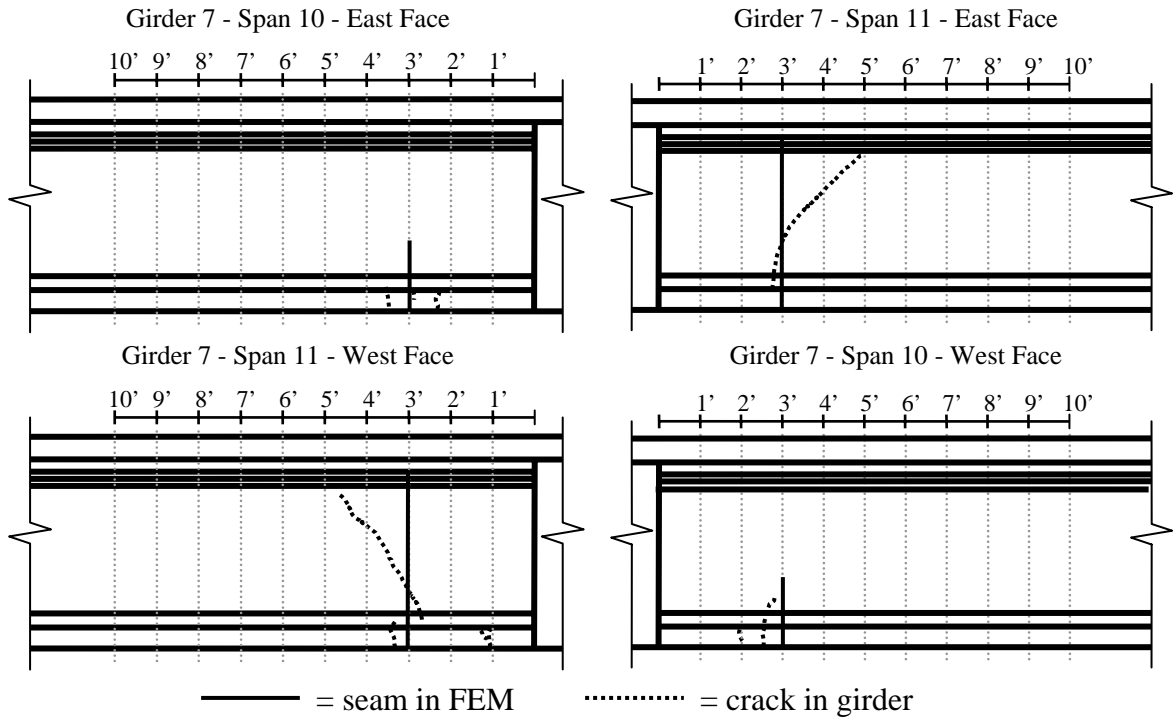
Figure 5.17 Girder Line 7 Cracks with Seams Superimposed (Fason and Barnes 2004)

Girder 8 - Span 10 - East Face

Girder 8 - Span 11 - East Face

Girder 8 - Span 11 - West Face

Girder 8 - Span 10 - West Face

———— = seam in FEM   ·············· = crack in girder
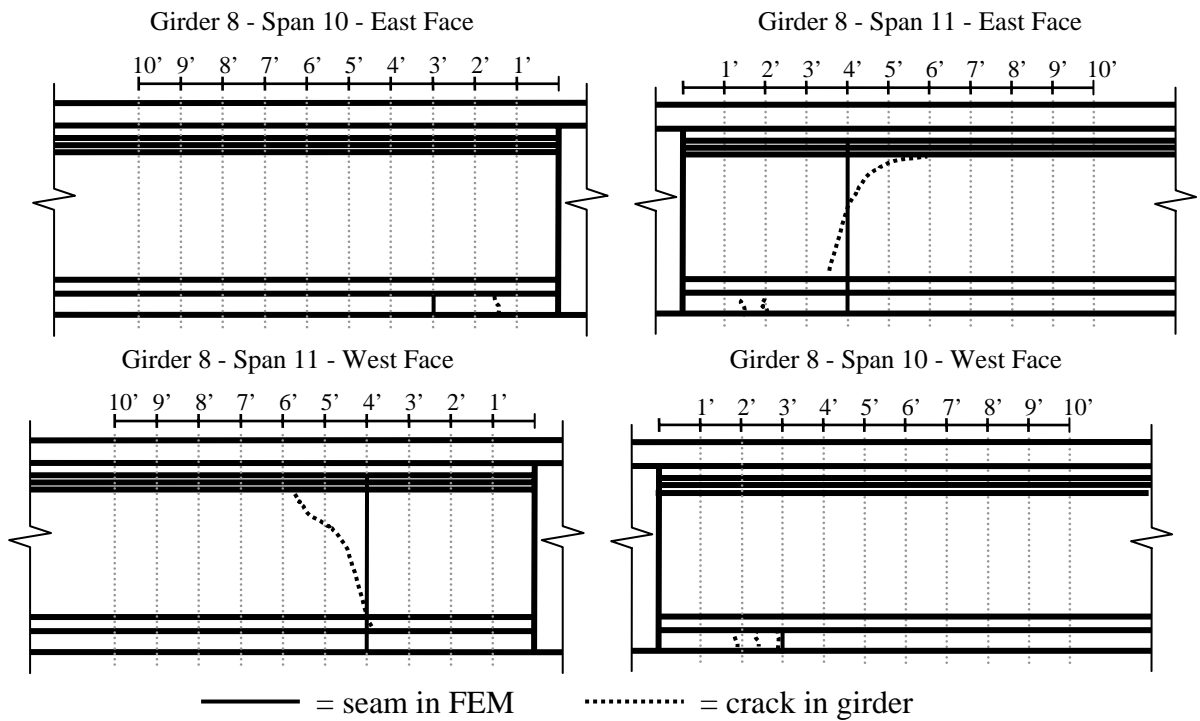
Figure 5.18 Girder Line 8 Cracks with Seams Superimposed (Fason and Barnes 2004)

5.11 PRESTRESSED REINFORCEMENT

Although it was determined to not explicitly model the prestress force in the prestressing strands, the presence of the prestressed reinforcing steel within the girders was not discounted. The stiffness of the prestressing steel should only have significant influence on the live load response of the girders near the cracked sections. Because of the proximity of these cracked regions to the ends of the girders, only the strands which were fully bonded were modeled explicitly. It was assumed that the partially debonded strands would add no stiffness to the cracked sections because they have little or no embedment beyond the cracked sections. As depicted in Figure 5.19, two groups of strands were modeled explicitly using the Rebar option for shell elements in ABAQUS. One line of shell elements, with a rebar layer representative of the sum of all of the straight strands in the bottom flange, was placed at the centroidal location of those strands. The draped strands were modeled in a similar manner, with one line of shell elements with a rebar layer oriented along the line of the centroid of the draped strands.

In ABAQUS, the Rebar option "is used to define layers of uniaxial reinforcement in membrane, shell, and surface elements (such layers are treated as a smeared layer with a constant thickness equal to the area of each reinforcing bar divided by the reinforcing bar spacing)… [These] can be used to add layers of reinforcement in a solid by embedding reinforced surface or membrane elements in the 'host' solid elements" (ABAQUS 2006). For more about embedding elements, see Section 5.12.

Midspan · Span 10 · Span 11 · Midspan

120" · 472" · 472" · 120"

Bent 11
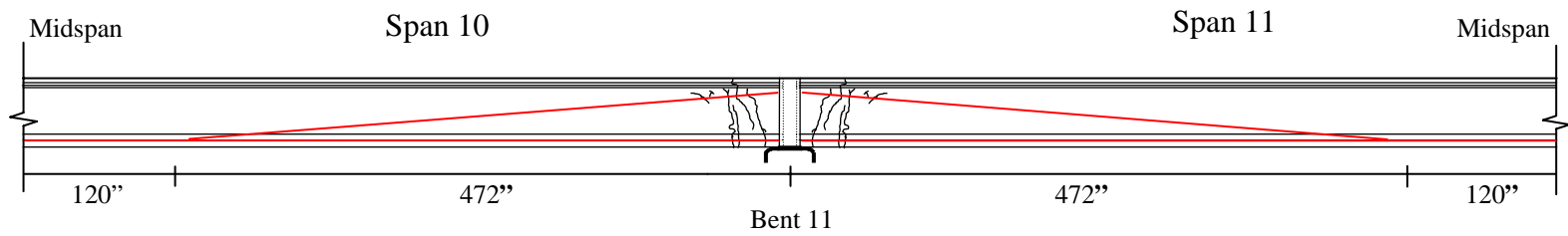
Figure 5.19 Prestressing Reinforcement Profile. Note: The height of the centroid of the horizontal straight strands is 5". The draped strands start at the face of the continuity diaphragm at a height of 45.5".

88

5.12 CONNECTIONS

As only the superstructure is expected to deform significantly and the substructure is

not damaged, the model includes only the parts of the bridge above and including the

girder bearing pads. Simplifications were made because the load tests measure the

effects of live loads only and do not reflect changes due to the dead loads, which are

always present. For example, the prestress force can be neglected in the linear elastic

portion of the model if the actual structure does not crack in these regions under the

effects of the test loads. Furthermore, it is not necessary to model the influence of the

prestressing force on the damaged sections if, as suspected (Barnes et al. 2006), there is

no longer an effective prestress force in these regions that could influence the opening

and closing of the pre-existing cracks under loads.

The connections between components were modeled as ties rather than as contact

connections, where two components can resist each other in one direction but can

separate in the other direction. A tie "make[s] the translational and rotational motion as

well as all other active degrees of freedom equal for a pair of surfaces" (ABAQUS

2006). The diaphragms are tied to the girders, just as the deck is tied to both the girders

and the diaphragms. This simulates the composite action which should be occurring in

the bridge structure. Also, the girders are connected to the bearing pads using a tie

constraint because the dead load forces contact between these elements regardless of

placement of truck loads.

Another type of connection used in the model is an embedment. "The embedded

element technique… is used to specify an element or a group of elements that lie

embedded in a group of host elements whose response will be used to constrain the

89

translational degrees of freedom of the embedded nodes (i.e., nodes of embedded

elements)" (ABAQUS 2006). Shell elements employing the Rebar option were

embedded into the corresponding girders. This effectively assumes a perfect bond

between the reinforcing steel and the concrete.

5.13 SUPPORT CONDITIONS

As explained in Section 5.12, only the superstructure of the bridge was modeled for this

study. The boundary condition which accomplished this was a pinned support along the

entire base of the bearing pads to approximate the bridge bent cap. Because this

effectively restrained all translational movement at the base of the bearing pads, the

vertical deformations of the bents were neglected in the finite-element analysis.

5.14 LOAD APPLICATION

As per AASHTO LRFD (2004) which specifies that the wheel loads on the deck be

modeled as patch loads distributed over an area approximating the wheel contact

surface, the truck loads were approximated by means of planar shells that each represent

one of the six main wheel groups on each of the two trucks, as depicted in Figure 5.20.

The dimensions of the planar shell were 8 in. by 21.5 in. by 0.1 in. The modulus of

elasticity for these elements was the same as that used for the deck—4,000,000 psi. The

shell surface was then connected with tie constraints—which are explained in Section

5.12—to the deck in the proper location for each of the wheel group positions. The

truck weight was applied as a pressure load distributed over the area of each wheel

group element. These pressures are listed, with the truck weights they represent, in

Table 5.3.
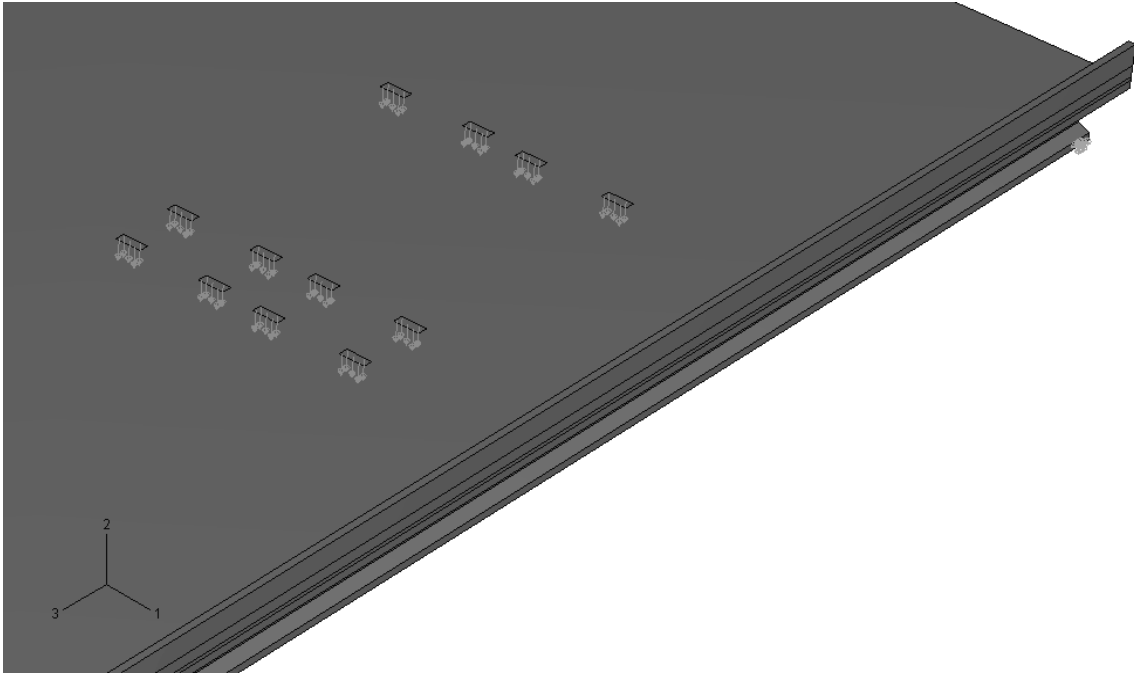
Figure 5.20 Truck Loading with Load Arrows Indicating Wheel Group Loads

Table 5.3 Test Truck Wheel Group Pressure Loads

Axle	Wheel Group	Truck Weight (lbs)		Wheel Group Pressure (psi)	
		ST-6400	ST-6902	ST-6400	ST-6902
Front	Left	10,750	7,850	62.5	45.6
	Right	10,900	7,450	63.4	43.3
Rear 1	Left	18,900	19,350	110	113
	Right	18,350	18,750	107	109
Rear 2	Left	17,200	18,600	100	108
	Right	17,500	19,250	102	112
Total		93,600	91,250	--	--

5.15 MODEL REFINEMENT

The model was created in three broad stages. This section describes those stages

briefly, while Section 6.2 presents them more comprehensively.

5.15.1 Uncracked Model

Originally, the model was created using uncracked girders with no explicit steel

reinforcement. This *Uncracked* model was used as a baseline for the ideal response of

the bridge to live loads, as it was originally intended. It incorporated all of the basic

structural features such as midspan diaphragms and barrier rails that were included in

the later models. Because no cracking was expected under service-load conditions in

the undamaged structure, this model did not include the Seams, nor was girder

reinforcement explicitly modeled.

5.15.2 Cracked Model

After the *Uncracked* model was completed, the *Cracked* model was created using the

Seam feature described in Section 5.10. The locations of the Seams along the girders

were determined from the pictures of the crack locations found in Figures 3.13 through

3.21 and are summarized in Table 5.2.

Where the *Uncracked* model was the ideal model for the behavior of the bridge, the

Cracked model was used as the worst-case scenario for the behavior of the damaged

bridge. The actual bridge could be expected to exhibit response corresponding to this

model if the prestressing strands that cross the cracks offer no resistance to crack

opening or closing under live loads.

5.15.3 Cracked-with-Reinforcement Model

It was hypothesized that because of the location and width of the original cracks, the

prestressing strands had lost their prestressing force through excessive slip in this region

and were functioning merely as nonprestressed reinforcement at best. To test whether

the strands were still able to function as nonprestressed reinforcement across the cracks,

the reinforcement was applied to the *Cracked* model as described in Section 5.11, and

the resulting *Cracked-with-Reinforcement* model was analyzed.

5.15.4 Pre-Repair Model

The final *Pre-Repair* model differs from the *Cracked-with-Reinforcement* model in only

one way. After beginning to model the FRP repair on the *Cracked-with-Reinforcement*

model, an error in modeling the Seams explained in Section 5.10 and identified in Table

5.2 was discovered. While the Seams away from the face of the diaphragm were all

defined correctly, the Seams which were supposed to be present in some of the girders

at the face of the continuity diaphragm had not been defined. It was judged that

because the inclusion of the Seams would not affect the global behavior of the bridge—

which is demonstrated through the bottom-fiber strain results depicted in Figure 5.21,

where the results of the two models overlap one another—the decision to use the

Cracked-with-Reinforcement model, as opposed to the *Uncracked* or *Cracked* models,

would not be affected. As a result, the Seams were corrected in only two models—the

Pre-Repair model and the *Post-Repair* model. The *Pre-Repair* model was then used to

compare the current analytical behavior of the bridge with the expected behavior

predicted by the *Post-Repair* model.
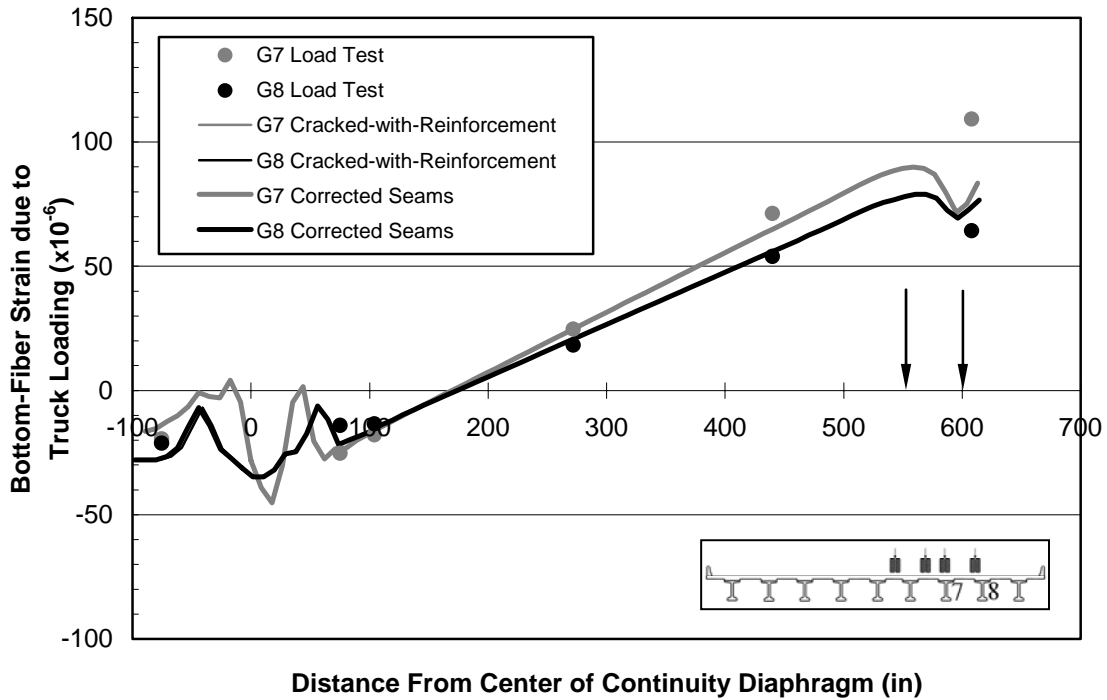
Figure 5.21 Comparison Between Models with and without Correctly Defined Seams

5.16 MODELING OF FRP

After a model was created which accurately reflected the current, pre-repair behavior

of the bridge, the proposed FRP repair was modeled and the results analyzed. The wet

lay-up FRP system proposed for repair of the I-565 structures is expected to behave as a

laminate, or thin plate. The FRP reinforcement was modeled using shell elements with

a variable thickness representing the different number of layers at each position along

each girder. Each layer of a composite material is referred to as a "ply" for the purposes

of this investigation (Swenson 2003). Multiple plies can be layered in order to achieve

the desired material strength. The design thickness of one ply of the Tyfo SCH-42

composite that will be used for the repair is 0.04 in., so when 4 plies are present, the

thickness of the shell element is 0.16 in.; for 3 plies it is 0.12 in., etc. See Section 5.8.2

for more details on the properties of the shell elements used to model the FRP reinforcement. The bond of the FRP to the concrete was modeled using a tie constraint as explained in Section 5.12.

5.16.1 Mechanical Theory of Fiber-Reinforced Polymers

A composite material, such as fiber-reinforced polymer, is a material composed of either continuous or noncontinuous fibers which are surrounded by a weaker matrix material. This matrix serves to both distribute the fibers and transfer the load to them (Gay 2003). For a unidirectional ply, the mechanical characteristics of the fiber/matrix mixture can be calculated from the known characteristics of each of the constituents.

The modulus of elasticity along the direction of the fiber depends almost entirely on the longitudinal stiffness of the fibers. In the transverse direction, the modulus of elasticity is defined by Equation 5.1 (Gay 2003):

$$E_t = E_m \left[\frac{1}{\left(1 - V_f\right) + \dfrac{E_m}{E_{ft} V_f}} \right] \qquad \text{Eq. 5.1}$$

where

E_t = Modulus of elasticity in the transverse direction

E_m = Modulus of elasticity of the matrix

E_{ft} = Modulus of elasticity of the fiber in the direction that is transverse to the fiber
   longitudinal axis

V_f = Fiber volume fraction

A guideline for the shear modulus of the composite (G_{lt}) is given by Equation 5.2 (Gay 2003):

$$G_{lt} = G_m \left[\frac{1}{(1-V_f) + \dfrac{G_m}{G_{flt}V_f}} \right]$$

Eq. 5.2

where

G_m = Shear modulus of the matrix

G_{flt} = Shear modulus of the fiber

V_f = Fiber volume fraction

The value for Poisson's ratio (ν_{lt}) is approximated by Equation 5.3 (Gay 2003):

$$\nu_{lt} = \nu_f V_f + \nu_m V_m$$

Eq. 5.3

where

ν_f = Poisson's ratio of the fiber

ν_m = Poisson's ratio of the matrix

V_f = Fiber volume fraction

V_m = Matrix volume fraction

5.16.2 FRP as an Isotropic Material

Isotropic materials are those "having the same properties in all directions (whether

axial, lateral, or any other direction)" (Gere 2001). While this is not the case with fiber-

reinforced polymer, an attempt was made to model it as such for simplicity. The

possibility existed that because the loading imposed on the FRP reinforcement was

predominantly in the longitudinal direction, an isotropic material, which modeled the

material properties of the fiber-reinforced polymer as being identical in all directions,

would be sufficiently representative. In the event that modeling the FRP reinforcement

with laminar properties represented a significant increase in the computational burden, the potential for accurately modeling it as an isotropic material was explored.

5.16.3 FRP as a Laminar Material

When "the properties in a particular direction are the same throughout the material and the properties in all directions perpendicular to that direction are the same (but different from the first properties); then the material is classified as *orthotropic*" (Gere 2001). To define an orthotropic material, nine material properties are required. These include the elastic moduli in the three principle directions, the three Poisson's ratios between those three principle directions, and the three shear moduli between them.

"Under plane stress conditions, such as in a shell element," fewer material properties are necessary than the nine required to "define [a conventional] orthotropic material" (ABAQUS 2006). In all of the plane stress elements, the stress perpendicular to the shell surface is equal to zero. Under these circumstances, only six material properties are required to describe the behavior: the elastic moduli of the two principal directions (E_l and E_t), Poisson's ratio between the two principal directions (v_{tl}), and the three shear moduli between the two principal directions and their orthogonal direction (G_{tl}, G_{tp}, G_{lp}). This simplified form of defining an orthotropic material is referred to as a *laminate* in ABAQUS.

As explained in Section 6.3.1, this is the representation used for the FRP in the final *Post-Repair* model. The longitudinal elastic modulus was assumed equal to the published design value for the FRP system to be employed: 11,900,000 psi. The transverse elastic modulus was calculated from the known longitudinal elastic modulus and the Poisson's ratio between the two principal directions provided by the

manufacturer, $v_{tl} = 0.086$, using Equation 5.4 (ABAQUS 2006), which dictates the minimum requirement for material stability.

$$\left(\frac{E_l}{E_t}\right) \cdot v_{tl} = \frac{1}{2}$$

Eq. 5.4

From this equation, the transverse elastic modulus was determined to be 2,200,000 psi.

Published design values for the three shear moduli were unavailable from the manufacturer, so the values were estimated from the known, composite make-up of the material. Two of the shear moduli, G_{tl} and G_{lp}—where t is the transverse direction, l is the longitudinal direction, and p is the direction perpendicular to the plane—are taken from a published design value for the shear modulus of an unspecified, unidirectional carbon/epoxy composite. That value is 610 x 10^3 psi (Gay 2003). The third shear modulus, G_{tp}, was calculated using the isotropic relationship of epoxy between the elastic modulus and the shear modulus—which is given in Equation 5.5 (Gere 2001):

$$G = \frac{E}{2(1+v)}$$

Eq. 5.5

E was taken as the tensile modulus of the epoxy as given by the manufacturer—461 x 10^3 psi—and v was taken as the published design value for Poisson's ratio of an unspecified epoxy—0.4 (Gay 2003). From these, the final shear modulus was calculated to be 165 x 10^3 psi.

CHAPTER 6: RESULTS

6.1 INTRODUCTION

This chapter presents analytical results generated from the various finite-element

models developed for this study. The load test results which were used to verify the

accuracy of these models are presented in summary in Appendix H. Where applicable,

they are compared to the relevant FEM results in this chapter.

The analytical results presented in this chapter are organized into two groups: results

from modeling the existing structure and results from modeling the FRP-repaired

structure. Both of these groups include both longitudinal strains and deflections which

were output from the analysis of the corresponding FEMs. In addition to the bottom-

fiber strains, which are presented in this chapter, longitudinal surface strains were also

measured at various depths at several instrumented cross sections—as described in

Section 4.3.4.1 and discussed in Section 7.2.1. These experimental values and the

corresponding FEM results are presented graphically in Appendices D through G.

6.2 FINITE-ELEMENT MODELING OF THE EXISTING STRUCTURE

6.2.1 Uncracked Model

The *Uncracked* model was intended to represent the behavior of the bridge if the

damage had no effect on its performance. This model presents a picture of the ideal

bridge behavior if no cracks were present—the intended behavior of the bridge design.

The longitudinal strain results for this model for each of the four representative load test positions can be seen in Figures 6.1 through 6.4.

For these figures—as well as for the other figures in this chapter—the positive values on the abscissa represent Span 11 while the negative values represent Span 10. The locations of wheel groups for the truck loads are indicated by vertical arrows. Length of the arrows indicates the relative loads on the axles. The inset picture indicates the transverse position of the load trucks. The individual data markers represent strain measurements obtained during the actual load testing of the structure.

The girders, deck, diaphragms, and barrier rails were modeled as discussed in Sections 5.2, 5.3, 5.5, and 5.6, respectively. This model consisted entirely of C3D8R brick elements, S4R shell elements, and C3D4 tetrahedral elements, as explained in Section 5.8. Aside from its indirect influence on the assumption of uncracked concrete behavior, the prestressing force was not explicitly considered in this model. Because the concrete was assumed to be uncracked, the stiffening attributable to steel reinforcement was neglected, except for the selection of the modulus of elasticity for the nonprestressed deck elements as described in Section 5.9.

The *Uncracked*-model results generally exhibit more compression (or less tension) strain at the girder bottom fiber than was measured in the load tests. This is particularly evident at the cross sections near the cracked regions. The discrepancy is pronounced for the load positions near midspan (A9 and C9). This indicates that the girder bending moments in the actual structure are less negative than in the *Uncracked* model. Thus, this model overestimates the continuity of the cracked-girder system.

100

Figure 6.1 Bottom-Fiber Strain Data for the Uncracked Bridge Model—A7 Load Position

Figure 6.2 Bottom-Fiber Strain Data for the Uncracked Bridge Model—A9 Load Position

101

Figure 6.3 Bottom-Fiber Strain Data for the Uncracked Bridge Model—C7 Load Position

Figure 6.4 Bottom-Fiber Strain Data for the Uncracked Bridge Model—C9 Load Position

102

6.2.2 Cracked Model

Comparison of the *Uncracked* model results to the corresponding load test results indicates that the cracks obviously have *some* effect on the bridge behavior; therefore, an attempt was made to accurately model the effects of the cracking. To this end, seams were created in the bridge girders that had visible cracking. The longitudinal strain results for the resulting *Cracked* model, when subjected to the four representative load test positions, can be seen—superimposed on the graphs of the corresponding results for the *Uncracked* model—in Figures 6.5 through 6.8.

The seams were created as explained in Section 5.9, and the seam locations are detailed in Table 5.2. The effect of a seam is to create independent nodes along the two faces of the seam; this allows each side of the seam to move independently of the other side, somewhat like a tear in a piece of paper. This model represents the worst-case scenario—the bridge behavior if the steel that crosses these cracks does not contribute to the superstructure's resistance to applied loads. This would be the case if all of the steel crossing each crack had fractured, or if the bond between the prestressing reinforcement and concrete had deteriorated to the extent that no stresses can be transferred from the concrete to the steel.

**Figure 6.5 Bottom-Fiber Strain Data for the Cracked Bridge
Model—A7 Load Position**

Distance From Center of Continuity Diaphragm (in)

**Figure 6.6 Bottom-Fiber Strain Data for the Cracked Bridge
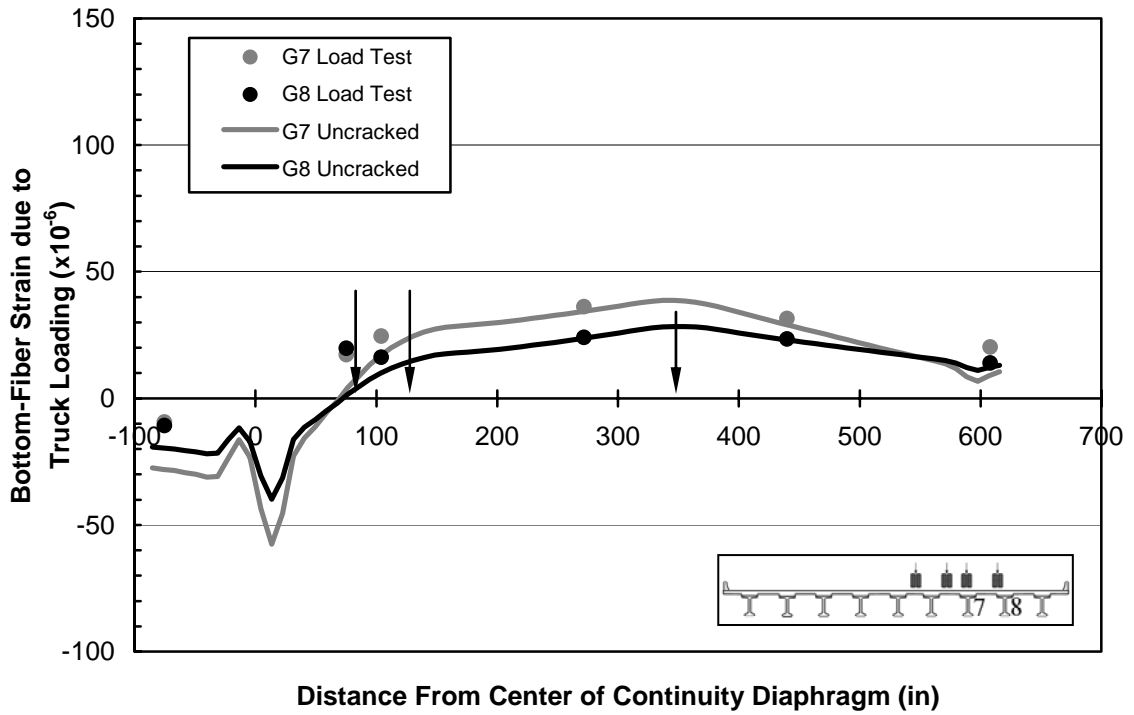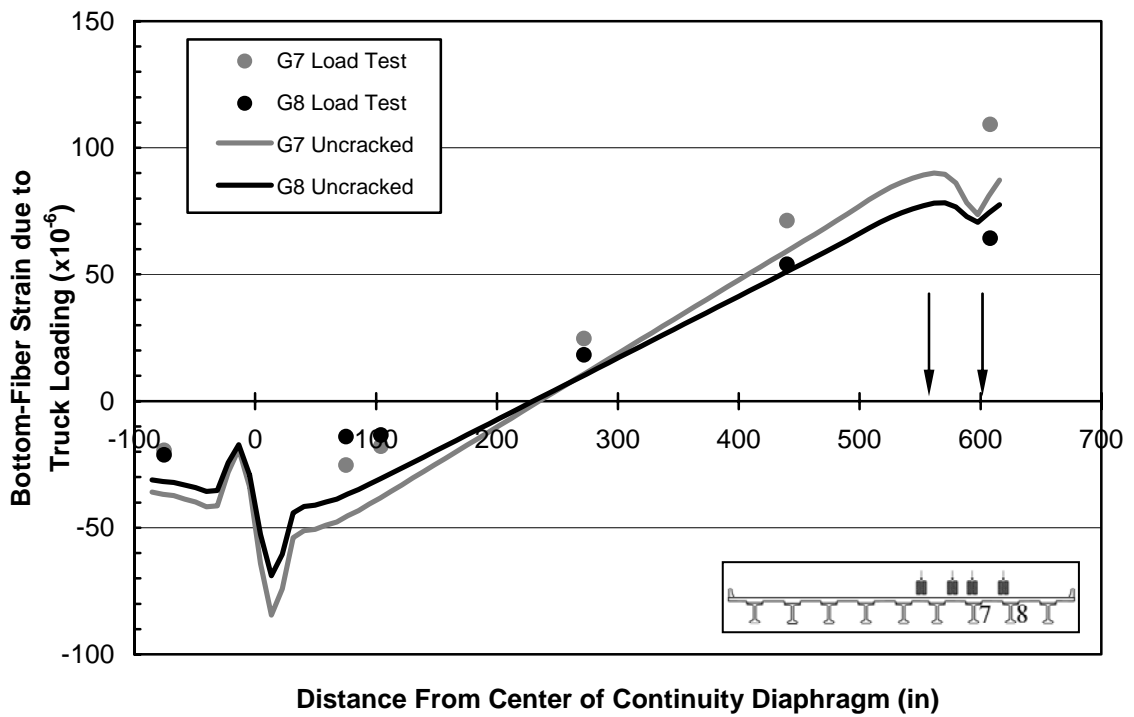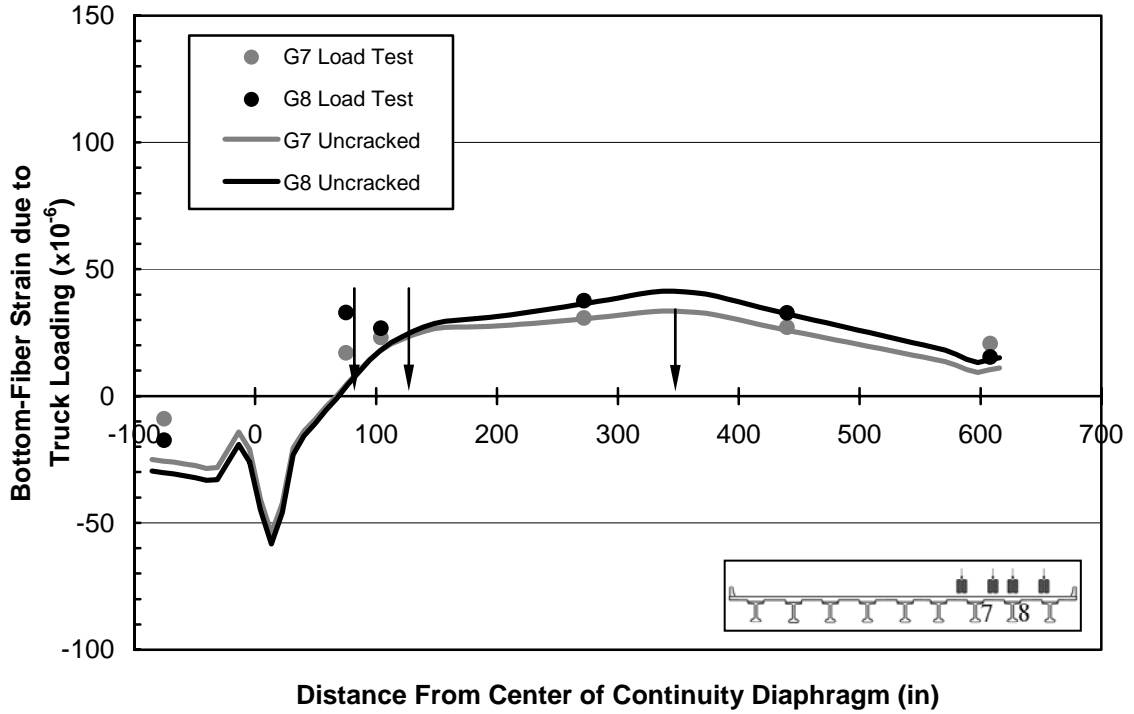Model—A9 Load Position**

104

Figure 6.7 Bottom-Fiber Strain Data for the Cracked Bridge Model—C7 Load Position

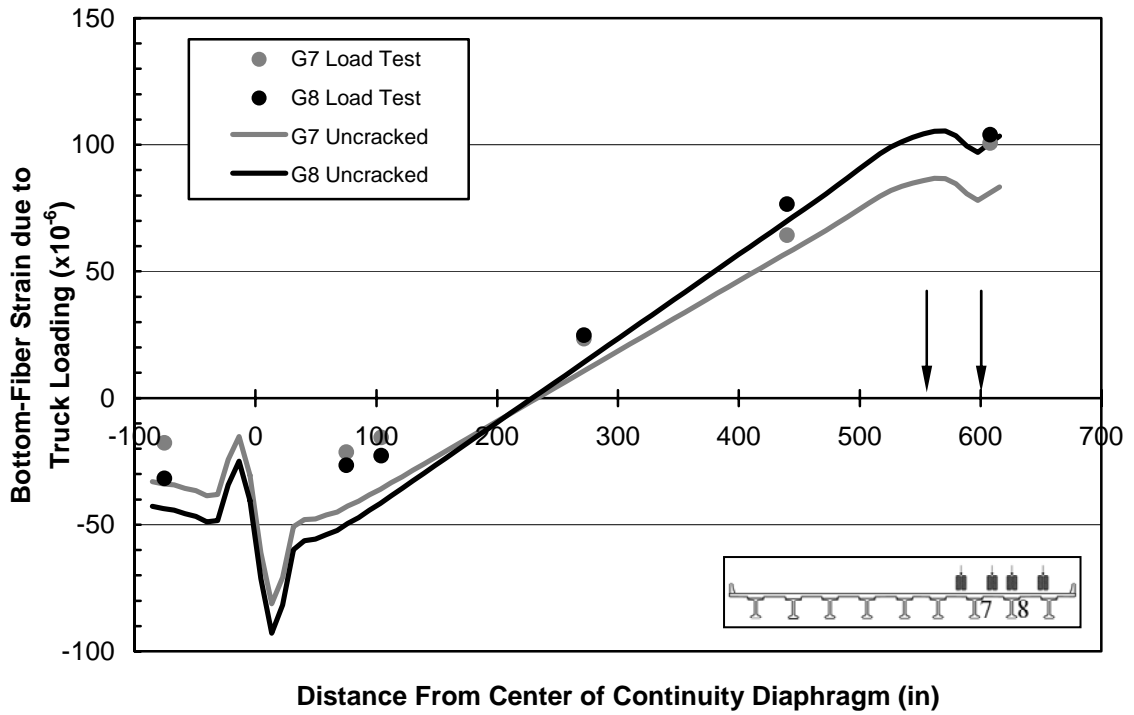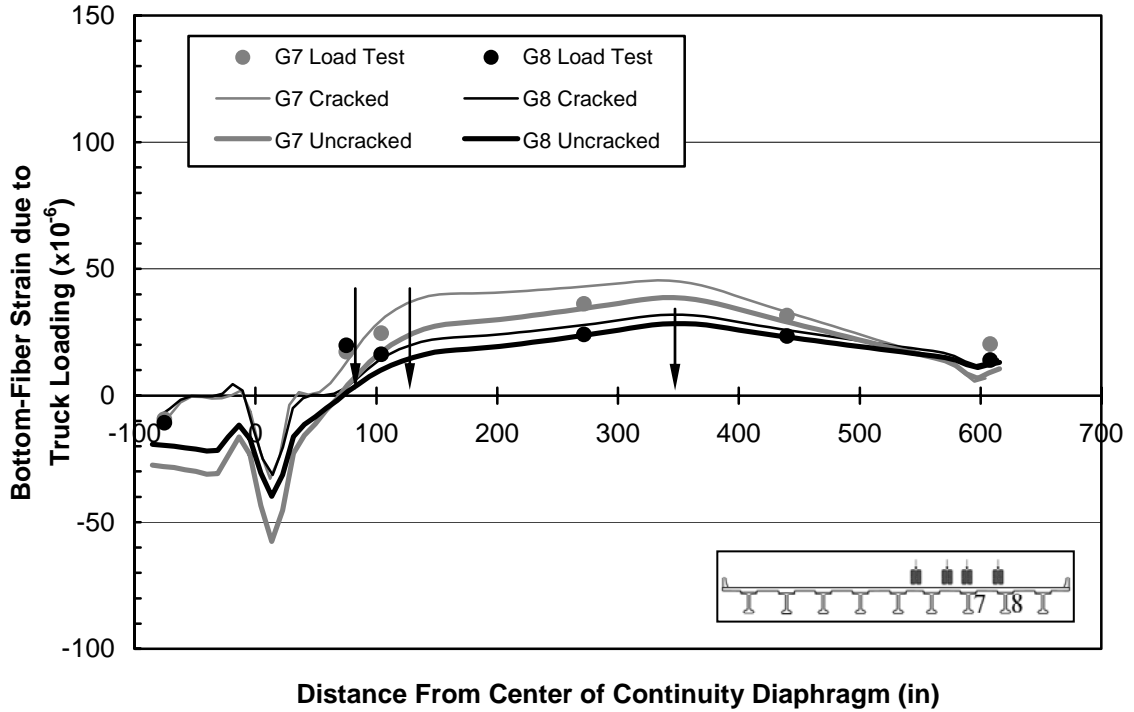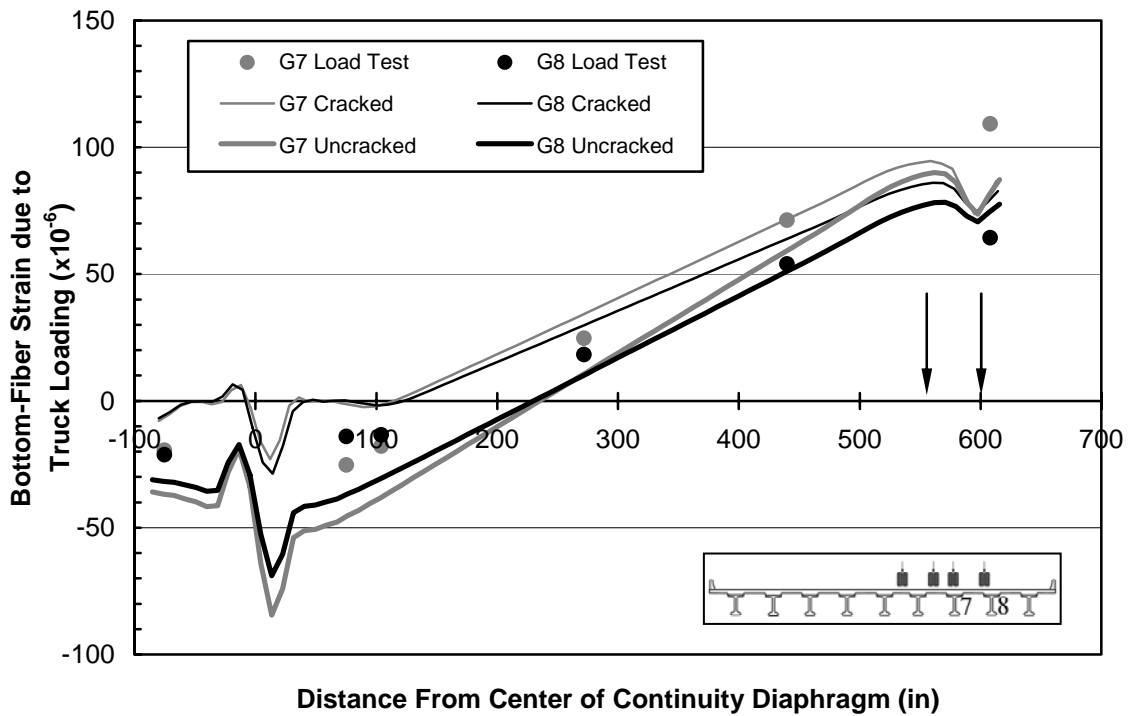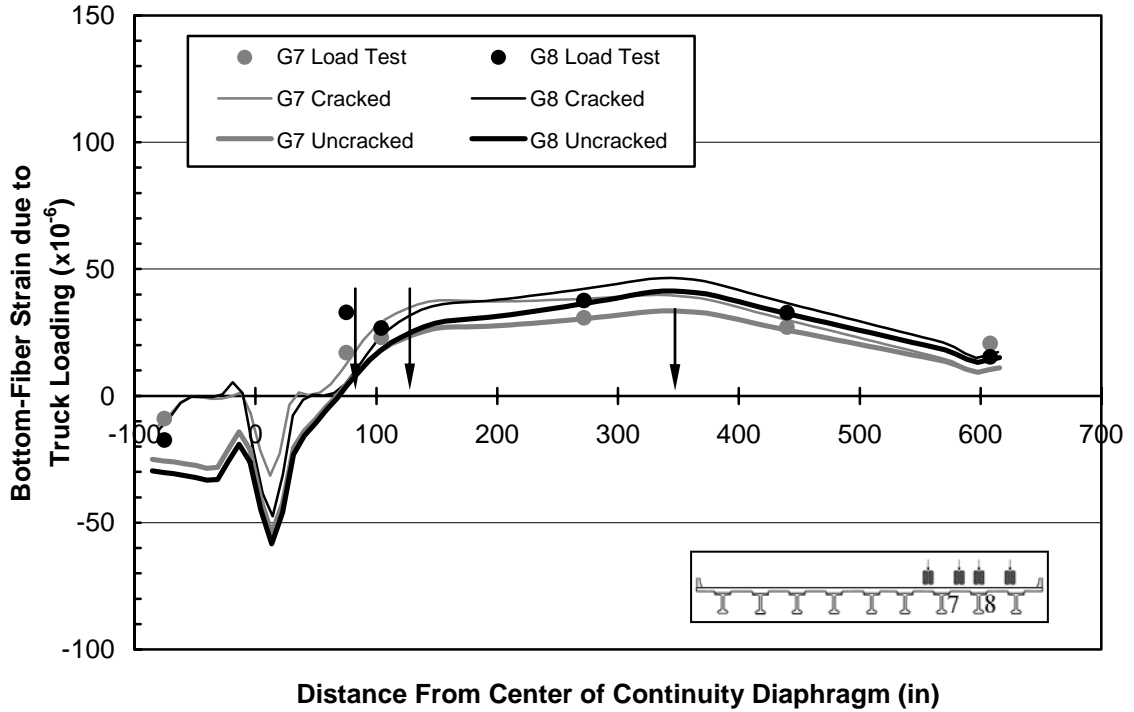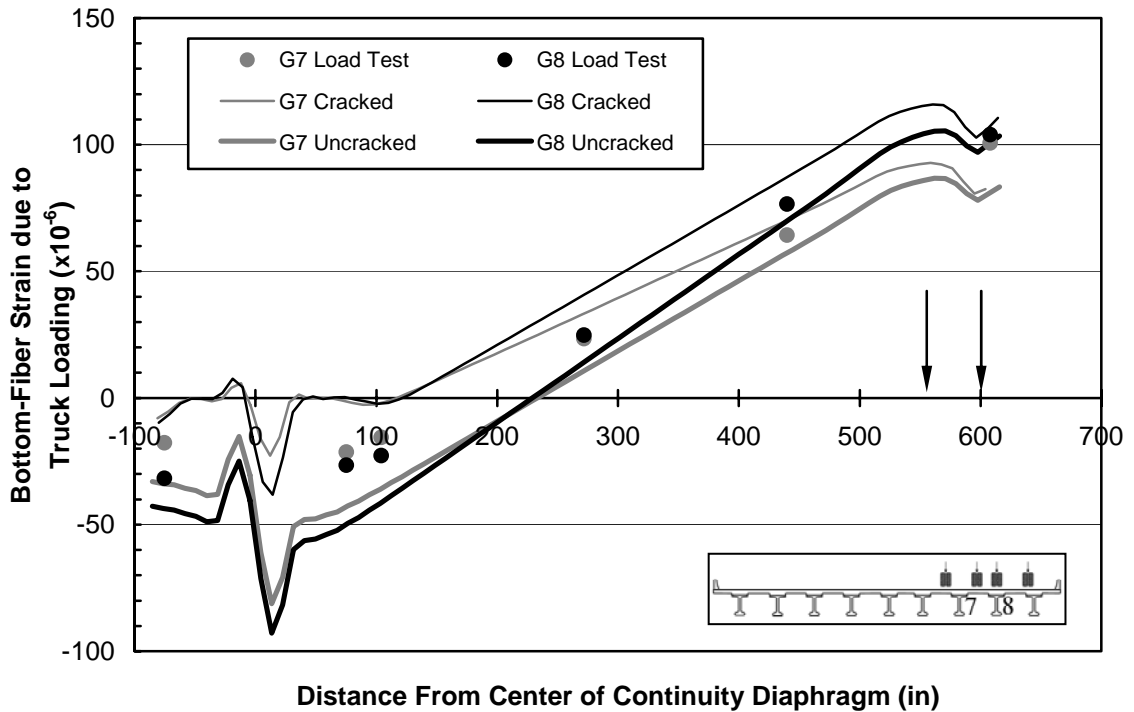**Figure 6.8 Bottom-Fiber Strain Data for the Cracked Bridge Model—C9 Load Position**

As expected, the FEM results from this model indicate no bending moment being developed near the cracks. This can be seen in the graphs where the bottom-fiber strains equal zero. However, this does not reflect the behavior observed in the load test results. The load test results indicate that bottom-fiber strains are developed at the gauge sections near the cracks. These measured strains indicate compression near the cracks when the loads are near midspan (A9 and C9). However, when the test trucks are near the cracked section in Span 11 (A7 and C7), the behavior is more complex. The measured strains near the cracks in the loaded span (Span 11) indicate bottom-fiber tension, while compression is evident near the crack on the far side of the continuity diaphragm (Span 10).

6.2.3 Cracked-with-Reinforcement Model

Comparison of the results of the *Cracked* model to the load test results indicates that the actual cracked structure is somewhat stiffer (or more continuous) than the *Cracked* model. The *Cracked* and *Uncracked* model results seem to bracket the actual bridge behavior. This is particularly evident for the bottom-fiber strains for the A9 and C9 load positions. The compressive strains measured near the cracked regions indicate that significant negative moments are being developed at the crack sections for these load positions. Therefore, an attempt was made to gauge whether the additional stiffness in these regions is commensurate with the stiffness of the prestressing strands that cross the cracks. A *Cracked-with-Reinforcement* model was developed using the rebar function in ABAQUS as explained in Section 5.11. Two groups of reinforcing steel, the draped and undraped strands, were each modeled as one bundle. As the model only describes the response of the bridge to *changes* in truck loadings—and, as explained in

Section 3.4.2, it is unlikely that the prestress force is effective at the cracked section—no attempt was made to apply a prestressing force to the model.

The longitudinal strain results for the *Cracked-with-Reinforcement* model with loads placed at each of the four representative load test positions can be seen—superimposed on the graphs of the *Uncracked* and *Cracked* models—in Figures 6.9 through 6.12. The deflection results for these three models are presented in Figures 6.13 through 6.16. For the strain results—and except for the Girder 7 gauge at midspan of Span 11, as explained in Section 6.5.1—the *Uncracked* and *Cracked* models consistently bracket the load test results and the *Cracked-with-Reinforcement* model results. This is seen most strikingly in the A9 and C9 Load Positions for the two strain gauges nearest the continuity diaphragm on each girder of Span 11. There is between a 30×10^{-6} in./in. and 50×10^{-6} in./in. difference at those points between the *Uncracked* and the *Cracked* models. And both the load test results and the *Cracked-with-Reinforcement* results fall directly in the middle of this range.

For the deflection results, this relationship holds true between the three models, but the load test results generally indicate *less* deflection than the *Cracked* and *Cracked-with-Reinforcement* models predict. This is most pronounced for the Girder 8 results and is most evident in the A9 and C9 Load Positions. While Girder 7 exhibits the bracketing relationship of the model data to the load test data for the A9 Load Position, Girder 8 predicts more deflection in even the *Uncracked* model than is occurring. For the C9 Load Position at midspan, the *Uncracked* model predicts more deflection for both girders. This is also seen on the unloaded span for all four load positions on the *Uncracked* and *Cracked-with-Reinforcement* models. Most likely this is because the

concrete used in the FEMs is less stiff than the concrete in the bridge. In addition, it is possible that the pretensioning force in the bridge results in less deflection than the FEMs—which do not have a pretension force applied—predict. This could be due to the slight increase in stiffness which results from the partially debonded strands. Though these strands were not included in the models because they were not effective at the cracks, they could add a slight amount of stiffness in the middle regions on the span(s). Also, as explained in Section 6.3.2, the FEM does not reflect the build-up of the deck over the girders. This build-up would slightly increase the composite girder stiffness due to the increased total depth of the cross section.

After comparative evaluation of both the strain and deflection results, it was determined that—of the three—the *Cracked-with-Reinforcement* model best represents the bridge behavior.

Figure 6.9 Bottom-Fiber Strain Data for the Model Refinement—A7 Load Position

Figure 6.10 Bottom-Fiber Strain Data for the Model Refinement—A9 Load Position

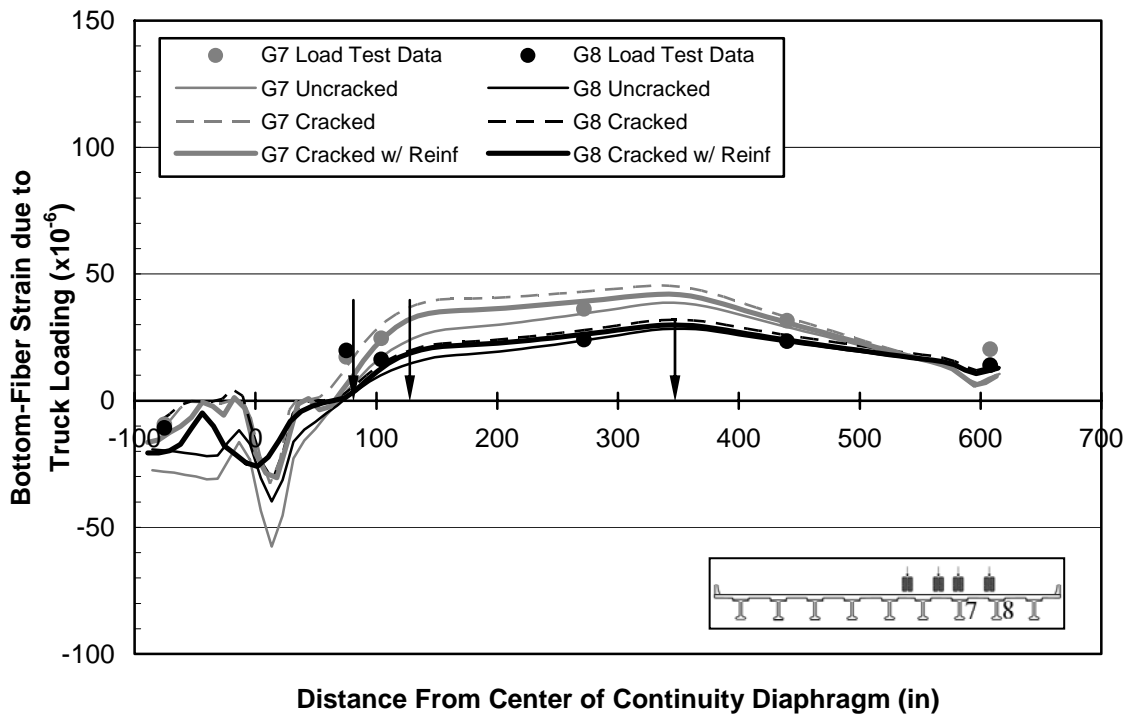**Figure 6.11 Bottom-Fiber Strain Data for the Model Refinement—C7 Load Position**

109
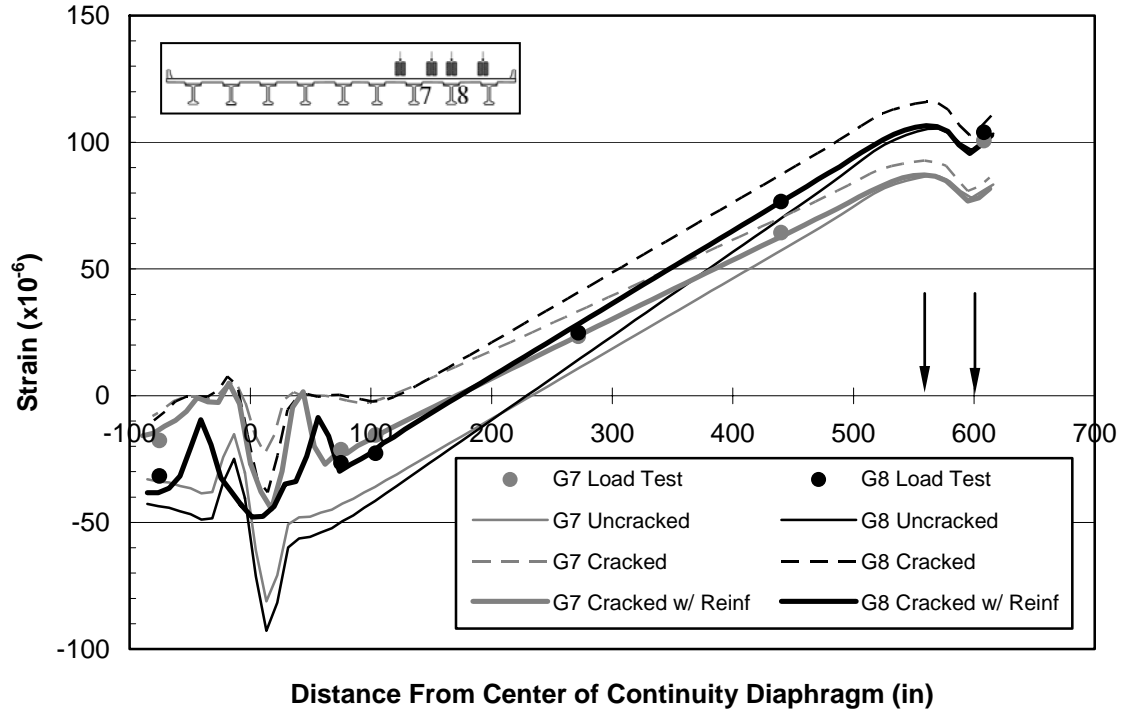
**Figure 6.12 Bottom-Fiber Strain Data for the Model
Refinement—C9 Load Position**
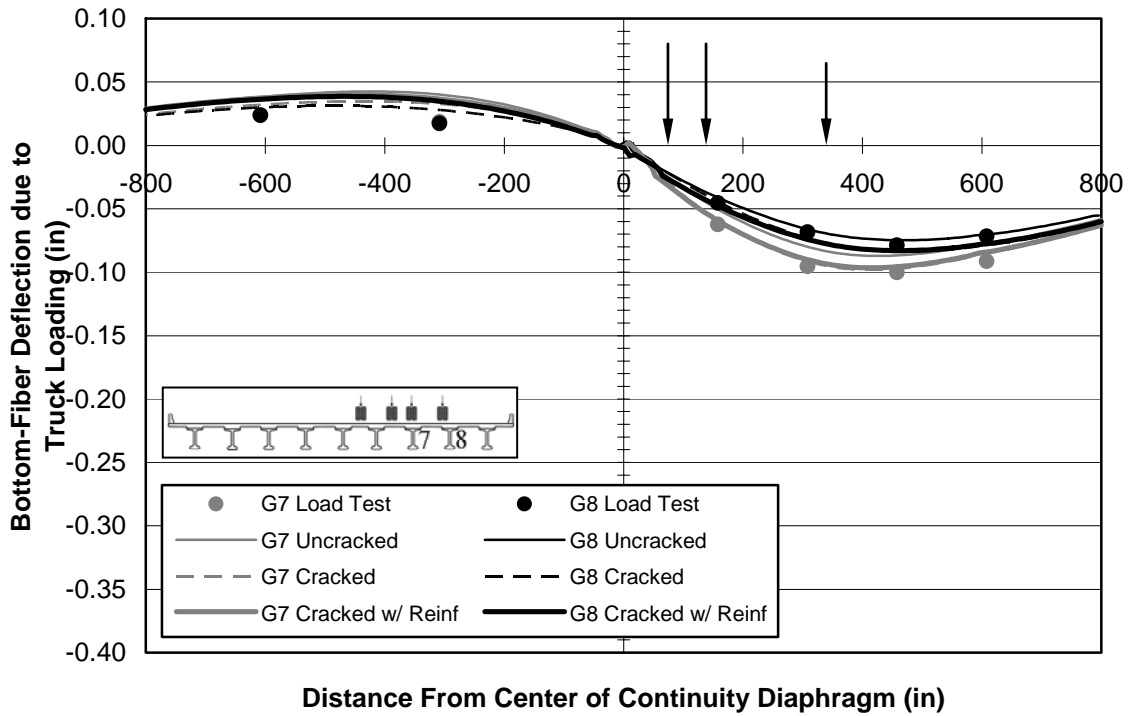
**Figure 6.13 Bottom-Fiber Deflections for the Model
Refinement—A7 Load Position**
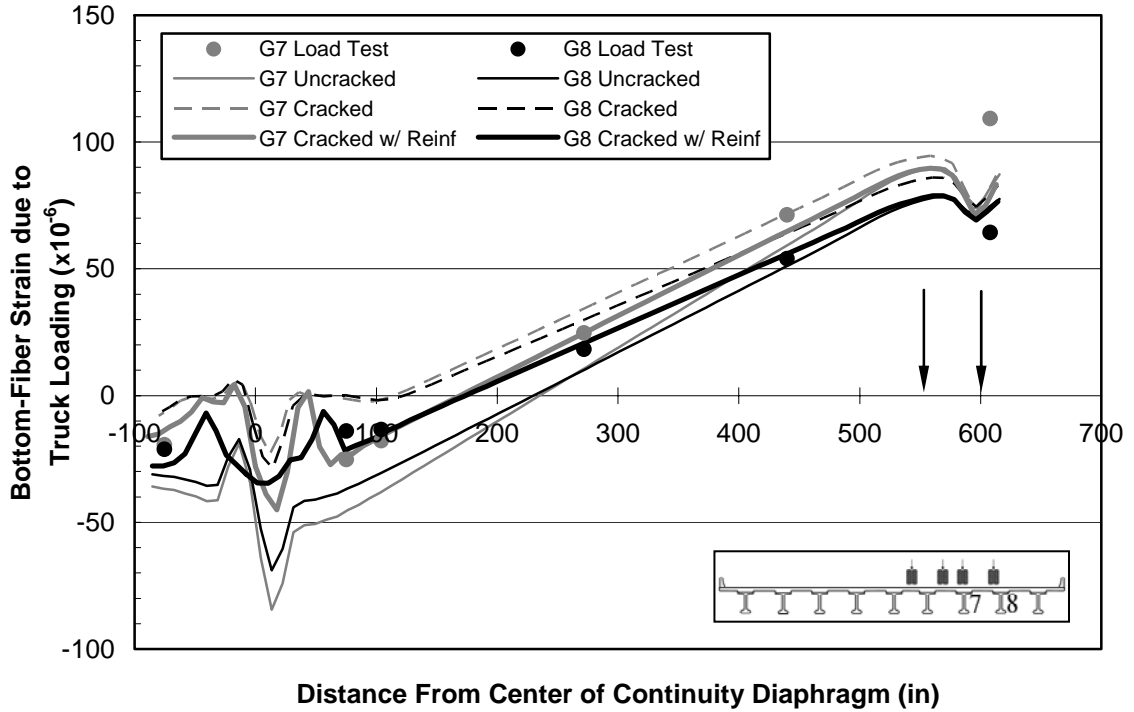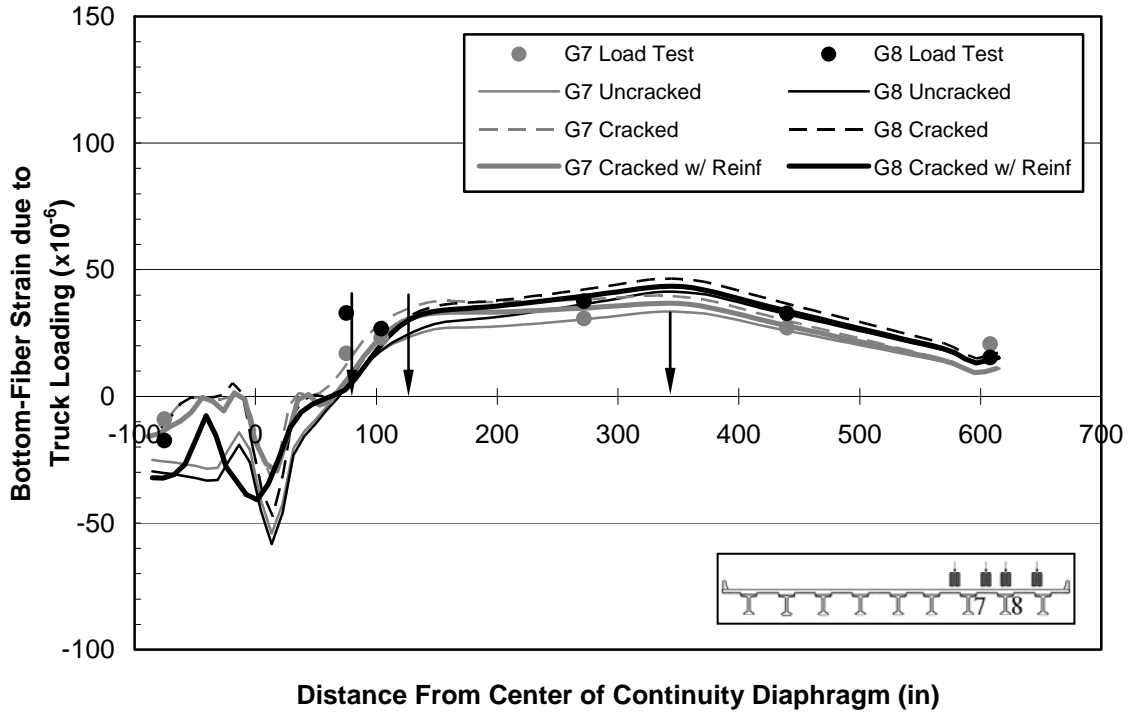
110
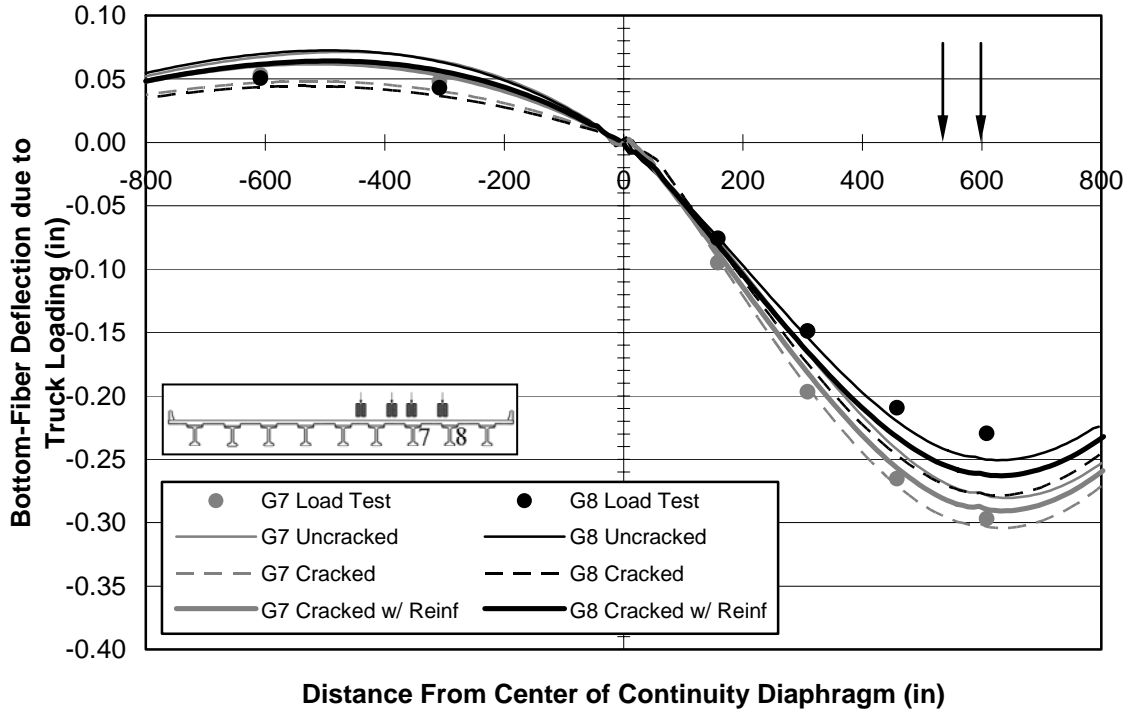
Figure 6.14 Bottom-Fiber Deflections for the Model Refinement—A9 Load Position
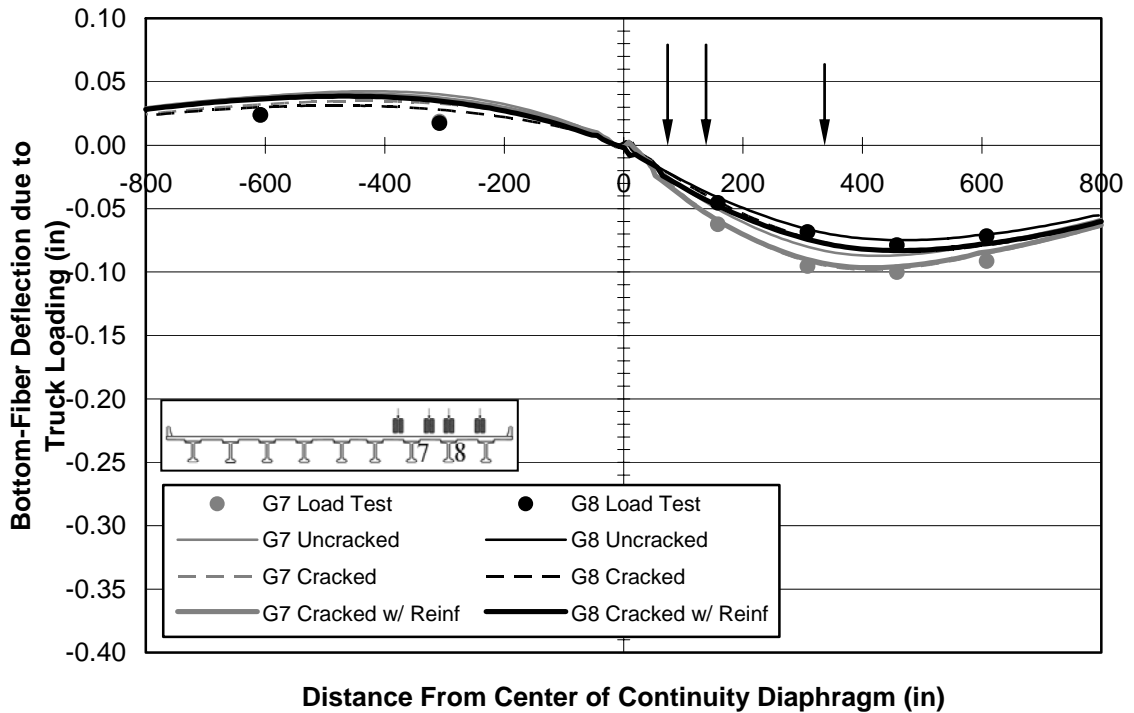
Figure 6.15 Bottom-Fiber Deflections for the Model Refinement—C7 Load Position

111
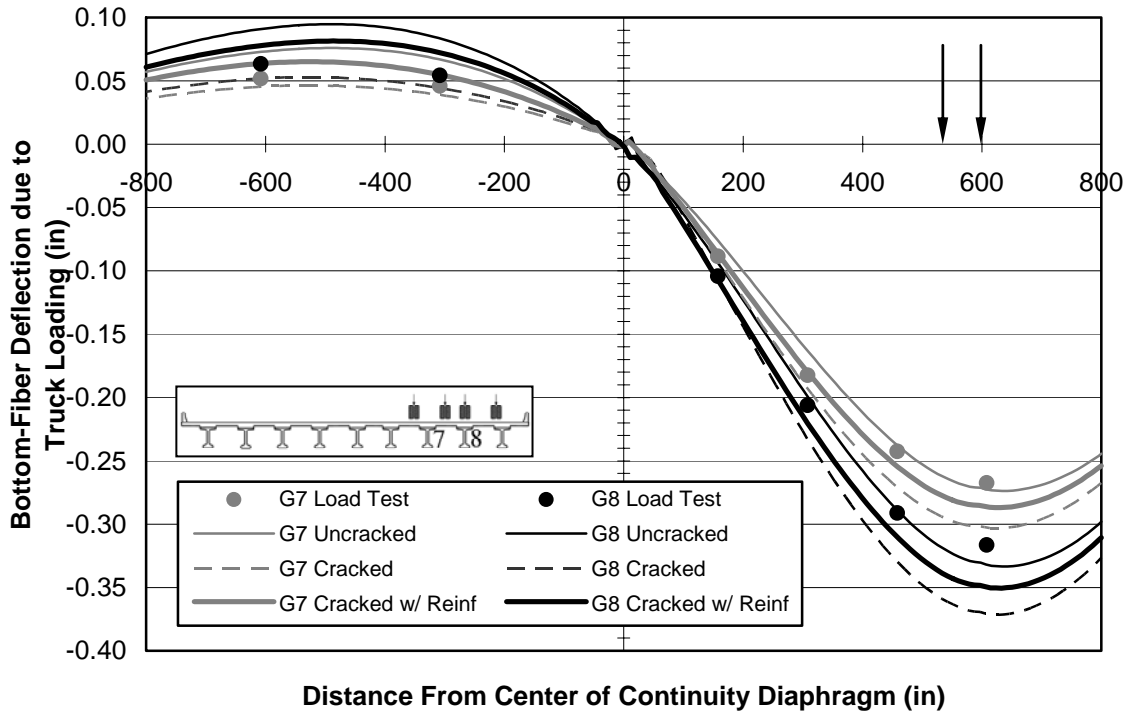
**Figure 6.16 Bottom-Fiber Deflections for the Model
Refinement—C9 Load Position**

6.2.4 Exploration of Midspan Diaphragm Effects

When looking at Figures 6.9 through 6.12, there is a noticeable discrepancy between the

experimental value of Girder 7 strain at midspan and the corresponding FEM results.

Although the *Cracked-with-Reinforcement* model best represents the strain results at the

other strain gauge locations, the discrepancy at this location is large regardless of which

FEM is employed. In order to investigate whether this discrepancy is related to

overestimating the influence of the midspan diaphragms, a comparison FEM without

midspan diaphragms was created. Apart from the omission of these diaphragms, this

model was identical to the *Cracked-with-Reinforcement* model. Comparisons between

the results of these two models, along with the corresponding load test results, are

depicted in Figures 6.17 through 6.20, with the divergent point labeled as 'A'.

112
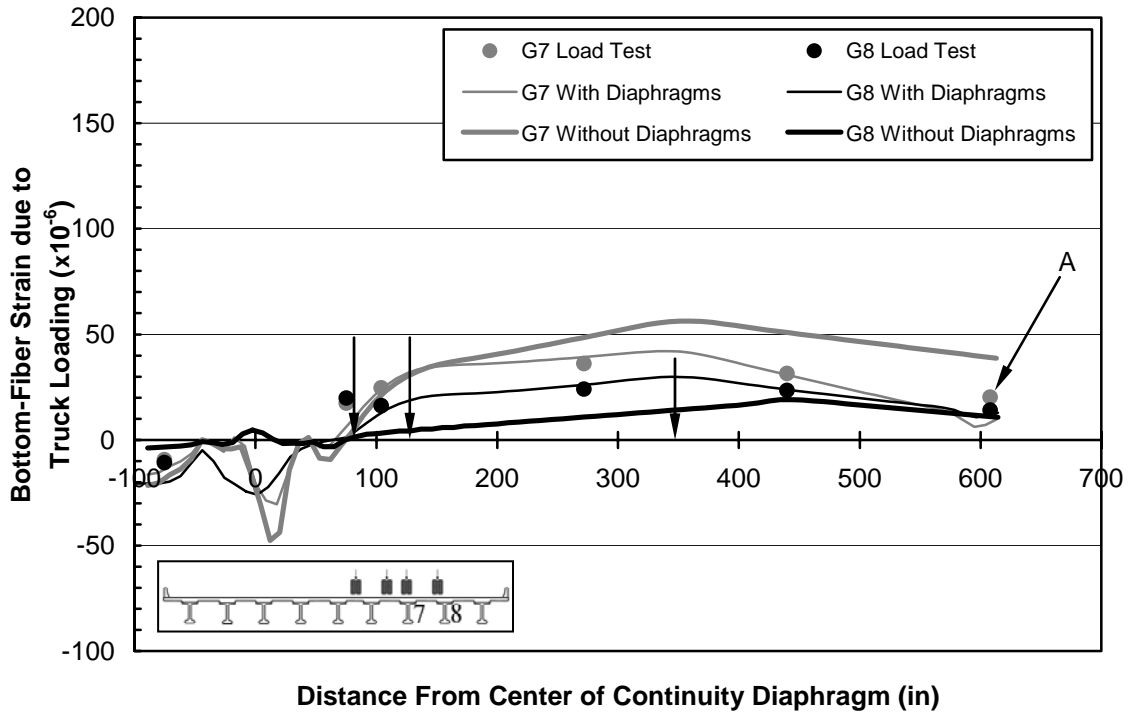
Figure 6.17 Comparing the Models with and without Diaphragms—A7 Load Position
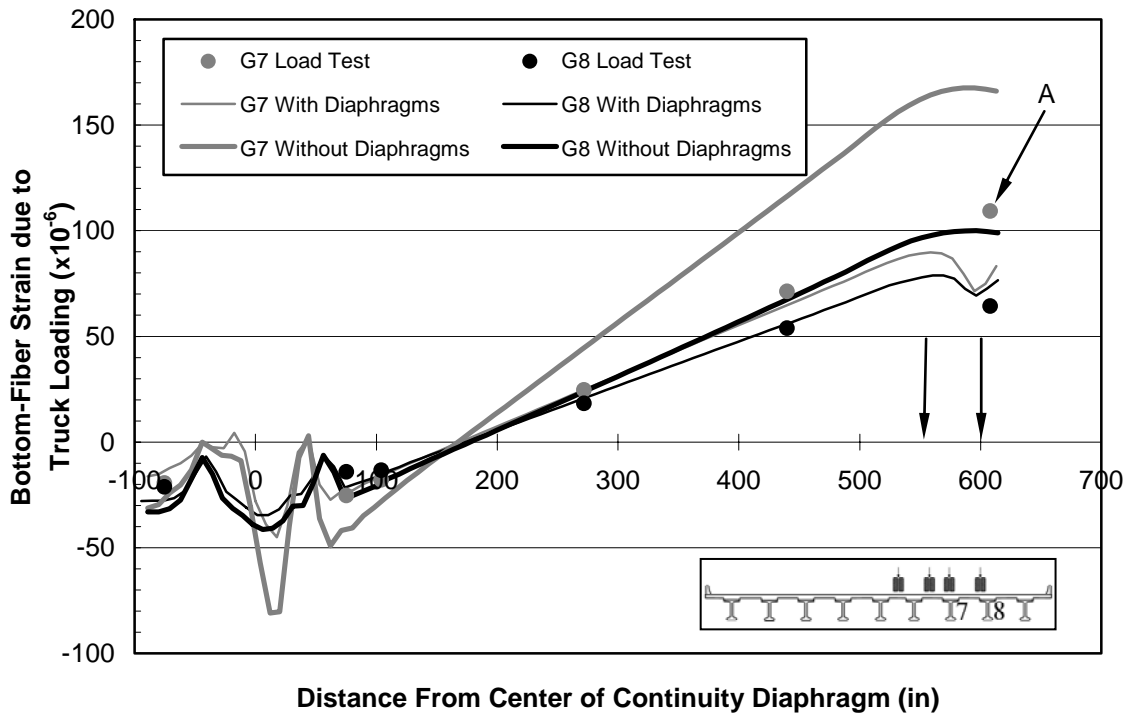
Figure 6.18 Comparing the Models with and without Diaphragms—A9 Load Position

113
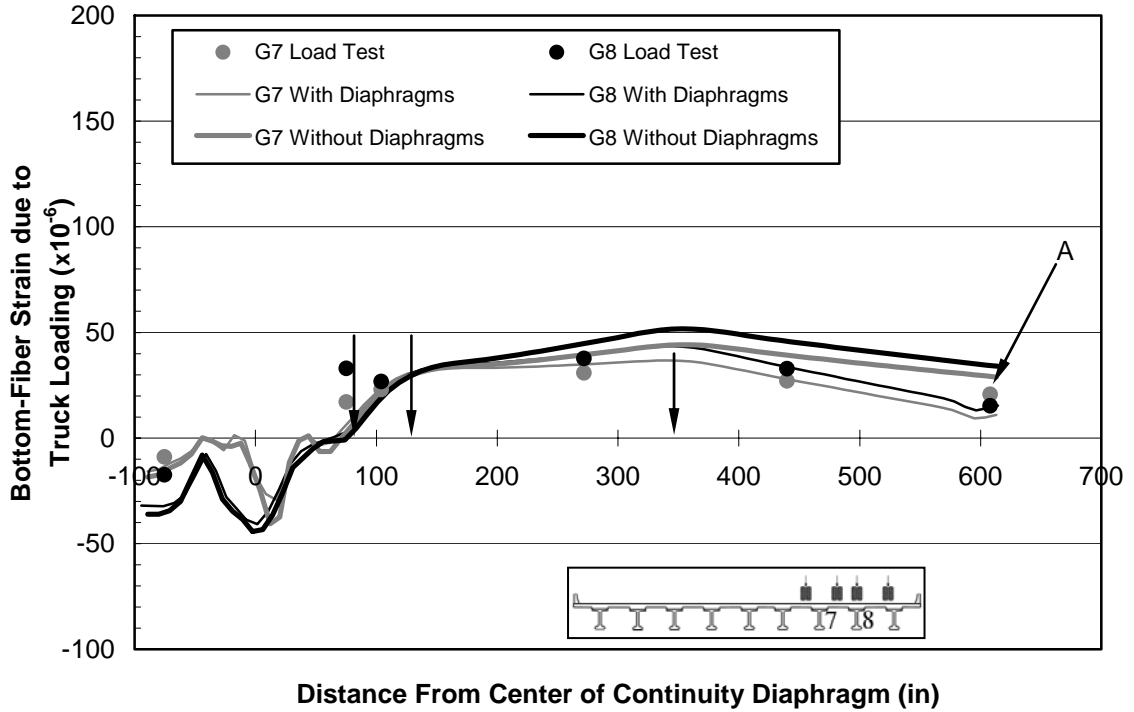
Figure 6.19 Comparing the Models with and without Diaphragms—C7 Load Position
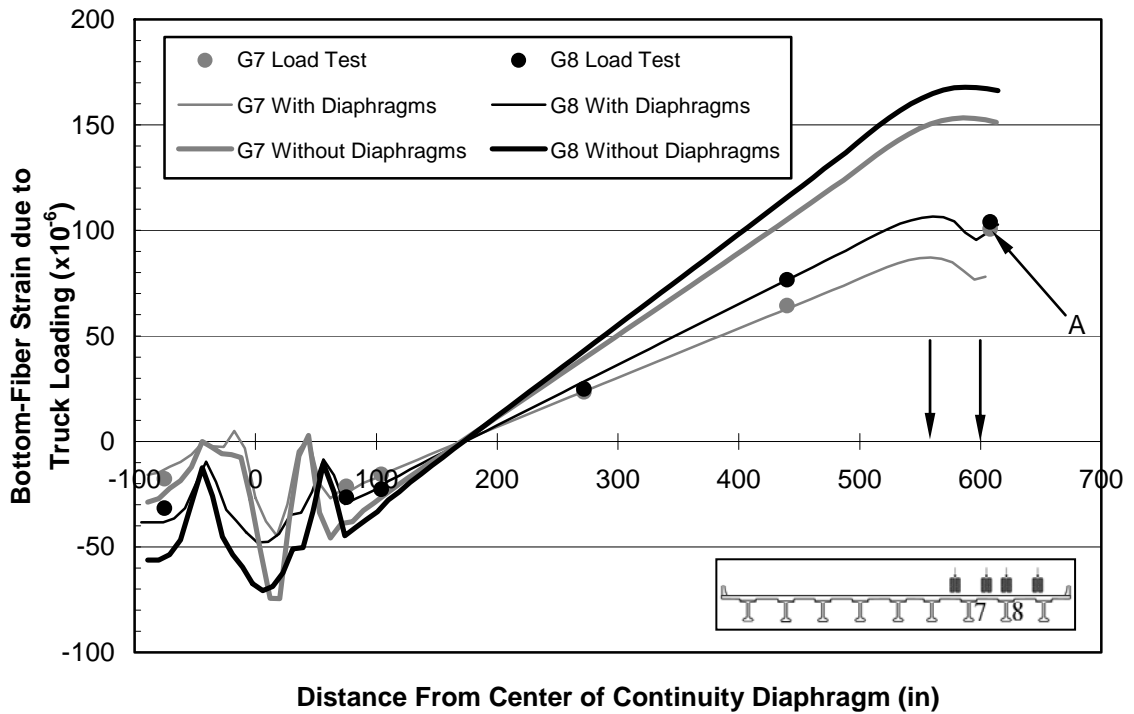
Figure 6.20 Comparing the Models with and without Diaphragms—C9 Load Position

114

It is apparent from the figures that the FEM that includes the midspan diaphragms better reflects the behavior of the bridge than the FEM without diaphragms. This differs significantly from the results of the study conducted by Tedesco, Stallings, and Tow (1995) in which they determined that the removal of diaphragms would *not* have a significant effect on the bridge response. While this matter warrants further investigation, for this study it was decided to include the midspan diaphragms in the final model of the existing bridge behavior. The effects of the midspan diaphragms are discussed further in Section 7.2.3.

### *6.2.5 Further Discrepancies*

It is interesting to note that there is also a discrepancy between the FEMs and the load test results for some of the gauges nearer to the continuity diaphragm. Looking at Figures 6.9 and 6.11—the results for Load Positions A7 and C7, respectively—there is an obvious disparity in the results for the gauges located approximately 70 in. from the center of the continuity diaphragm. On Span 11 this is present in both girders, while on Span 10 it is only present in Girder 8. This discrepancy is not discernible when the truck is positioned away from these sections, but presents itself when a wheel group is very close to these sections—which are also very close to cracks. It is possible this may indicate some inaccuracy in crack placement on the FEM or some local effect of the concentrated load on the bridge that the FEM is not reflecting. The accuracy of the FEM results in these cracked regions is likely to be very sensitive to minor differences between the actual crack location(s) and the positioning of the seams in the model.

6.2.6 Final Pre-Repair Model

Originally, the *Cracked-with-Reinforcement* model was selected as the final pre-FRP repair model. Section 5.14.4 details the changes that were made to it to produce the *Pre-Repair* model—seams along the face of the continuity diaphragm, which were not included in the *Cracked-with-Reinforcement* model, were added to create the final *Pre-Repair* model. Figures 6.21 through 6.24 show the analytical results of this model compared to the experimental results. The next step was to model the effects of the fiber-reinforced polymer repair on the damaged structure.

Figure 6.21 Bottom-Fiber Strain Data for the Pre-Repair Model—A7 Load Position

Figure 6.22 Bottom-Fiber Strain Data for the Pre-Repair Model—A9 Load Position

Figure 6.23 Bottom-Fiber Strain Data for the Pre-Repair Model—C7 Load Position

117
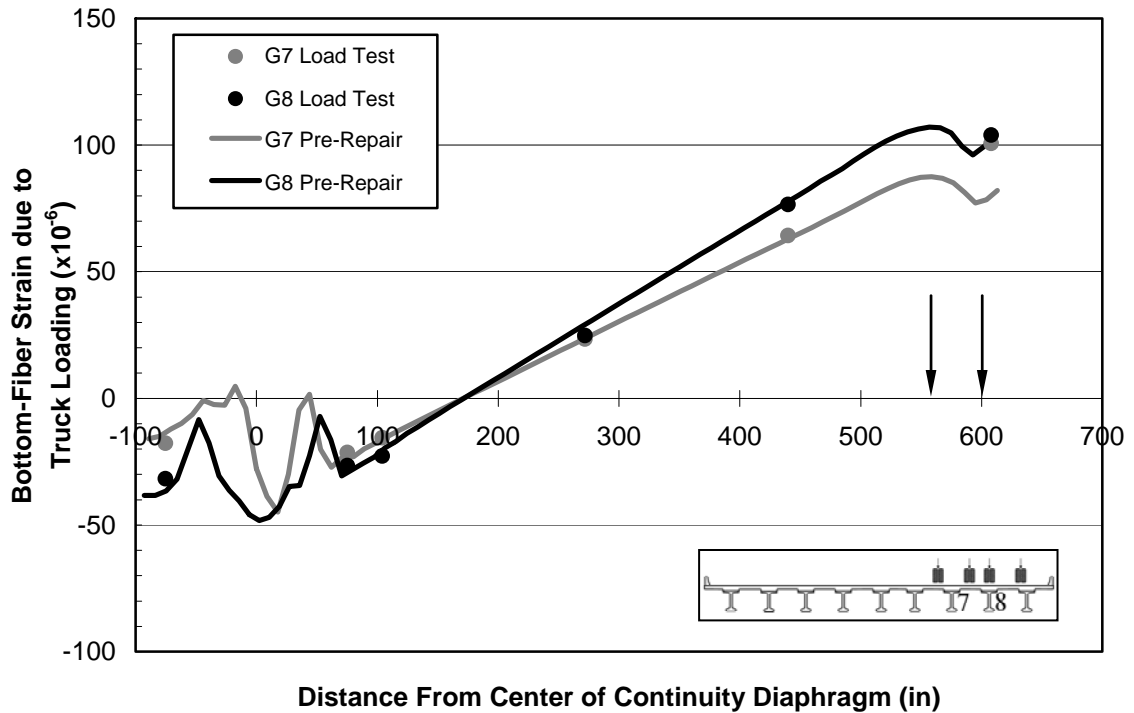
**Figure 6.24 Bottom-Fiber Strain Data for the Pre-Repair
Model—C9 Load Position**

6.3 FINITE-ELEMENT MODELING OF THE FRP-REPAIRED STRUCTURE

6.3.1 Comparison between Isotropic and Laminar Models for FRP

The FEMs for the *Post-Repair* model were created by adding the fiber-reinforced

polymer repair—created as explained in Sections 5.16.2 and 5.16.3—to the *Pre-Repair*

model. Figures 6.25 through 6.28 present a bottom-fiber longitudinal strain comparison

between models with isotropic FRP and laminar FRP. Section 5.16 presents the details

of these FRP modeling options.

118
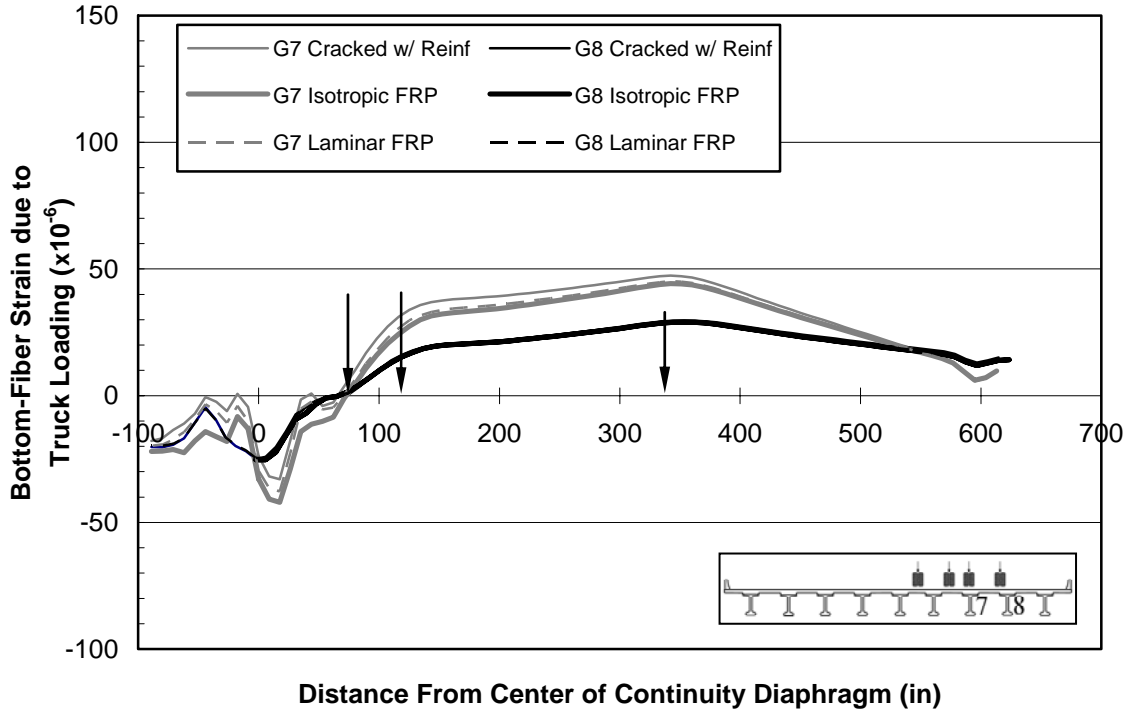
**Figure 6.25 Bottom-Fiber Strain Data for the Isotropic v. Lamina FRP Models—
A7 Load Position**
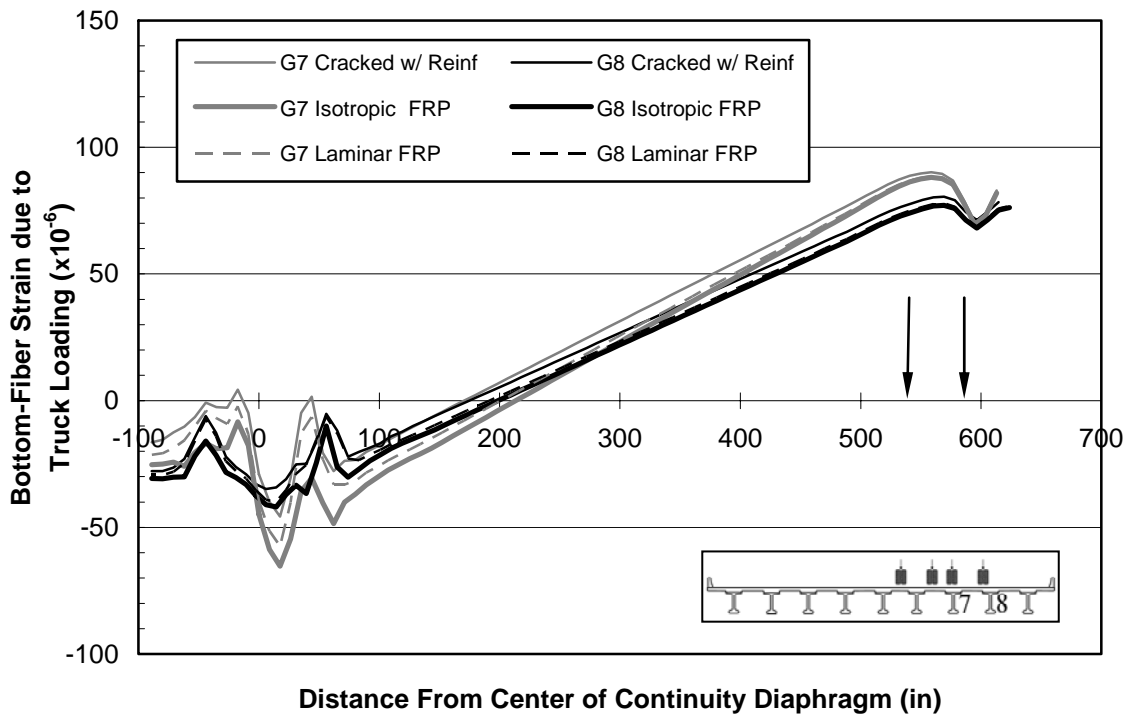
**Figure 6.26 Bottom-Fiber Strain Data for the Isotropic v. Lamina FRP Models—
A9 Load Position**

119
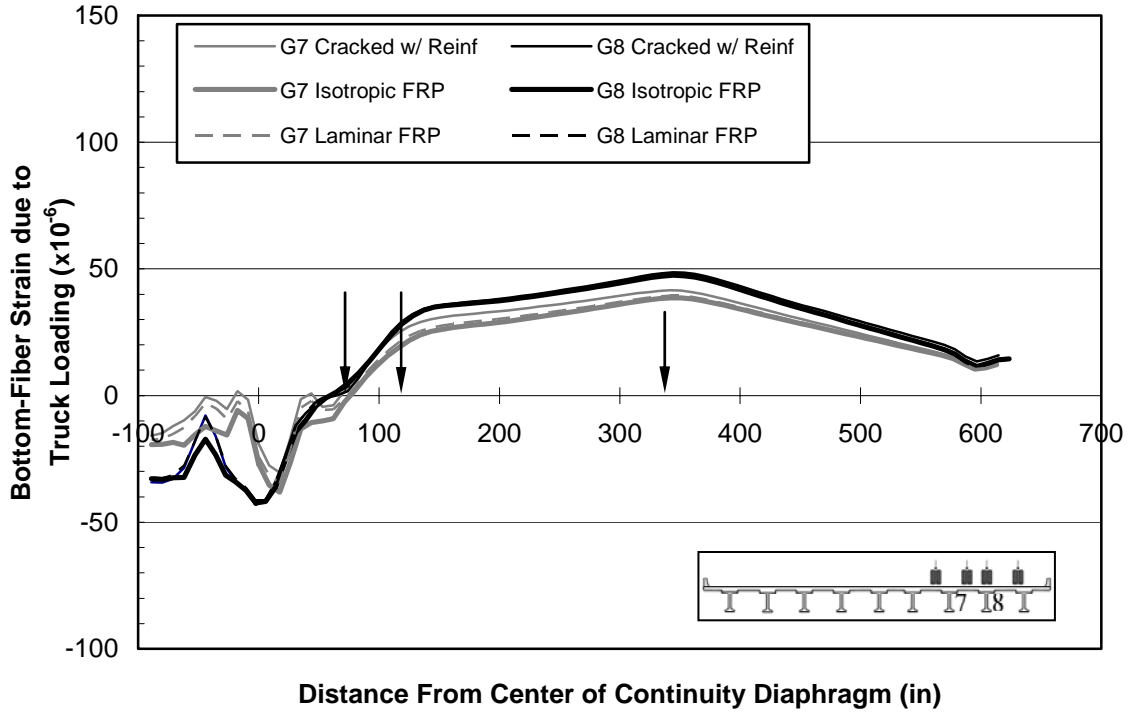
Figure 6.27 Bottom-Fiber Strain Data for the Isotropic v. Lamina FRP Models—C7 Load Position
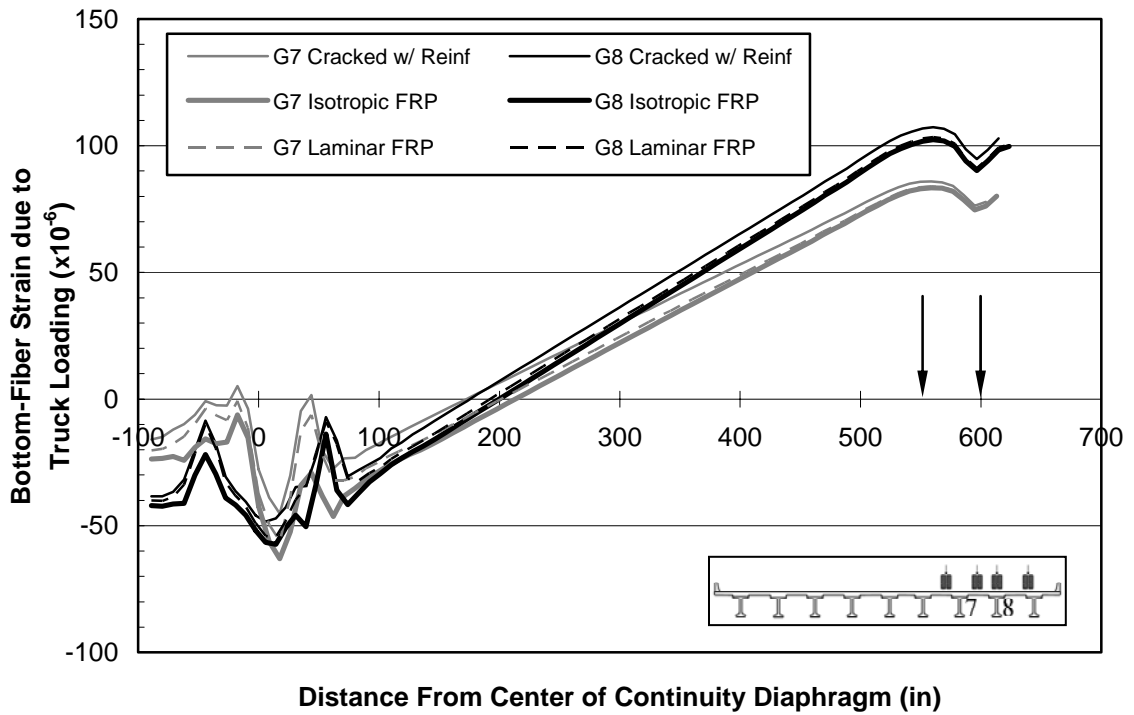
Figure 6.28 Bottom-Fiber Strain Data for the Isotropic v. Lamina FRP Models—C9 Load Position

120

Referring to the figures, it is apparent that the behavior of the model with the laminar FRP is slightly closer than the model with the isotropic FRP to the behavior of the *Cracked-with-Reinforcement* model—and therefore slightly more conservative with respect to the overall contribution of the FRP to the stiffness of the bridge. Because the laminar representation more accurately models the orthotropic FRP material than the isotropic representation—and the increase in computational burden was not significant—it was determined to use the laminar FRP representation for the final *Post-Repair* model.

6.3.2 Pre-Repair Model vs. Post-Repair Model

The longitudinal strain comparison between the final pre-FRP repair model and the post-FRP repair model is shown in Figures 6.29 through 6.32. The deflection comparison between the two models is shown in Figures 6.33 through 6.36. As explained in Section 5.7.4, the FRP was first modeled with reduced integration elements. As explained in Section 5.8.4, when it became apparent that reduced integration was insufficient for the task, full integration was utilized.

Not surprisingly, the FRP has the greatest effect on the resulting strains near the cracked region. For all four load positions, there is between 0 and 25×10^{-6} in./in. increase in compressive strain at the location of the Seams. It is interesting to note that for all four load positions, the repair acts to decrease the predicted deflection more at the midspan of the loaded girder—regardless of the longitudinal position of the load trucks—than at any other location. This effect is more evident at the A9 and C9 Load Positions than at the A7 and C7 Load Positions. The repair appears to be equally effective for both Girder 7 and Girder 8.
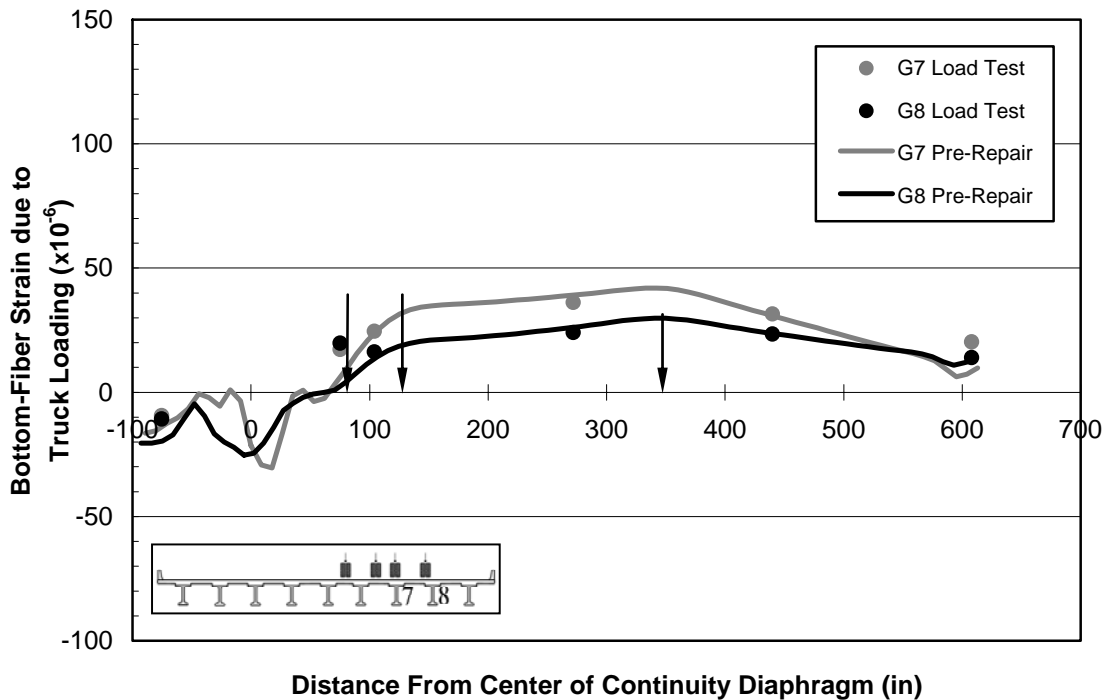
121
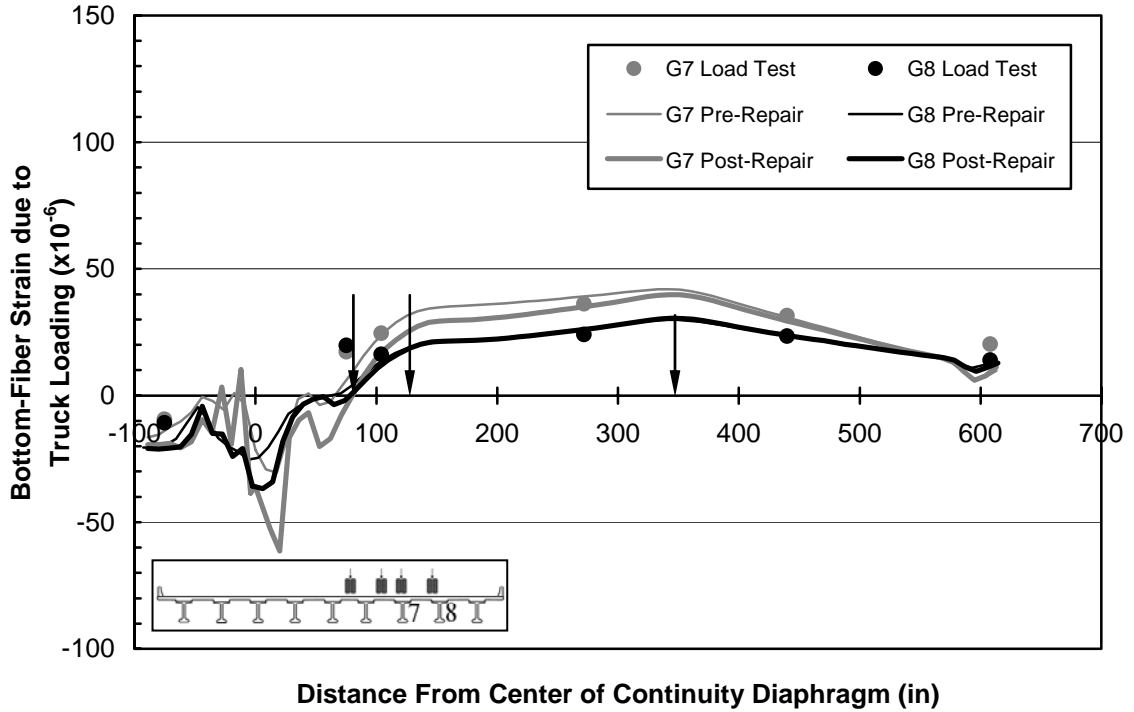
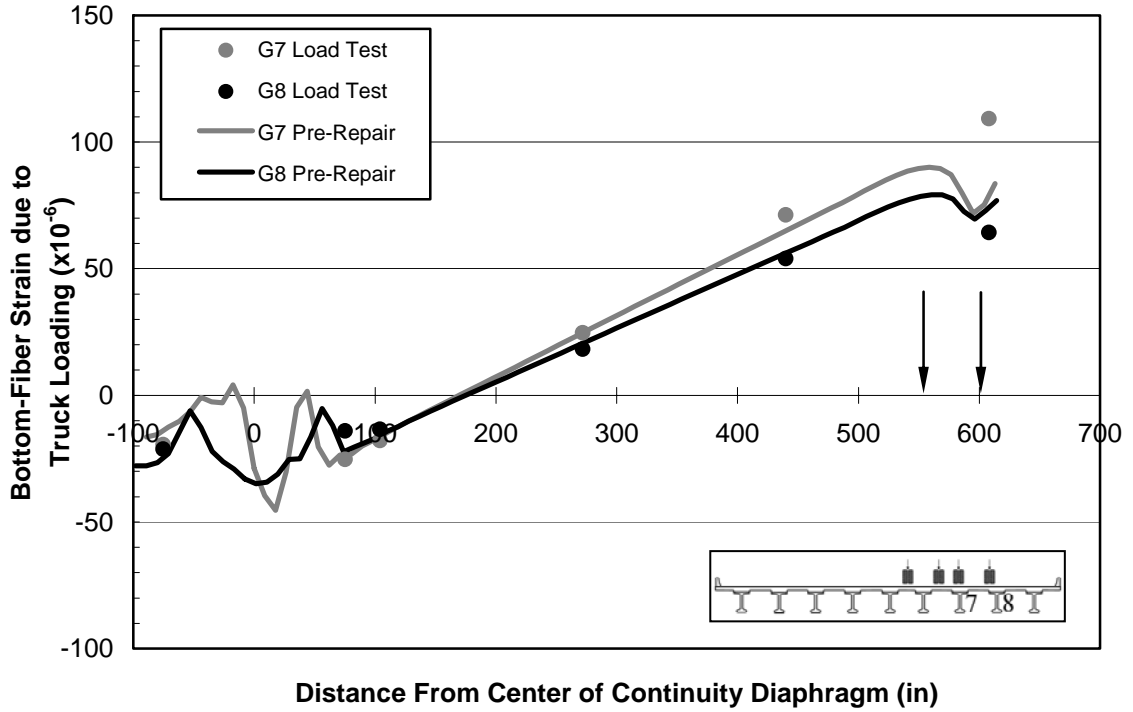**Figure 6.29 Bottom-Fiber Strain Data for the Pre- v. Post-Repair Models—A7 Load Position**
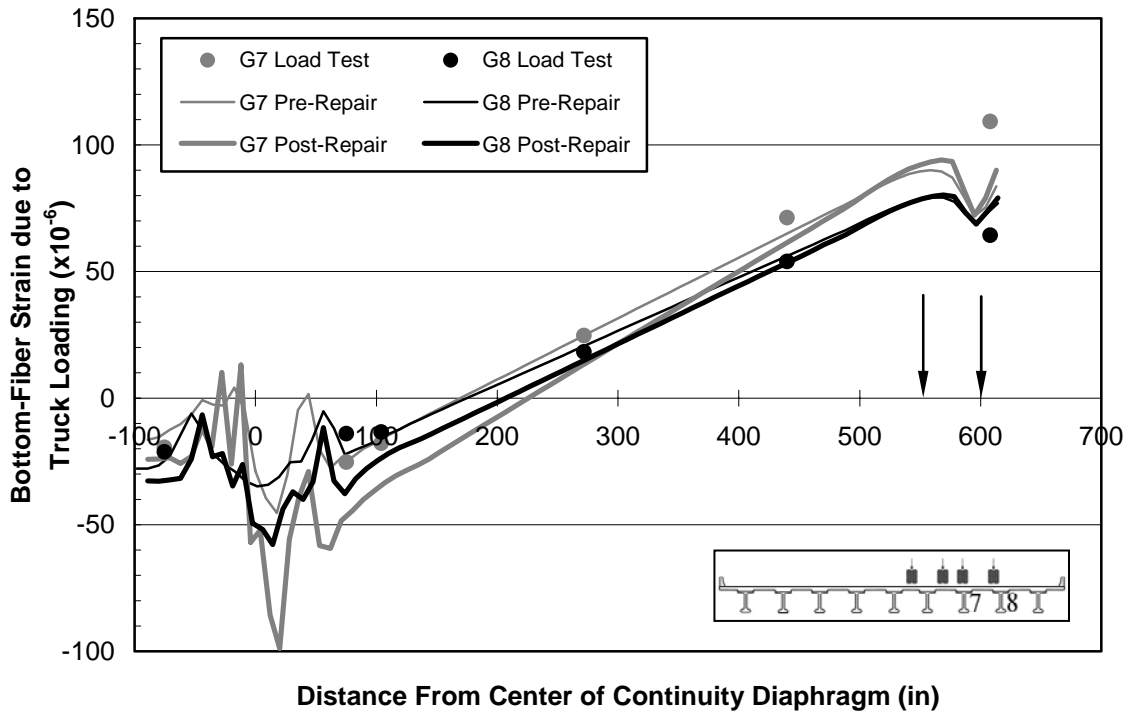
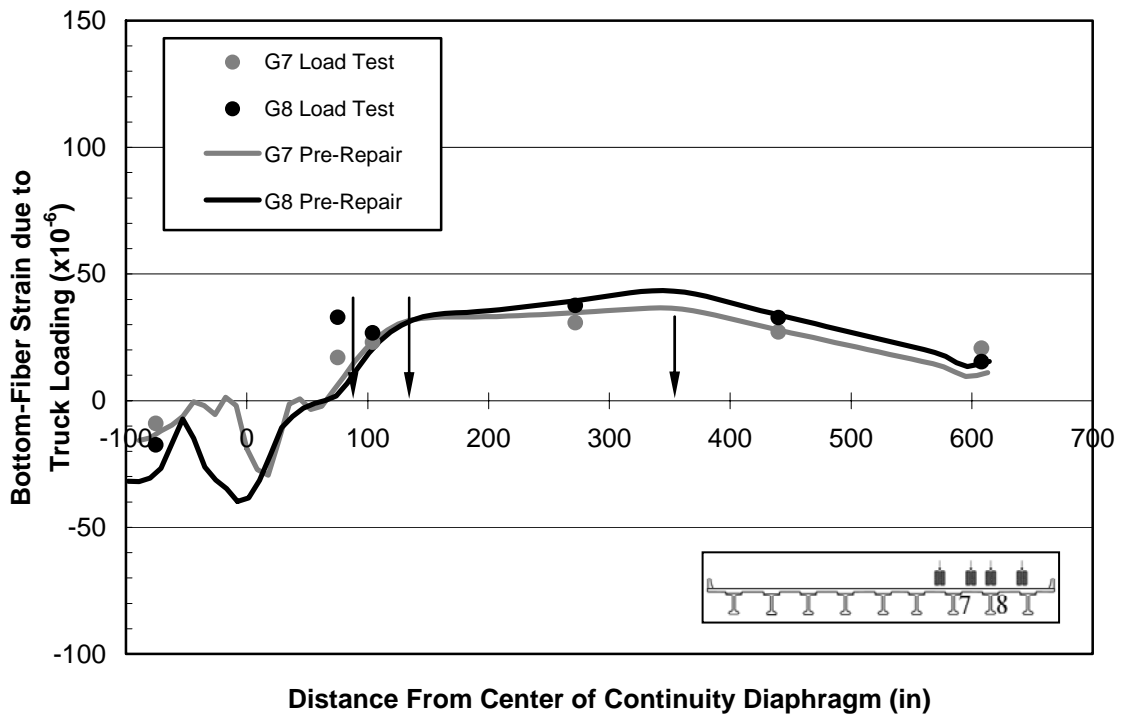**Figure 6.30 Bottom-Fiber Strain Data for the Pre- v. Post-Repair Models—A9 Load Position**
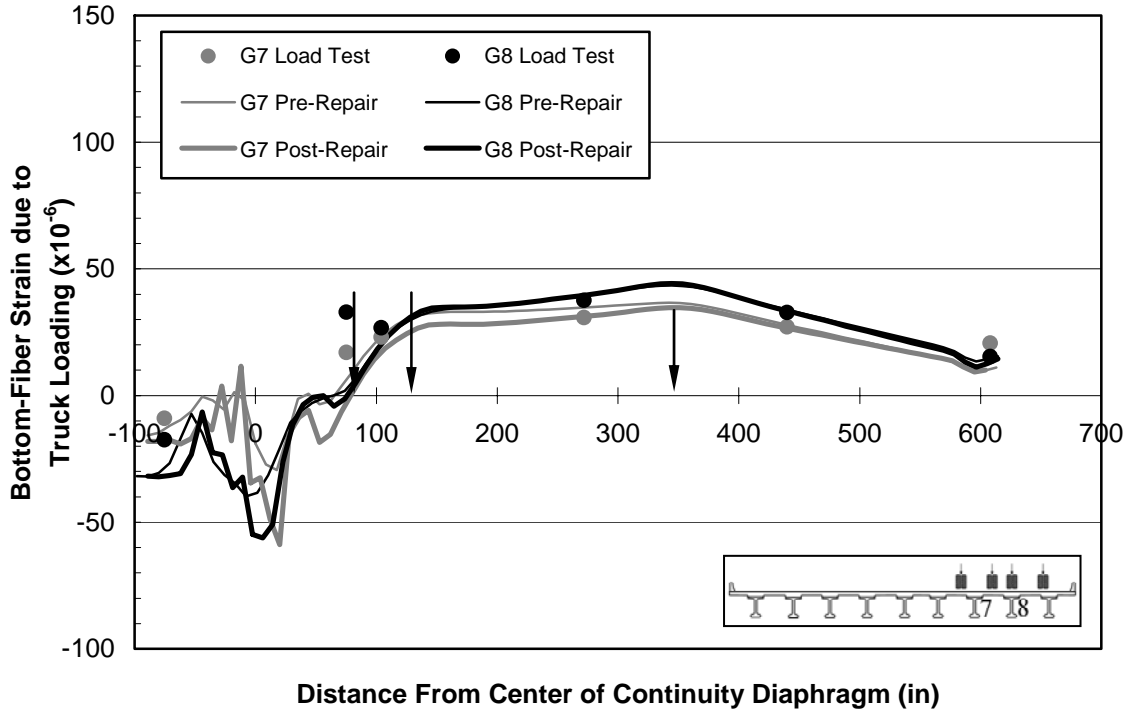
Figure 6.31 Bottom-Fiber Strain Data for the Pre- v. Post-Repair Models—C7 Load Position
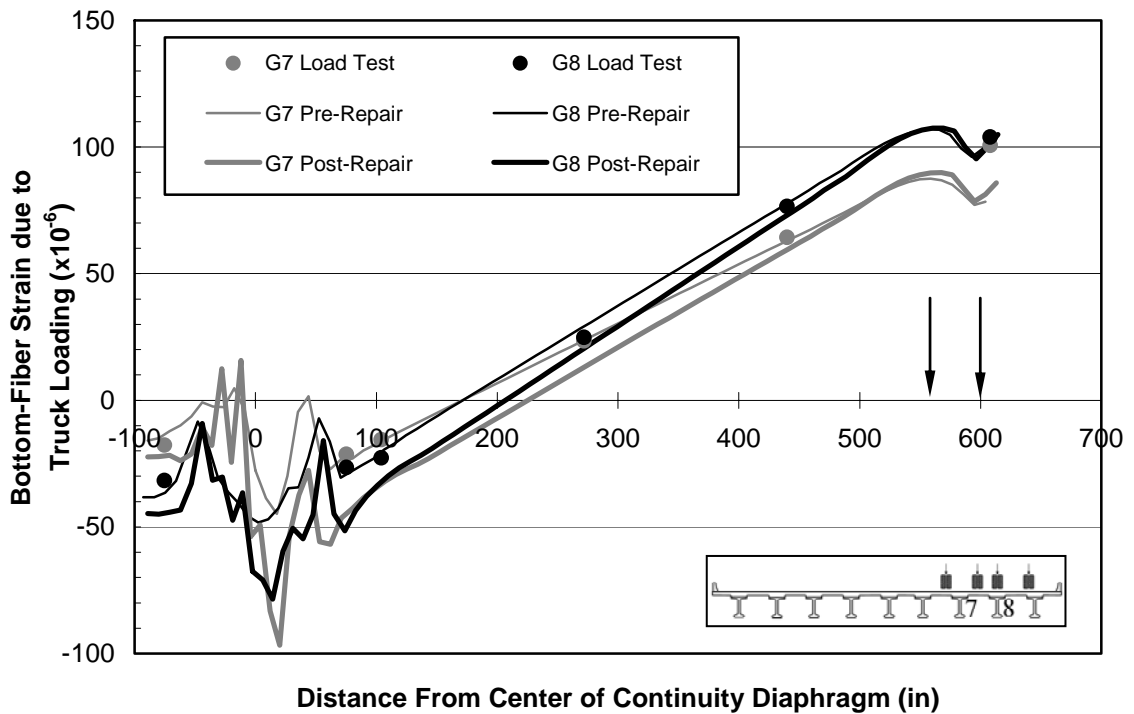
Figure 6.32 Bottom-Fiber Strain Data for the Pre- v. Post-Repair Models—C9 Load Position

123
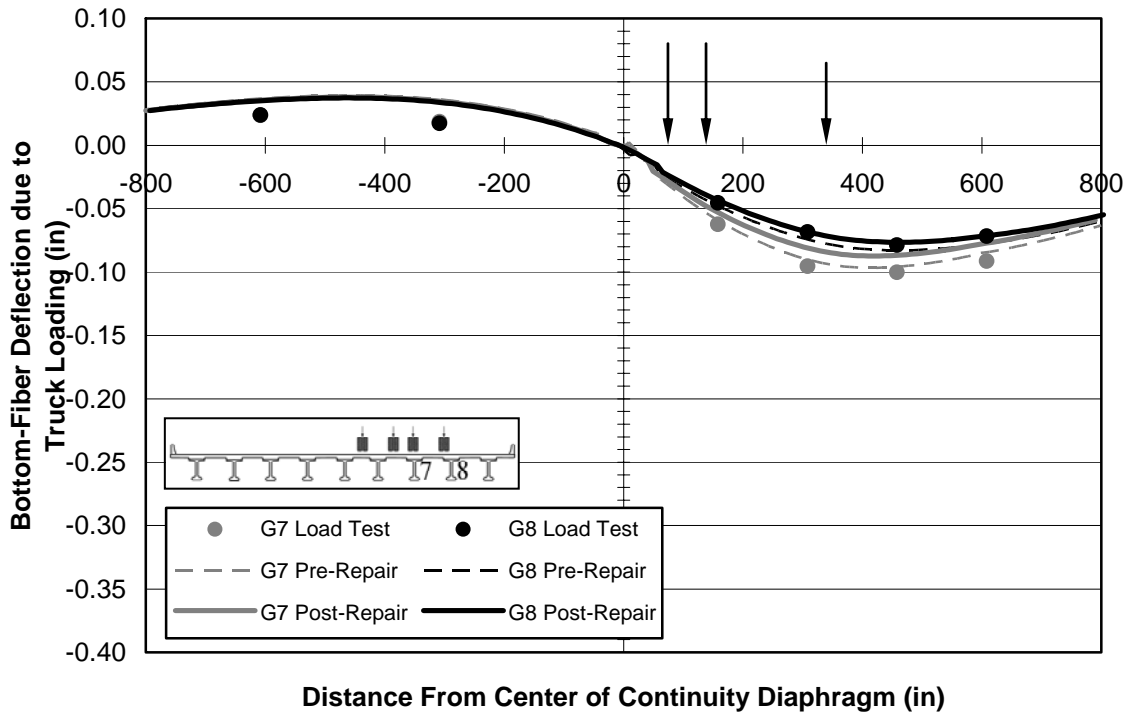
Figure 6.33 Bottom-Fiber Deflections for the Pre- v. Post-Repair Models—A7 Load Position
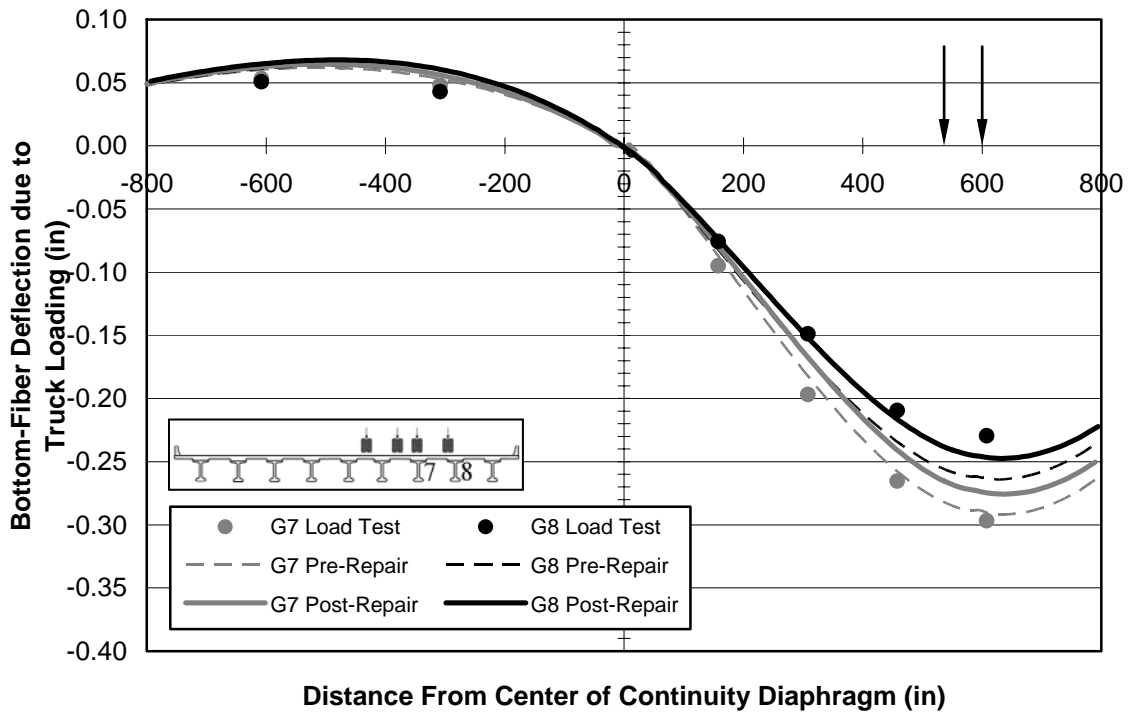
Figure 6.34 Bottom-Fiber Deflections for the Pre- v. Post-Repair Models—A9 Load Position

124
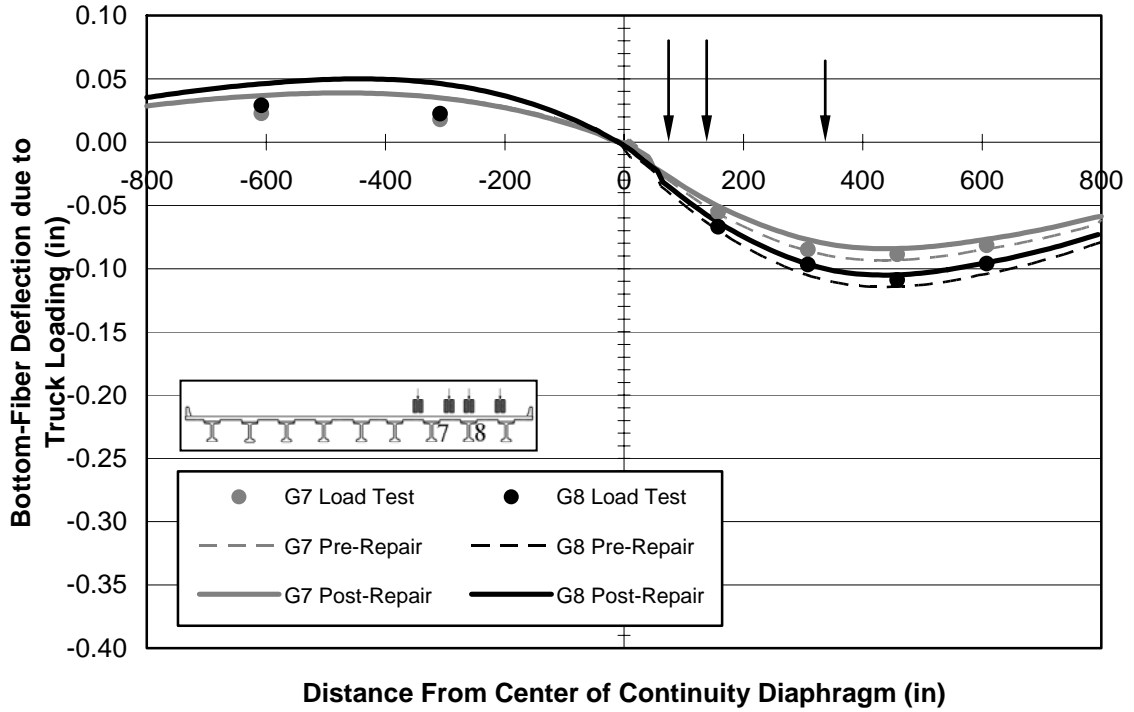
Figure 6.35 Bottom-Fiber Deflections for the Pre- v. Post-Repair Models—C7 Load Position
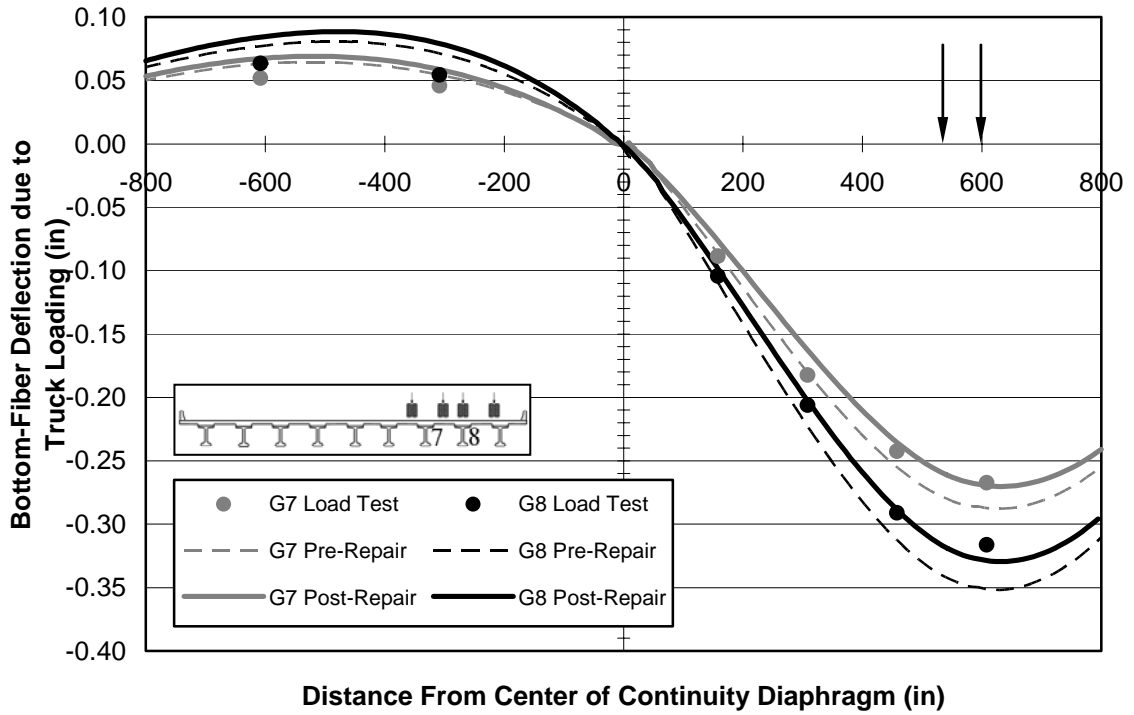
Figure 6.36 Bottom-Fiber Deflections for the Pre- v. Post-Repair Models—C9 Load Position

125

The deflections at midspan of Span 11 for the *Pre-Repair* and *Post-Repair* models are compared in Table 6.1. At the four load positions, the change in deflection due to the repair is on the order of 5–9 percent. For the A9 and C9 Load Positions, the change ranges between approximately 5.5–6.5 percent. For the A7 and C7 Load Positions, the change ranges from approximately 8–9 percent.

Table 6.1 Comparison between *Pre-* and *Post-Repair* Models of Midspan Deflection Measured on Span 11

	Load Position	Deflection (in.)		Change (in.)	Percent Change
		Pre-Repair	Post-Repair		
Girder 7	A7	0.084	0.078	-0.007	-8.2
	A9	0.290	0.274	-0.016	-5.6
	C7	0.085	0.077	-0.008	-8.9
	C9	0.287	0.270	-0.018	-6.1
Girder 8	A7	0.078	0.071	-0.006	-7.9
	A9	0.264	0.247	-0.017	-6.4
	C7	0.104	0.095	-0.009	-8.5
	C9	0.351	0.329	-0.023	-6.4

The deflections at midspan of Span 11 are also compared between the *Uncracked* and the *Post-Repair* models. This comparison is presented in Table 6.2. The purpose of this comparison is to provide a reference for the efficacy of the repair and its effect on the global behavior of the bridge. Surprisingly, the *Post-Repair* model predicts results within 2 percent of the *Uncracked* model for all of the reported midspan deflections. At the precision which can be reliably and practically measured, the model results imply that the deflection behavior of the repaired bridge will closely match that of the original uncracked structure.

It is interesting to note that the results of the A9 and C9 Load Positions predict less

deflection in the *Post-Repair* model than is present in the *Uncracked* model. This can

be attributed to at least two possible causes. One is that the prestressing steel, which is

present in the *Post-Repair* model, is not explicitly included in the *Uncracked* model.

The *Uncracked* model, therefore, does not include the extra stiffness attributable to the

steel within the uncracked girder cross section. In addition, the FEM does not account

for the build-up of the deck over the girders. This build-up would slightly increase the

composite girder stiffness because of the increased total depth of the cross section.

Table 6.2 Comparison between *Uncracked* and *Post-Repair* Models of Midspan Deflection Measured on Span 11

Load Position	Deflection (in.)		Difference (in.)	Percent Difference
	Uncracked	Post-Repair		
A7	0.077	0.078	0.000	0.3
A9	0.279	0.274	-0.005	-1.6
C7	0.076	0.077	0.001	1.6
C9	0.273	0.270	-0.003	-1.2
A7	0.071	0.071	0.001	0.8
A9	0.249	0.247	-0.003	-1.1
C7	0.094	0.095	0.002	1.9
C9	0.332	0.329	-0.003	-1.0

Note: Rows A7–C9 (first group) are labeled "Girder 7"; rows A7–C9 (second group) are labeled "Girder 8".

6.3.3 Concrete Strains versus FRP Strains

Due to practical limitations on instrumentation capabilities, some of the strain gauges

that were employed in the pre-repair load testing must be abandoned in order to

instrument critical portions of the newly installed FRP. In order to help determine

which of the existing strain gauges to continue using during the post-FRP repair load

tests, the longitudinal strains in the FRP were compared with the longitudinal strains in

the concrete that lies directly below it. In an effort to determine whether the FRP

strains are expected to be the same as the adjacent concrete strains, comparisons were

made for the bottom-fiber strain gauges as well as the strain gauges on the faces of the

girders. The results for the bottom-fiber strain gauge comparisons are shown in Figures

6.37 through 6.44. For each of the four truck load positions, the figure of the entire

instrumented length is presented first; a close-up figure with the repaired region directly

follows each.

   From these figures, it can be observed that the strain in the FRP is relatively close to

the value of the strain in the concrete toward the beginning and the end of the FRP

regions—particularly at the end away from the continuity diaphragms and the cracks.

At the seam locations, the strain in the FRP increases markedly while the strain in the

concrete fluctuates slightly. This is reasonable because the FRP would be

compensating for the lack of tension capacity in the concrete caused by the cracks. This

also suggests that high bond stress demands are being placed on the FRP-concrete

interface in these regions. In addition, it is likely—because the FRP is being put into

compression—that some of the seams are closing. The horizontal displacements at the

seams are further explored in Section 7.5.

   The experimental results for the entire girder-section strain profiles are shown with

the corresponding analytical results of the *Pre-Repair* and *Post-Repair* models in

Appendices D through G.
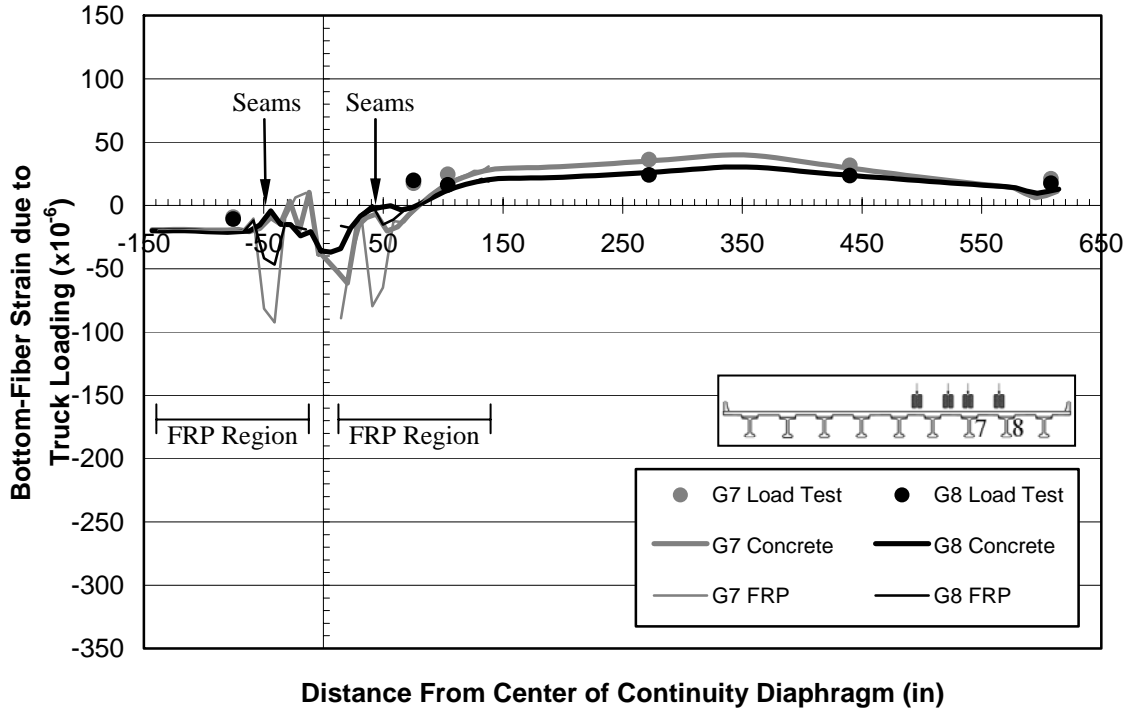
Figure 6.37 Bottom-Fiber Strain Data for the Concrete v. FRP for the Post-Repair Model—A7 Load Position
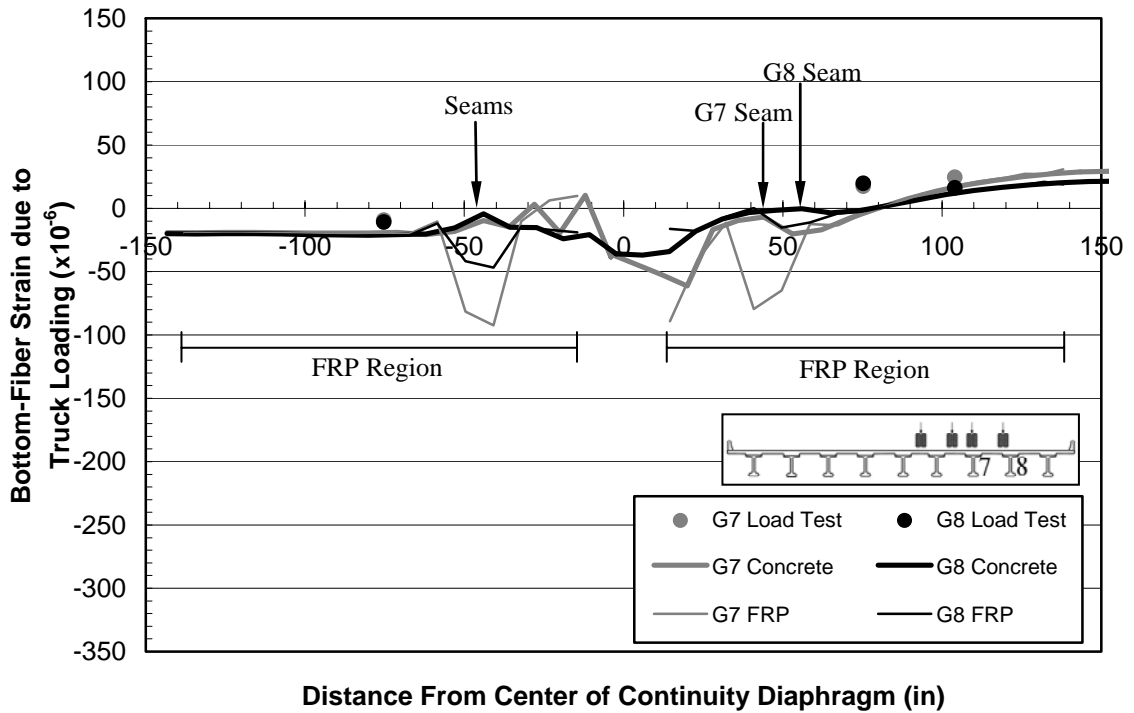
Figure 6.38 Bottom-Fiber Strain Data for the Concrete v. FRP for the Post-Repair Model (close-up view)—A7 Load Position

129
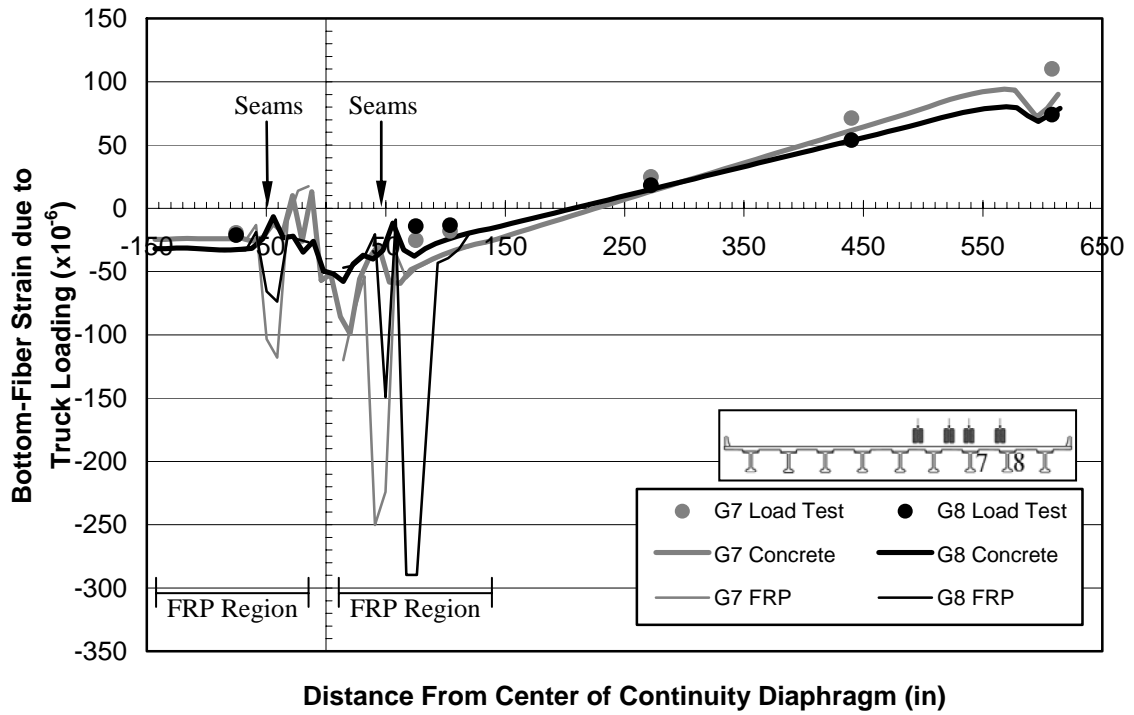
Figure 6.39 Bottom-Fiber Strain Data for the Concrete v. FRP for the Post-Repair Model—A9 Load Position
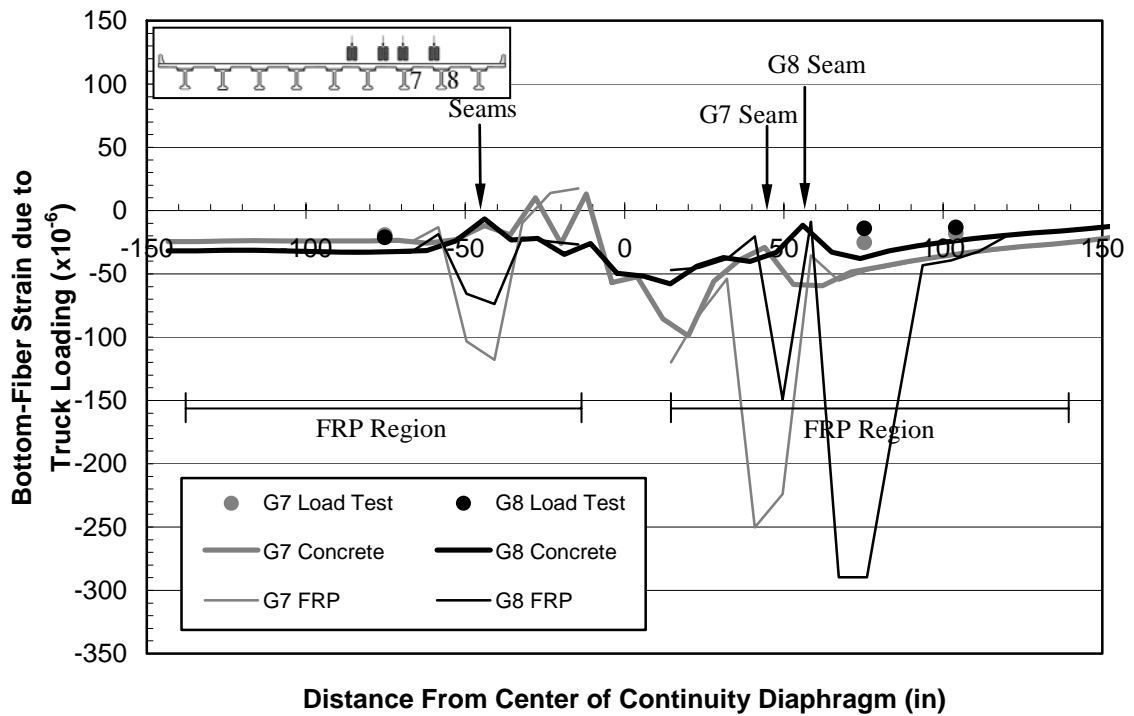
Figure 6.40 Bottom-Fiber Strain Data for the Concrete v. FRP for the Post-Repair Model (close-up view)—A9 Load Position

130
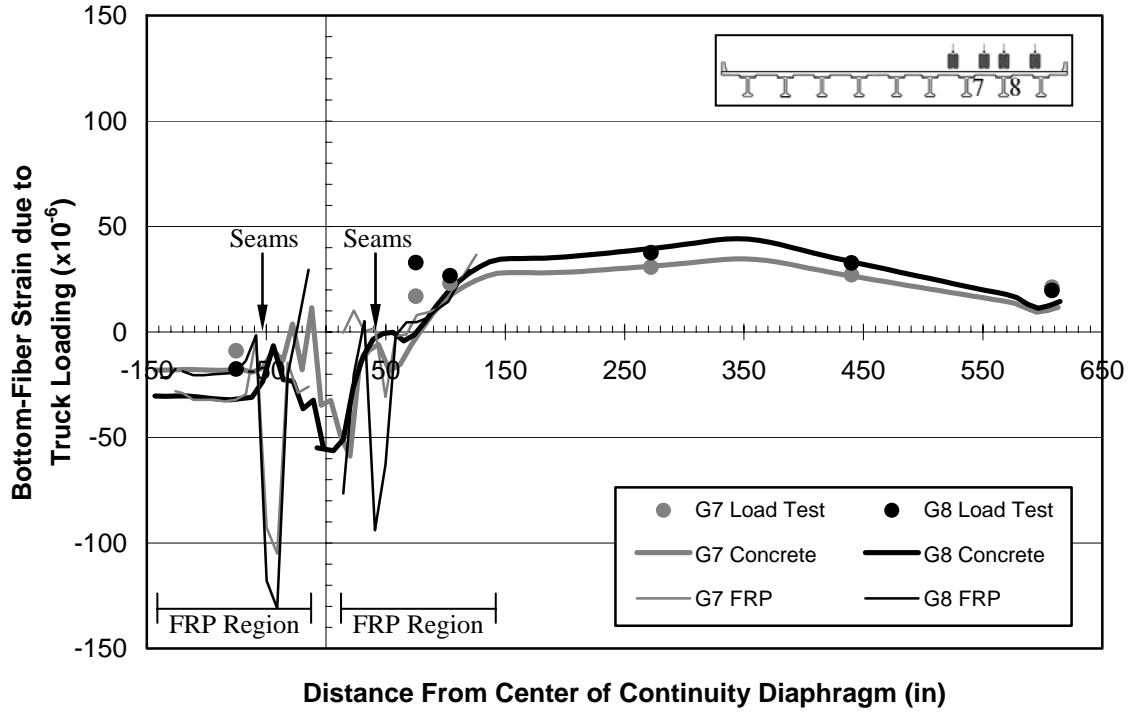
Figure 6.41 Bottom-Fiber Strain Data for the Concrete v. FRP for the Post-Repair Model—C7 Load Position
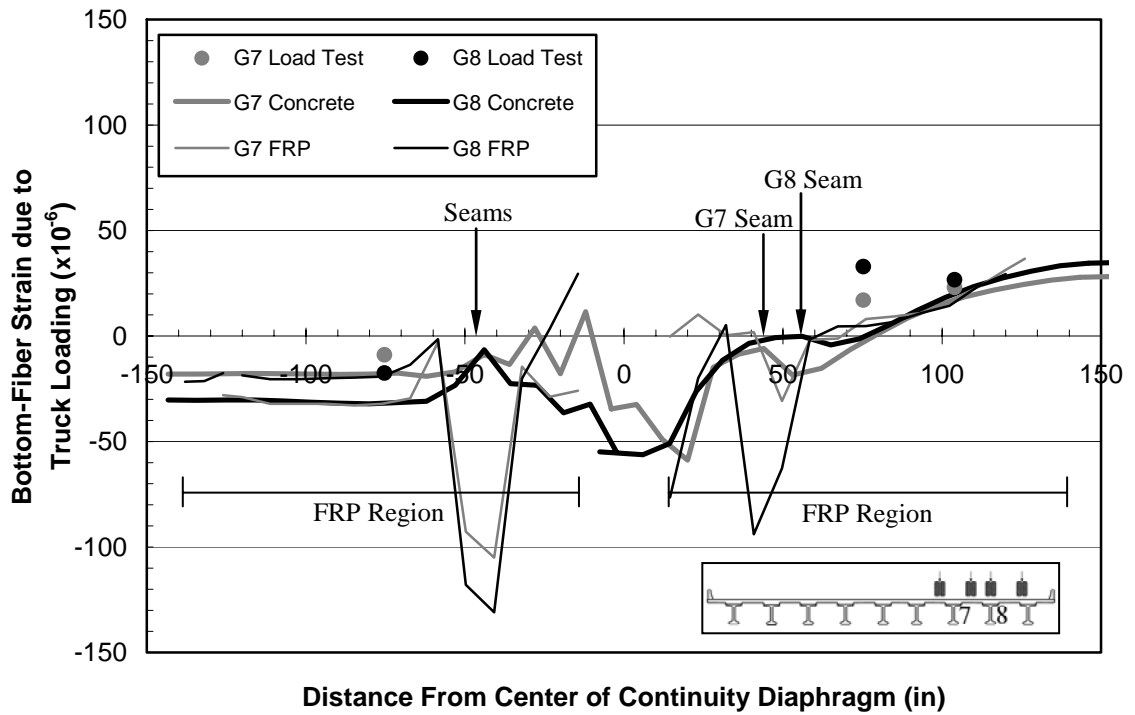
Figure 6.42 Bottom-Fiber Strain Data for the Concrete v. FRP for the Post-Repair Model (close-up view)—C7 Load Position
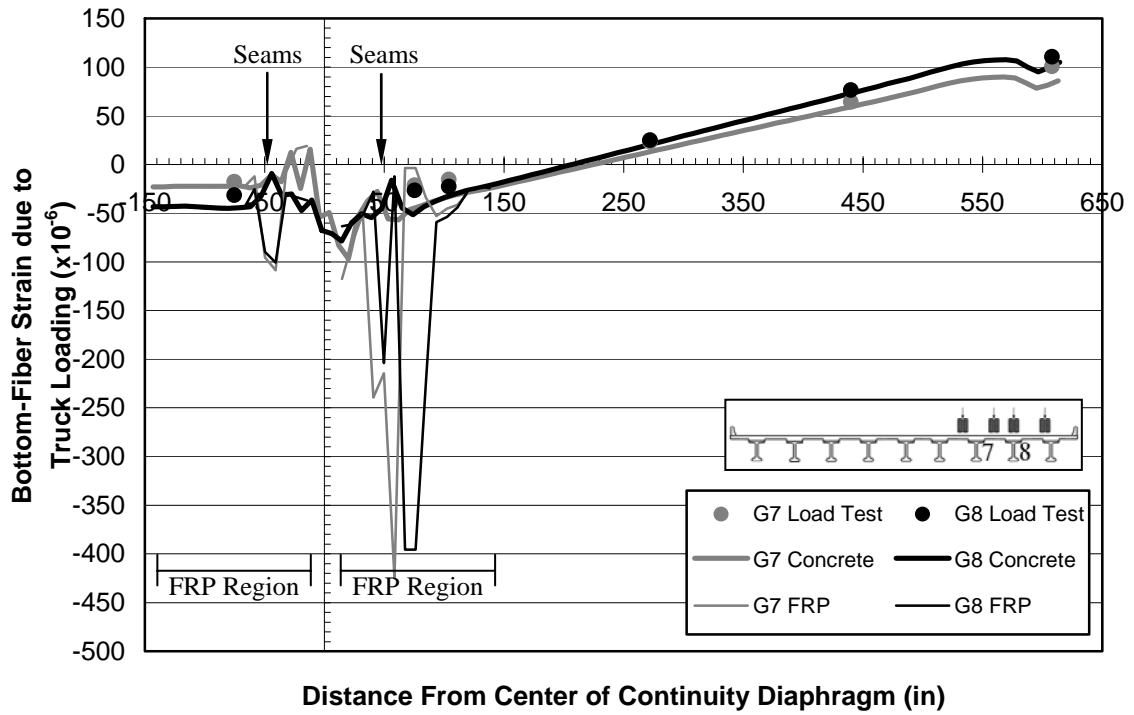
Figure 6.43 Bottom-Fiber Strain Data for the Concrete v. FRP for the Post-Repair Model—C9 Load Position
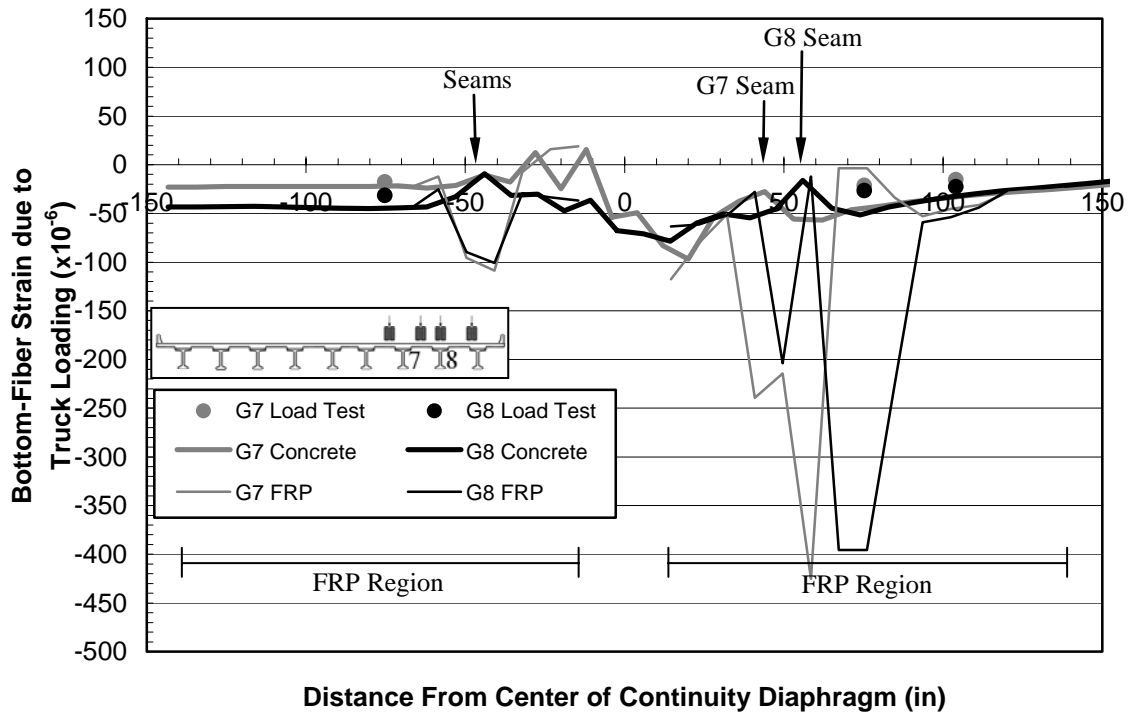
Figure 6.44 Bottom-Fiber Strain Data for the Concrete v. FRP for the Post-Repair Model (close-up view)—C9 Load Position

132

CHAPTER 7: DISCUSSION

7.1 INTRODUCTION

In analyzing the strains and deflections measured during the pre-repair load tests and those from the FEM models, it is useful to consider the information in terms of either pre-repair or post-repair results. In comparing the results of the *Pre-Repair* model to those of the pre-repair load tests, several conclusions can be drawn regarding the current behavior of the bridge as well as the effects of certain structural elements—such as midspan diaphragms. The *Post-Repair* model results provide a guideline for improving data gathering during the post-repair load test by indicating which of the existing gauges are singularly informative and which could be sacrificed in favor of collecting measurements at a different location. They also help predict the effects of the FRP repair on the bridge's behavior.

7.2 ANALYSIS

7.2.1 Stress Contours Due to Seams

In refining the *Pre-Repair* model, bottom-fiber strain measurements, bottom-fiber deflection measurements, and girder-section strain profile measurements were all available for comparison between the load test results and the FEM models. As can be seen in Figures 6.9–6.16—and addressed in Section 6.2—the bottom-fiber strain measurements and the bottom-fiber deflection measurements provided a feasible point of reference for this purpose.

Figures 7.1 and 7.2 provide a good example of how the girder-section strain profile measurements are not so useful. These illustrate the strain values at various depths on one face of a specific cross section of a girder. These figures are from Cross Section 2—which is 4.75 in. from the face of the continuity diaphragm on Span 10—and Cross Section 3—which is 4.75 in. from the face of the continuity diaphragm on Span 11— respectively. Figure 7.1 shows the strain along the East face of Girder 7 for the A7 (near cracked region) Load Position, and Figure 7.2 shows the strain along the West face of Girder 8 for the C9 (midspan) Load Position. From these figures, it is apparent that the FEM results predict a strain profile quite different from that which was measured during the bridge testing. Other profiles can be seen in Appendices D–G.
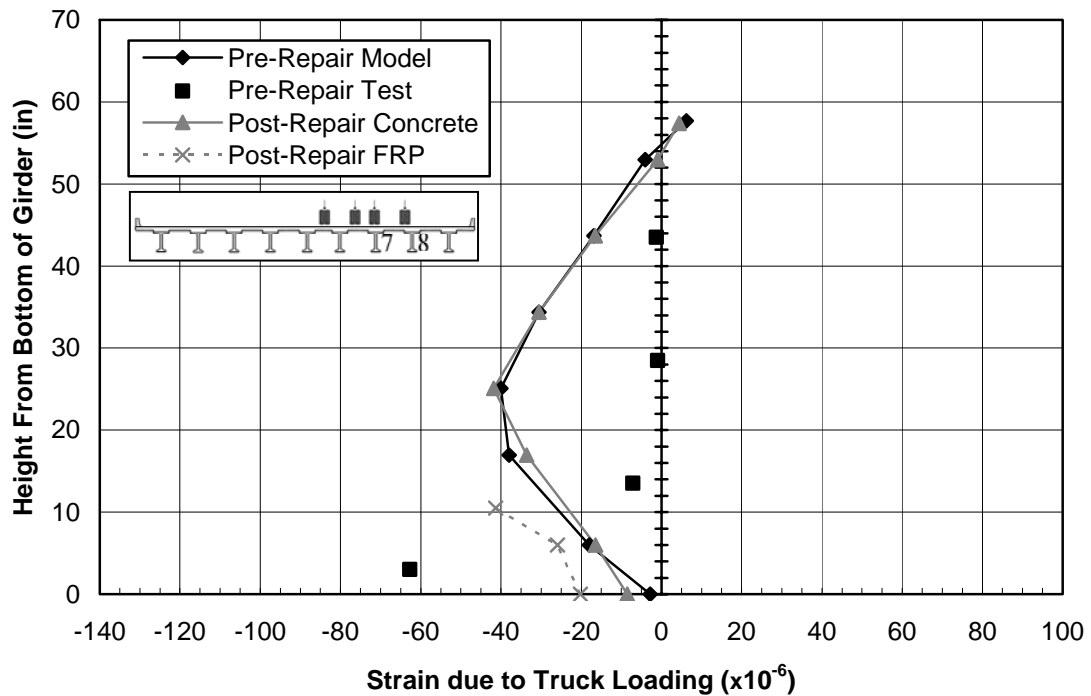
Figure 7.1 Strain Profile—A7 Load Position, Section 2, Girder 7, East Face

134
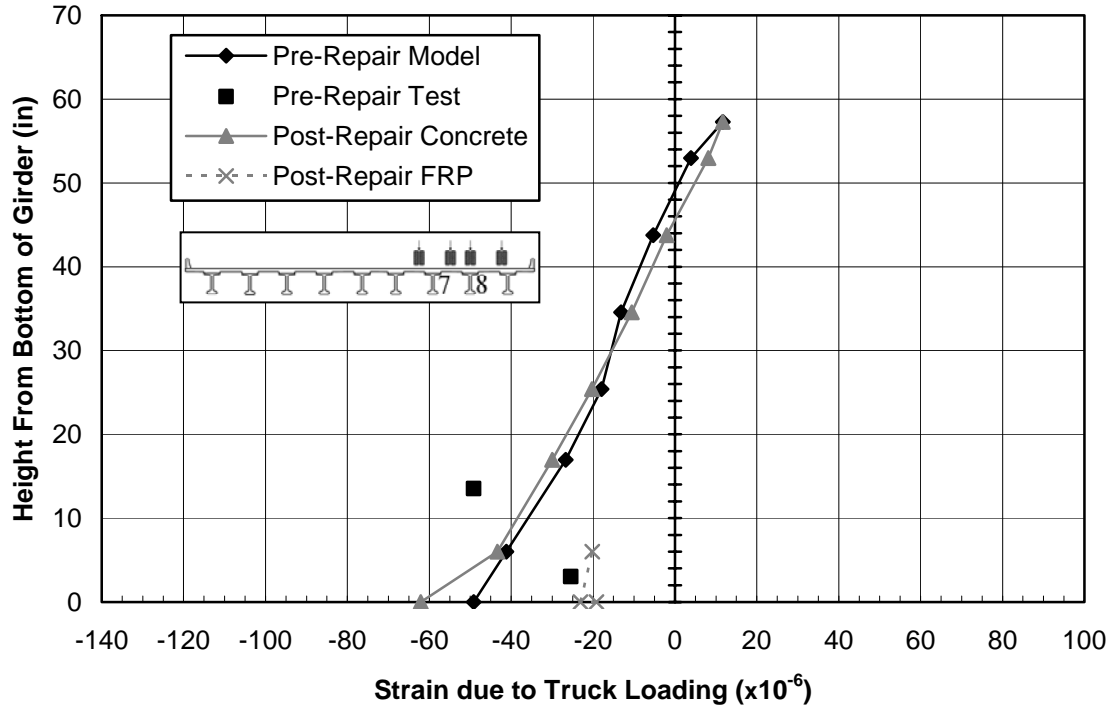
Figure 7.2 Strain Profile—C9 Load Position, Section 3, Girder 8, West Face

By evaluating the strain contours of the ABAQUS *Cracked-with-Reinforcement*

model shown in Figure 7.3, the reason for the disparity becomes apparent. The stress

contours that result from the modeled seam are significantly different from the stress

contours that are present on the real structure as a result of the crack groups—which are

illustrated in Figures 3.6–3.14. In addition to the fact that multiple cracks are modeled

as one seam, the cracks on the physical structure tend to run in a more diagonal fashion

along the girder than was used in the seam approximations. Because the stresses and

strains within this cracked region change drastically over a relatively small distance,

this deviation from the actual cracking pattern causes the FEM results within that

cracked region to be significantly different from the load test results.

135

E, E33
(Avg: 75%)
+6.348e-05
+4.500e-05
+3.704e-05
+2.909e-05
+2.113e-05
+1.317e-05
+5.215e-06
-2.742e-06
-1.070e-05
-1.866e-05
-2.661e-05
-3.457e-05
-4.253e-05
-5.048e-05

Stress contours
due to Seam

Continuity
Diaphragm

Span 10   Span 11

——— Seam in FEM
··········· Actual Crack Location
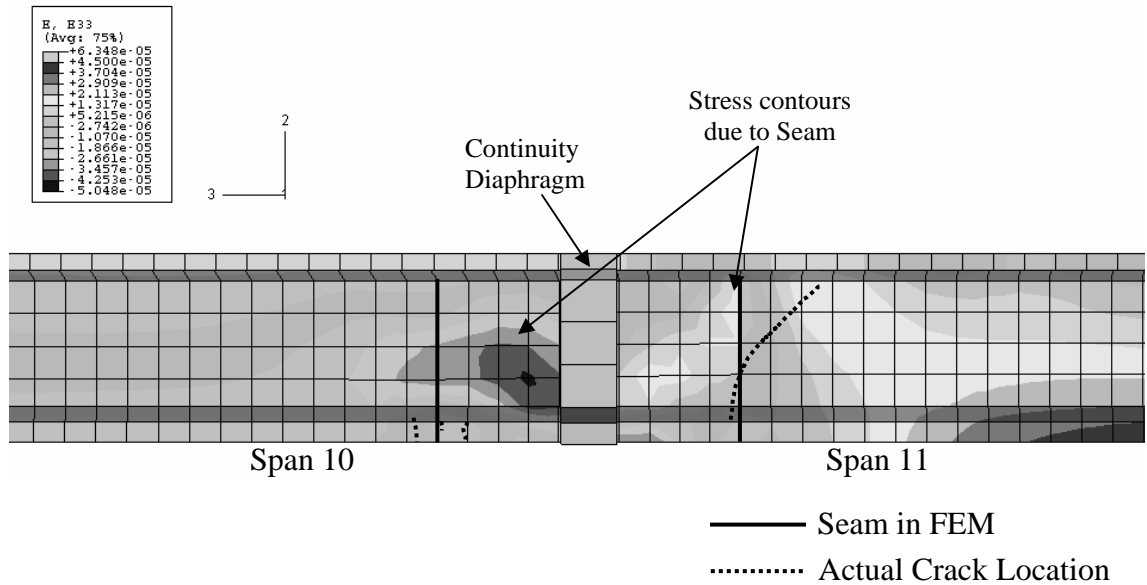
Figure 7.3 Longitudinal Strain Contours for the Cracked-with-Reinforcement Model, A7 Load Position, Girder 7, East Face

This does not necessarily mean, however, that the FEM results from within these cracked regions are useless. Though the differences here make a comparison between the analytical and the experimental results somewhat impractical at times, comparison between the *Pre-Repair* and *Post-Repair* results within these zones is still informative.

Among others, there are two likely possibilities:

1.   The global, post-repair behavior of the bridge will remain consistent with the overall behavior of the bridge prior to repair. This would result in the strain changes predicted by the FEMs being very close to the changes in strains measured during the two load tests. In other words, any discrepancies that exist between the *Pre-Repair* model and the behavior of the existing bridge would remain approximately constant after the bridge is repaired.

136

2.   The repair of the bridge will reestablish continuity and the post-repair behavior

of the bridge will more effectively be described by the *Post-Repair* model than the

behavior of the existing bridge was predicted by the *Pre-Repair* model.

In the event that the first possibility occurs, the change in longitudinal strains

between the *Pre-Repair* and *Post-Repair* models will still accurately reflect the change

in longitudinal strains on the bridge due to the repair. In this case, the strain gauges

within the cracked regions will still be useful for comparative purposes.

If continuity is reestablished, however, comparisons between the *Pre-Repair* and

Post-Repair models will no longer effectively predict the change from the pre-repair to

the post-repair behavior of the actual bridge. In contrast, the analytical results for the

Post-Repair model will more closely match the experimental results of the post-repair

load test than the *Pre-Repair* model matches the pre-repair load test results. Section 7.5

details the forecasted behavior of the repaired structure and the resultant effects on the

continuity of the bridge girders.

7.2.2 Tension Due to Cracking at the Face of the Continuity Diaphragm

As the strains along the faces of the girders were compared at the various instrumented

cross sections, it was interesting to discover that the seam along the face of the

continuity diaphragm on Girder 6 on Span 11 appears to correspond with tension in the

FRP of Girder 7. For the A9 Load Position, which has strong influence on Girder 7, the

strain profile on Girder 7 for the East face of Cross Section 3—the instrumented cross

section nearest the seam at the face of the continuity diaphragm in Girder 6—is shown

in Figure 7.4. Figure 7.5 shows the strain contours in the FRP with the tension area

indicated. Figure 7.4 indicates that the bottom flange of the concrete is in compression but the adjacent FRP is in tension. The strain contours in Figure 7.5 show that this area of tension is located primarily at a corner of the FRP. Most likely, this tension results from a combination of two factors: both the seam at the face of the continuity diaphragm *and* the mesh pattern of Girder 7.

To explain the effect that the mesh pattern of Girder 7 has on the analytical results of the FRP strains, it is first important to understand how the results of the models for the various gauge locations are obtained. The strain values reported to be at distances—where gauges are located—from the face of the continuity diaphragm are an interpolation of the strain values obtained from ABAQUS at the nodes on the near side and far side of the elements at that point. The locations of those nodes result from the mesh size. For instance, the values for the strains shown in Figure 7.1 are an interpolation—for a location 4.75 in. from the face of the continuity diaphragm—of strain values 4 in. and 12 in. from the face of the continuity diaphragm. The tie constraint—as explained in Section 5.12—between the FRP and Girder 7 is the final link leading to the tension reading. It seems most likely that the tension reported in the FRP is due to the FRP being tied to a node nearer to the bearing pad than the node from which the strain readings are taken for the concrete. Most likely the corner FRP node is tied to the concrete node at the center of the continuity diaphragm rather than the concrete node located 4 in. from the face, which is where ABAQUS reports the concrete strain.

138
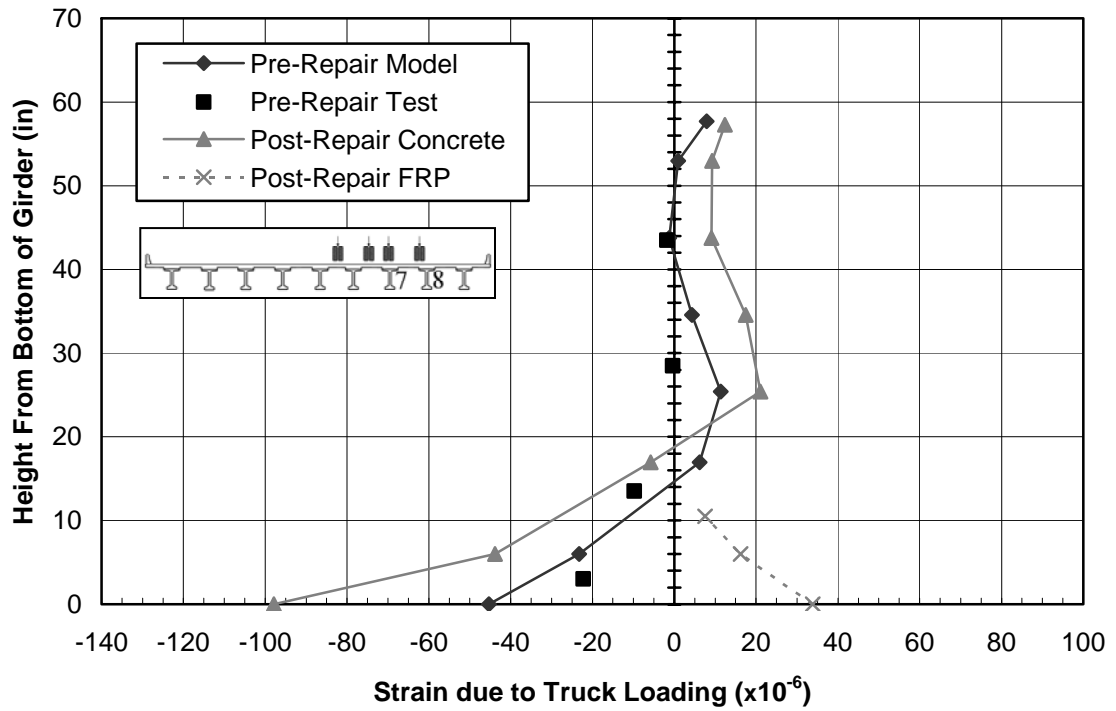
Figure 7.4 Strain Profile—A9 Load Position, Section 3, Girder 7, East Face
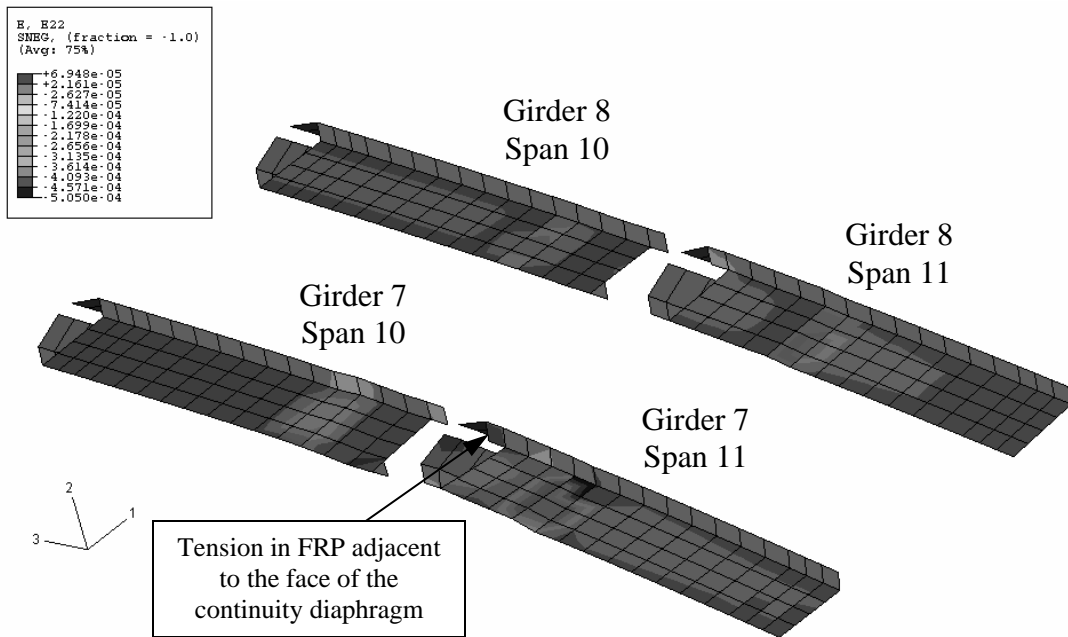
Figure 7.5 Strain Contours in FRP for Load Position A9

139

Finally, the continuity diaphragm between Girders 6 and 7—as well as the tie connection between the girders and the bridge deck—transfers the effects of the truck loading from the cracked region in Girder 6 to Girder 7. The tie connection between the Girder and the FRP—which connects the FRP to the concrete at the center of the continuity diaphragm location rather than at a distance 4 in. from the face of the diaphragm where the concrete strains are measured—then transmits this load through the tied nodes.

7.2.3 Force Developed in Strands at Cracks

As explained in Section 3.4.2, it is most likely that the prestressing tendons have slipped as a result of the cracks in the girder end and all of the prestressing force in the tendons between the crack and the end of the girder has been lost (Barnes et al. 2006). It is not feasible to test this hypothesis with the FEMs created for this project because these FEMs only reflect changes due to applied external loads.

Figures 6.5–6.8 indicate that the results of the *Cracked* model imply that no moment will be transmitted across the crack through the concrete, but the load tests reveal that a significant amount of strain does transmit within that cracked region. This suggests that regardless of whether the prestressing is still effective in the end regions, the strands are at least anchored well enough to resist some moment at the cracked sections in the service-load range. Because these FEMs do not include complex mechanical relationships for the bond interaction between the steel and concrete, this does not indicate whether the steel will stay anchored up to yield.

It can be noted by evaluating Figures 6.9–6.12 that the *Cracked-with-Reinforcement*
model reproduces the behavior of the bridge, as determined by the pre-repair load test,
accurately to within 5% at four of the six bottom-fiber gauges on each girder line. If the
prestressing strands were moving freely within the concrete, the *Cracked* model—rather
than the *Cracked-with-Reinforcement* model—would more closely reflect the behavior
of the bridge.

The stress changes resulting from the A7, A9, C7 and C9 Load Positions in the *Pre-
Repair* model in the prestressing steel at the crack locations are presented in Table 7.1.
These stress changes represent reasonably low stress ranges and could likely be
anchored by surrounding concrete despite any previous slip. However, it *cannot* be
safely inferred from this whether the strands would remain anchored for a significantly
greater load approaching ultimate strength.

**Table 7.1 Compressive Stress Changes, due to Truck Loads, in Prestressing Steel
at the Seam Locations of the *Pre-Repair* Model**

| | | Compressive Stress Change in Prestressing Steel (ksi) | | | |
| | | Girder 7 | | Girder 8 | |
		Span 10	Span 11	Span 10	Span 11
Load Positions	A7	3.7	1.6	1.2	0
	A9	3.6	12	1.6	5.3
	C7	3.5	1.5	1.8	0.2
	C9	3.5	12	2.2	7.4

7.2.4 Effectiveness of Midspan Diaphragms

As the model was created and the strains were compared to those of the 2005 pre-repair
load tests, a question arose as to how effective the midspan diaphragms are. As can be

seen from Figures 6.17–6.20, there is a disparate point—labeled as point 'A'—in the

FEM models at the location of the midspan diaphragms. As explained in Section 6.2.4,

a model was created that did not include the diaphragms, and the results were compared

to those of the *Cracked-with-Reinforcement* model and the test results. Again looking

at Figures 6.17–6.20, it is apparent that the diaphragms are at least somewhat effective

because the FEM model *with* the midspan diaphragms more closely models the overall

behavior of the bridge than does the FEM model *without* the midspan diaphragms.

It is also interesting to note from the figures the extent to which the midspan

diaphragms distribute the load between the girders. This is particularly apparent in

Figure 6.18—which is the graph for the A9 Load Position. The resultant strains in

Girder 7 are approximately twice as great for the model without diaphragms as for the

model with diaphragms. This effect can be seen—though not quite as drastically—for

each of the other load positions. It can therefore be concluded that, with all other

structural elements being equal, the load-carrying capacity of a bridge without

diaphragms should be significantly less than the load-carrying capacity for a bridge with

diaphragms. The bridge with diaphragms does a much better job of distributing the

applied deck loads among the supporting girders. This effect contradicts the findings of

Tedesco, Stallings, and Tow (1995). In addition, this effect was not considered in the

creation of the FEMs used to develop the AASHTO-LRFD live load distribution factors

for girder bridges, which were formulated for bridges without midspan diaphragms

(Zokaie 2000). Further exploration of this effect could prove useful for future bridge

design applications.

The cause of the discrepancy was not determined. Possibly the diaphragms are effective in only one global direction—which is not accurately modeled by the tie constraint between the diaphragm, girders, and bridge deck in the model. Another possibility is that the midspan gauge on Girder 7 is measuring the strains incorrectly. Looking again at Figures 6.17 through 6.20, one can see that for each load position, the Girder 7 measurement is the only midspan reading that is significantly different between the FEM results and the load test results. It would be prudent to test—and hopefully disprove—this theory prior to the post-repair load testing.

After evaluation of the figures, because the global behavior of the bridge model was consistent with the global behavior of the bridge as measured by the pre-repair load test, it was determined not to pursue the cause of the possibly erroneous gauge reading at midspan.

7.3 INFERENCES REGARDING BRIDGE BEHAVIOR

As presented in Section 3.4.2, Swenson (2003) considered the possibility that the bridge was behaving such that the girders were continuous across the span but with hinged behavior at the crack locations near the bent. A hinge describes a relationship in a beam where the relative translation of points on the neutral axis on either side of a cross section are identical but the planes on either side of the cross section are free to rotate relative to one another. This is similar to the relationship that was created in the FEM model when the seams were defined within the girders. However, in the FEM, nodes on the faces of the seam are free to move relative to each other, while continuity is retained at points on the cross section beyond the extent of the seam. Nonetheless, the relatively

143

small amount of bending moment that can be resisted at the seam locations when unreinforced (*Cracked* model) is not enough to cause a significant difference with respect to a hinge in a beam model. As can be seen in Figures 6.5–6.8, the cracked girders exhibit more effective continuity than would be expected if the *Cracked* model (hinged behavior) was accurate.

However, it is also apparent that the bridge is not behaving in a manner consistent with the best-case scenario of an uncracked—and therefore fully continuous across the span—bridge unit. What is apparently occurring is that the prestressing strands, regardless of whether or not they are actively carrying a prestressing force, are still acting as reinforcement across the cracks and effectively acting as a rotational spring which helps to partially resist bending in a simple beam model.

7.4 GAUGE LOCATION ANALYSIS

One main purpose when analyzing the data of the *Post-Repair* model was to determine which of the concrete strain gauges to retain and which to abandon in favor of gathering data at other positions. Because there are a limited number of channels for data gathering, it is important that each of the seventy-two channels be used to collect singularly useful information.

In order to determine which of the gauges were least useful, the *Pre-Repair* and *Post-Repair* model results were compared, and the differences between the two were computed at each of the gauge locations. This difference is useful because, as explained in Section 7.2.1, the change in behavior resulting from the FRP repair is of interest. If there is little change expected due to the repair, it would not be very informative to

measure that lack. These predicted change calculations are presented in Tables 7.2 and 7.3. If the difference was less than five microstrain for multiple load positions, the gauge was possibly not in a very vital location for assessing the change in performance attributable to the FRP repair. Another criterion by which to judge the importance of a gauge location was to evaluate the results from the pre-repair load test. If the strain was consistently between negative ten and ten microstrain for all four load positions, this also indicated that the location was not as informative as another position might be— unless a large *change* in strain was predicted using the *Post-Repair* model.

From Tables 7.2 and 7.3, it is apparent that the top-most strain gauge positions, located 43.5 in. above the base of the girder—labeled as Gauge F in Figures 4.21 and 4.22—provide significantly less noteworthy information than the other girder-section strain profile gauges. This is unsurprising given the gauges' nearness to the neutral axis of the composite girder. For example, at Cross Section 2 on Girder 8, the topmost gauge location—Gauge F—indicated changes of only 1, 2, 2, and 3 microstrain for the A7, A9, C7, and C9 Load Positions, respectively. Gauge A, located 13.5 in. above the base of the girder, on that same cross section, is predicted to experience changes of 15, -40, 8, and -5 microstrain. While the changes in strain for the Gauge A location for two of these load positions are not very significant, the changes in strain for the other load positions are very informative. Therefore, use of the topmost gauge locations should be discontinued for the post-repair load test.

145

Table 7.2 Strain Gauge Evaluation—Girder 7

	Gauge ID	Ht. from Girder Base	Change[a] due to FRP Repair				Load test data within 10 $\mu\varepsilon$ of zero?			
			A7	A9	C7	C9	A7	A9	C7	C9
Cross Section 1	F[c]	43.5	8	5	6	7	Y	Y	Y	Y
	E	28.5	9	3	8	5	Y	Y	N	Y
	D[b]	13.5	0	-4	0	-2	N	N	N	N
	A	13.5	0	-6	0	-5	Y	N	Y	N
	C	3.0	-3	-6	-3	-5	N	N	N	N
	M	0.0	-5	-10	-4	-10	Y	N	Y	N
Cross Section 2	F[b,c]	43.5	0	-4	-2	-3	Y	Y	Y	Y
	E[c]	28.5	0	-10	-3	-8	Y	Y	Y	Y
	D[b]	13.5	2	0	3	1	Y	N	Y	N
	A	13.5	-8	-30	-10	-30	Y	N	Y	N
	C	3.0	-2	1	0	8	N	N	N	N
	B	3.0	10	15	0	-7	Y	N	N	N
Cross Section 3	F[c]	43.5	6	10	7	12	Y	Y	Y	Y
	E[c]	28.5	7	12	13	12	Y	Y	Y	Y
	D	13.5	-12	-18	-12	-8	Y	Y	Y	N
	A	13.5	50	20	20	15	Y	Y	Y	Y
	C	3.0	-30	-33	-20	-25	Y	N	N	N
	B	3.0	0	-35	-12	-20	N	N	Y	Y
Cross Section 4	F[b,c]	43.5	-4	3	-2	3	Y	Y	Y	Y
	E[b,c]	28.5	-2	-5	-5	-4	Y	Y	Y	Y
	D	13.5	-4	-15	-8	-12	Y	N	Y	N
	A	13.5	-8	-14	-10	-12	Y	N	Y	N
	C	3.0	-3	-22	-7	-20	N	N	N	N
	M	0.0	-10	-22	-9	-23	N	N	N	N

[a] (-) represents a negative change from the pre-repair model to the post-repair model

[b] Absolute value of all changes for this gauge are less than or equal to five microstrain

[c] All load test results for this gauge are less than or equal to ten microstrain

Table 7.3 Strain Gauge Evaluation—Girder 8

	Gauge ID	Ht. from Girder Base	Change[a] due to FRP Repair				Load test data within 10 με of zero?			
			A7	A9	C7	C9	A7	A9	C7	C9
Cross Section 1	F[b,c]	43.5	1	1	2	2	Y	Y	Y	Y
	E[b]	28.5	2	1	5	2	Y	Y	Y	N
	D[b]	13.5	0	-2	0	-4	Y	N	N	N
	A	13.5	3	-32	4	-2	Y	N	N	N
	C	3.0	-5	-5	-3	-6	N	N	N	N
	M	0.0	0	-42	0	-8	N	N	N	N
Cross Section 2	F[b,c]	43.5	1	2	2	3	Y	Y	Y	Y
	E[b,c]	28.5	1	1	4	3	Y	Y	Y	Y
	D	13.5	-6	-10	-4	-12	Y	Y	Y	N
	A	13.5	15	-40	8	-5	Y	N	Y	N
	C	3.0	-14	-10	-8	-7	N	N	N	N
	B	3.0	20	-40	12	-8	Y	N	N	N
Cross Section 3	F[b,c]	43.5	-1	1	3	2	Y	Y	Y	Y
	E[b]	28.5	-1	-3	0	-1	Y	N	Y	N
	D	13.5	6	6	6	12	Y	Y	Y	N
	A	13.5	15	-25	12	-2	Y	N	N	N
	C	3.0	-8	0	-3	3	Y	N	N	N
	B	3.0	16	-39	10	-10	N	N	N	N
Cross Section 4	F[c]	43.5	-1	5	0	7	Y	Y	Y	Y
	E[b]	28.5	0	2	0	2	Y	N	Y	N
	D[b]	13.5	4	-4	3	-5	Y	N	Y	N
	A	13.5	-7	-22	-3	-8	Y	N	Y	N
	C	3.0	8	-10	7	-10	Y	N	N	N
	M	0.0	-3	-42	-2	-20	N	N	N	N

[a] (-) represents a negative change from the pre-repair model to the post-repair model

[b] Absolute value of all changes for this gauge are less than or equal to five microstrain

[c] All load test results for this gauge are less than or equal to ten microstrain

The eight newly available gauge channels should be transferred elsewhere. In Figures 6.37–6.44 it can be observed that at the beginning and the end of the repaired region, the strains in the concrete and the FRP reinforcement approximate one another very closely. They come closest to matching one another at the end of the repaired region farthest from the seams. In the middle of the repaired region, the strains for the concrete and FRP reinforcement differ greatly. The strains in the FRP are significantly larger than those of the concrete. If the FRP is compensating for the weakening in the concrete, this would be expected. To measure this effect in the bridge—as well as to verify that the strain in the concrete and the FRP are the same where they should be—strain gauges should be placed on the FRP reinforcement on Span 11 at the bottom-fiber gauge locations at 75.25 in. and 104 in. from the face of the continuity diaphragm on each girder. These gauges would therefore be virtually on top of the strain gauges already present on the concrete. The remaining four gauges should also be placed on the FRP reinforcement along the bottom-fiber line, but these should be located directly under the main crack location for each span of both girders. These would measure the FRP strains to see if they match the predictions of the model where there is zero concrete strain.

7.5 FORECAST FOR REPAIR

Evaluating the analytical deflection results presented in Section 6.3.2, it can be concluded that the FRP repair will likely result in the bridge behavior tending towards that of a continuous structure. In addition to the additional stiffness of the FRP, any closing of cracks under applied loads would move the structural behavior of the bridge

toward the *Uncracked* model behavior for additional loads. This could occur if the starting crack width is less than the closing displacement of the seam.

As explained in Section 5.10, the seam used to approximate the effects of the crack allowed the sides of the "crack" to move both apart and towards (and past) one another in the FEM. This was acceptable because in the concrete in the actual structure a space was already physically present between the two faces of the crack, and as such, some movement in either direction was possible. However, no initial condition in the FEM established that pre-existing gap. It is possible that this lack results in the discrepancy between the model data and the load test data at the location 75.25 in. from the face of the continuity diaphragm on Spans 10 and 11, as seen in Figures 6.21 and 6.23 and discussed in Section 6.2.5.

On the instrumented girders, the *Post-Repair* model predicted longitudinal closing displacements at the bottom-fiber seam locations of 0.0005 in. to 0.004 in—as presented in Table 7.4. Existing crack widths vary throughout the day and have been reported to range up to 0.03 in. (Swenson 2003). However, measurements taken at the time of the pre-repair load test did not indicate widths greater than 0.01 in. (Fason and Barnes 2004). More precise measurements of the existing crack widths are presently not available. It is possible that at least some of the cracks will close when external loads are applied— which would further serve to increase the continuous behavior of the bridge.

Given the additional stiffness due to the FRP and the closing of some cracks, it seems probable that the strain results predicted for the *Post-Repair* model are fairly accurate. This accuracy will be higher for the bottom-fiber strains than for the girder-profile strains

149

because of the variation in stress contours near the cracks—as discussed in Section

7.2.1—which may still potentially affect the comparison between analytical and

experimental results.

Table 7.4 Maximum Closing Displacements for Each Seam and Load Position

		Closing Displacements ($\times 10^{-3}$ in.)			
		Girder 7		Girder 8	
		Span 10	Span 11	Span 10	Span 11
Load Position	A7	1.5	2	1.5	0.5
	A9	2	4	1.5	3
	C7	1.5	1.5	1.5	0.5
	C9	1.5	4	1.5	4

However, there is, among others, one possible situation wherein the additional

continuity predicted by the *Post-Repair* model would not occur. When looking at the

strain results presented for the girder profiles in Appendices D–G, one can see that the

model predicts that in much of the length of the repair, the FRP reinforcement will be in

compression. This is also readily apparent when looking at the bottom-fiber strain results

of the post-repair model presented in Figures 6.29–6.32. As explained in Section 5.16,

fiber-reinforced polymer is a composite material of Tyfo SCH-41 reinforcing fabric and

Tyfo S epoxy. Just as with a piece of cloth, the material can resist a great deal of tension,

but there is little resistance to compression.

However, given the short unbraced length present at the crack and the resultant high

elastic buckling capacity, it is unlikely that this lack would affect the efficacy of the

repair. For a unit width of a four-ply portion of the reinforcing fabric, the stiffness—

EI—is approximately 4000 lb-in^2. From Equation 7.1 (Gere 2001) and for a crack width

of 0.01 in.—a width larger than any of the cracks present on the bridge at the time of the pre-repair load testing—this results in a buckling load of 400×10^3 kips and a critical elastic buckling stress of 2.5×10^6 ksi. The largest compressive strain predicted in the FRP corresponds to a stress of only 6 ksi. Because the elastic buckling stress is more than four hundred thousand times greater than the compressive stress predicted in the FRP, second-order effects should have negligible impact on the FRP strength.

$$P_{cr} = \frac{\pi^2 EI}{L^2}$$
Eq. 7.1

where

P_{cr} = Critical load

E = Modulus of elasticity

I = Moment of inertia

L = Crack width

Given that buckling of the FRP is not likely if the bond to the concrete remains effective on either side of the crack, it *is* possible that cyclic loading and unloading action could serve to deteriorate the bond between the FRP and the concrete. If this occurred, the unbraced length would increase, and it is possible that the material would buckle before it reached the compressive loads predicted in the *Post-Repair* model and prior to reestablishing bridge continuity. Recommendations for monitoring the FRP Repair and the ensuing bridge behavior are presented in Section 8.3.

151

CHAPTER 8: SUMMARY AND CONCLUSIONS

8.1 SUMMARY OF STUDY

Spans 10 and 11 of the Interstate Highway 565 bridge structure in Huntsville, Alabama were noticed to be cracked shortly after their completion in the early 1990's. After investigation, it was concluded that stress due to the temperature differential between the bridge deck and the bulb tee girders was the probable cause. Further research into the cause of the cracking, the results of the cracking, and the possible repair methods was conducted by ALDOT in cooperation with Auburn University personnel. It was concluded that fiber-reinforced polymer (FRP) repair was feasible, and a repair procedure was devised. In order to measure the efficacy of the repair, load tests were conducted on June 1 and 2, 2005 prior to the repair. Post-repair load tests are slated to be conducted after the FRP application.

A finite-element model (FEM) was created to provide a basis for an analytical comparison to measured data and observed bridge behavior. Several models were created to simulate the current behavior of the bridge. Three models of the pre-repaired bridge were created: *Uncracked*, *Cracked*, and *Cracked-with-Reinforcement*. When compared to the load test data, the *Cracked-with-Reinforcement* model was determined to be a sufficiently accurate representation of the overall behavior of the physical structure. The model results imply that rather than behaving as a continuous two-span beam—as it

was designed to behave—the bridge is behaving somewhere between a fully continuous structure and a continuous beam with a hinge in the cracked region.

The FRP repair was then modeled to analyze the expected effects of the FRP application and to determine which of the strain gauges used in the pre-repair load tests should be relocated for the post-repair tests.

8.2 CONCLUSIONS

1.   Of the *Uncracked*, *Cracked*, and *Cracked-with-Reinforcement* models, the *Cracked-with-Reinforcement* model best represents the current behavior of the bridge.

2.   The girder strain profiles within the cracked regions are strongly influenced by the specific crack patterns near the location of the strain gauges. The *Pre-Repair* model insufficiently represents the strains on the bridge within the cracked zone. For a global representation of the behavior of the bridge, however, the *Pre-Repair* model with the single, representative seam per girder span is sufficient.

3.   Even if the prestressing force in the tendons is lost between the crack and the end of the girder, the strands are anchored well enough to resist girder moments at the cracked section in the service load range.

4.   The diaphragms have a large effect on the live load distribution between the girders of the bridge.

5.   Modeling the FRP as a laminar material is more conservative than modeling it as an isotropic material.

6.   For this particular repair scheme, the FRP has the greatest effect on the strains in the concrete near the cracks.

7.   As expected, the *Post-Repair* model predicts less change in strain is expected at locations closer to the neutral axis than at locations nearer to the FRP.

8.   The repair is equally effective for Girder 7 and Girder 8.

9.   For all four load positions, the repair acts to decrease the predicted change in deflection more at midspan of the loaded girder than at any other location.

10.   Though the FRP is expected to be in compression, it is expected that the induced force will not result in instability of the FRP.

11.   The repaired bridge should exhibit deflections approximately the same as the original, uncracked structure.

8.3 RECOMMENDATIONS

1.   Further exploration into the effects of the midspan diaphragms on the girder behavior should be conducted. The disparate point which is present in the analytical results suggests that the midspan diaphragms on the structure are not as effective as the midspan diaphragms in the model. Exploring other types of modeling connections between the girders and the diaphragms is one route for pursuing this question.

2.   Alternatively, it is possible that rather than being a function of the efficacy of the diaphragms, the disparate point is the result of a faulty gauge. It is important to test— and rule out or rectify—this possibility prior to the post-repair load testing.

3.   In addition to exploring the effects of the midspan diaphragms for this specific instance, further exploration into the effect of midspan diaphragms on live load distribution is recommended. AASHTO-LRFD live load distribution factors do not

currently incorporate the effects of midspan diaphragms, and accounting for their presence could greatly increase bridge efficiency.

4.   Prior to the FRP installation, more precise widths of the existing cracks should be measured, and the progression of cracks since the last inspection should be monitored.

5.   For the post-repair load test, eight gauges should be relocated from the face of the girder near the top of the web—43.5 in. from the girder base—to bottom-fiber gauge locations on the surface of the FRP reinforcement. A gauge should be placed 75.25 in. from the face of the continuity diaphragm on Span 11 on both Girder 7 and Girder 8. A gauge should also be placed 104 in. from the face of the continuity diaphragm on Span 11 on both Girder 7 and Girder 8. Each of the remaining four gauges should be placed on the bottom-fiber of the FRP so as to cross the main crack location of each instrumented girder span.

6.   The post-repair tests should occur within one year of the repair, within 30 days of June 1—the date of the pre-repair load tests—and the results should be compared with the results of the pre-repair tests. Of primary interest is the manner in which the repair affects the behavior of the bridge.

7.   The effectiveness of the repair should be monitored regularly.

REFERENCES

AASHTO. 2004. *AASHTO LRFD bridge design specifications*. 3rd ed. Washington, D.C.: American Association of State Highway and Transportation Officials (AASHTO).

ABAQUS. 2004. *ABAQUS analysis user's manual: version 6.5-1*. ABAQUS, Inc.

ABAQUS. 2006. *ABAQUS analysis user's manual: version 6.6-1*. ABAQUS, Inc.

ACI Committee 318. 2005. *Building Code Requirements for Structural Concrete (ACI 318-05) and Commentary (ACI 318R-05)*. Farmington Hills, MI, American Concrete Institute.

Alabama Department of Transportation (ALDOT). 1987. "Plan and Profile of Proposed State Highway: Project No. ID 565-5(21)358" Montgomery, Alabama.

Alabama Department of Transportation (ALDOT). 1994. "Cracks in Precast Prestressed Bulb Tee Girders on Structure No.'s I-565-45-11.5 A. & B. on I-565 in Huntsville, Alabama." Montgomery, Alabama.

American Association of State Highway and Transportation Officials (AASHTO). 1997 16th Ed., *Standard Specifications for Highway Bridges*, Washington, D.C.

Barker, Richard M, and Jay A. Puckett. 1997. *Design of Highway Bridges*. New York: John Wiley & Sons, Inc.

Barnes, Robert W., Anton K. Schindler, Kyle S. Swenson, Ningyu Gao, and William E. Fason. 2006. Cracking and repair of prestressed concrete bridge girders made continuous for live loads. In *Extending the Life of Bridges: Concrete and Composites Buildings, Masonry and Civil Structures held in Edinburgh, Scotland 13-15 June 2006, edited by M.C. Forde*. Galashiels, Scotland.

Barr, Paul J., Marc O. Eberhard, and John F. Stanton, 2001. Live-load distribution factors in prestressed concrete girder bridges. *Journal of Bridge Engineering* 6 (5): 298-306.

Chung, Wonseok, Judy Liu, and Elisa D. Sotelino, 2006. Influence of secondary elements and deck cracking on the lateral load distribution of steel girder bridges. *Journal of Bridge Engineering* 11 (2): 178-187.

Eamon, Christopher D., and Andrzej S. Nowak, 2002. Effects of edge-stiffening elements and diaphragms on bridge resistance and load distribution. *Journal of Bridge Engineering* 7 (5): 258-266.

Fason, Bill, and Robert Barnes. 2004. *I-565 Visual inspection*. Auburn: Auburn University Highway Research Center. Photocopied.

Fu, Kuan-Chen, and Feng Lu, 2003. Nonlinear finite-element analysis for highway bridge superstructures. *Journal of Bridge Engineering* 8 (3): 173-179.

Gao, N. 2003. *Investigation of cracking in precast prestressed girders made continuous for live load*, Thesis. Auburn University.

Gay, Daniel, 2003. *Composite materials: design and applications*. Translated by Suong V. Hoa and Stephen W. Tsai. Boca Raton: CRC Press LLC.

Gere, J. M. 2001. *Mechanics of materials*. 2d ed. Pacific Grove: Brooks/Cole.

Green, Tanya, Nur Yazdani, and Lisa Spainhour, 2004. Contribution of intermediate diaphragms in enhancing precast bridge girder performance. *Journal of Performance of Constructed Facilities* 18 (3): 142-146.

Huo, Xiaoming Sharon, Edward P. Wasserman, and Pingsheng Zhu, 2004. Simplified method of lateral distribution of live load moment. *Journal of Bridge Engineering* 9 (4): 382-390.

Ma, Z., X. Huo, M.K. Tadrous, and M. Baishya. 1998. Restraint moments in precast/prestressed concrete continuous bridges. PCI Journal 43 (6):40-56.

Mabsout, Mounir E., Kassim M. Tarhini, Gerald R. Frederick, and Charbel Tayar. 1997. Finite-element analysis of steel girder highway bridges. *Journal of Bridge Engineering* 2 (3): 83-87.

Roberts, James. 2005. *Evaluation of self-consolidating concrete for use in prestressed girder applications*, Thesis. Auburn University.

Schwarz, Michael, and Jeffrey A. Laman. 2001. Response of prestressed concrete I-girder bridges to live load. *Journal of Bridge Engineering* 6 (1): 1-8.

Swenson, K. 2003. *Feasibility of externally bonded FRP reinforcement for repair of cracked prestressed concrete girders*, Thesis. Auburn University.

Tedesco, J. W., J. M. Stallings, and D. R. Tow. 1995. Finite element method analysis of bridge girder-diaphragm interaction. *Computers & Structures* 56 (2/3): 461-473.

Tedesco, Joseph W., J. Michael Stallings, and Mahmoud El-Mihilmy. 1999. Finite element method analysis of a concrete bridge repaired with fiber reinforced plastic laminates. *Computers & Structures* 72: 379-407.

Wan, Baolin, Dimitris C. Rizos, Michael F. Petrou, and Kent A. Harries. 2004. Computer simulations and parametric studies of GFRP bridge deck systems. *Composite Structures* 69: 103-115.

Xia, Pin-Qi, and James M. W. Brownjohn. 2004. Bridge structural condition assessment using systematically validated finite-element model. *Journal of Bridge Engineering* 9 (5): 418-423.

Zhou, S., D. C. Rizos, and M. F. Petrou. 2003. Effects of superstructure flexibility on strength of reinforced concrete bridge decks. *Computers & Structures* 82: 13-23.

Zokaie, Toorak, 2000. AASHTO-LRFD live load distribution specifications. *Journal of Bridge Engineering* 5 (2): 131-138.

APPENDICES

APPENDIX A: EXPLANATION OF DATA PRESENTED IN
APPENDICES B THROUGH H

A.1 INTRODUCTION

Appendices B through G contain graphical results for the concrete surface strains and

girder deflections of the bridge models which have been discussed in this thesis.

Appendix H contains a summary of the load test data from the pre-FRP repair load test

which took place June 2, 2005 in Huntsville, Alabama. The girder numbering scheme,

load testing positions, measurement locations, and other reference information are

summarized in this Appendix.

A.2 GIRDER NUMBERING

When looking northward at the cross section of the bridge, the girders are numbered as

depicted in Figure A.1 with Girder 1 on the far left, proceeding through Girder 9 on the

far right. From this perspective, the west side of each of the girders is on the left of the

girder, and the east side of each of the girders is on the right of the girder.

A.3 LONGITUDINAL LOAD POSITIONS

As depicted in Figure A.2, there are nine longitudinal stop positions located along the

length of the bridge. Table A.1 describes each of these stop positions which are defined

by the middle axles of the trucks being centered on the location. They range from

midspan of Span 10 to midspan of Span 11. Five stop positions are located on Span 10,

and four stop positions are located on Span 11.

Cast-in-place
concrete barrier

6.5"

1 2 3 4 5 6 7 8 9

AASHTO
BT54 girders

3' - 4 ½" 8' – 0"

64' – 0"

70' – 9"
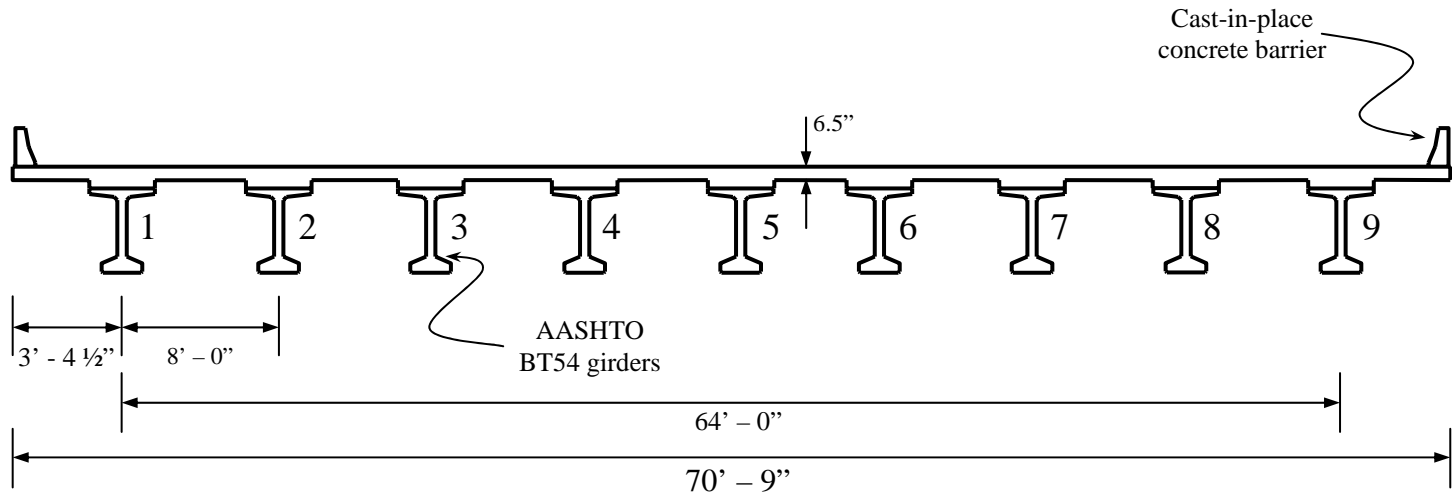
Figure A.1 Girder Numbering When Looking North

**Centerline
of
Continuity
Diaphragm
on Bent 11**

Span 10

Span 11

Stop
Line
4
70"

Stop
Line
6
70"

Stop
Line
1
600"

Stop
Line
2
291"

Stop
Line
3
151"

Stop
Line
5
12"

Stop
Line
7
128"

Stop
Line
8
300"

Stop
Line
9
600"

162

1200"
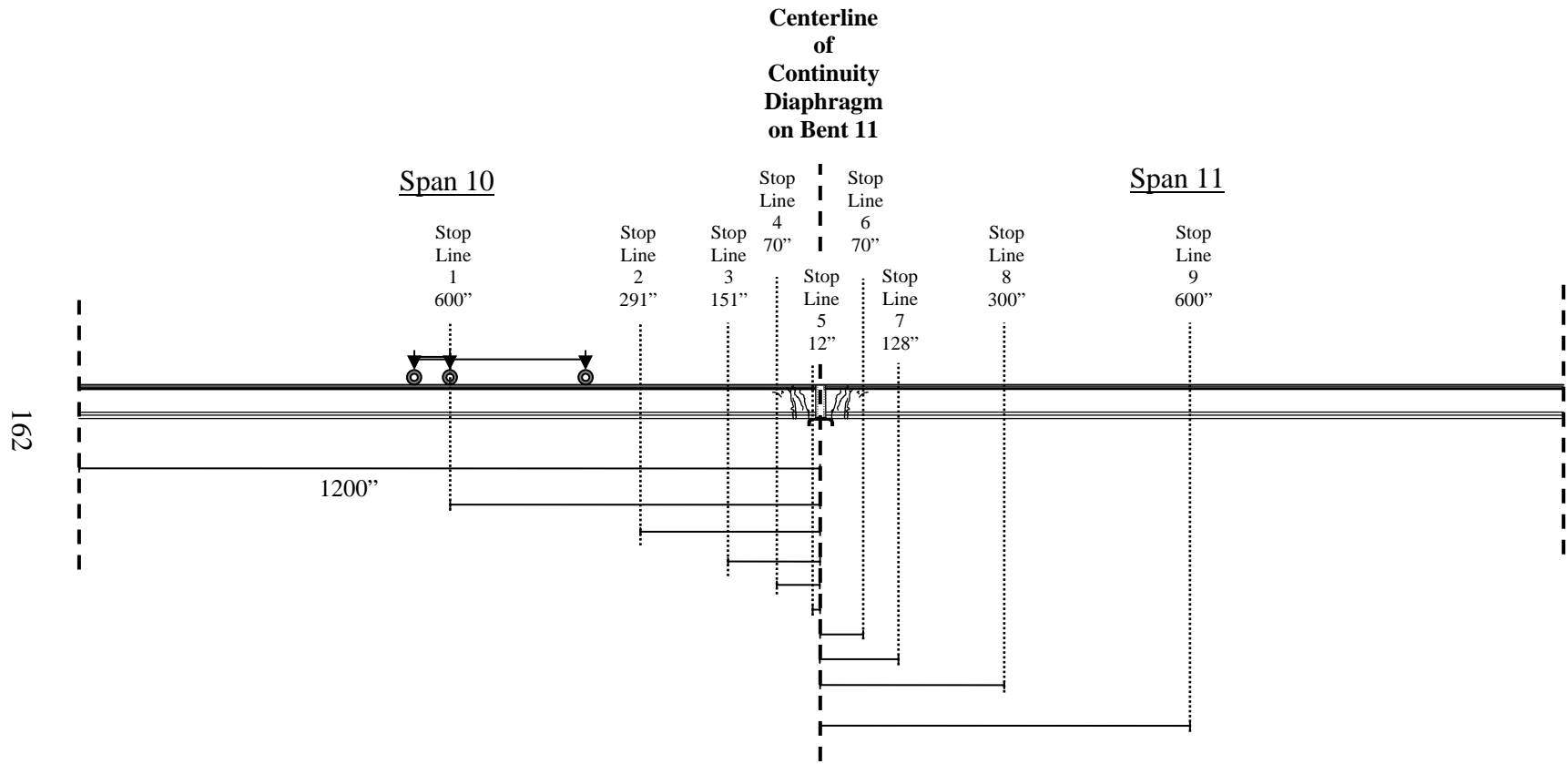
Figure A.2 Longitudinal Stop Positions for Test Trucks

There are three transverse positions defined for which data exists. Figures A.3 through A.5 depict cross-sectional images of the transverse lane positioning. Transverse Position A centers the west wheel group of the east truck on Girder 7. Transverse Position B centers the east wheel group of the west truck on Girder 7. Transverse Position C centers the west wheel group of the east truck on Girder 8. Table A.2 lists the distances between the trucks and the east barrier rail for each of the three lanes.
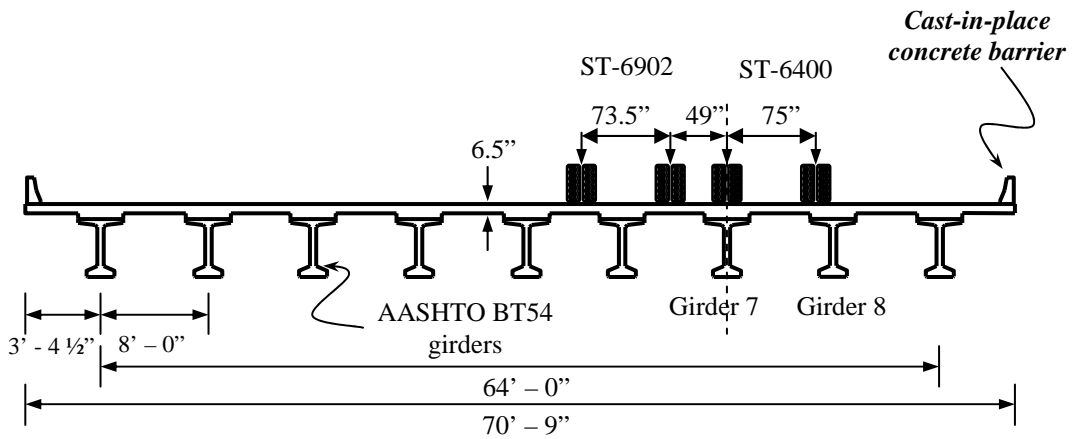
Figure A.3 Transverse Truck Position A
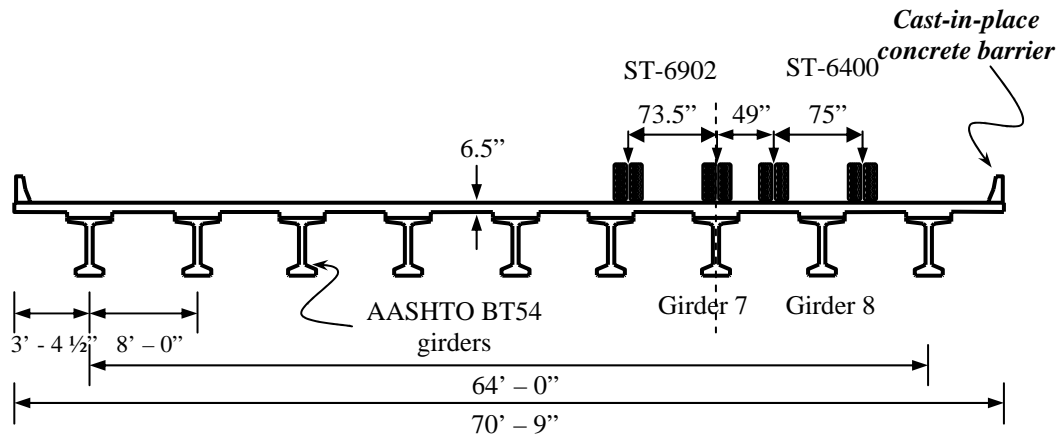
Figure A.4 Transverse Truck Position B
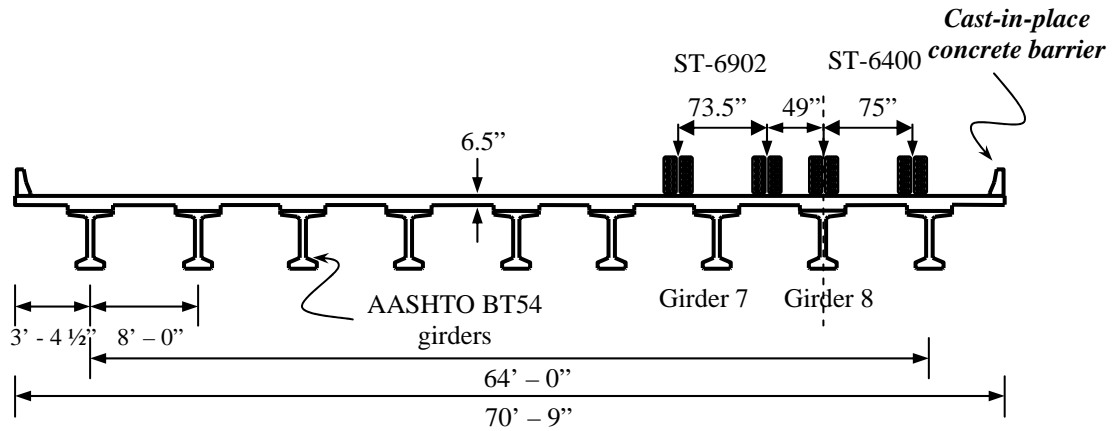
Figure A.5 Transverse Truck Position C

Table A.1 Locations of the Nine Longitudinal Stop Positions

Stop Position[a] No.	Position Description	Distance from Center of Continuity Diaphragm (in.)
1	Middle tire over the midspan of Span 10	-600
2	Front tire over Cross Section 1[b]	-291
3	Front tire over Cross Section 4	-151
4	Middle tire over Cross Section 1	-70
5	Rear tire over Cross Section 1	-12
6	Middle tire over Cross Section 4	70
7	Rear tire over Cross Section 4	128
8	Middle tire over the quarter-span of Span 11	300
9	Middle tire over the midspan of Span 11	600

[a] Trucks were stopped when the middle axles were located the specified distance from the center of continuity diaphragm

[b] The convention for the numbering of the cross sections is given in Section 4.3.4.1

164

Table A.2 Transverse Lane Positions

Lane	East Truck - Distance to East Barrier Rail (in.)	West Truck - Distance to East Barrier Rail (in.)
A	226.75	350.75
B	178.75	302.75
C	130.75	254.75

Note: Distances are measured from the outside edge of the west side of each truck

A.4 LOCATIONS FOR DEFLECTION MEASUREMENTS

Figure A.6 shows the six positions at which deflections were measured at the base of each of the two girders. There were two deflection measurements on each of the girders in Span 10 and four deflection measurements on each of the girders in Span 11.

A.5 LOCATIONS FOR STRAIN READINGS

Strain readings from the pre-repair load test are easily organized into groups according to the locations of the gauges. One group represents the bottom fiber gauges. These readings are best represented by looking at a profile view of the bridge section. Bottom fiber strains were taken at six places along each of the two girders. In Span 10, they were measured 75.25 in. from the center of the continuity diaphragm. In Span 11, they were measured 75.25 in., 104 in., 272 in., 440 in., and 608 in. from the center of the continuity diaphragm.

 The second group represents the strain along one of four cross-sectional profiles of each girder, the locations of which are shown in profile in Figure A.7. On each of the girders, two cross sections were instrumented with six gauges on the faces of the girders (Cross Sections 2 and 3), and two cross sections were instrumented with five gauges on

the faces of the girders (Cross Sections 1 and 4). Cross Sections 2 and 3 are located

4.75 in. from the face of the continuity diaphragm in each span. Cross sections 1 and 4

are located 67.25 in. from the face of the continuity diaphragm. The locations of the six

gauges (labeled A-F) are shown in Figure A.8. Cross Sections 1 and 4 do not have a

gauge B but do have bottom-fiber gauges.

A.6 LOCATIONS FOR CRACK OPENING DEVICES

There were four crack opening devices measuring the crack widths during the pre-repair

load tests. Two were on girder 7, and two were on girder 8. Each of the crack opening

devices was installed 13.5 in. from the girder base, and their locations are given in

Table A.3.

Table A.3 Crack Opening Device Locations

	Span 10		Span 11	
	Distance from Continuity Diaphragm (in.)	Face	Distance from Continuity Diaphragm (in.)	Face
Girder 7	49.5	East	47.75	East
Girder 8	40	West	56	East

Midspan Span 10 Span 11 Midspan

300" 300" 150" 150" 150" 150"

D-1 D-2 D-3 D-4 D-5 D-6

167

Bent 11
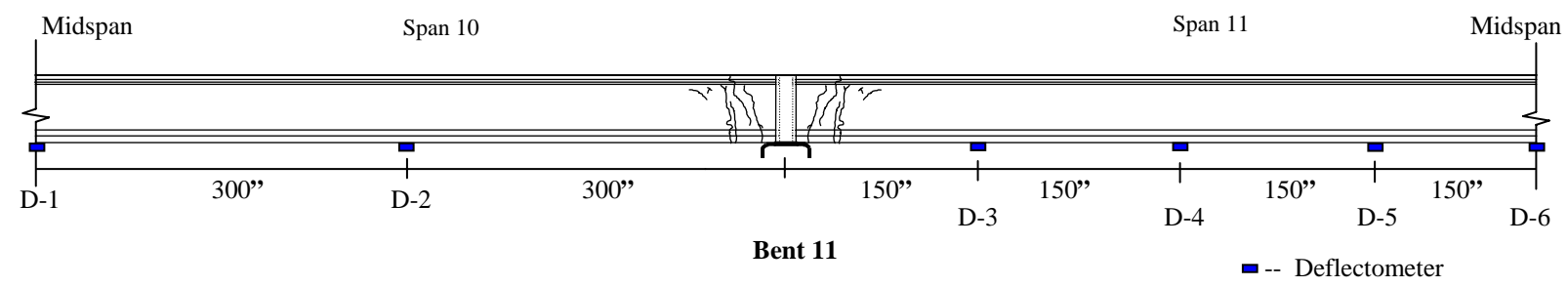
■ -- Deflectometer

Figure A.6 Installed Deflectometer Locations

16
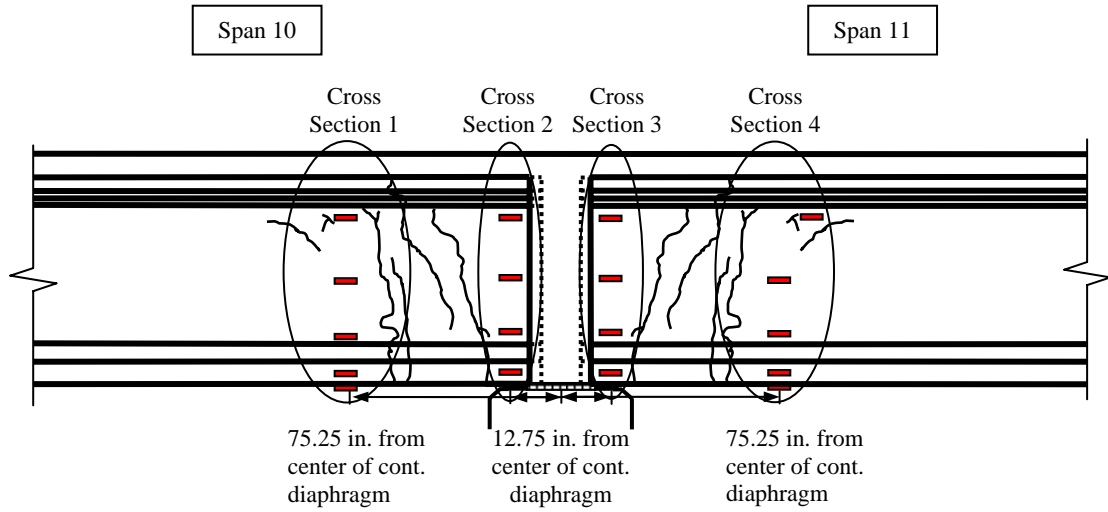
Figure A.7 Strain Profile Cross Section Locations
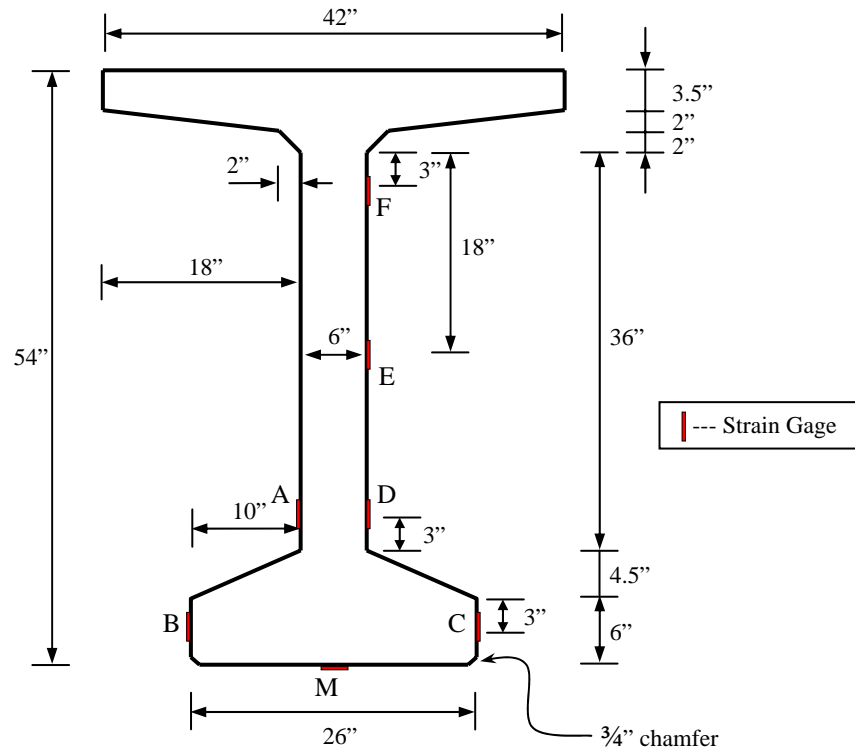
Figure A.8 Strain Gauge Locations

168

APPENDIX B: DEFLECTIONS

As explained in Appendix A, deflections were measured in six places along the bottom of each of the two girders, as depicted in Figure A.6. There were two deflection measurements on each of the girders in Span 10 and four deflection measurements on each of the girders in Span 11.

Figures B.1 through B.4 show the comparison between the experimental deflections and the analytical deflections for each of the *Uncracked*, *Cracked*, and *Cracked-with-Reinforcement* models. The deflection results of the *Pre-Repair* model are compared with those of the *Post-Repair* model in Figures B.5 through B.8.
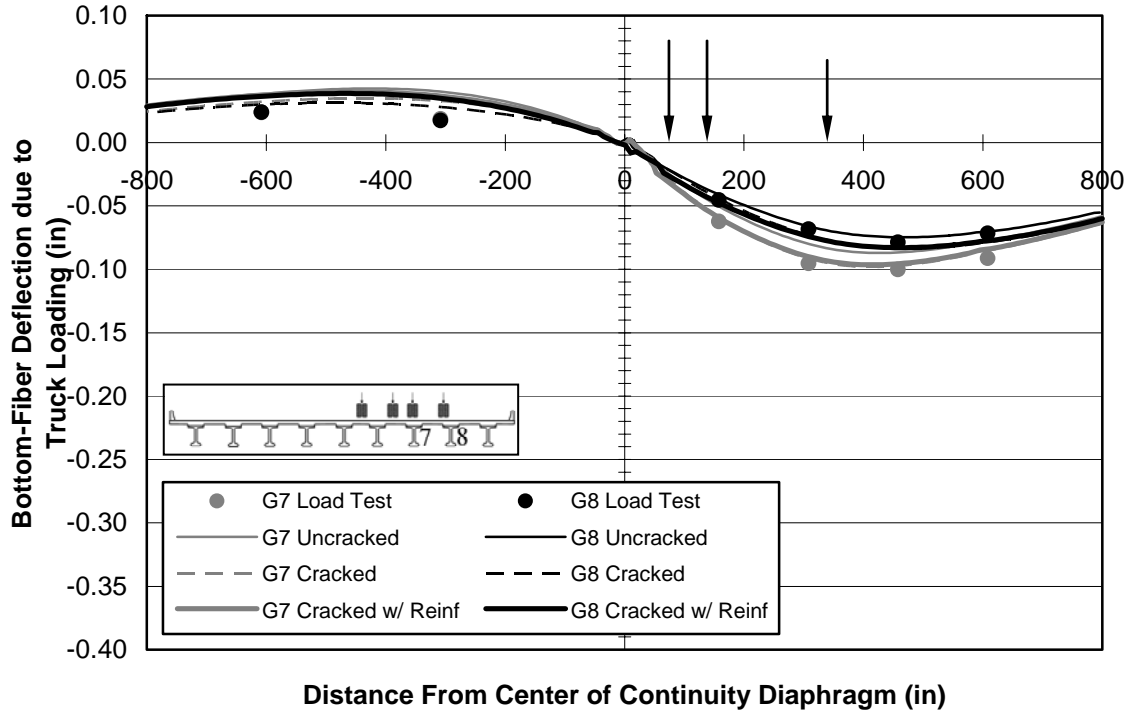
Figure B.1 Bottom-Fiber Deflections for the Model Refinement—A7 Load Position
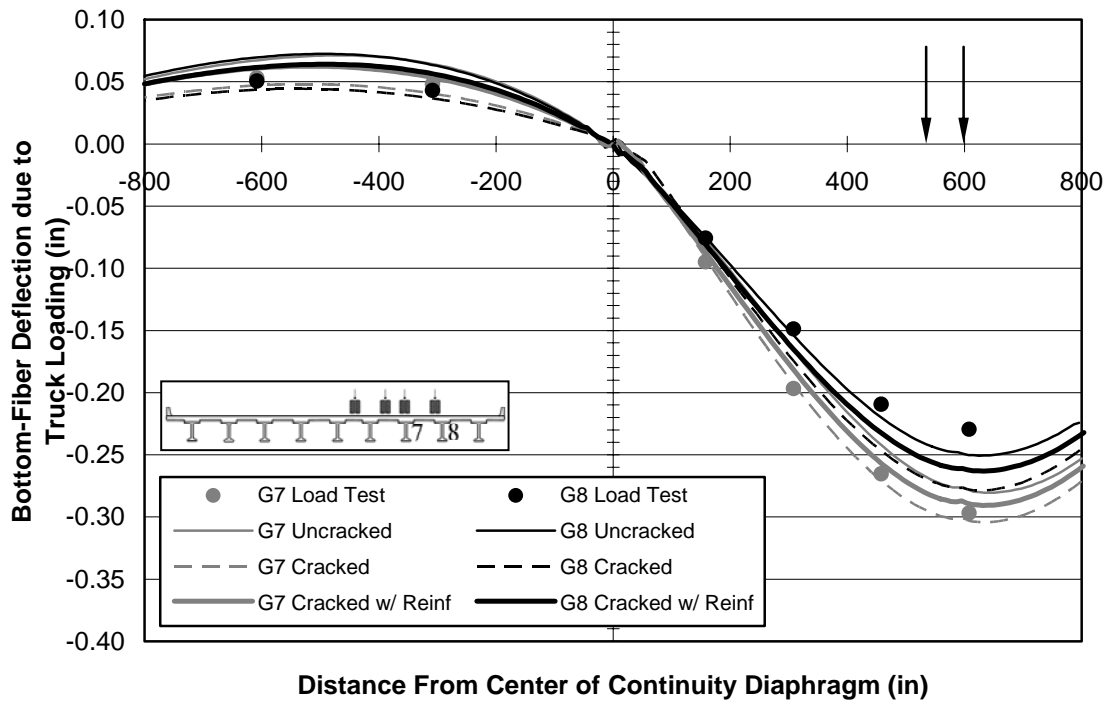
Figure B.2 Bottom-Fiber Deflections for the Model Refinement—A9 Load Position

170
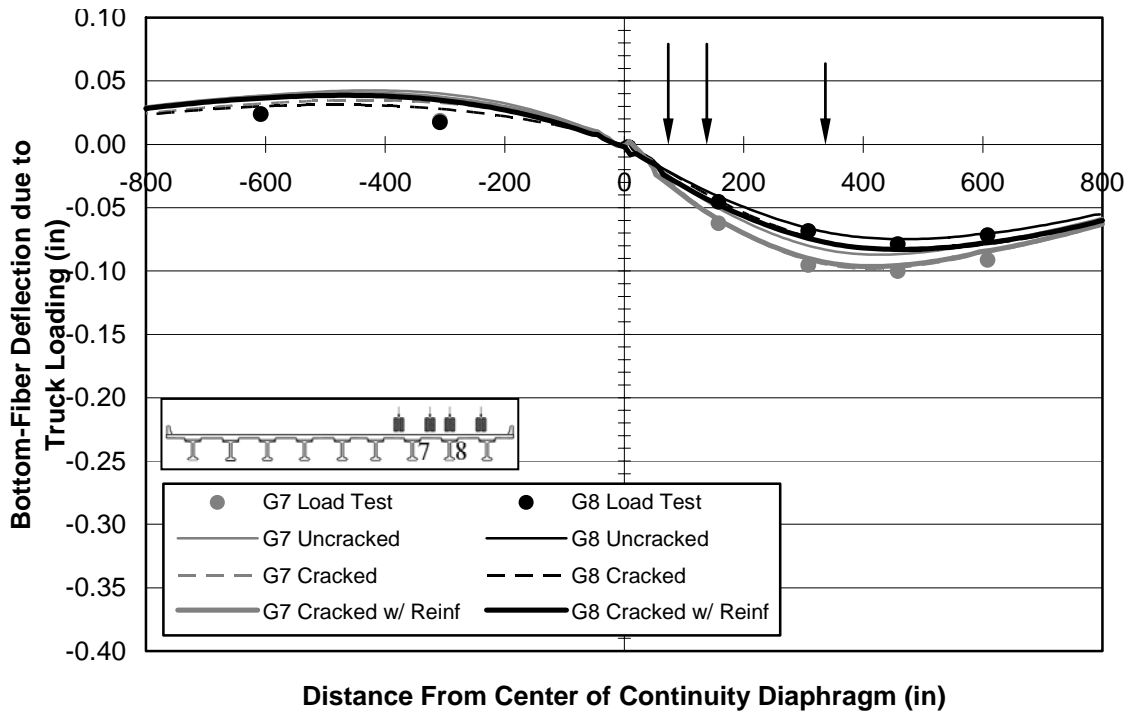
Figure B.3 Bottom-Fiber Deflections for the Model Refinement —C7 Load Position
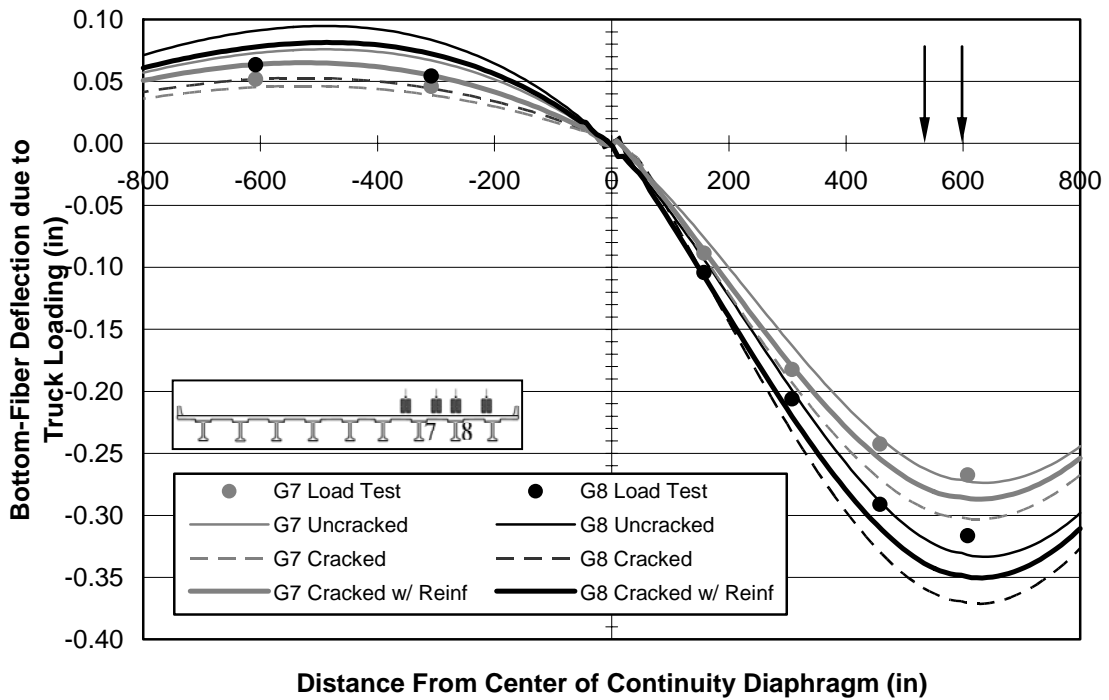
Figure B.4 Bottom-Fiber Deflections for the Model Refinement—C9 Load Position

171
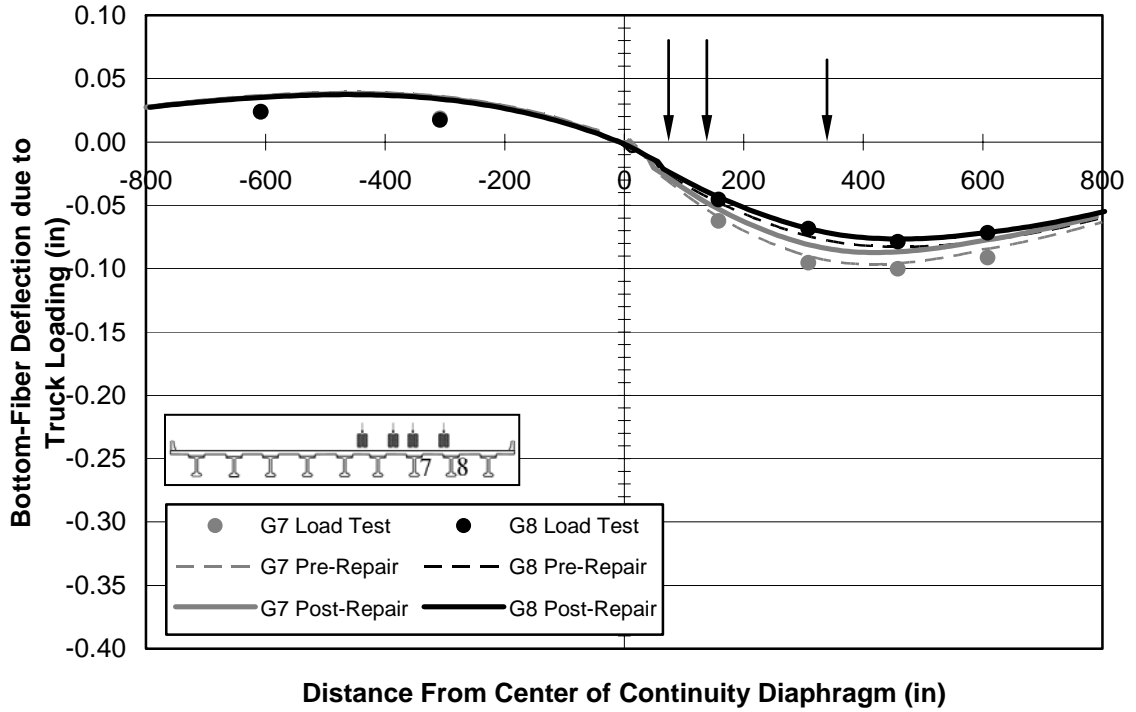
Figure B.5 Bottom-Fiber Deflections for the Pre- v. Post-Repair Models—A7 Load Position
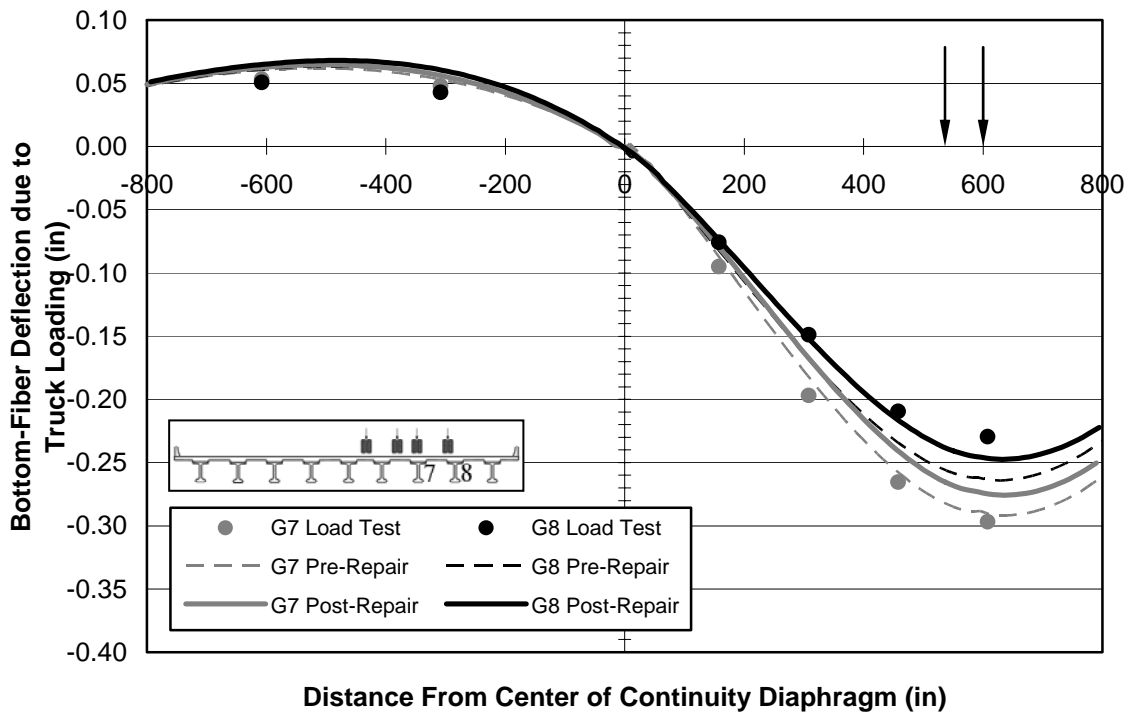
Figure B.6 Bottom-Fiber Deflections for the Pre- v. Post-Repair Models—A9 Load Position

172
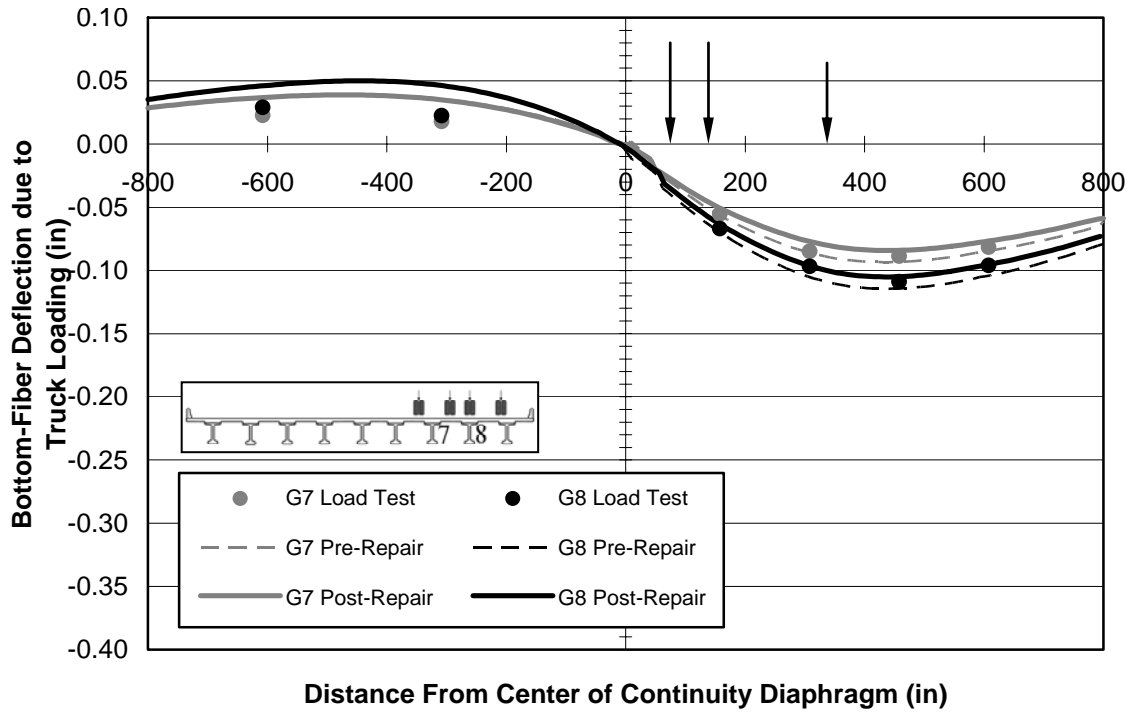
Figure B.7 Bottom-Fiber Deflections for the Pre- v. Post-Repair Models—C7 Load Position
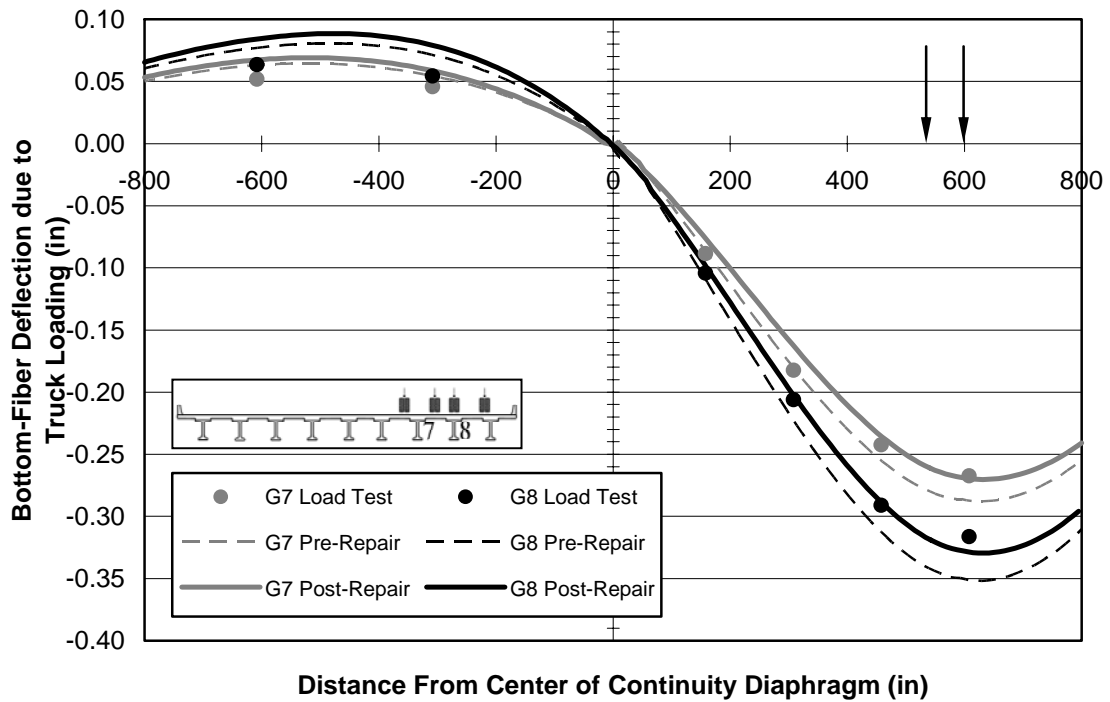
Figure B.8 Bottom-Fiber Deflections for the Pre- v. Post-Repair Models—C9 Load Position

173

APPENDIX C: BOTTOM-FIBER STRAINS

As explained in Appendix A, bottom-fiber concrete surface strain readings were taken at six locations along each of the two instrumented girders. On Span 10, they were measured 75.25 in. from the center of the continuity diaphragm. On Span 11, they were measured 75.25 in., 104 in., 272 in., 440 in., and 608 in. from the center of the continuity diaphragm.

Figures C.1 through C.4 depict the comparison between the bottom-fiber strains of the *Uncracked*, *Cracked*, and *Cracked-with-Reinforcement* models, as well as the load test results, at each of four load positions. The results from the *Pre-Repair* and *Post-Repair* models are presented in Figures C.5 through C.8.
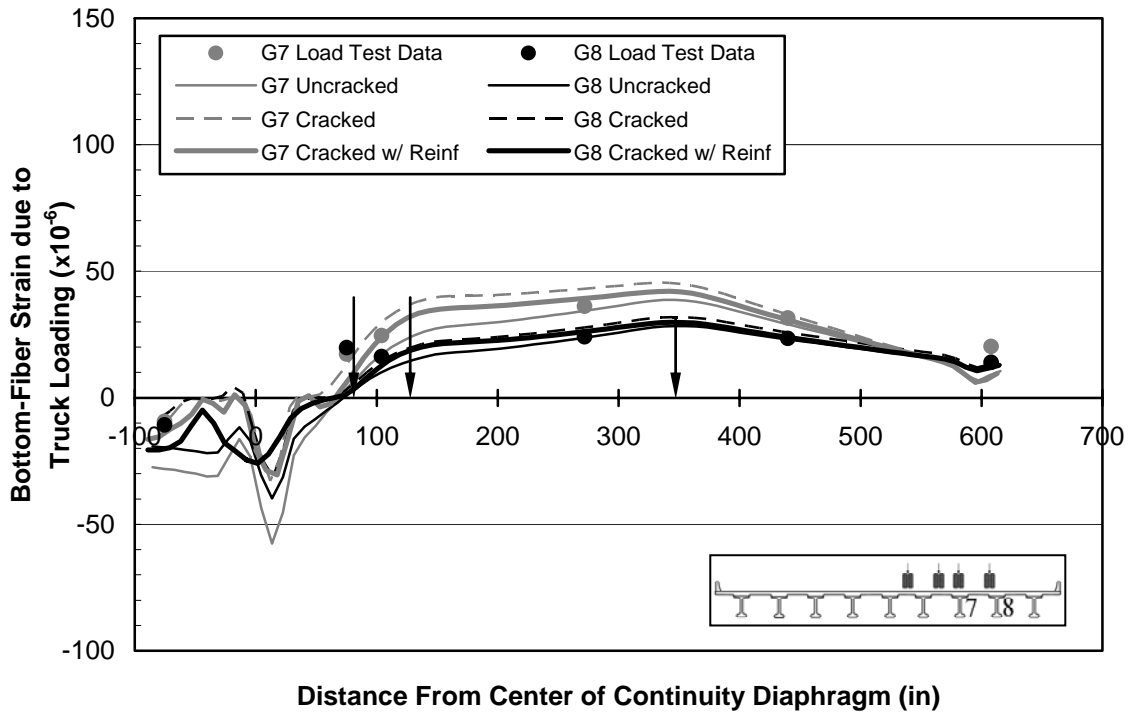
Figure C.1 Bottom-Fiber Strain Data for the Model Refinement—A7 Load Position

Distance From Center of Continuity Diaphragm (in)
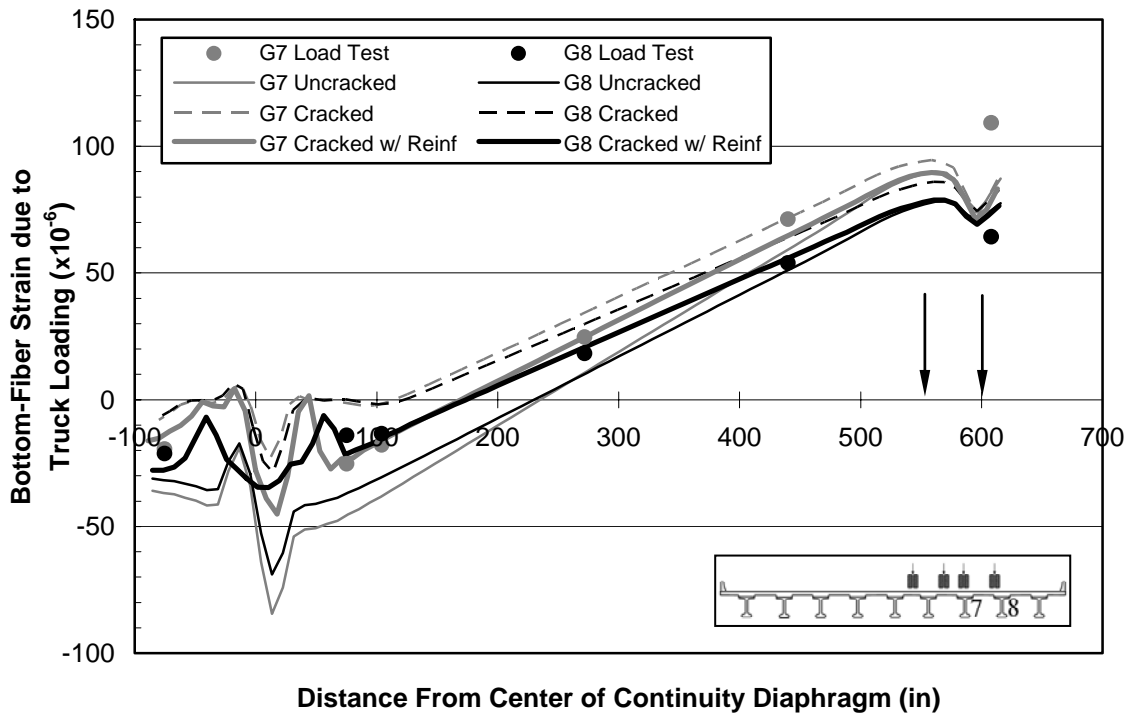
Figure C.2 Bottom-Fiber Strain Data for the Model Refinement—A9 Load Position

175
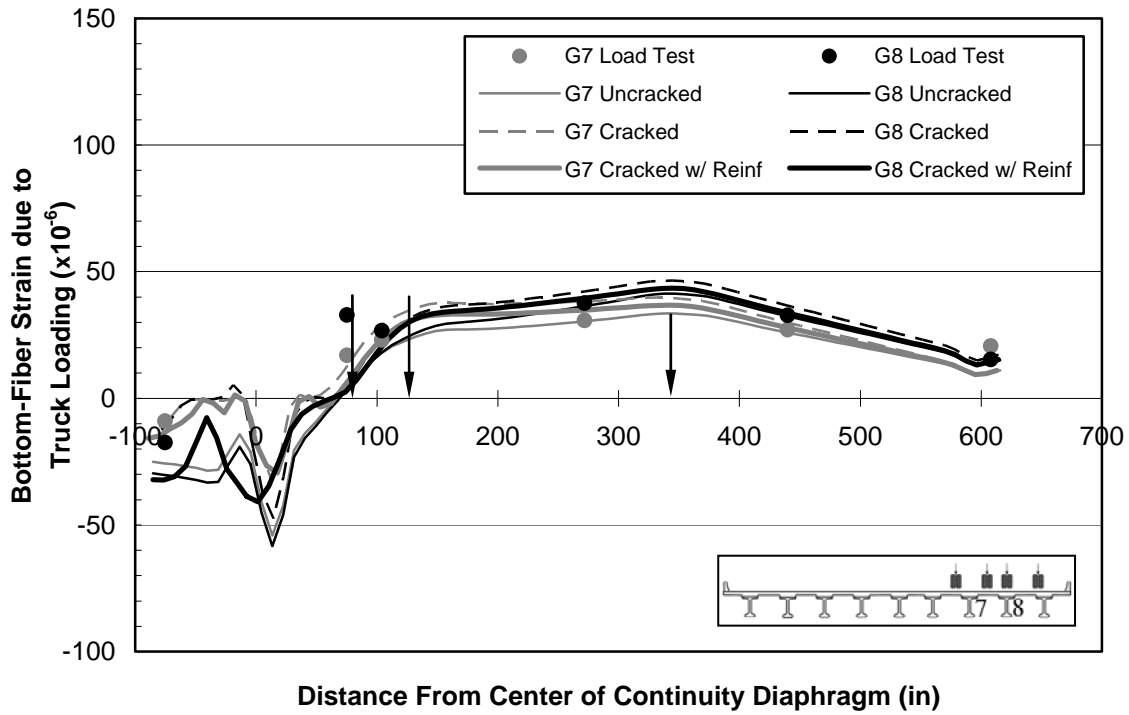
Figure C.3 Bottom-Fiber Strain Data for the Model Refinement—C7 Load Position
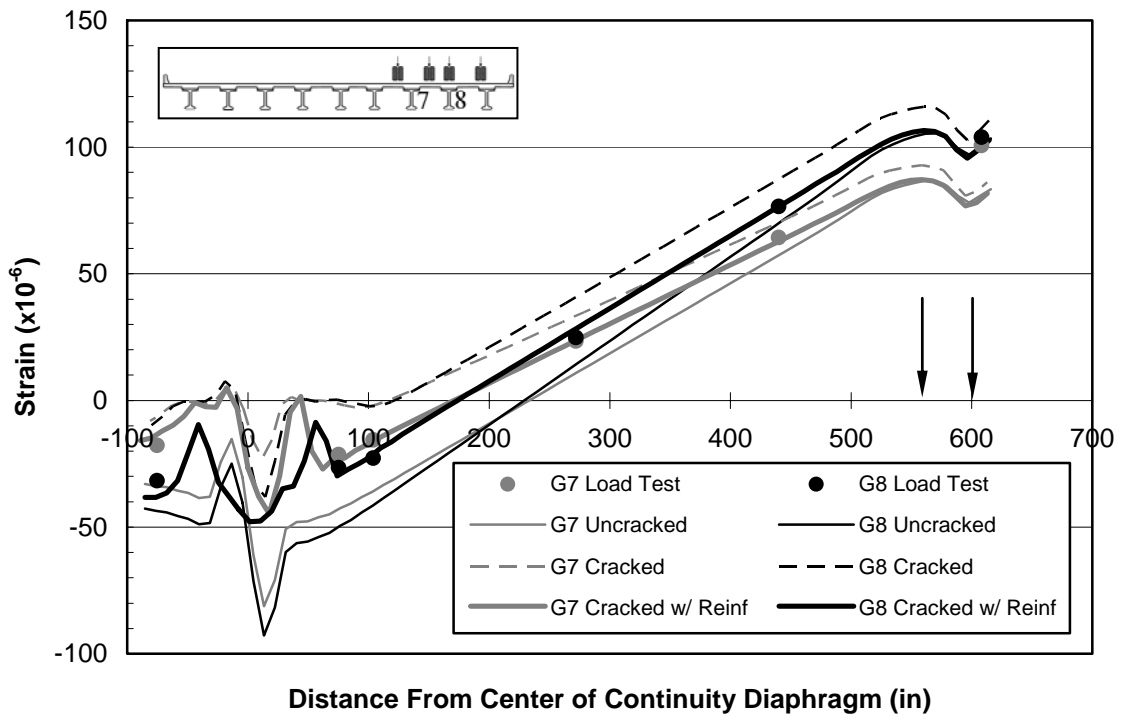
Figure C.4 Bottom-Fiber Strain Data for the Model Refinement—C9 Load Position

176
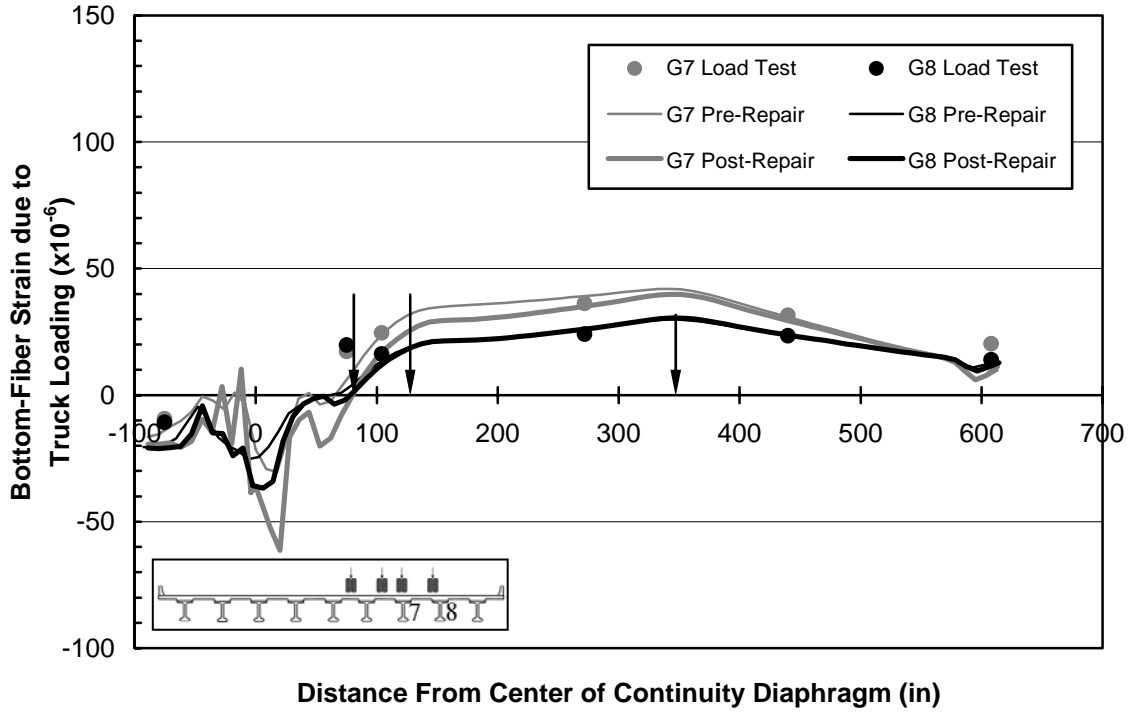
Figure C.5 Bottom-Fiber Strain Data for the Pre- v. Post-Repair Models—A7 Load Position
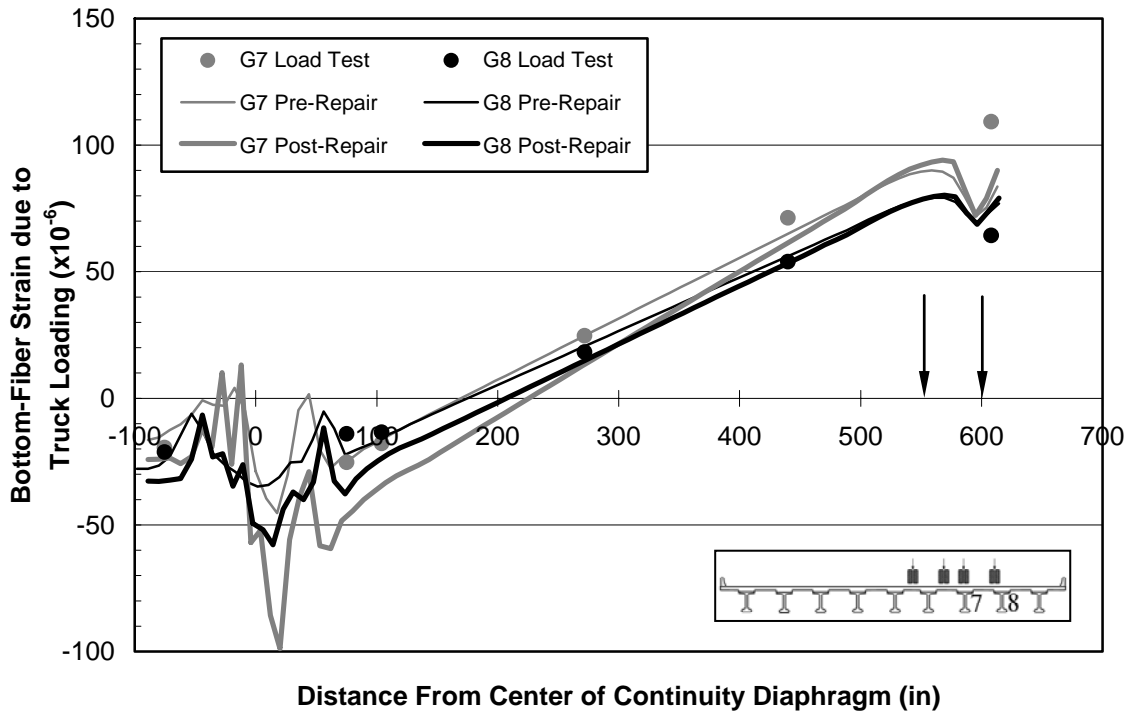
Figure C.6 Bottom-Fiber Strain Data for the Pre- v. Post-Repair Models—A9 Load Position

177
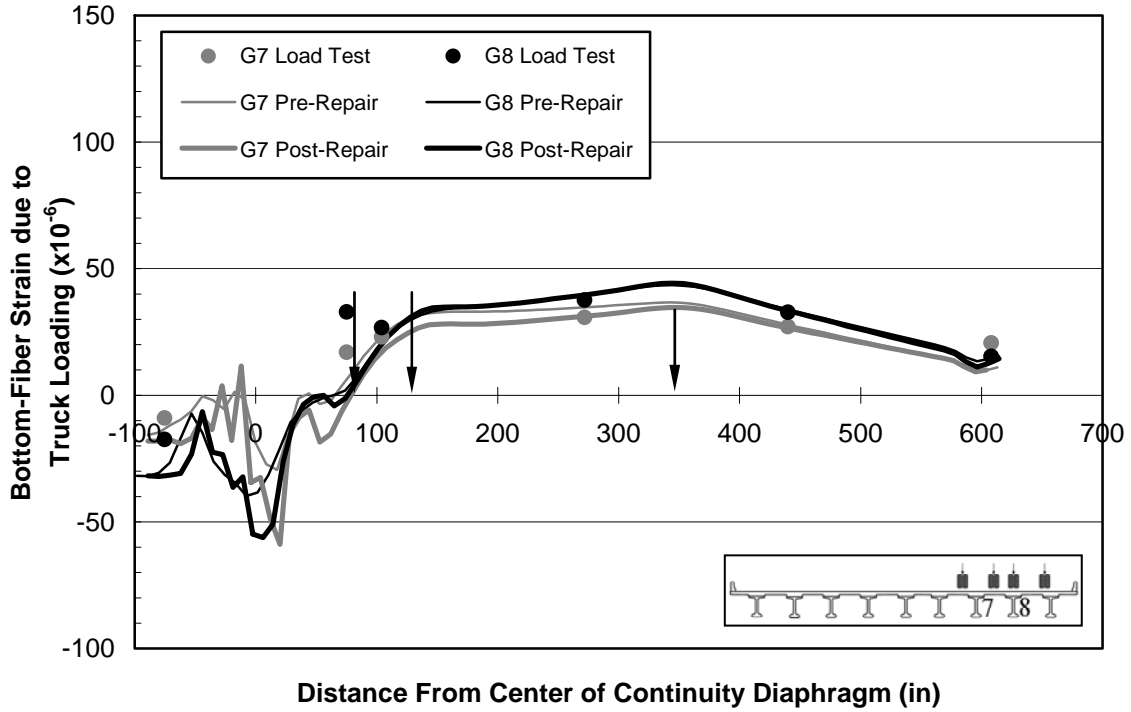
Figure C.7 Bottom-Fiber Strain Data for the Pre- v. Post-Repair Models—C7 Load Position
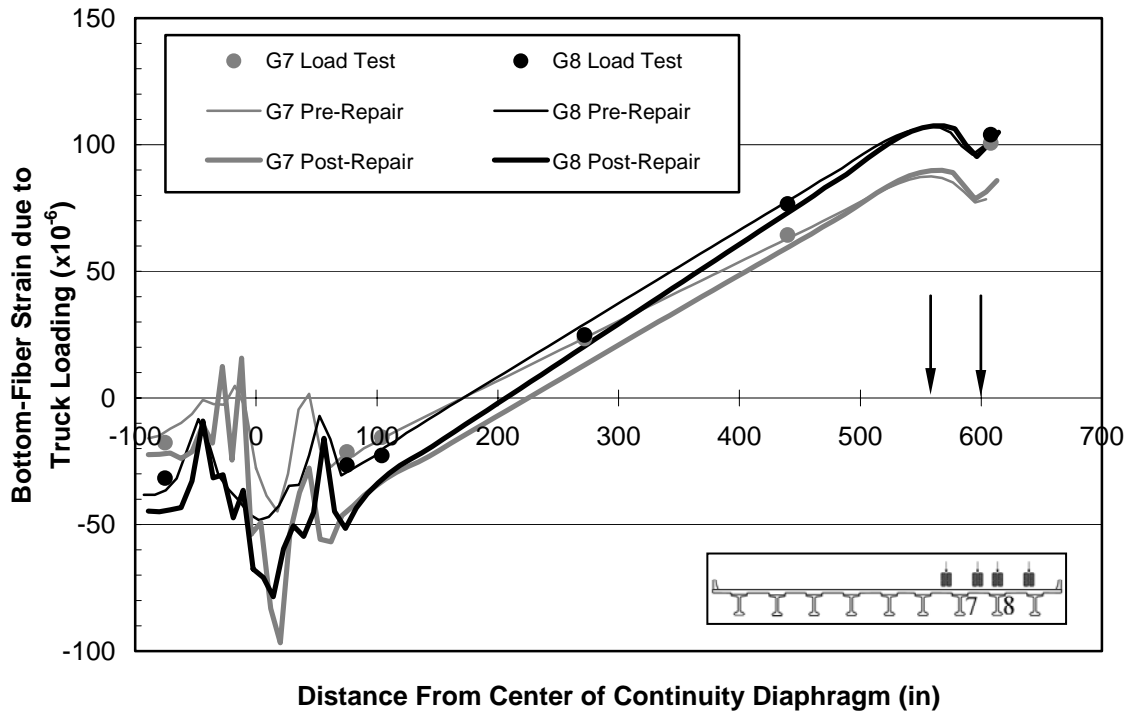
Figure C.8 Bottom-Fiber Strain Data for the Pre- v. Post-Repair Models—C9 Load Position

178

APPENDIX D: A7 LOAD POSITION STRAIN PROFILES

Strains were measured along the faces of specific, instrumented cross sections of the two girders, as explained in Appendix A. The A7 Load Position and the locations of the instrumented cross sections are illustrated in Figure D.1. Figures D.2–D.17 graphically compare the experimental strains along these cross sections to the analytical results from both the *Pre-Repair* and *Post-Repair* models. In addition, the strains at the corresponding locations on the FRP are presented.
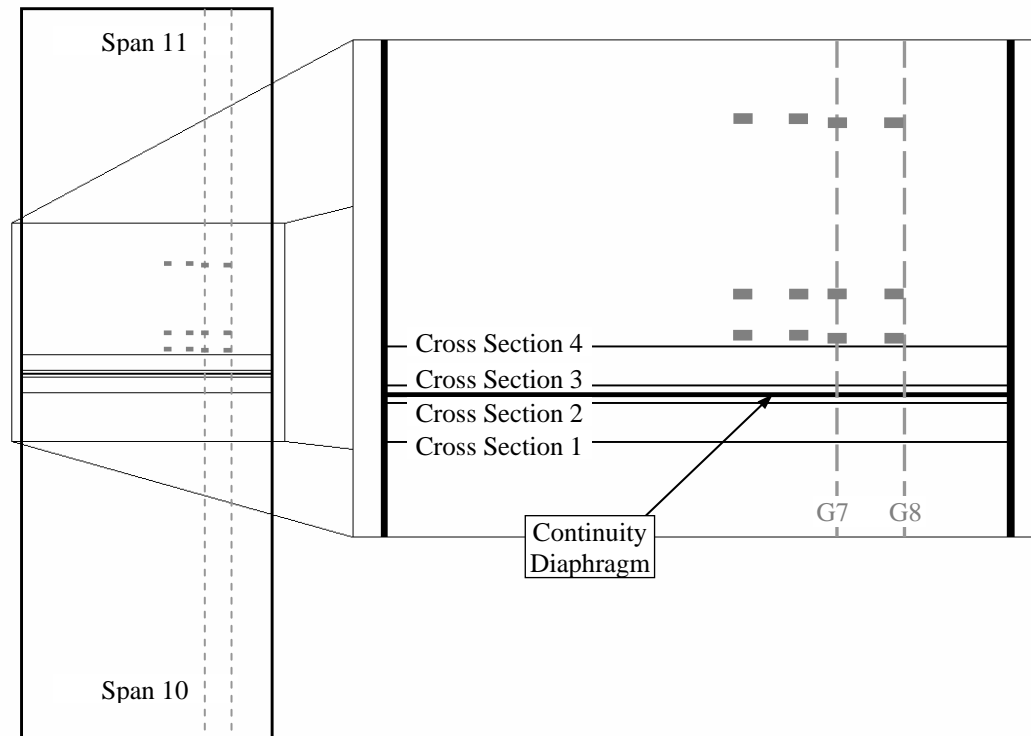
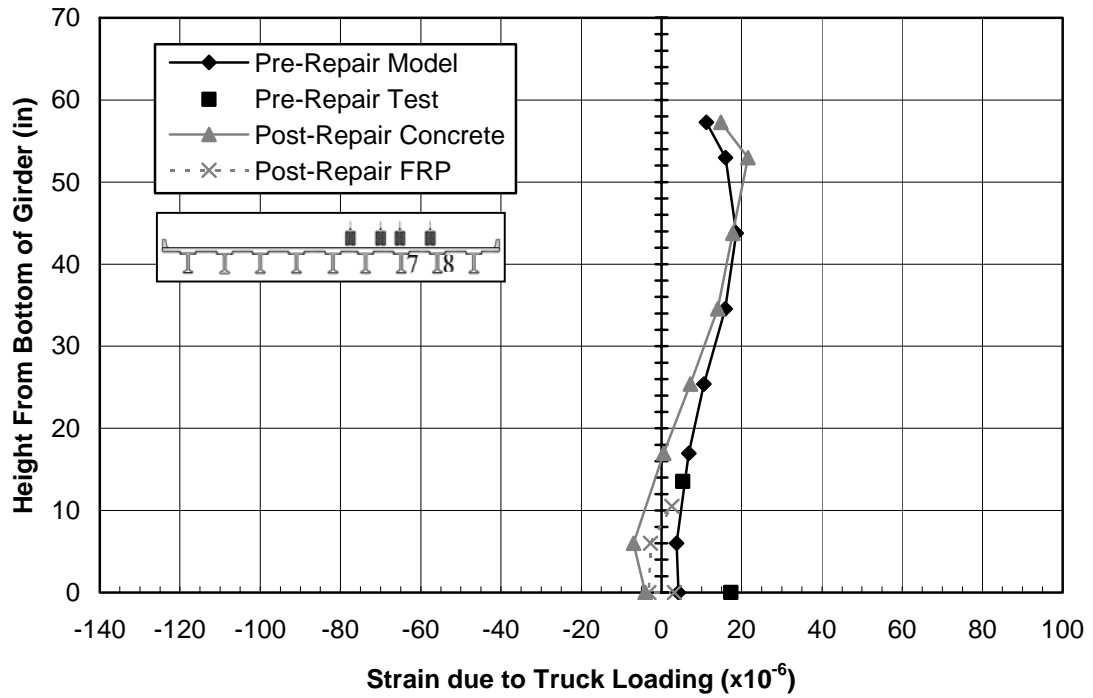**Figure D.1 Strain Profile Cross Section Locations for Load Position A7**
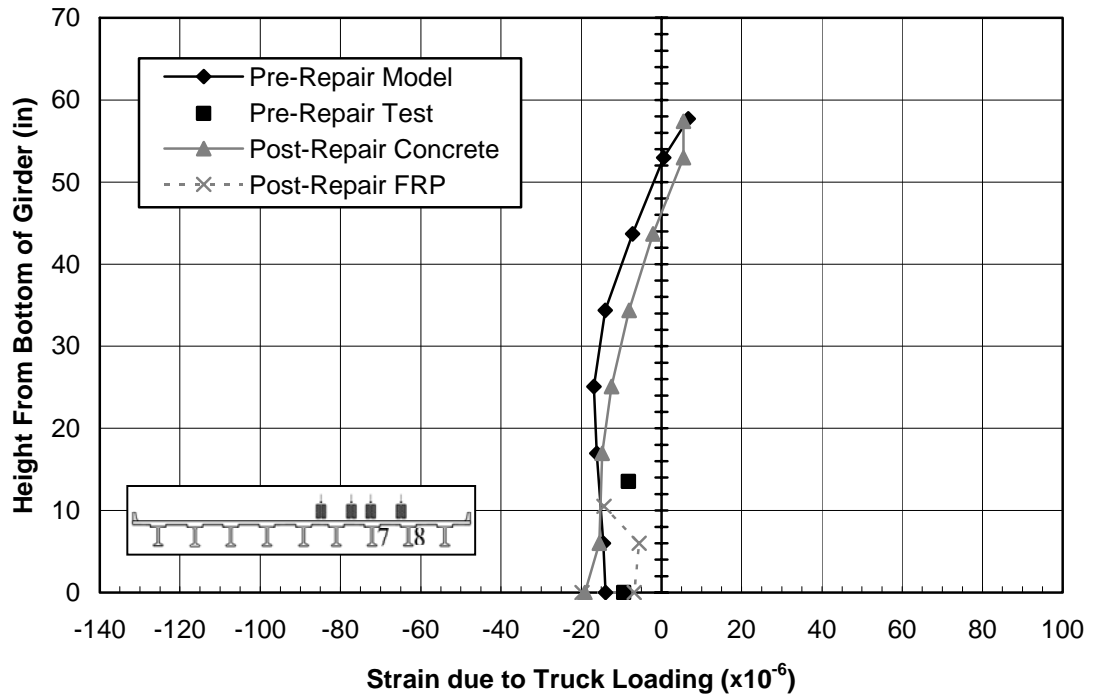
Figure D.2 Strain Profile—Load Position A7, Section 1, Girder 7, West Face
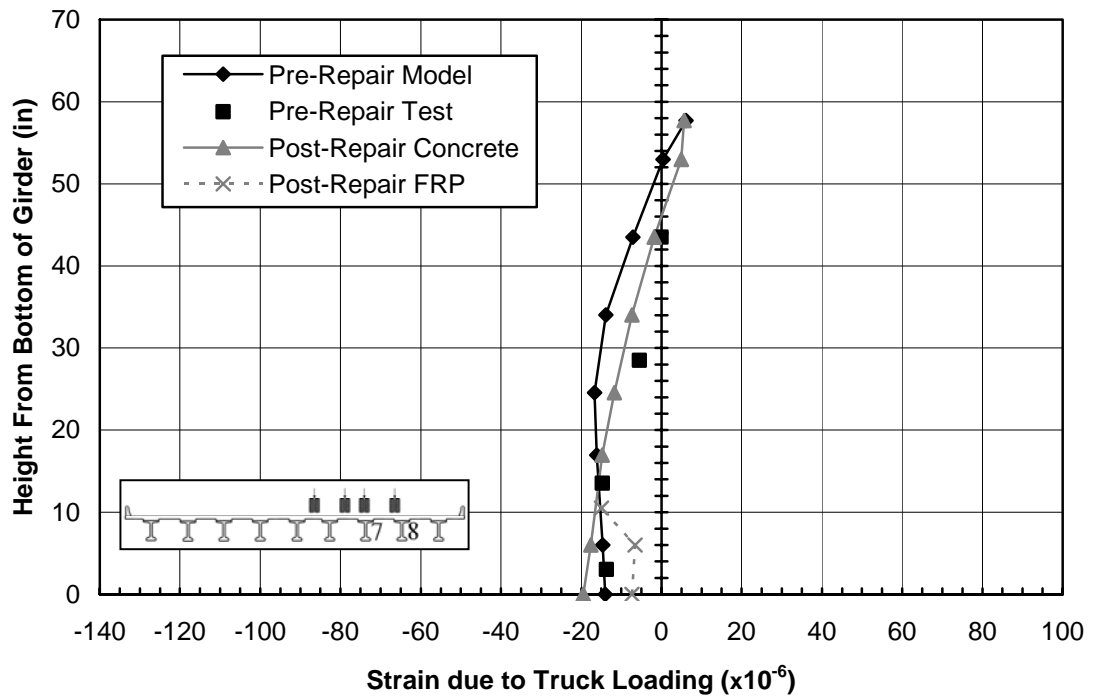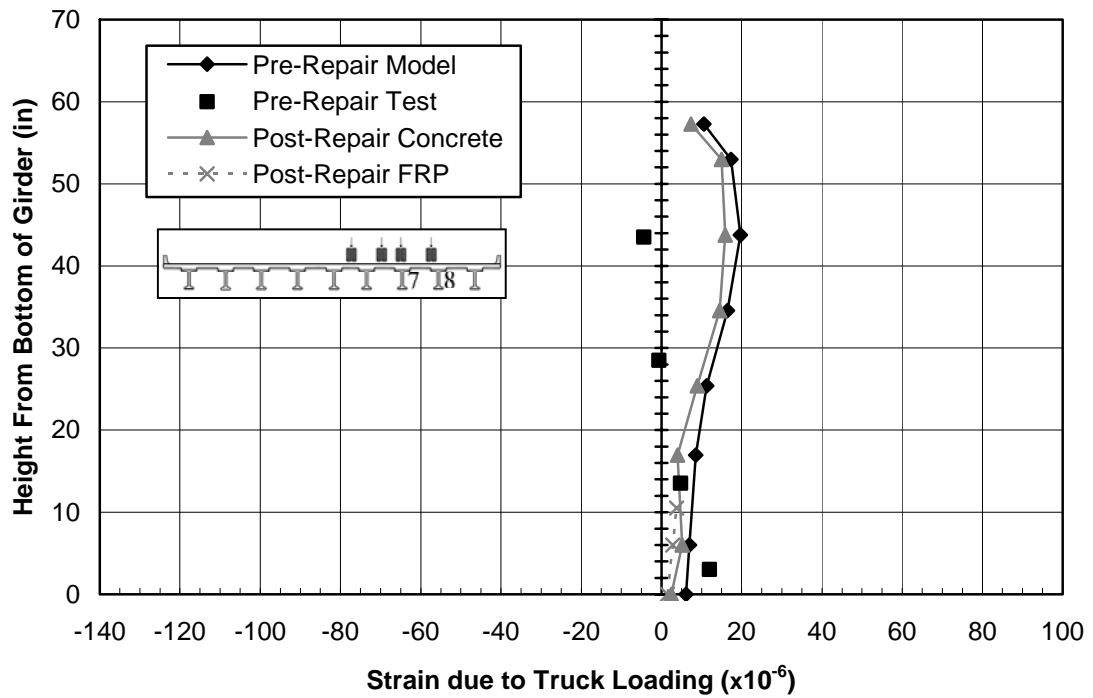

Figure D.3 Strain Profile—Load Position A7, Section 1, Girder 7, East Face
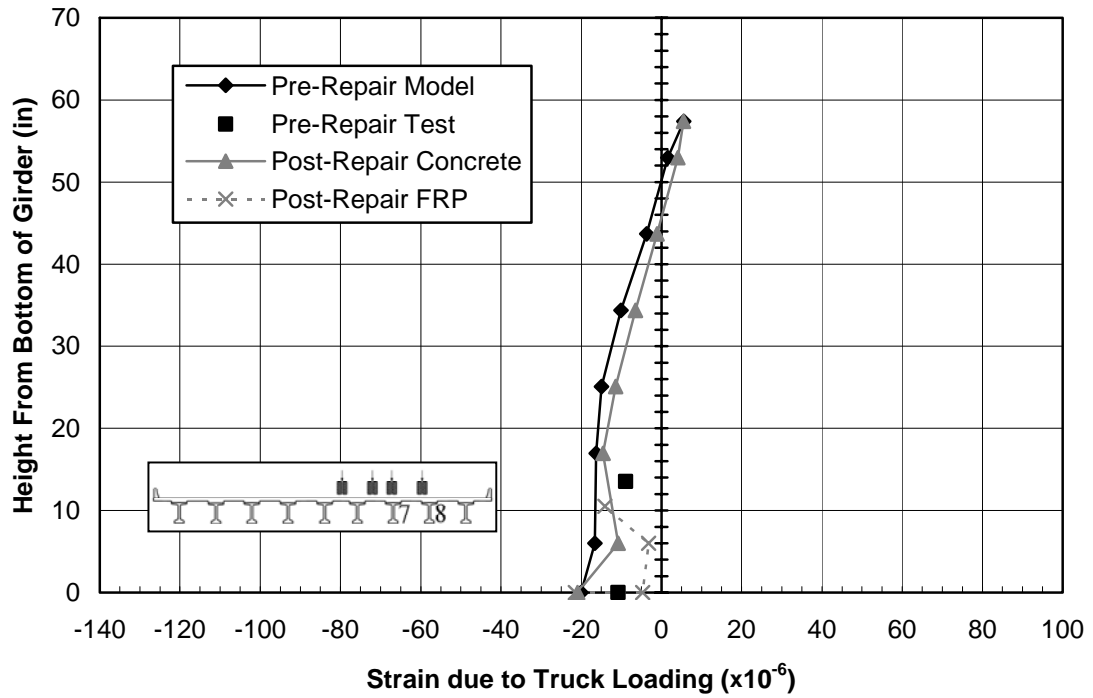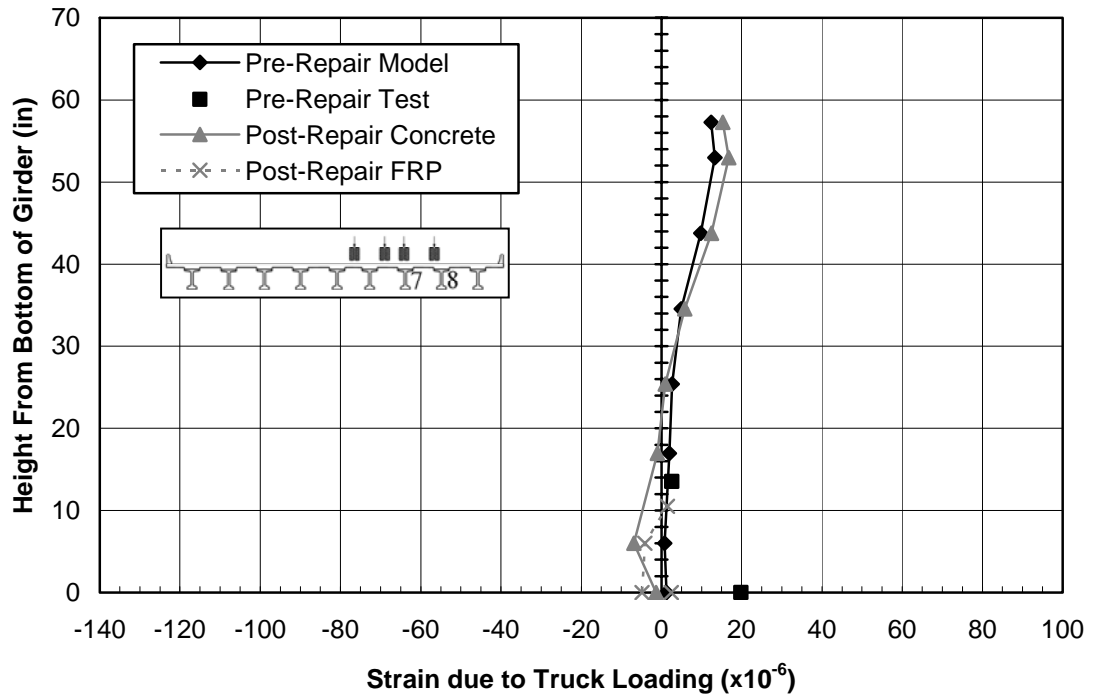
Figure D.4 Strain Profile—Load Position A7, Section 1, Girder 8, West Face
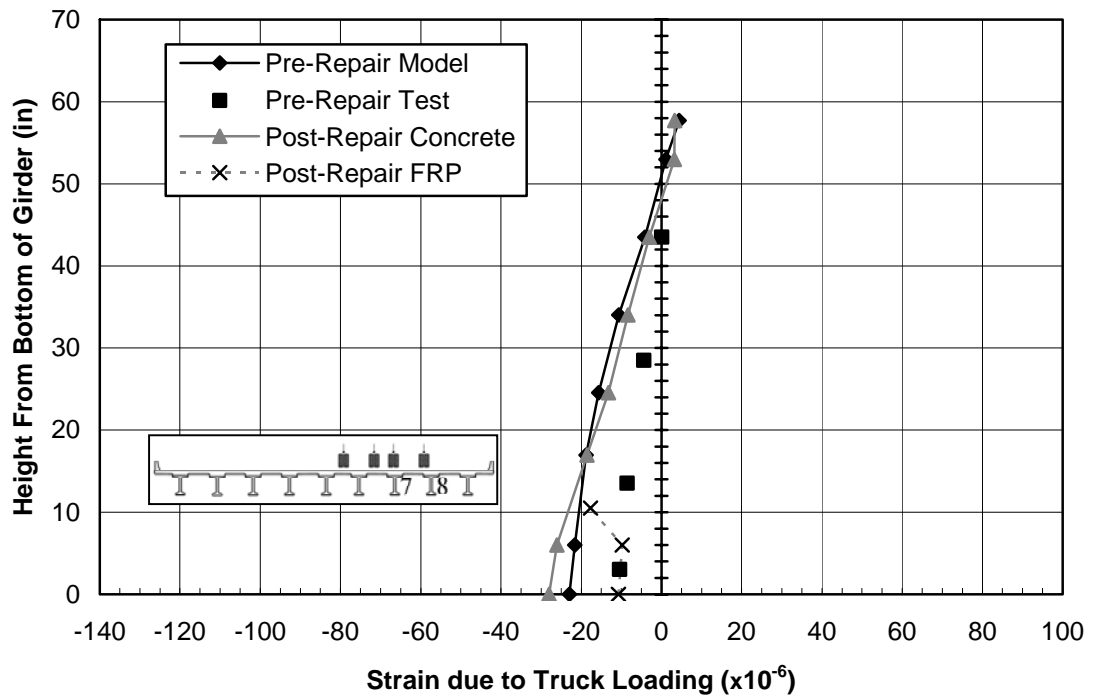
Figure D.5 Strain Profile—Load Position A7, Section 1, Girder 8, East Face

181
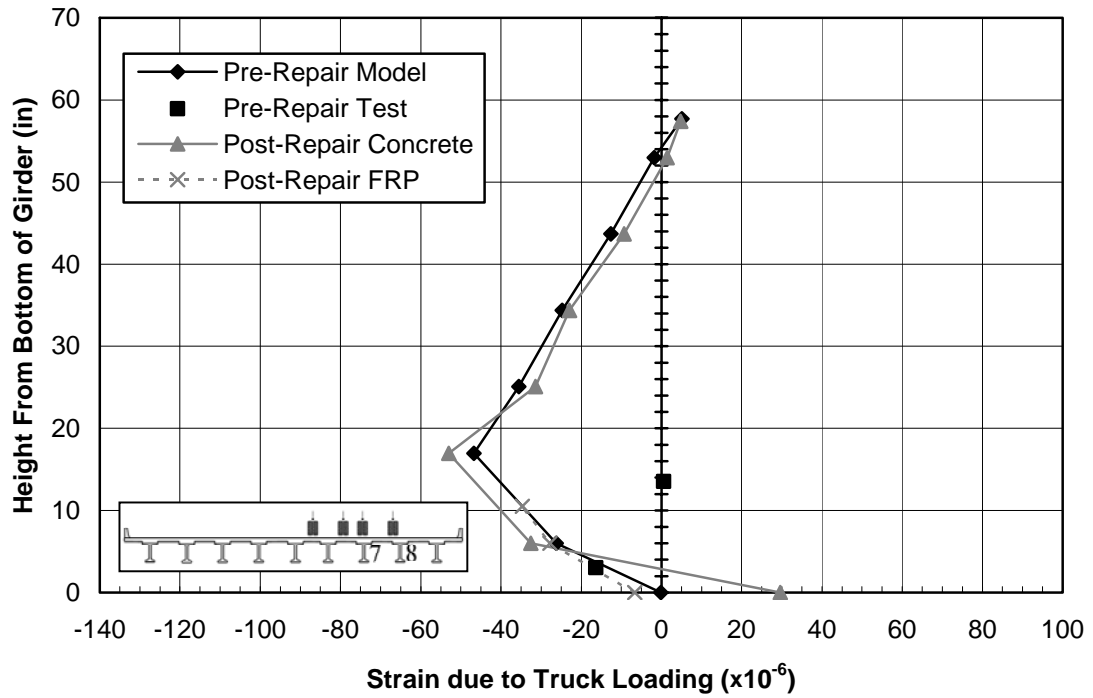
Figure D.6 Strain Profile—Load Position A7, Section 2, Girder 7, West Face
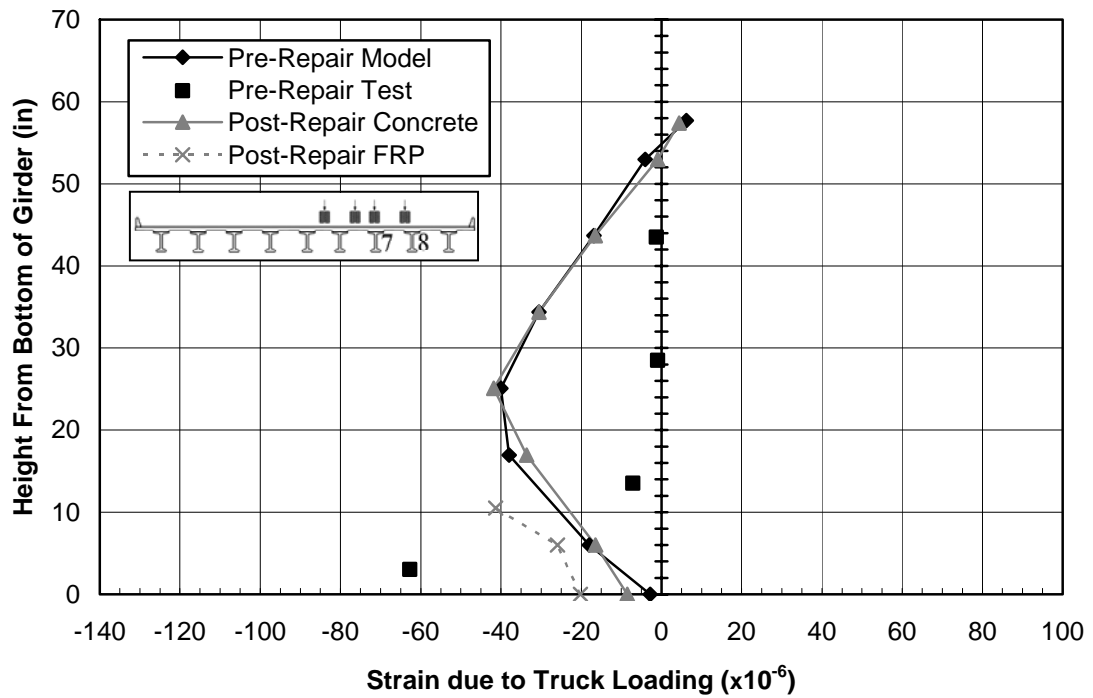
Figure D.7 Strain Profile—Load Position A7, Section 2, Girder 7, East Face
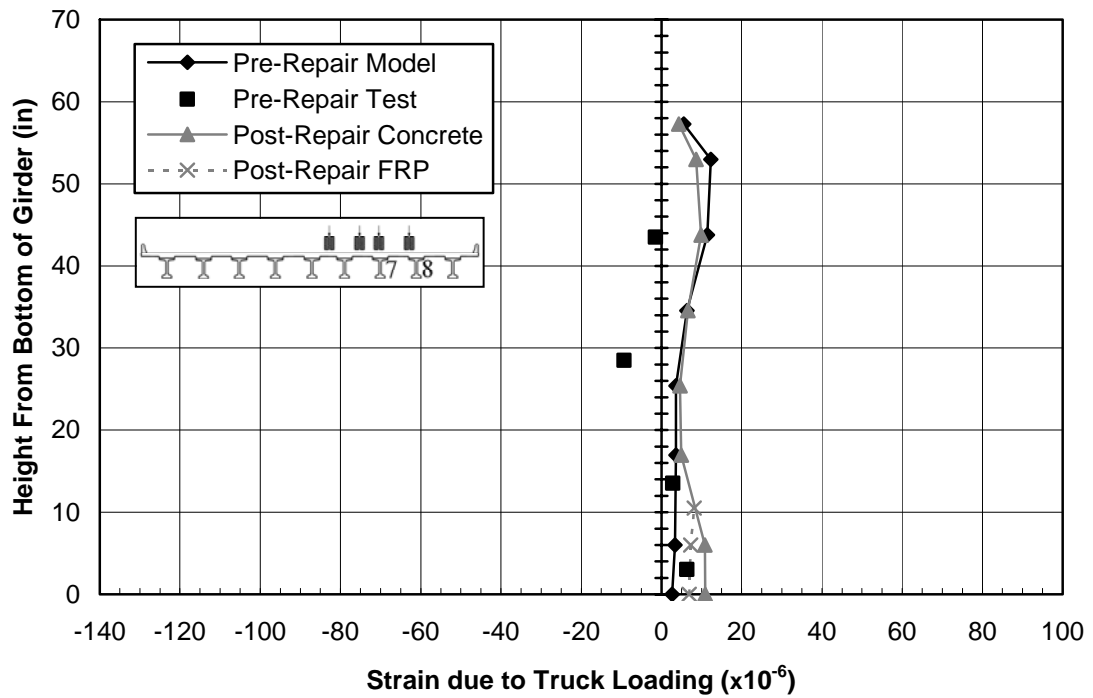
182
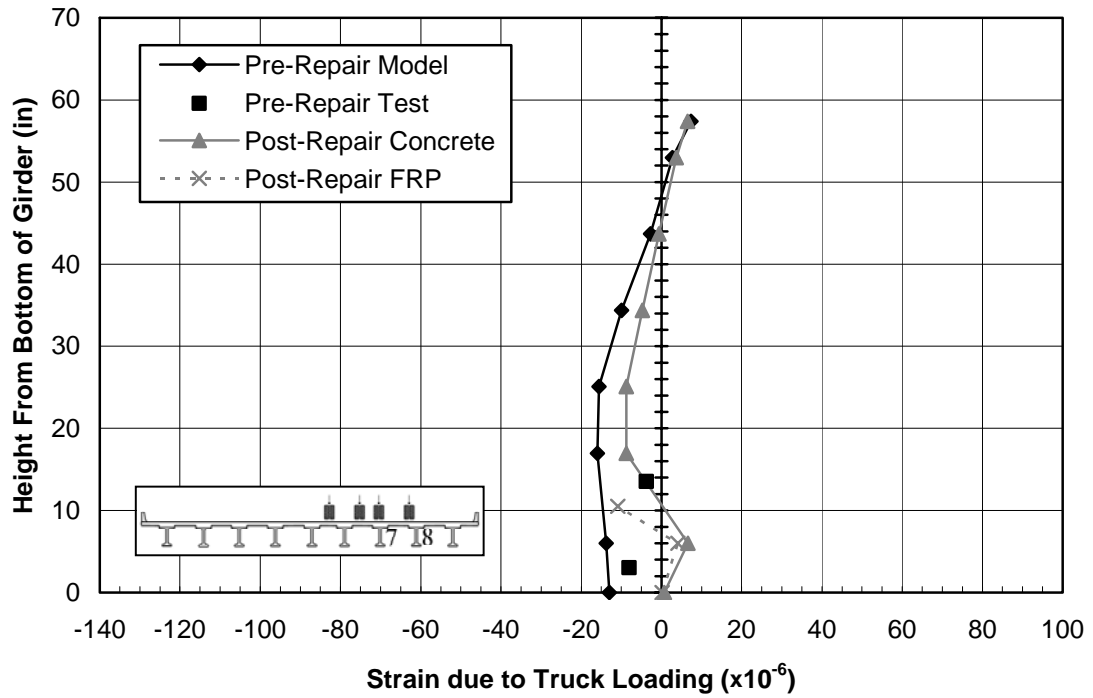
Figure D.8 Strain Profile—Load Position A7, Section 2, Girder 8, West Face
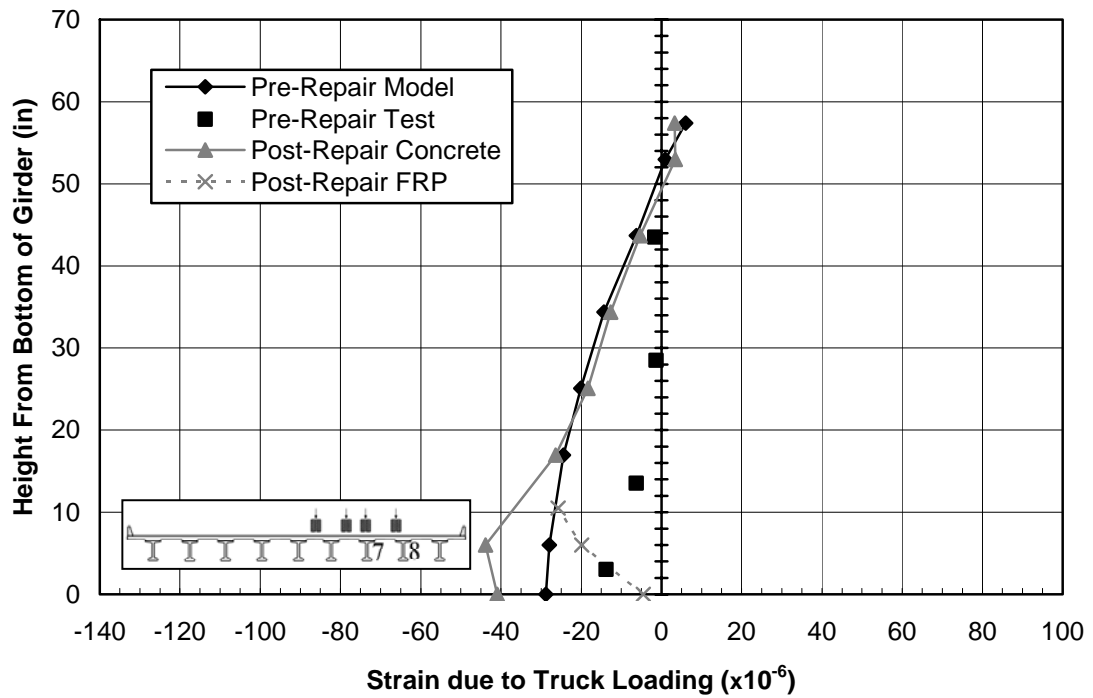
Figure D.9 Strain Profile—Load Position A7, Section 2, Girder 8, East Face
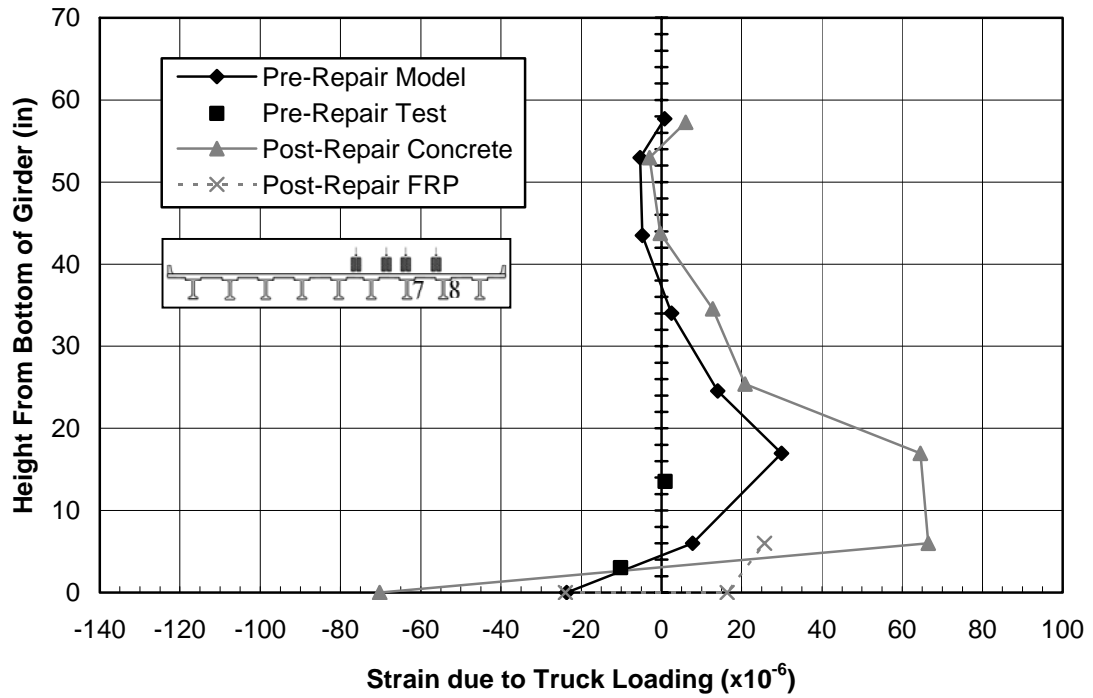
Figure D.10 Strain Profile—Load Position A7, Section 3, Girder 7, West Face
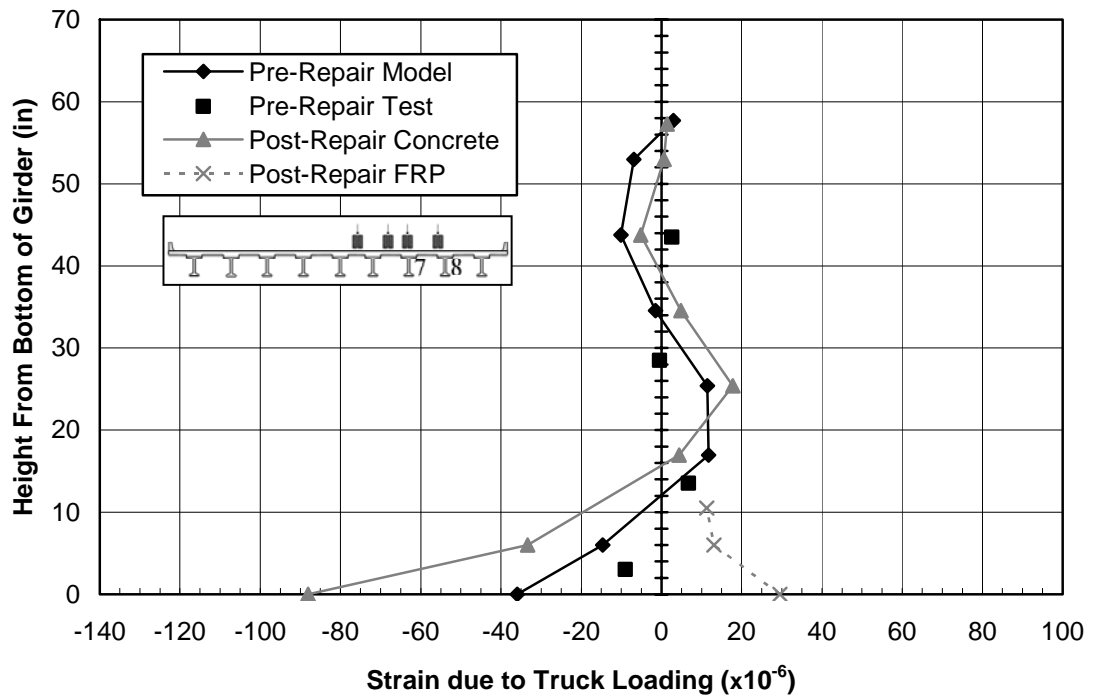
Figure D.11 Strain Profile—Load Position A7, Section 3, Girder 7, East Face

184
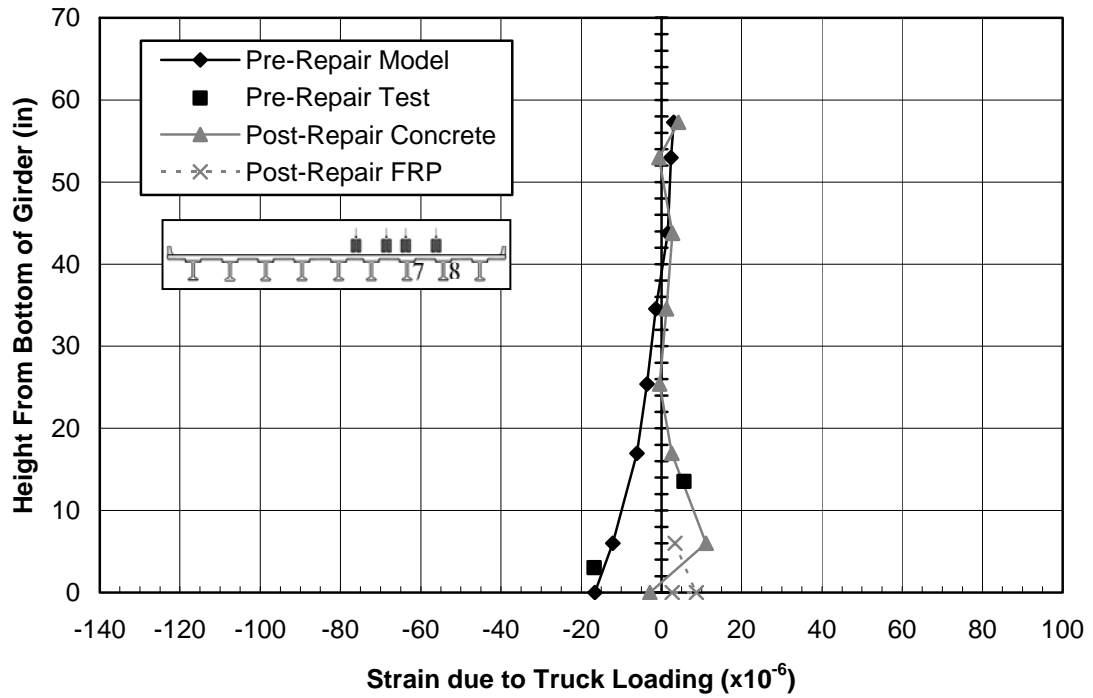
Figure D.12 Strain Profile—Load Position A7, Section 3, Girder 8, West Face
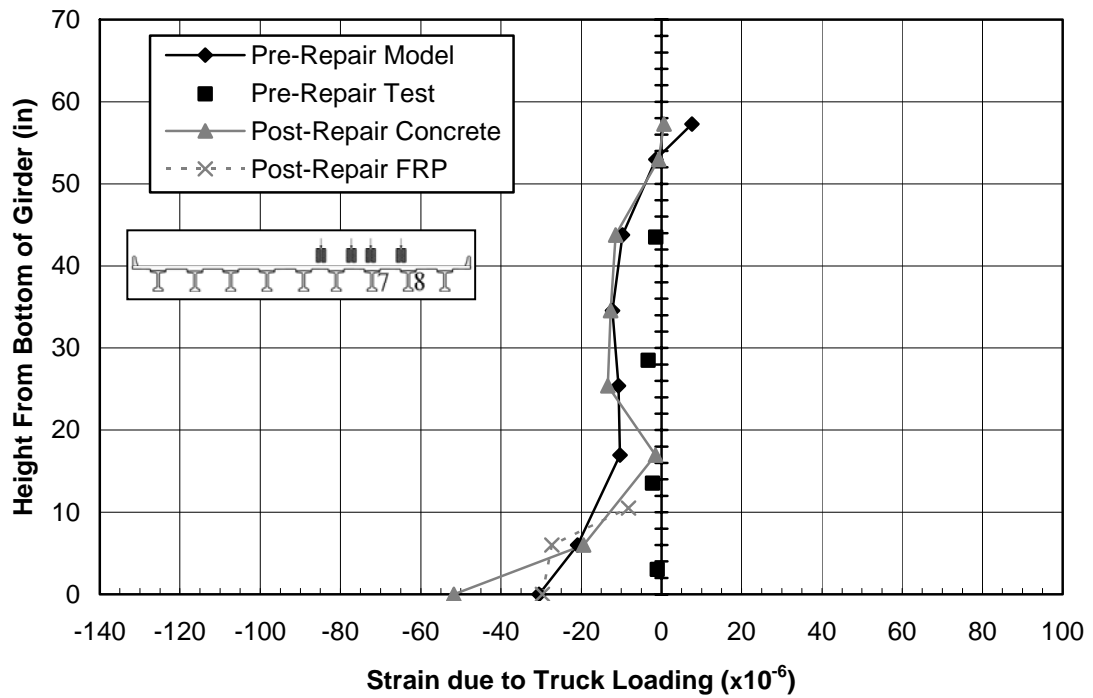
Figure D.13 Strain Profile—Load Position A7, Section 3, Girder 8, East Face

Figure D.14 Strain Profile—Load Position A7, Section 4, Girder 7, West Face

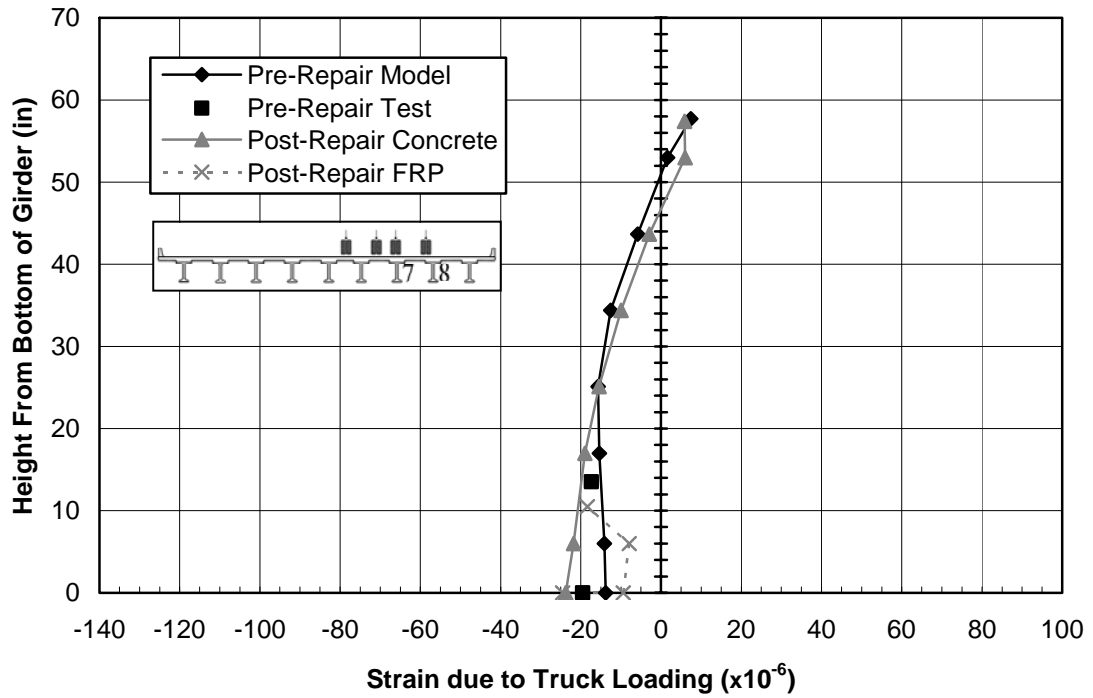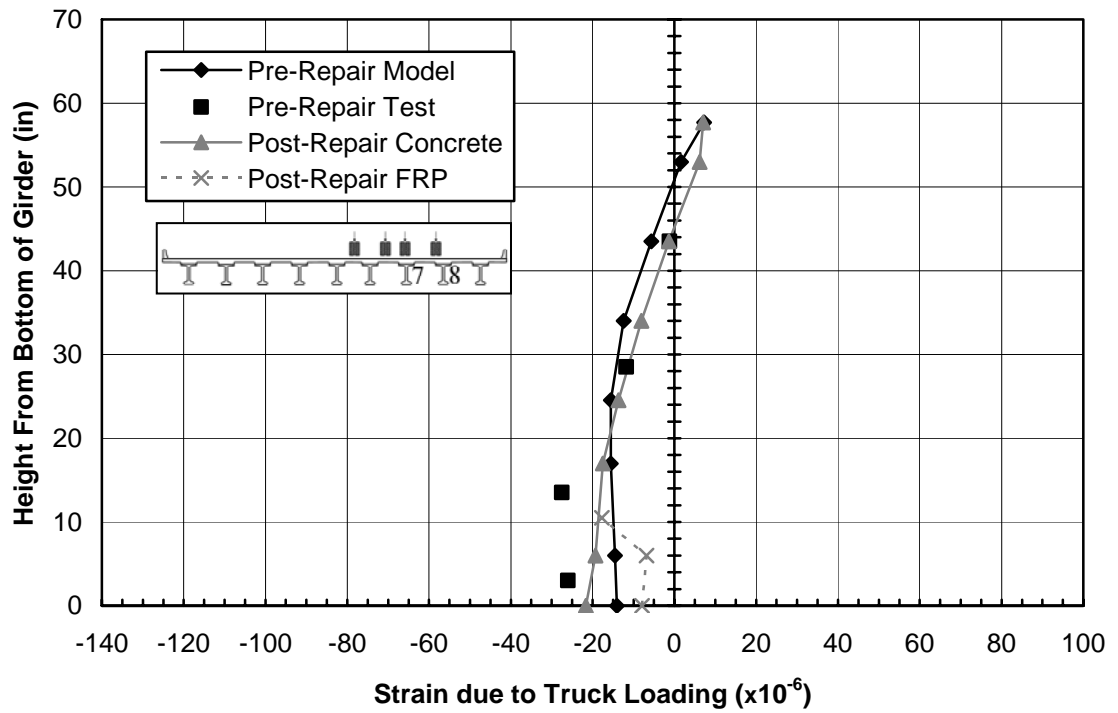**Figure D.15 Strain Profile—Load Position A7, Section 4, Girder 7, East Face**

Figure D.16 Strain Profile—Load Position A7, Section 4, Girder 8, West Face

Figure D.17 Strain Profile—Load Position A7, Section 4, Girder 8, East Face

APPENDIX E: A9 LOAD POSITION STRAIN PROFILES

Strains were measured along the faces of specific, instrumented cross sections of the

two girders, as explained in Appendix A. The A9 Load Position and the locations of the

instrumented cross sections are illustrated in Figure E.1. Figures E.2–E.17 graphically

compare the experimental strains along these cross sections to the analytical results

from both the *Pre-Repair* and *Post-Repair* models. In addition, the strains at the

corresponding locations on the FRP are presented.
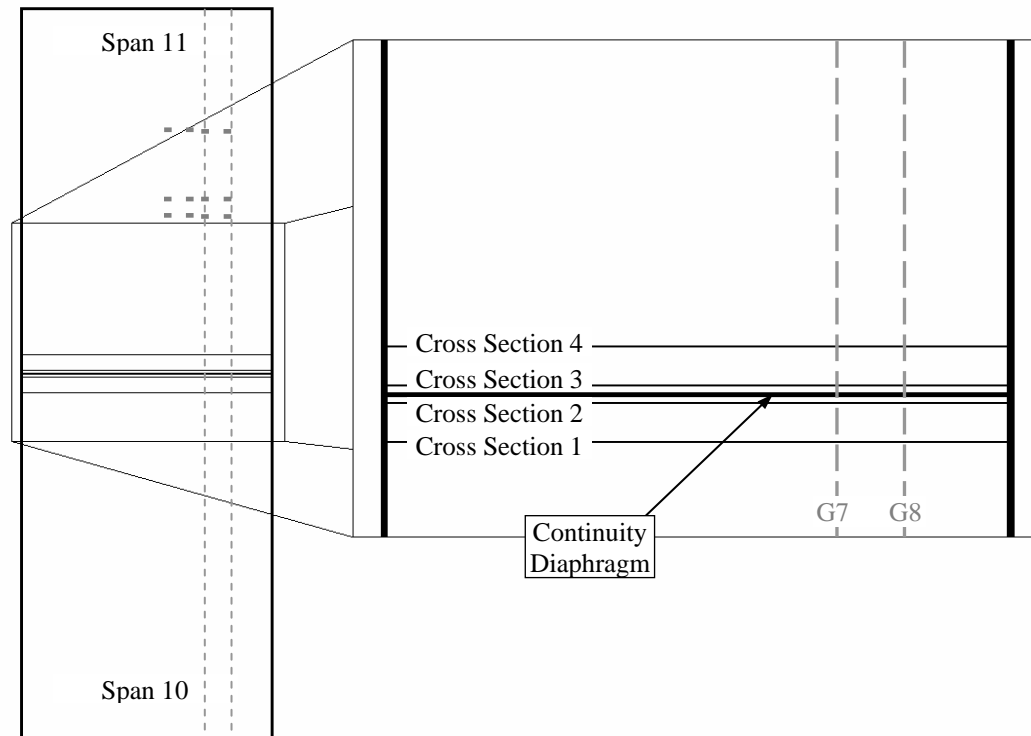
Figure E.1 Strain Profile Cross Section Locations for Load Position A9

Figure E.2 Strain Profile—Load Position A9, Section 1, Girder 7, West Face

Figure E.3 Strain Profile—Load Position A9, Section 1, Girder 7, East Face
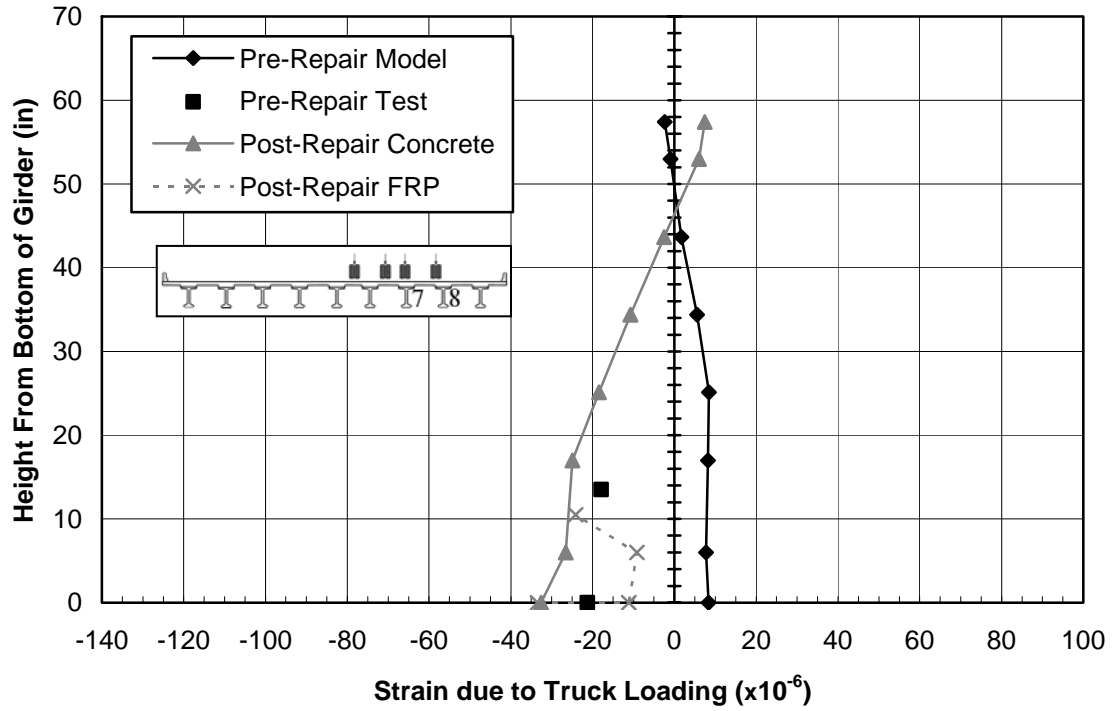
189

Figure E.4 Strain Profile—Load Position A9, Section 1, Girder 8, West Face
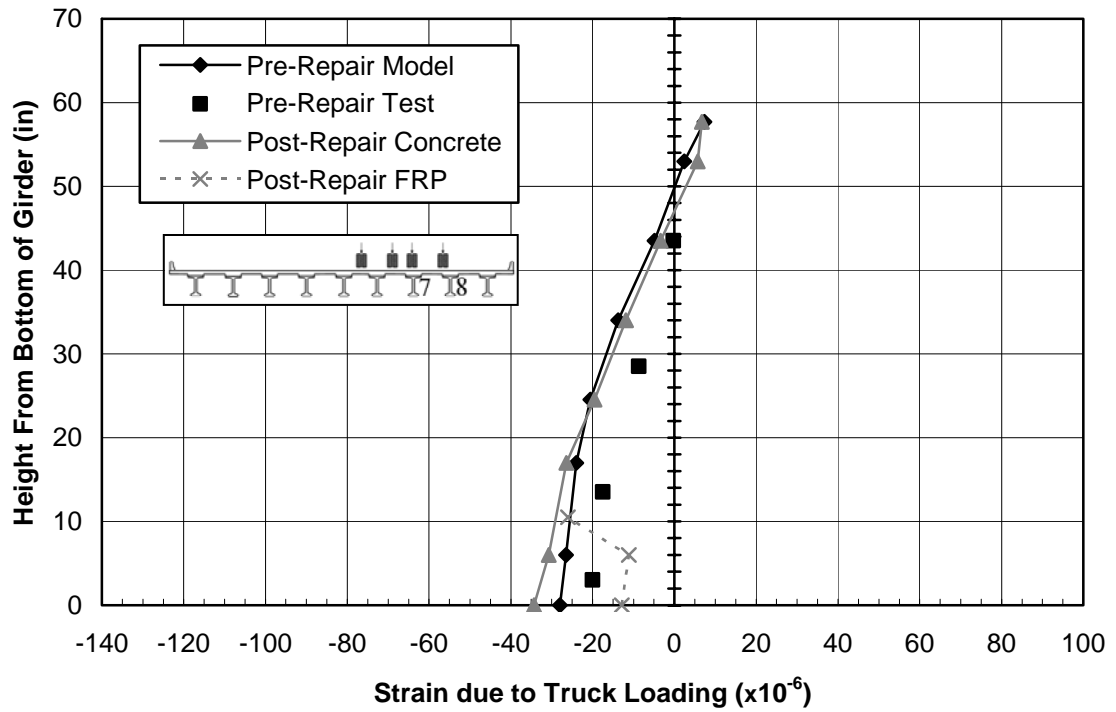

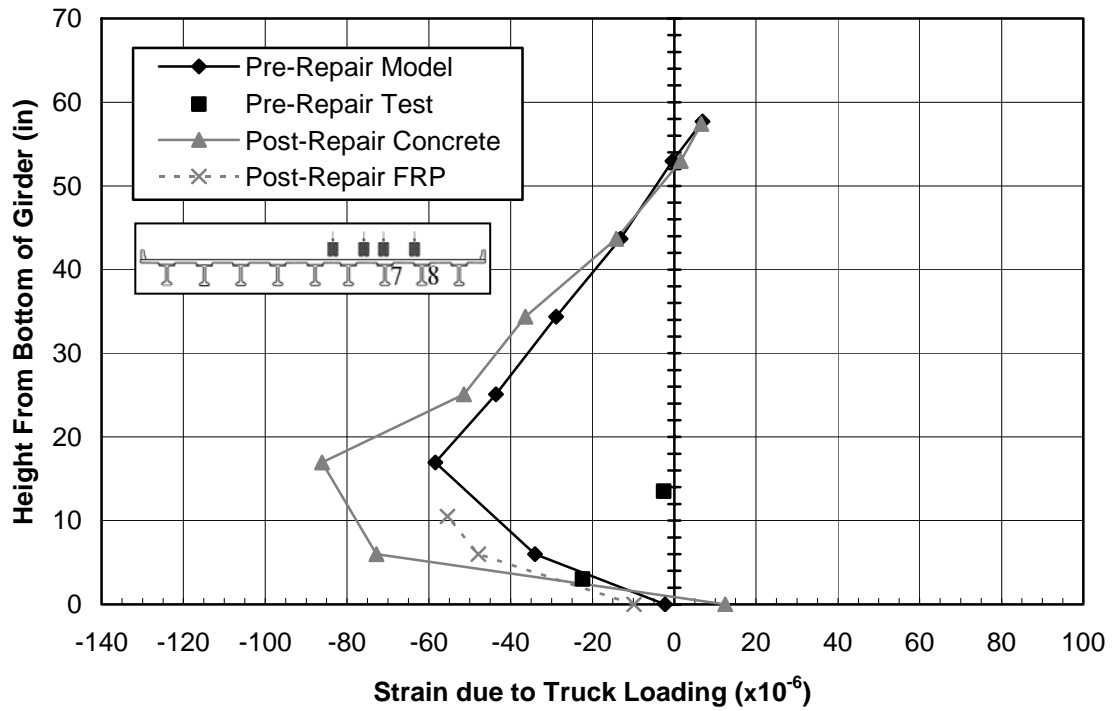**Figure E.5 Strain Profile—Load Position A9, Section 1, Girder 8, East Face**

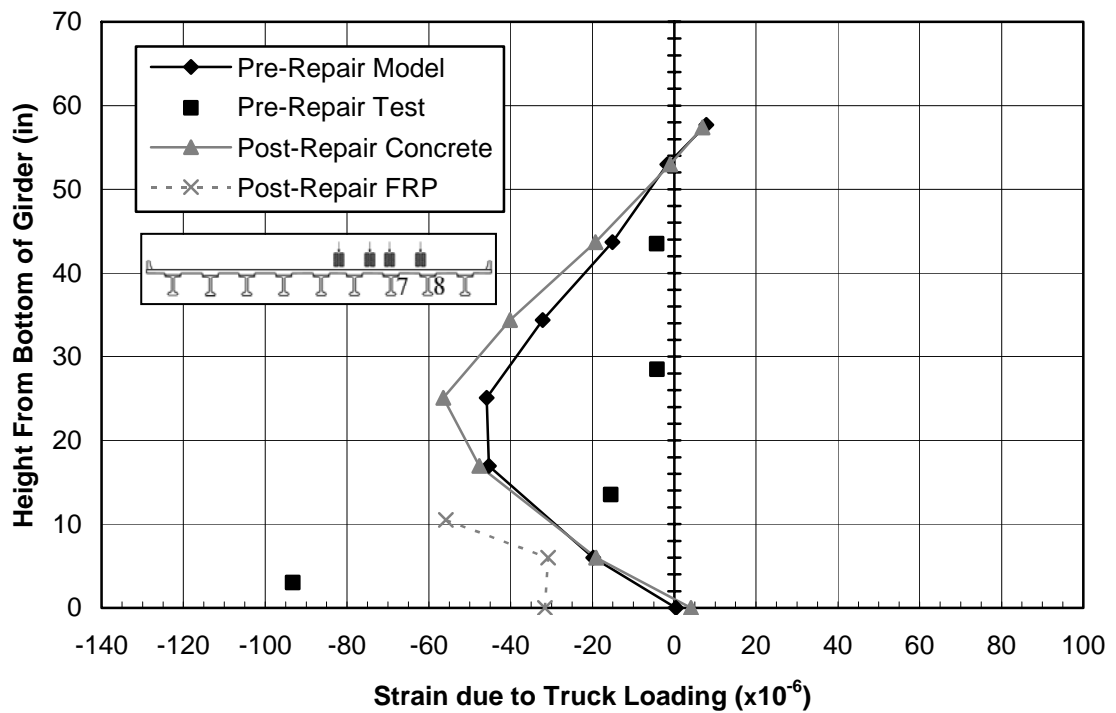**Figure E.6 Strain Profile—Load Position A9, Section 2, Girder 7, West Face**

Figure E.7 Strain Profile—Load Position A9, Section 2, Girder 7, East Face
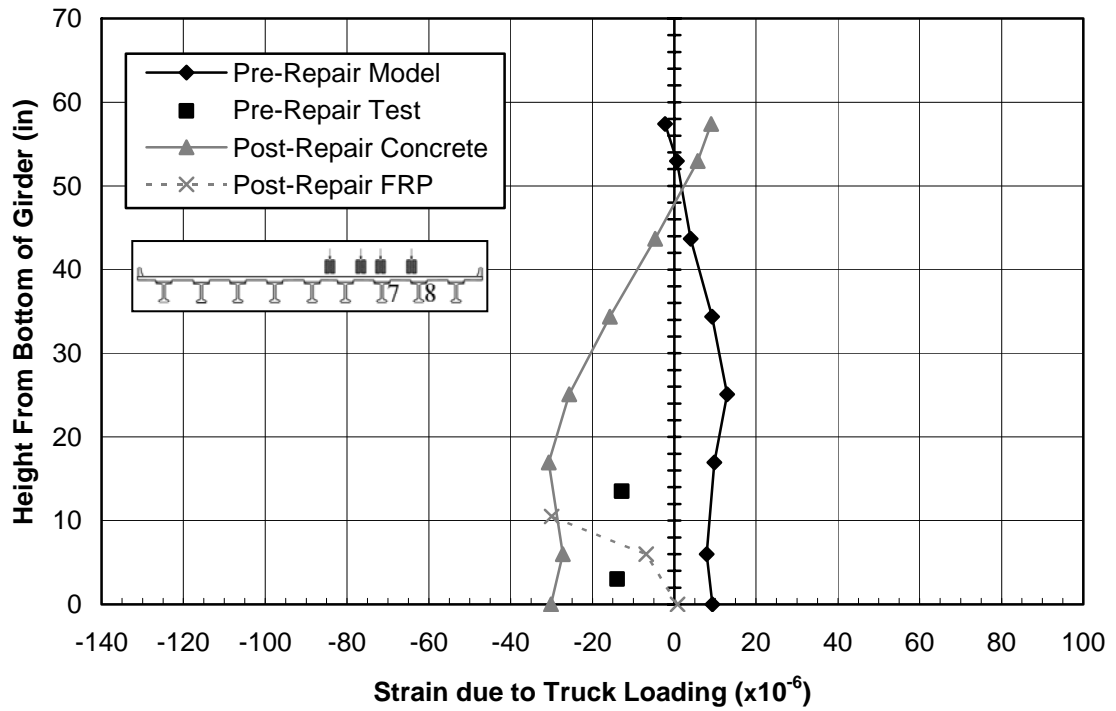
191

Figure E.8 Strain Profile—Load Position A9, Section 2, Girder 8, West Face
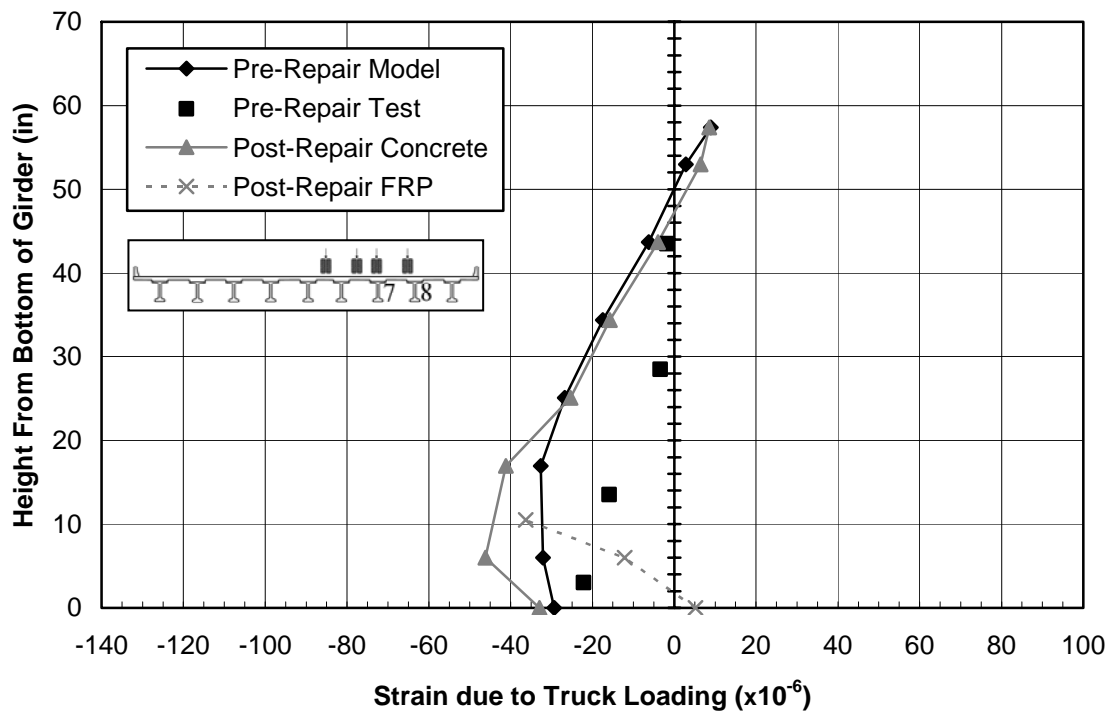

Figure E.9 Strain Profile—Load Position A9, Section 2, Girder 8, East Face
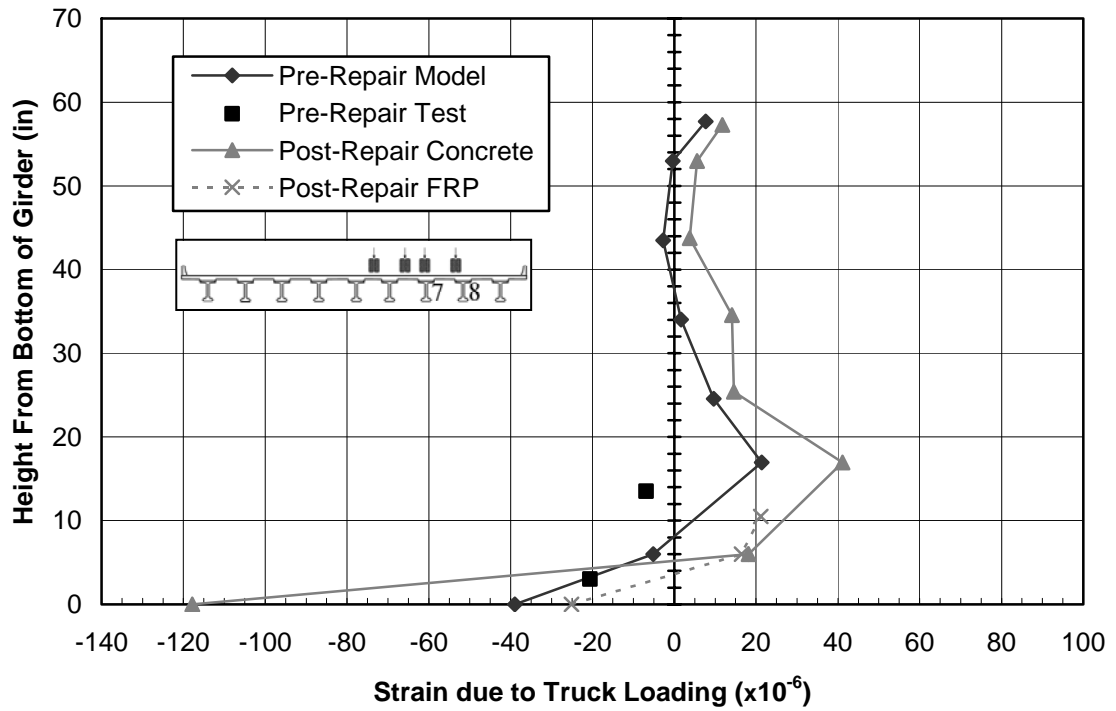
Figure E.10 Strain Profile—Load Position A9, Section 3, Girder 7, West Face

Figure E.11 Strain Profile—Load Position A9, Section 3, Girder 7, East Face

Figure E.12 Strain Profile—Load Position A9, Section 3, Girder 8, West Face

Figure E.13 Strain Profile—Load Position A9, Section 3, Girder 8, East Face

Figure E.14 Strain Profile—Load Position A9, Section 4, Girder 7, West Face
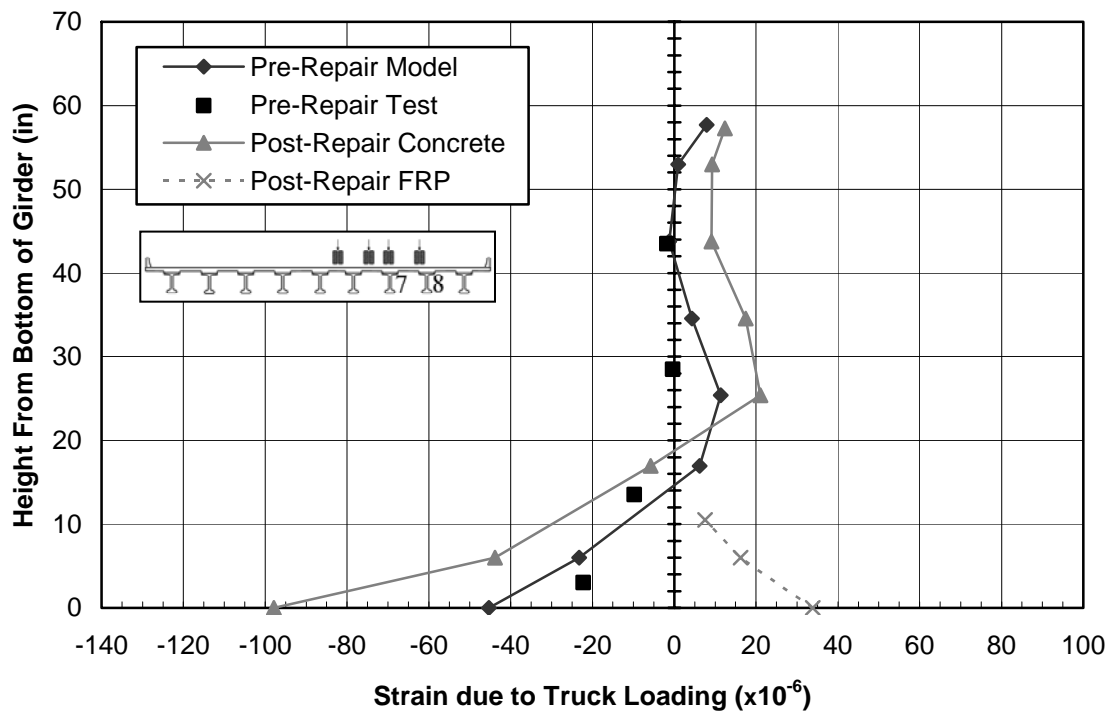

Figure E.15 Strain Profile—Load Position A9, Section 4, Girder 7, East Face
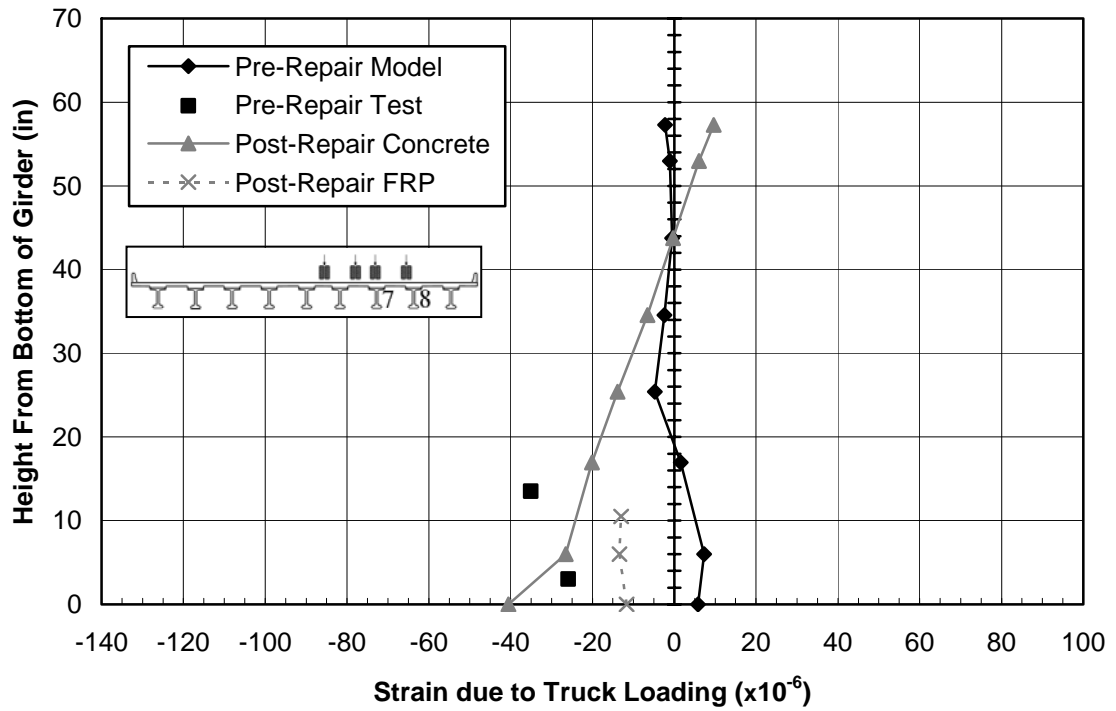
Figure E.16 Strain Profile—Load Position A9, Section 4, Girder 8, West Face
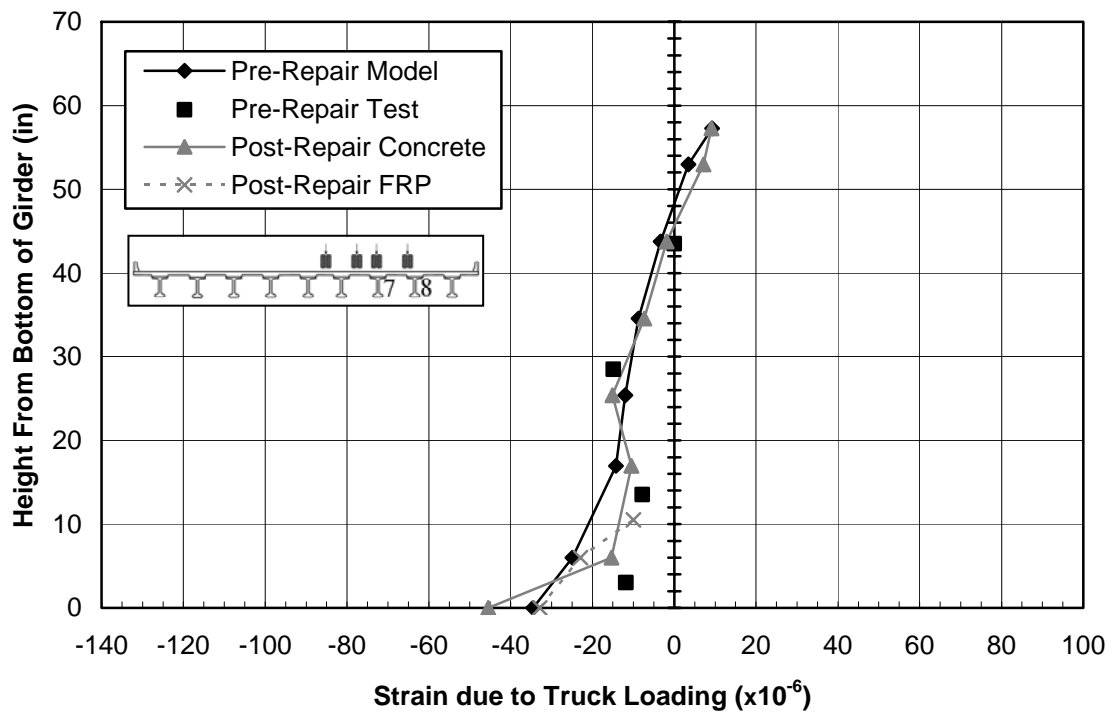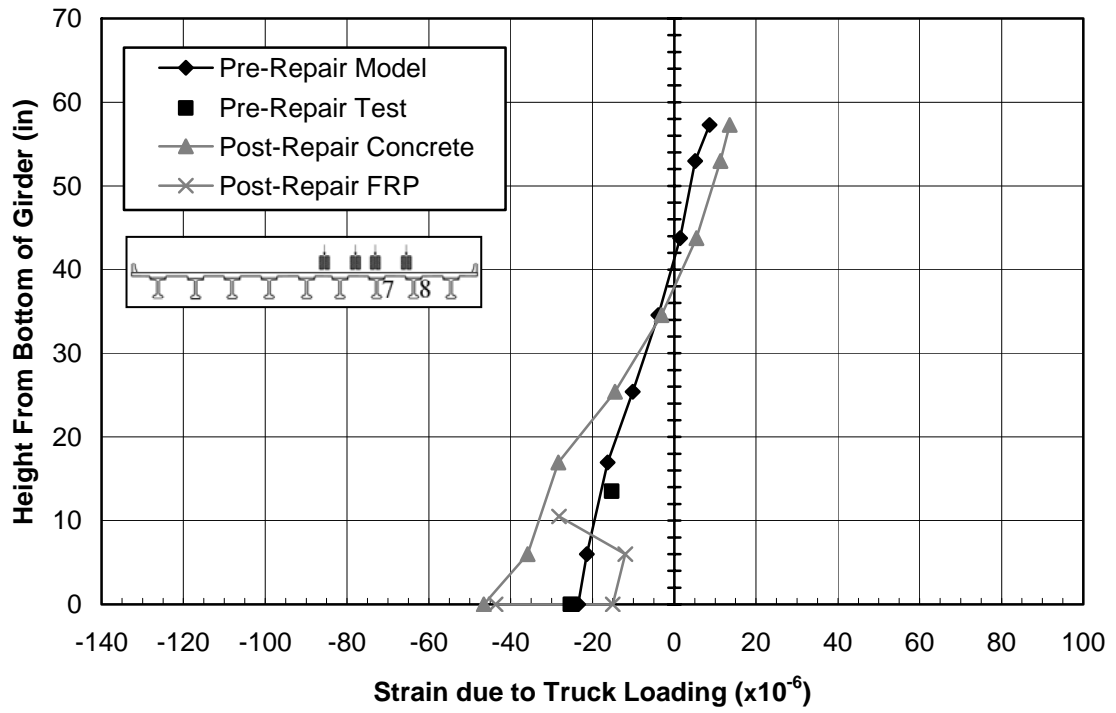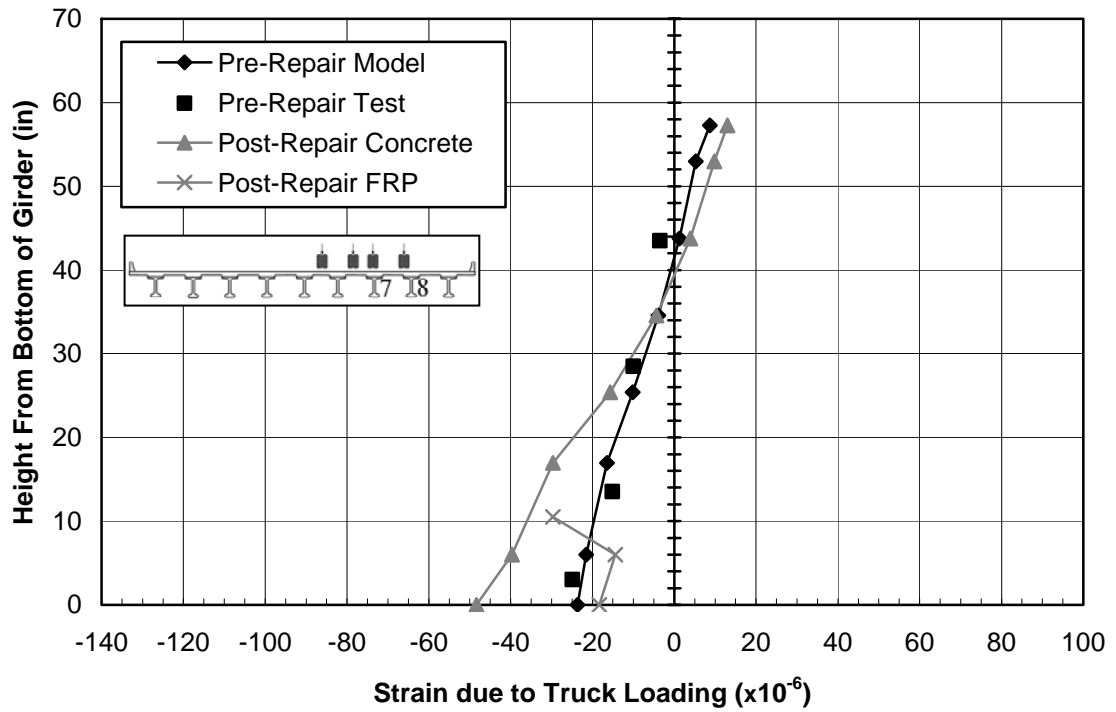

Figure E.17 Strain Profile—Load Position A9, Section 4, Girder 8, East Face

196

APPENDIX F: C7 LOAD POSITION STRAIN PROFILES

Strains were measured along the faces of specific, instrumented cross sections of the two girders, as explained in Appendix A. The C7 Load Position and the locations of the instrumented cross sections are illustrated in Figure F.1. Figures F.2–F.17 graphically compare the experimental strains along these cross sections to the analytical results from both the *Pre-Repair* and *Post-Repair* models. In addition, the strains at the corresponding locations on the FRP are presented.
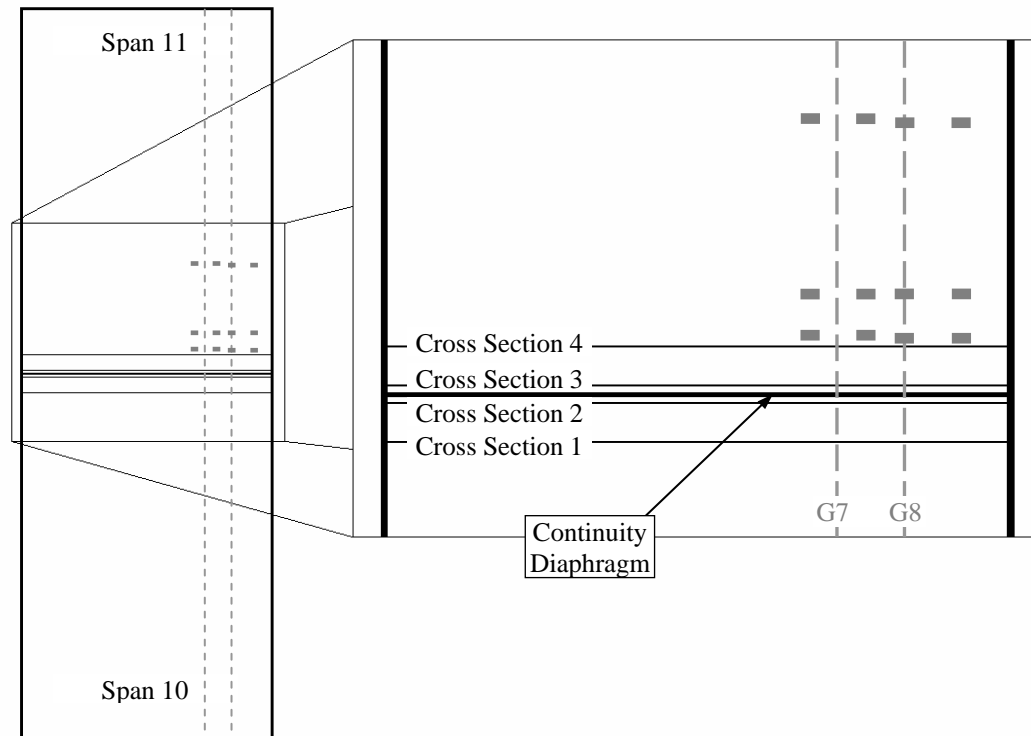
Figure F.1 Strain Profile Cross Section Locations for Load Position C7

Figure F.2 Strain Profile—Load Position C7, Section 1, Girder 7, West Face

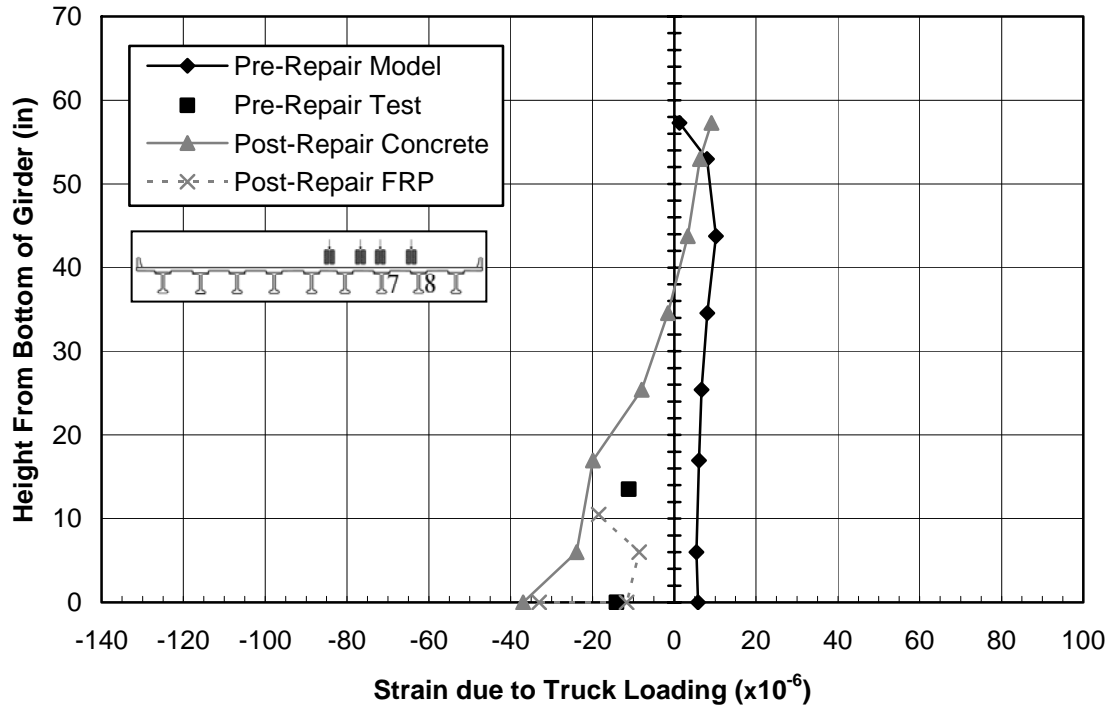**Figure F.3 Strain Profile—Load Position C7, Section 1, Girder 7, East Face**

Figure F.4 Strain Profile—Load Position C7, Section 1, Girder 8, West Face

Figure F.5 Strain Profile—Load Position C7, Section 1, Girder 8, East Face

199

Figure F.6 Strain Profile—Load Position C7, Section 2, Girder 7, West Face

Figure F.7 Strain Profile—Load Position C7, Section 2, Girder 7, East Face

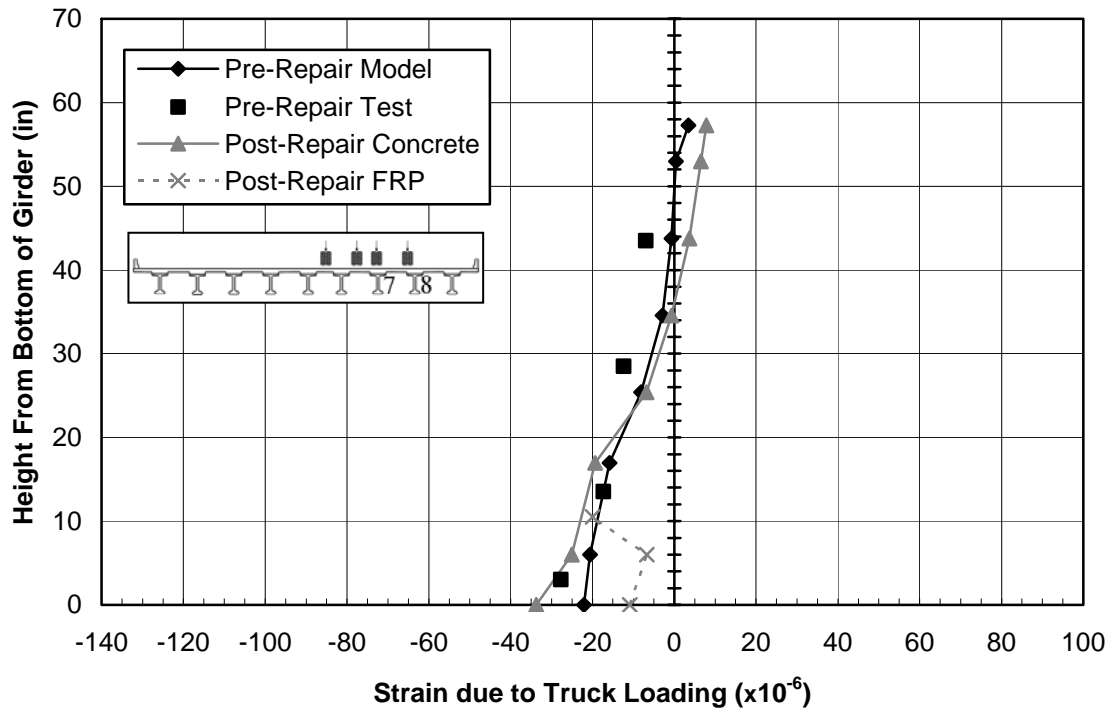**Figure F.8 Strain Profile—Load Position C7, Section 2, Girder 8, West Face**

Figure F.9 Strain Profile—Load Position C7, Section 2, Girder 8, East Face

Figure F.10 Strain Profile—Load Position C7, Section 3, Girder 7, West Face

Figure F.11 Strain Profile—Load Position C7, Section 3, Girder 7, East Face

Figure F.12 Strain Profile—Load Position C7, Section 3, Girder 8, West Face

Figure F.13 Strain Profile—Load Position C7, Section 3, Girder 8, East Face
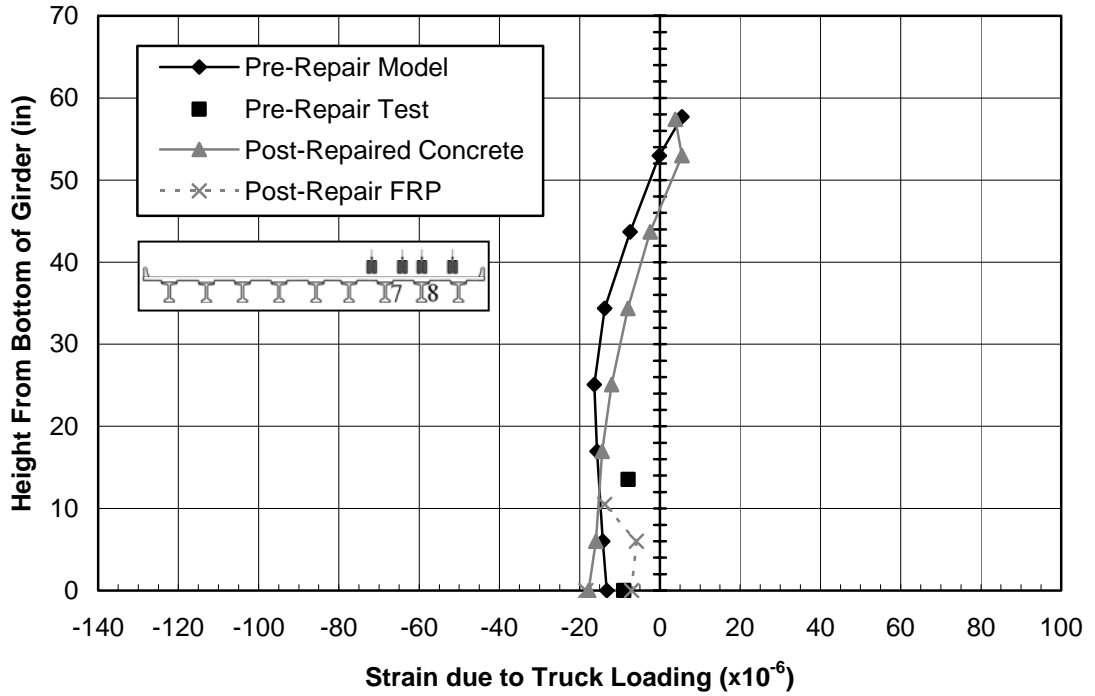
Figure F.14 Strain Profile—Load Position C7, Section 4, Girder 7, West Face
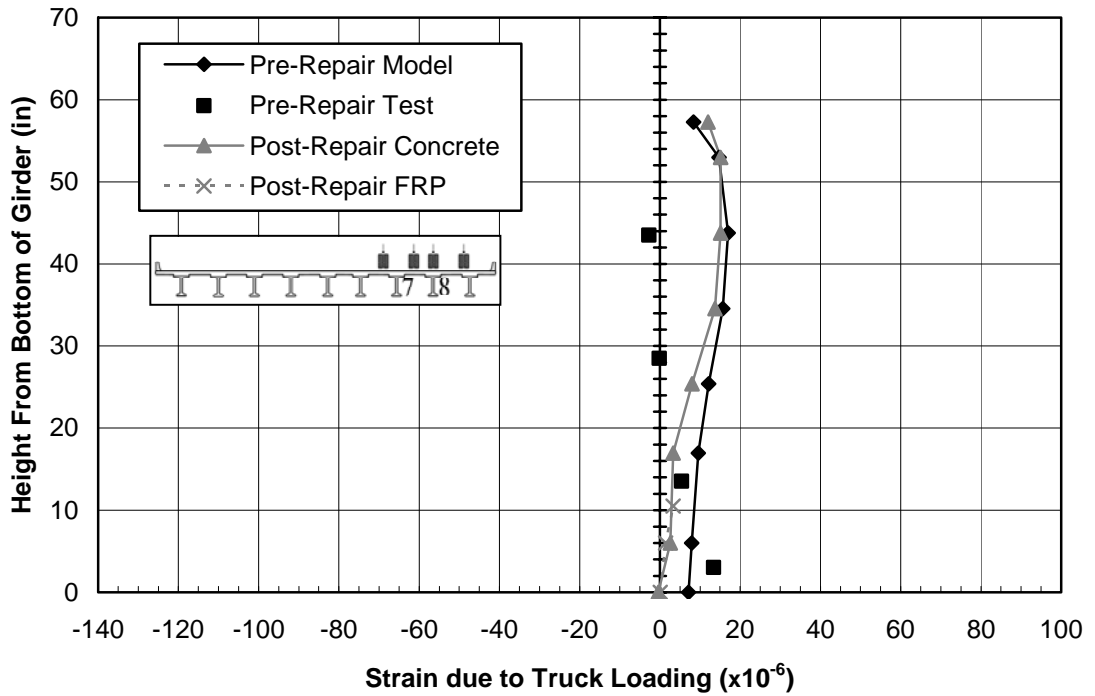
Figure F.15 Strain Profile—Load Position C7, Section 4, Girder 7, East Face

204
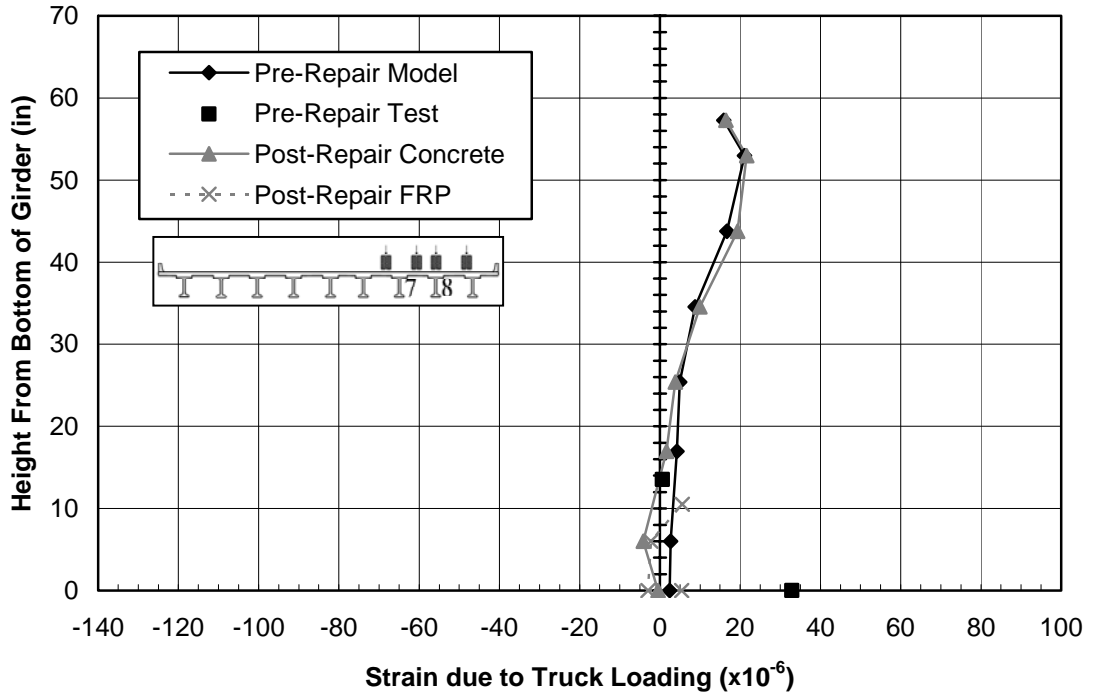
Figure F.16 Strain Profile—Load Position C7, Section 4, Girder 8, West Face
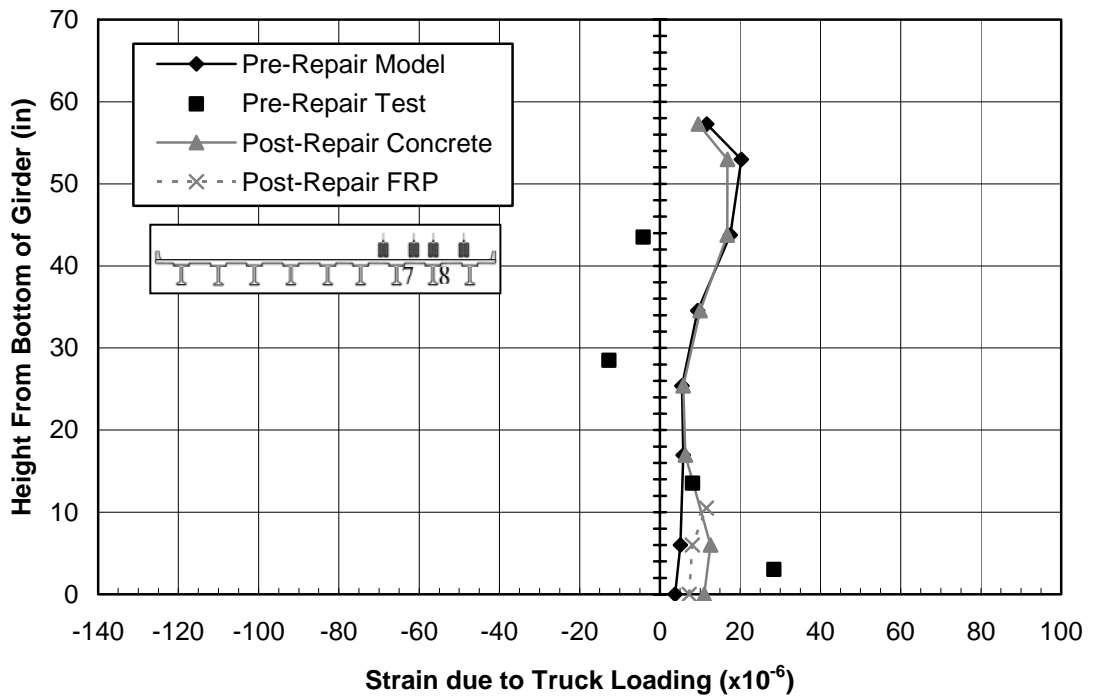
Figure F.17 Strain Profile—Load Position C7, Section 4, Girder 8, East Face

205

APPENDIX G: C9 LOAD POSITION STRAIN PROFILES

Strains were measured along the faces of specific, instrumented cross sections of the
two girders, as explained in Appendix A. The C9 Load Position and the locations of the
instrumented cross sections are illustrated in Figure G.1. Figures G.2–G.17 graphically
compare the experimental strains along these cross sections to the analytical results
from both the *Pre-Repair* and *Post-Repair* models. In addition, the strains at the
corresponding locations on the FRP are presented.
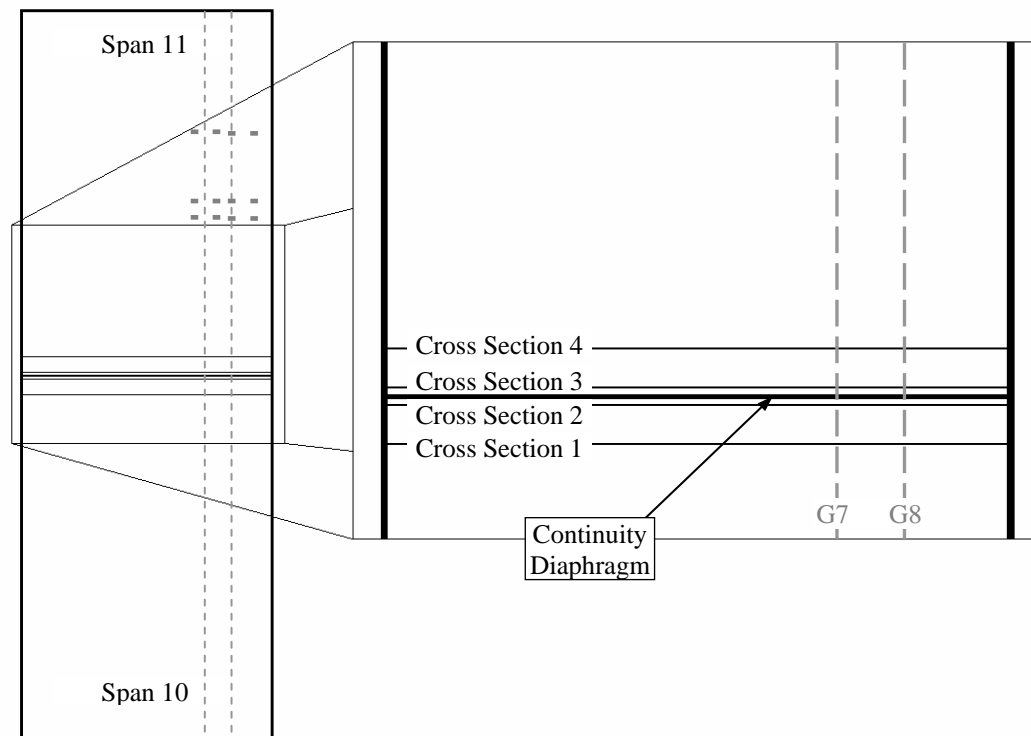
Figure G.1 Strain Profile Cross Section Locations for Load Position C9
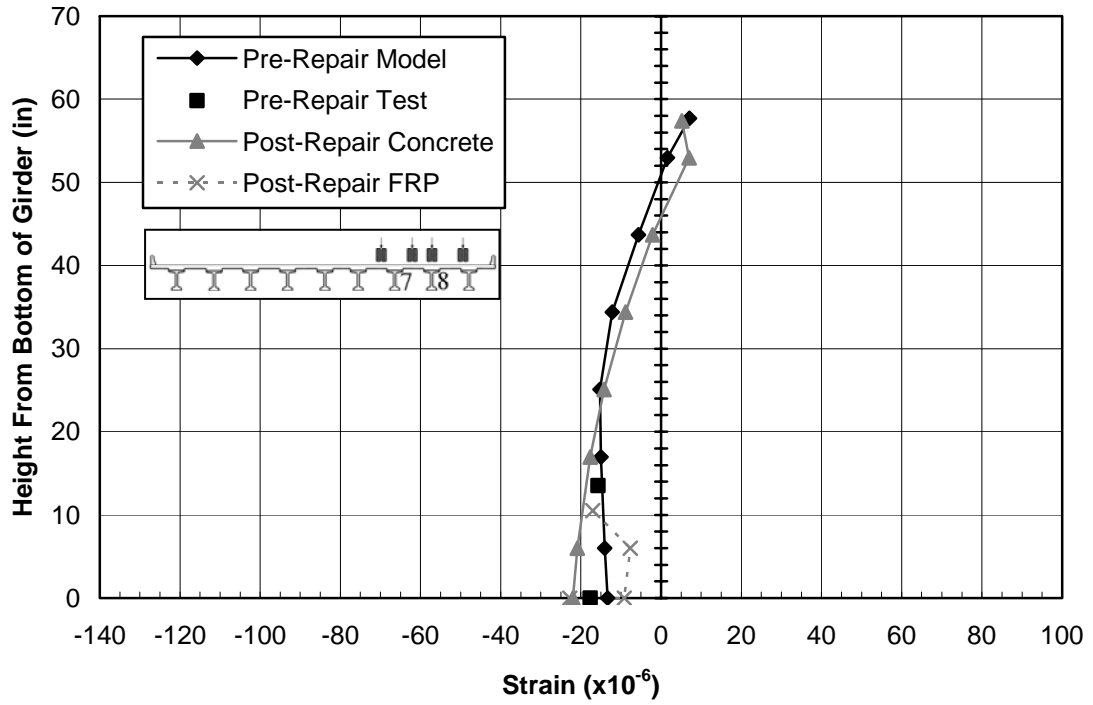
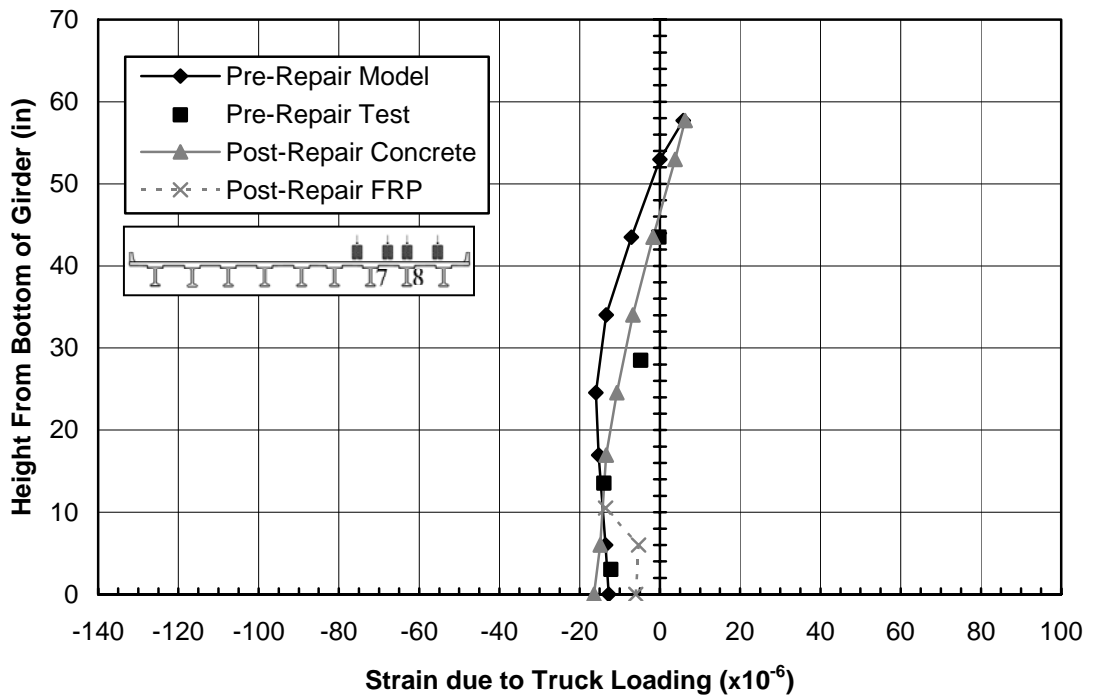**Figure G.2 Strain Profile—Load Position C9, Section 1, Girder 7, West Face**
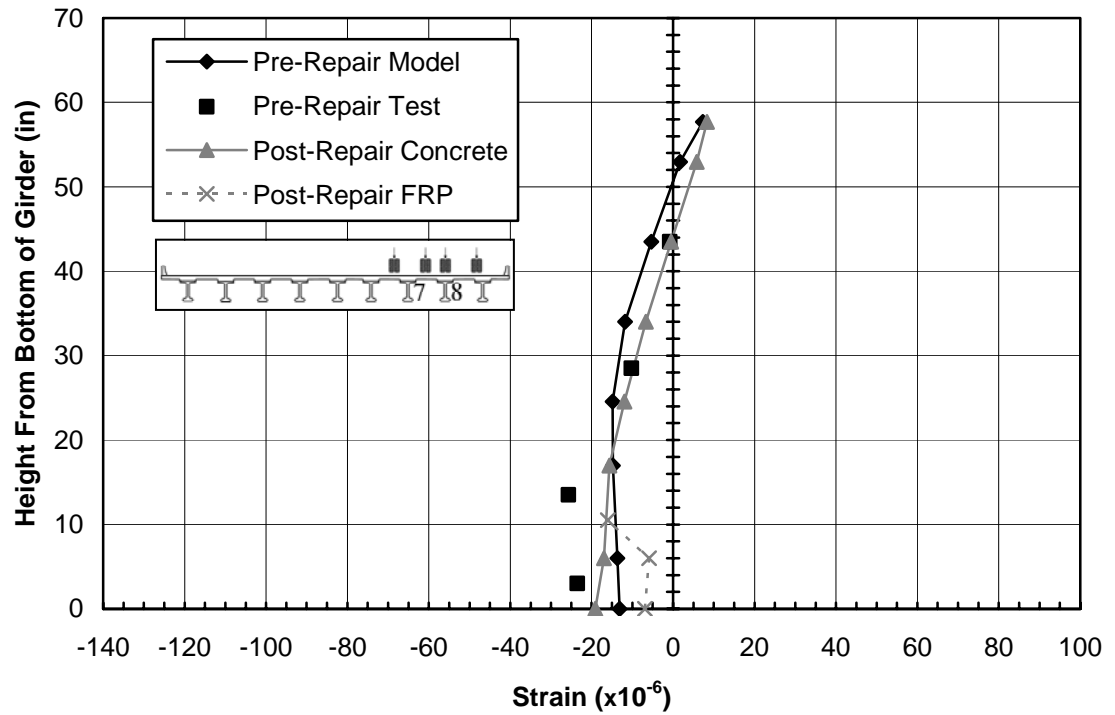
Figure G.3 Strain Profile—Load Position C9, Section 1, Girder 7, East Face
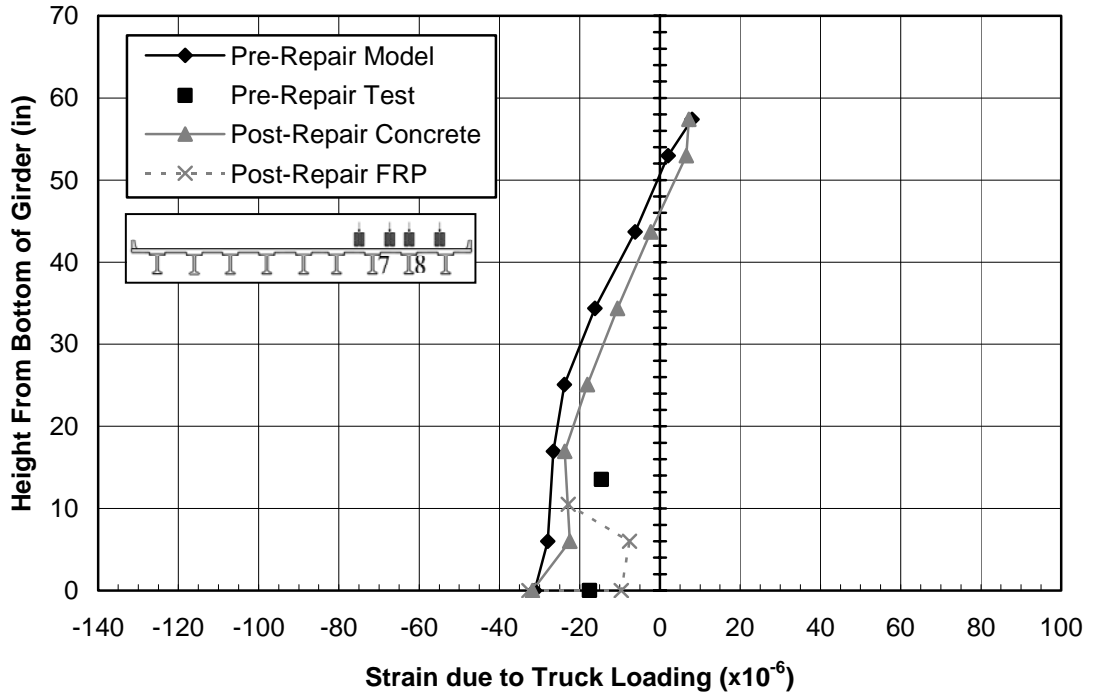
207
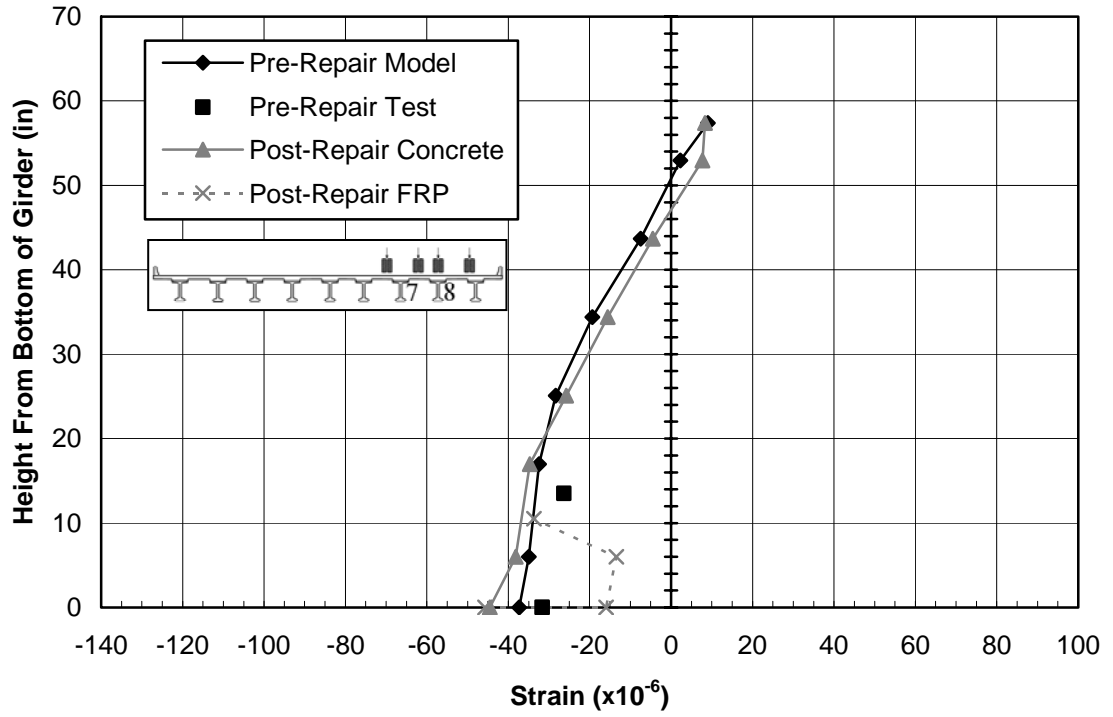
Figure G.4 Strain Profile—Load Position C9, Section 1, Girder 8, West Face
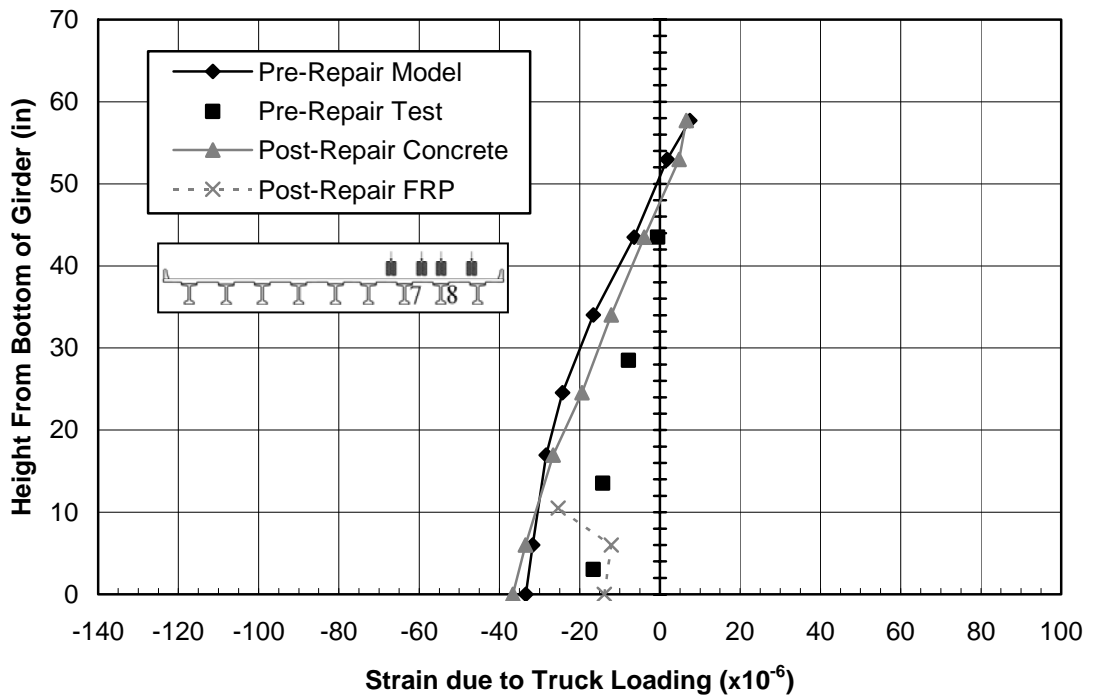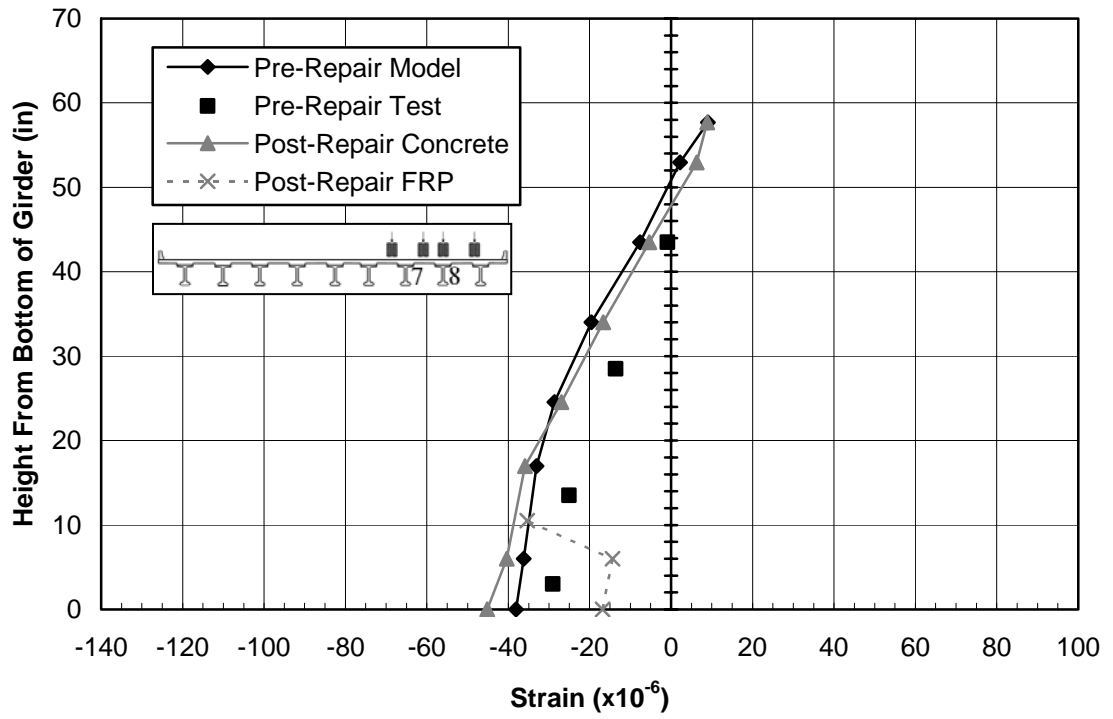

Figure G.5 Strain Profile—Load Position C9, Section 1, Girder 8, East Face
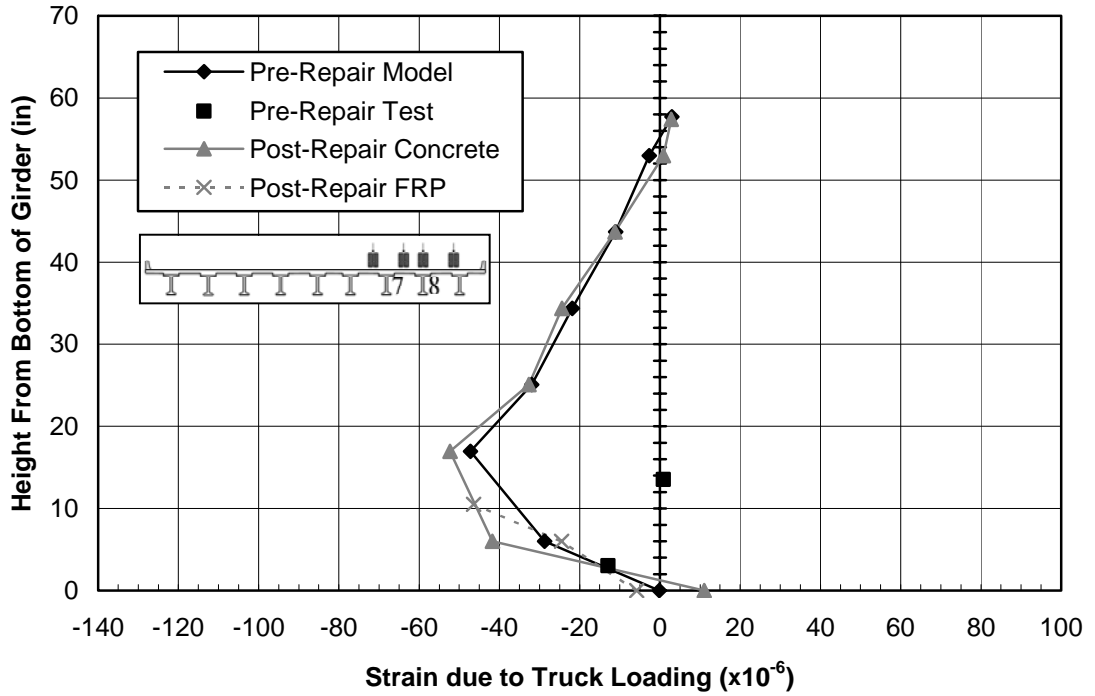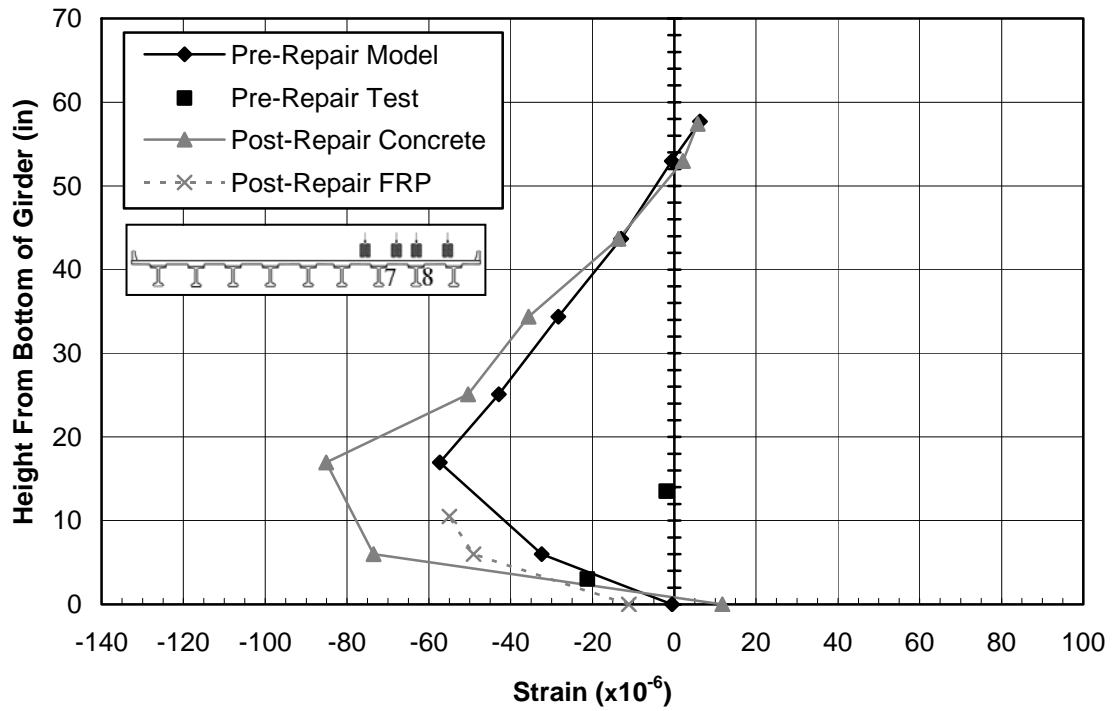
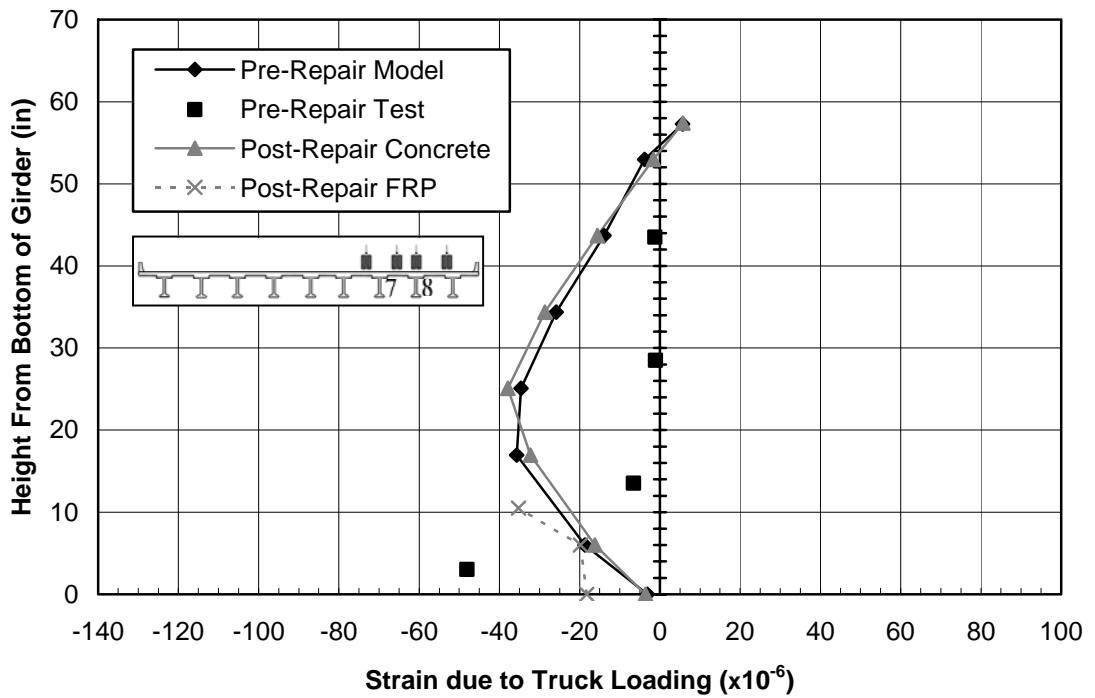**Figure G.6 Strain Profile—Load Position C9, Section 2, Girder 7, West Face**
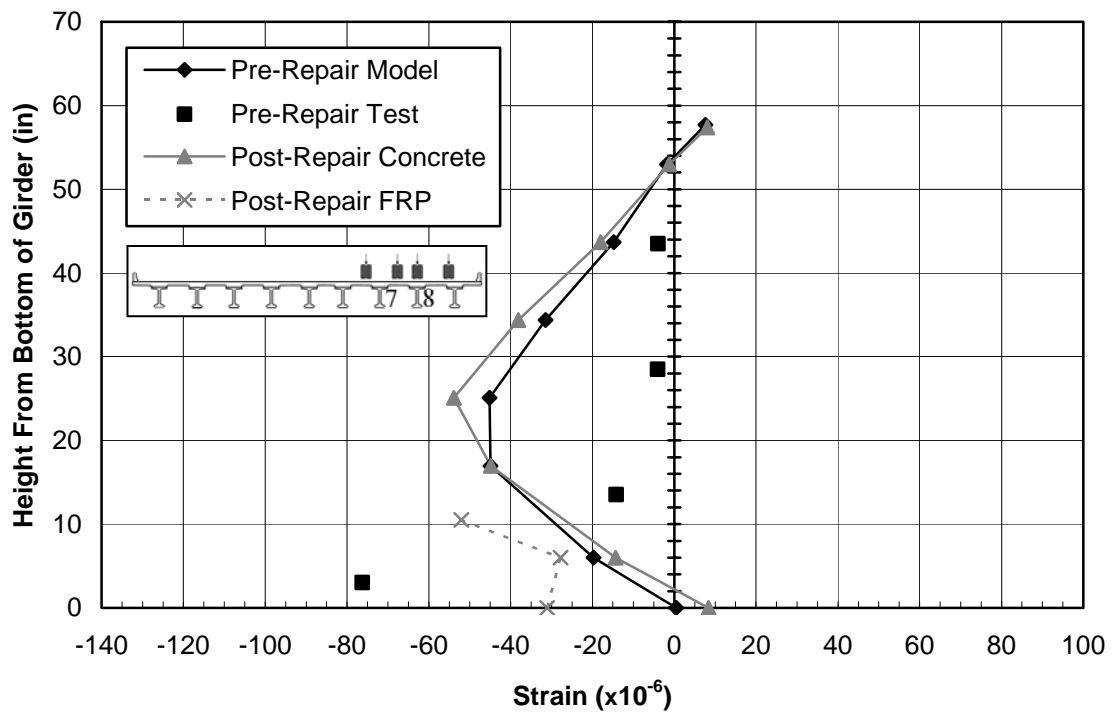
Figure G.7 Strain Profile—Load Position C9, Section 2, Girder 7, East Face
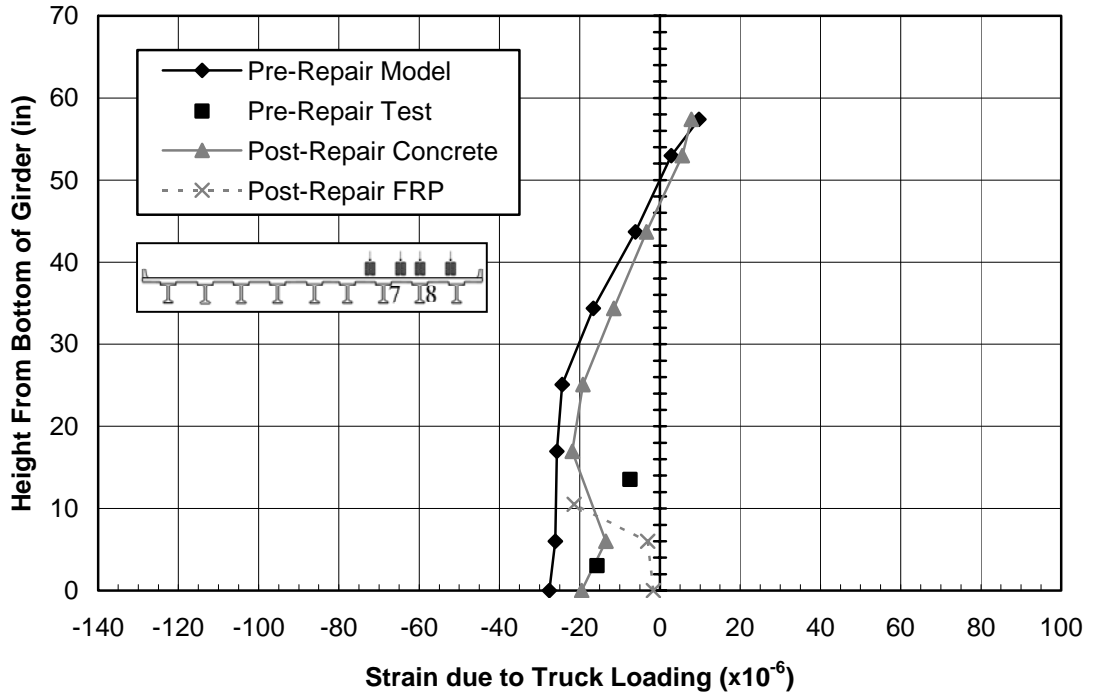
209
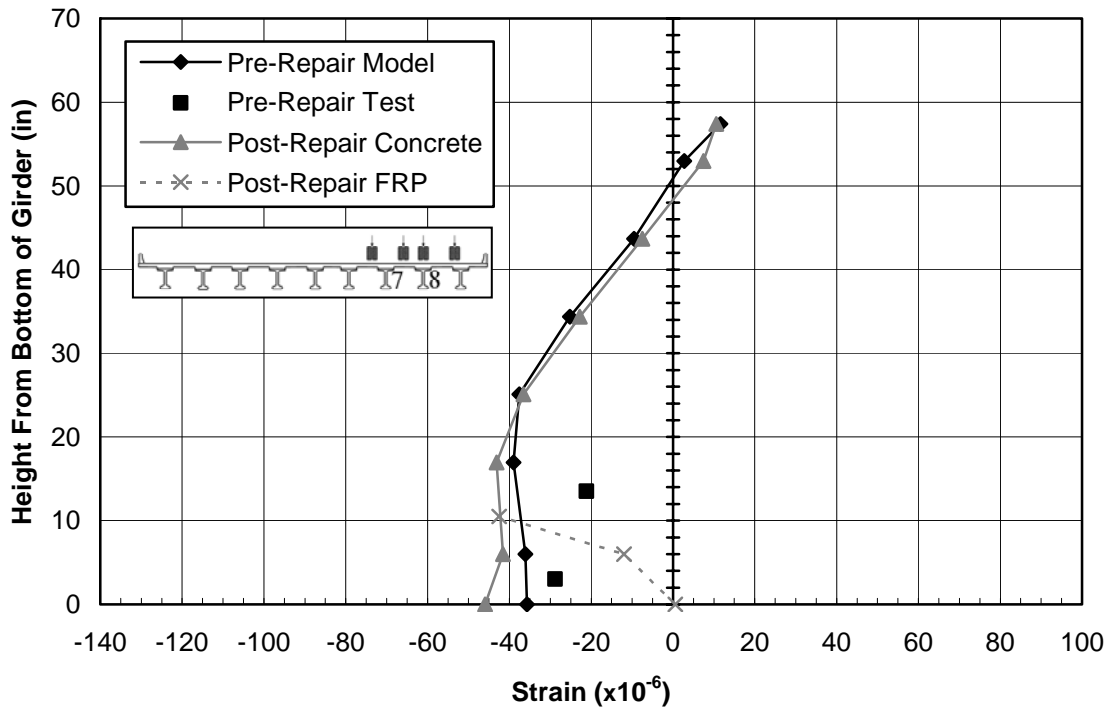
Figure G.8 Strain Profile—Load Position C9, Section 2, Girder 8, West Face
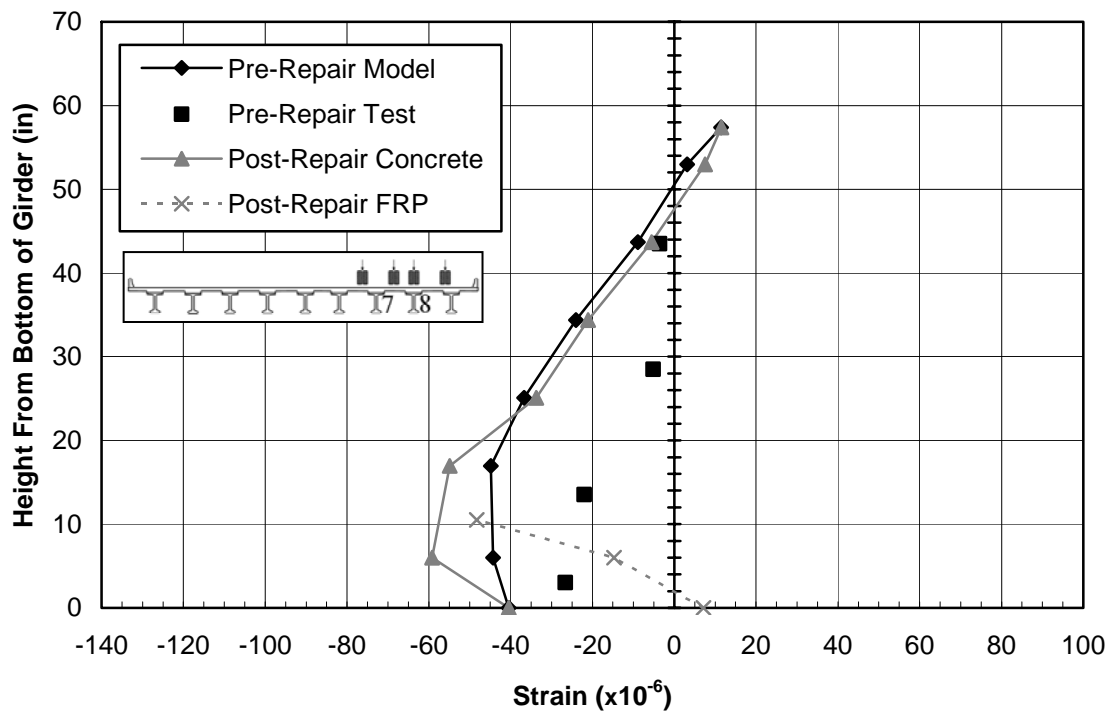
Figure G.9 Strain Profile—Load Position C9, Section 2, Girder 8, East Face

210
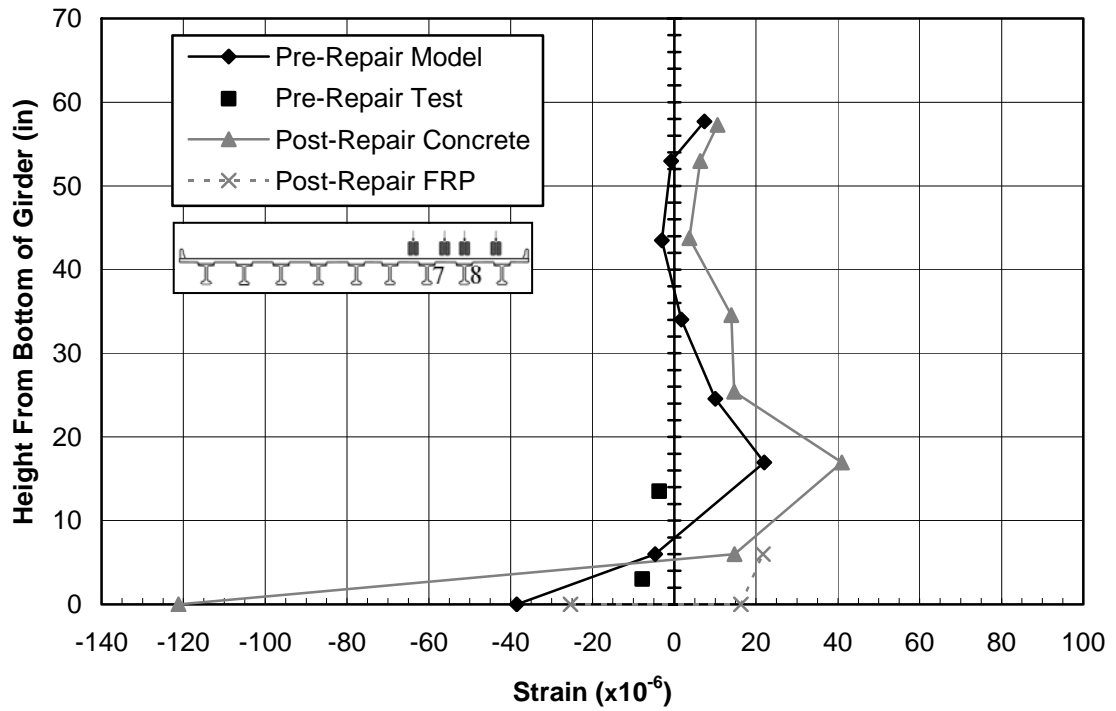
Figure G.10 Strain Profile—Load Position C9, Section 3, Girder 7, West Face
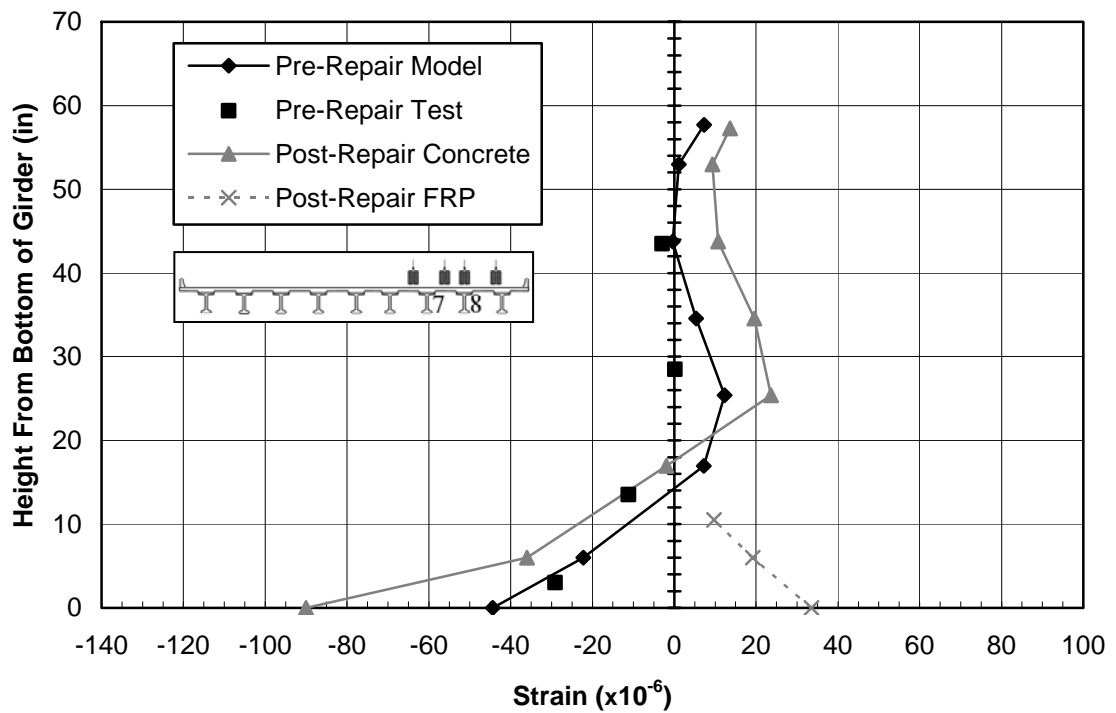
Figure G.11 Strain Profile—Load Position C9, Section 3, Girder 7, East Face
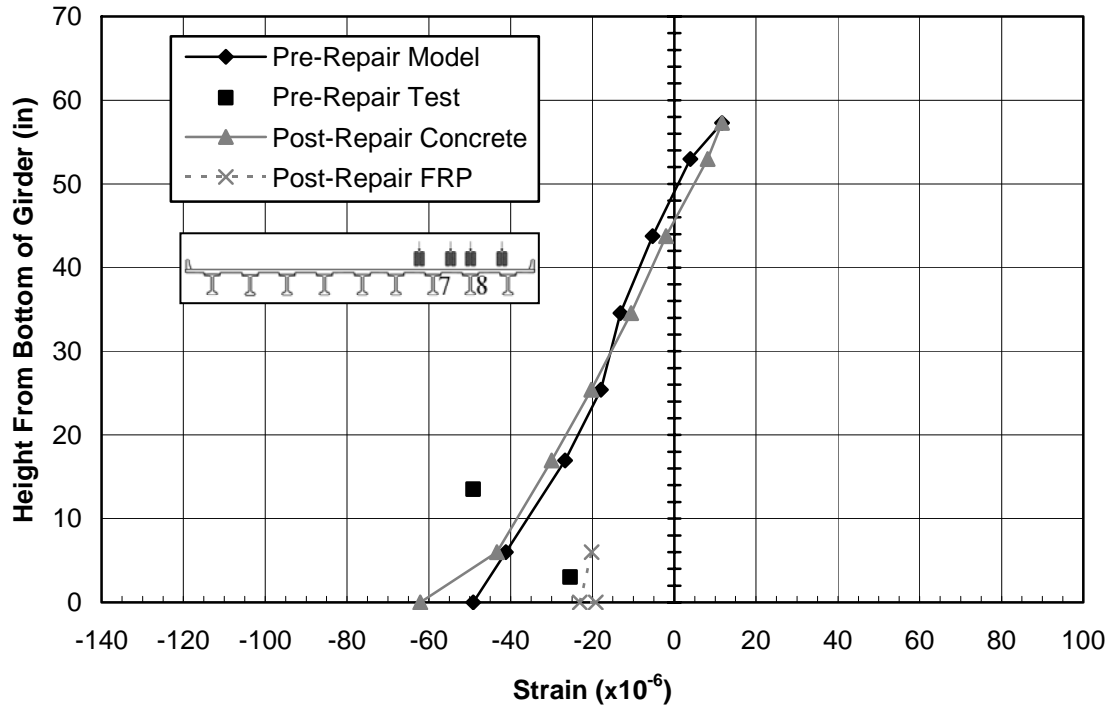
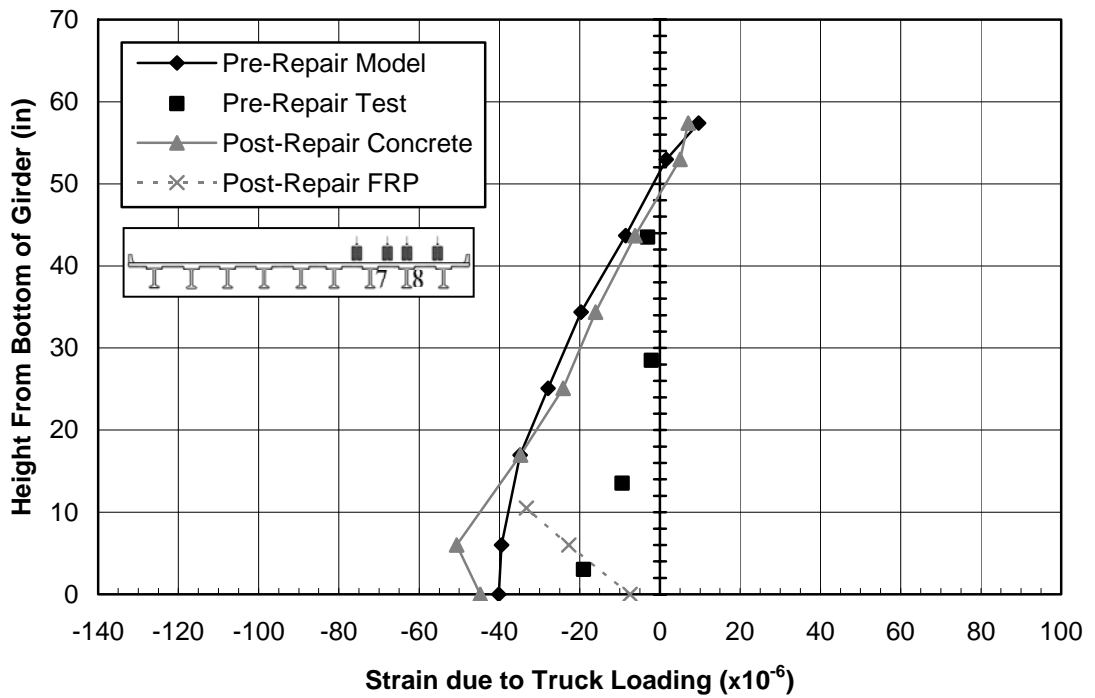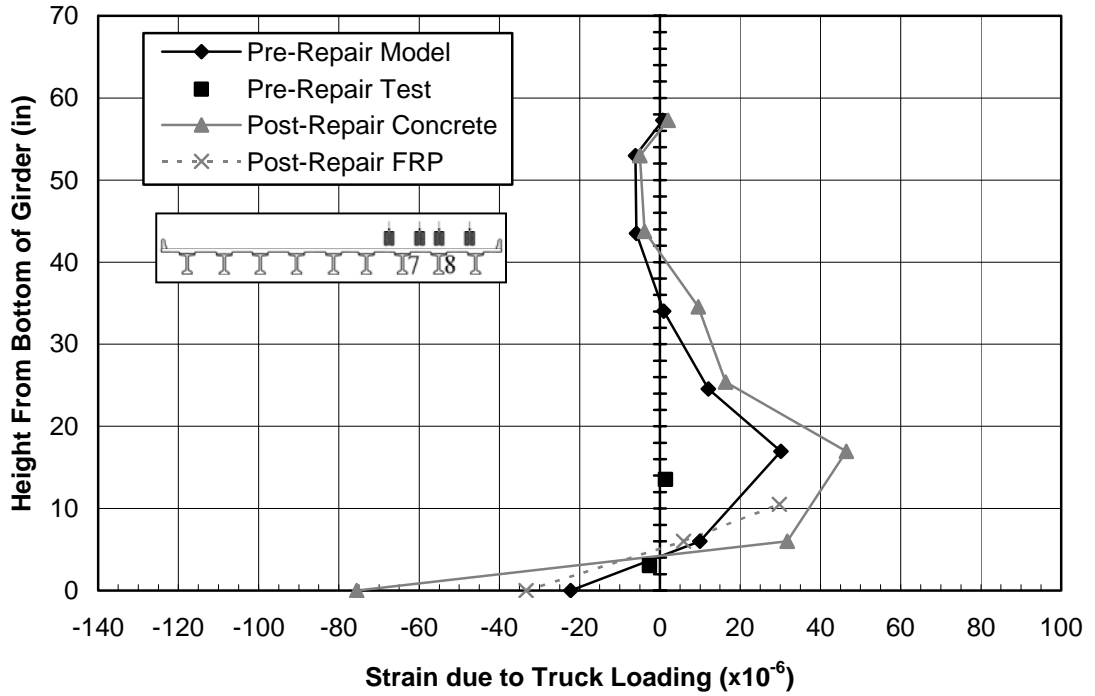**Figure G.12 Strain Profile—Load Position C9, Section 3, Girder 8, West Face**
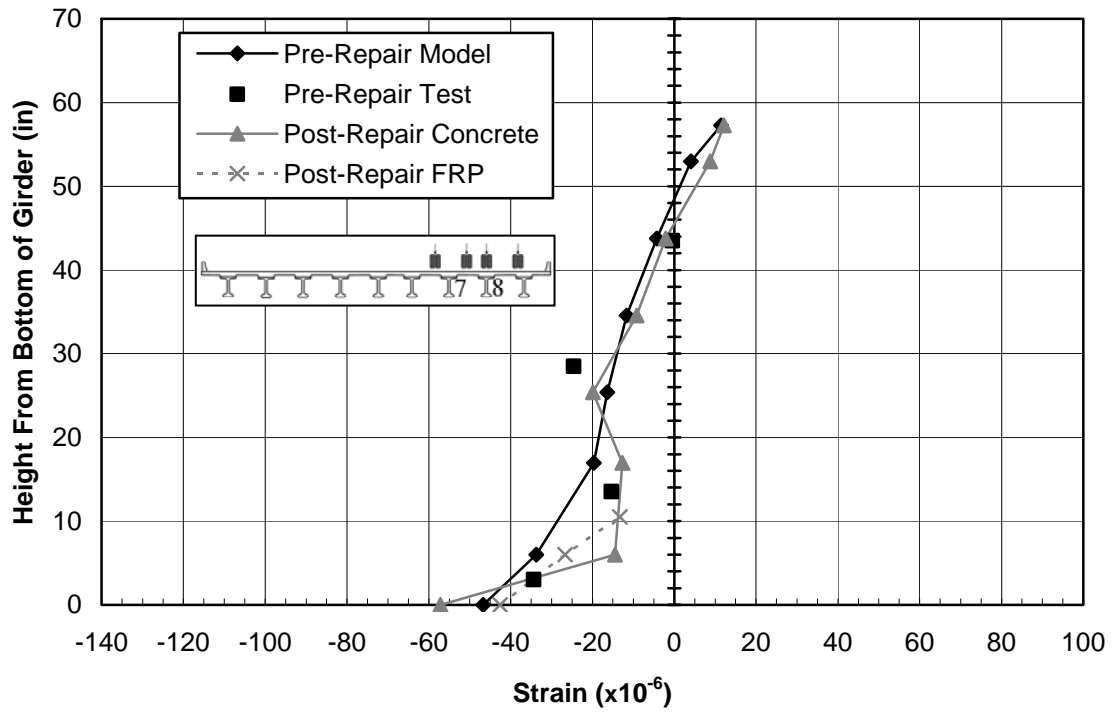
Figure G.13 Strain Profile—Load Position C9, Section 3, Girder 8, East Face
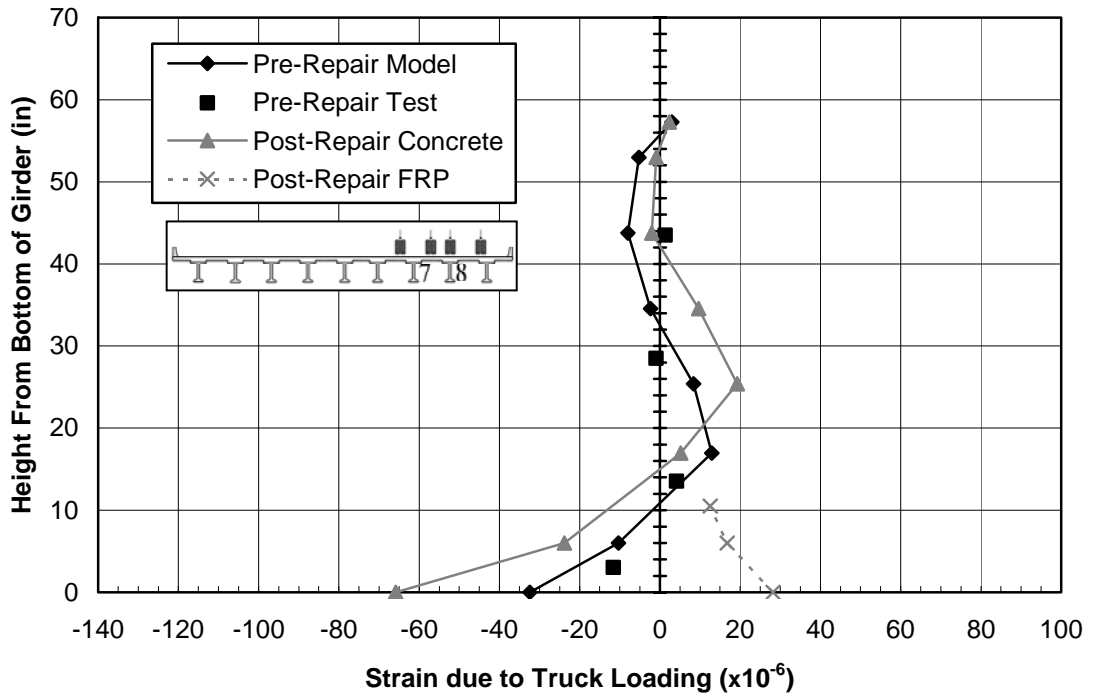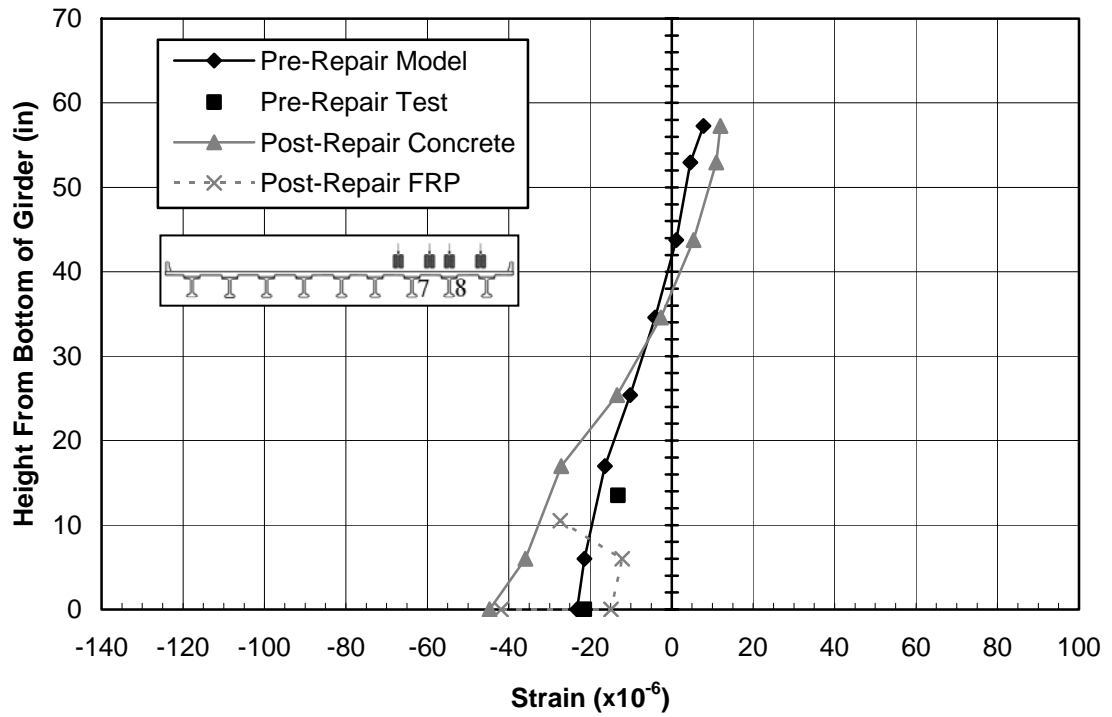
Figure G.14 Strain Profile—Load Position C9, Section 4, Girder 7, West Face
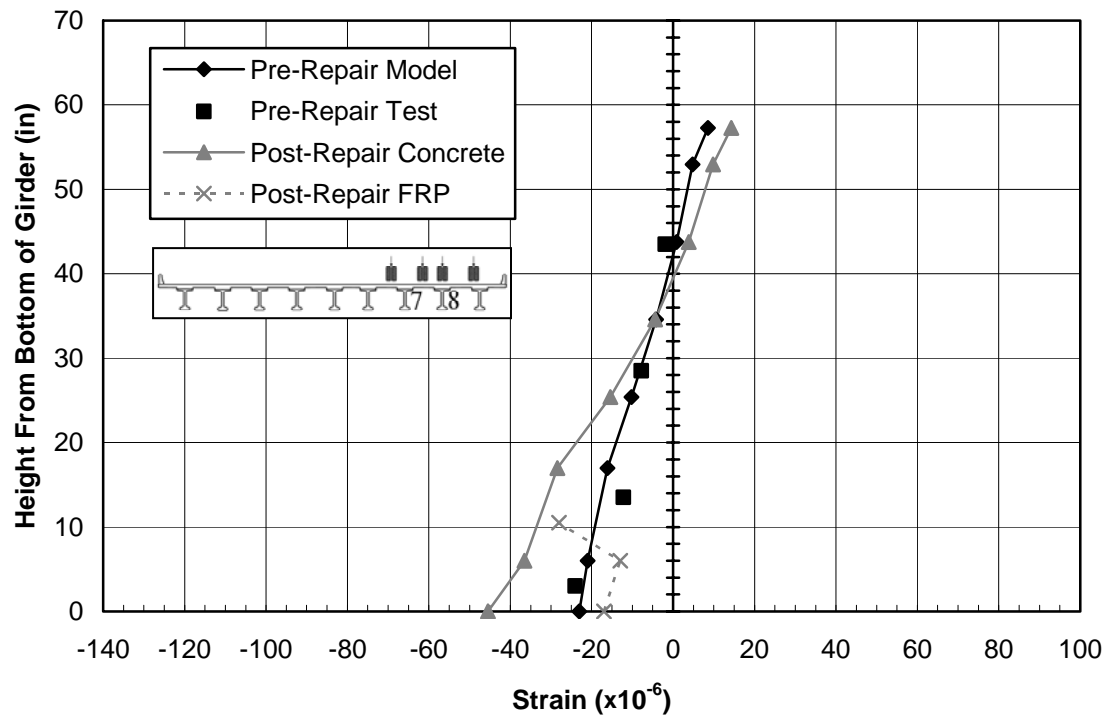
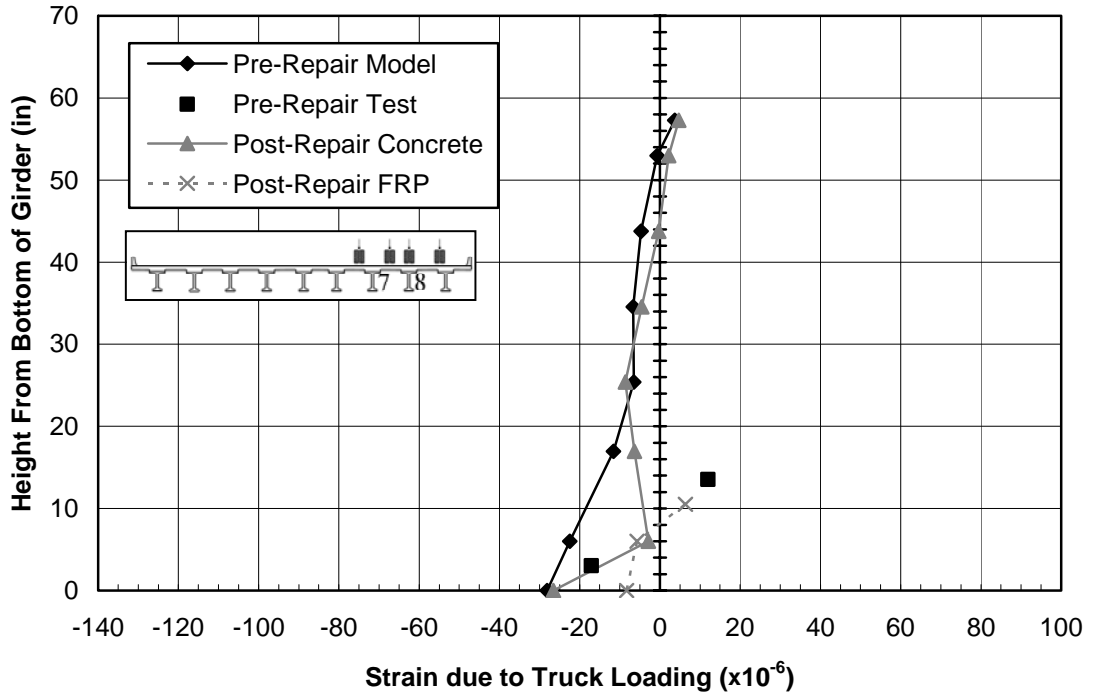**Figure G.15 Strain Profile—Load Position C9, Section 4, Girder 7, East Face**
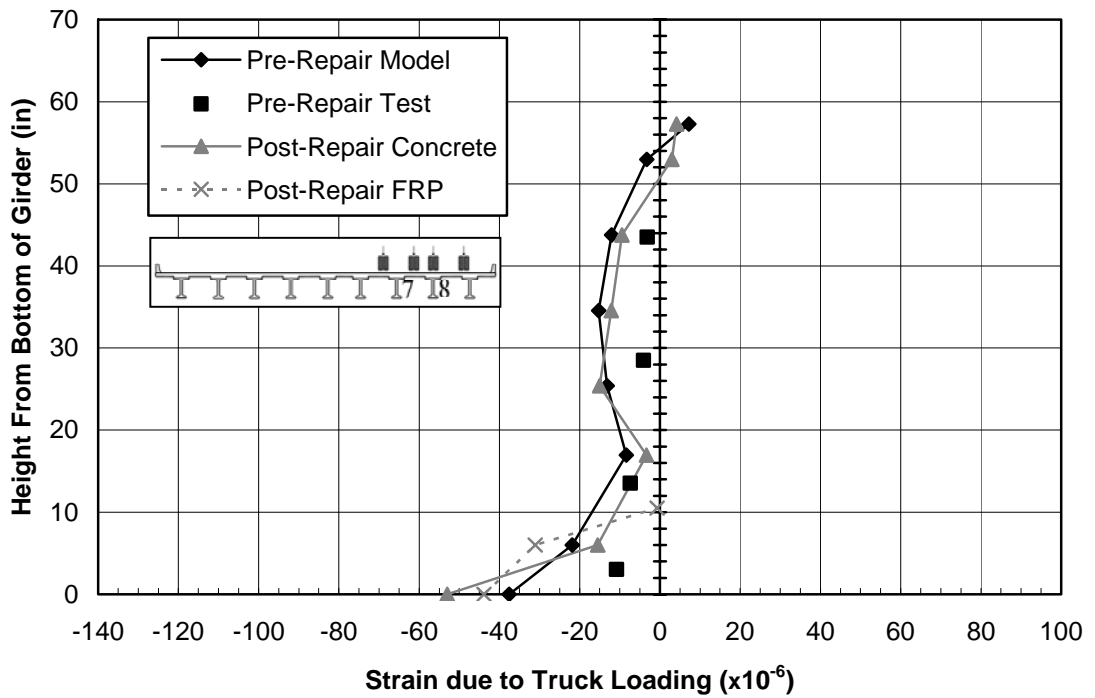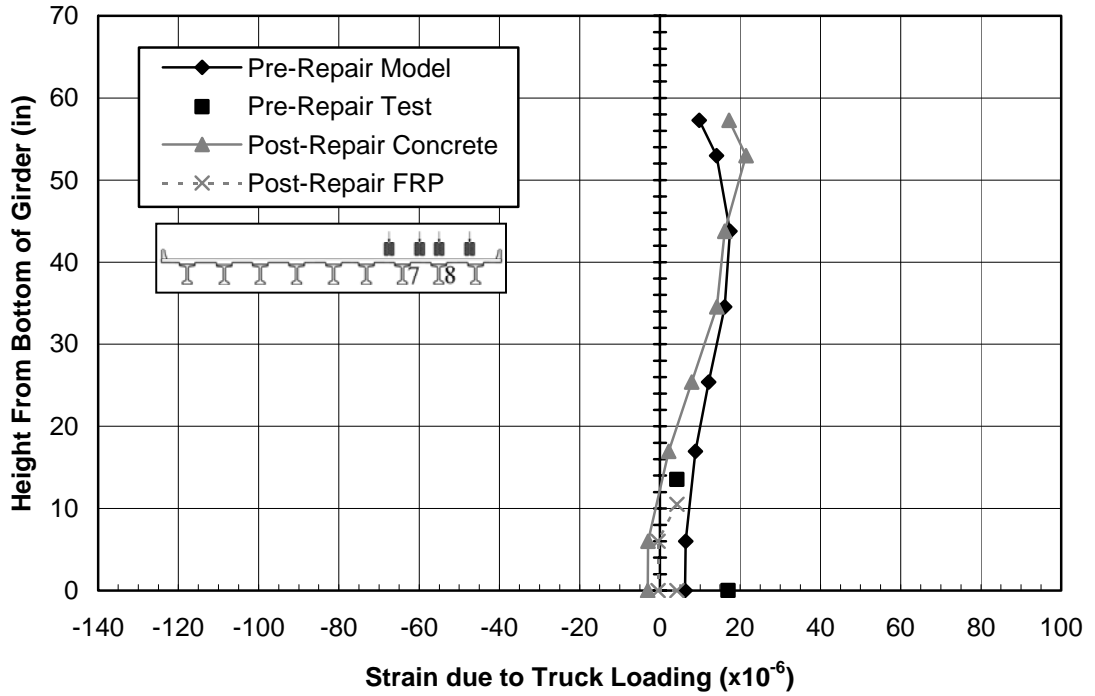
213
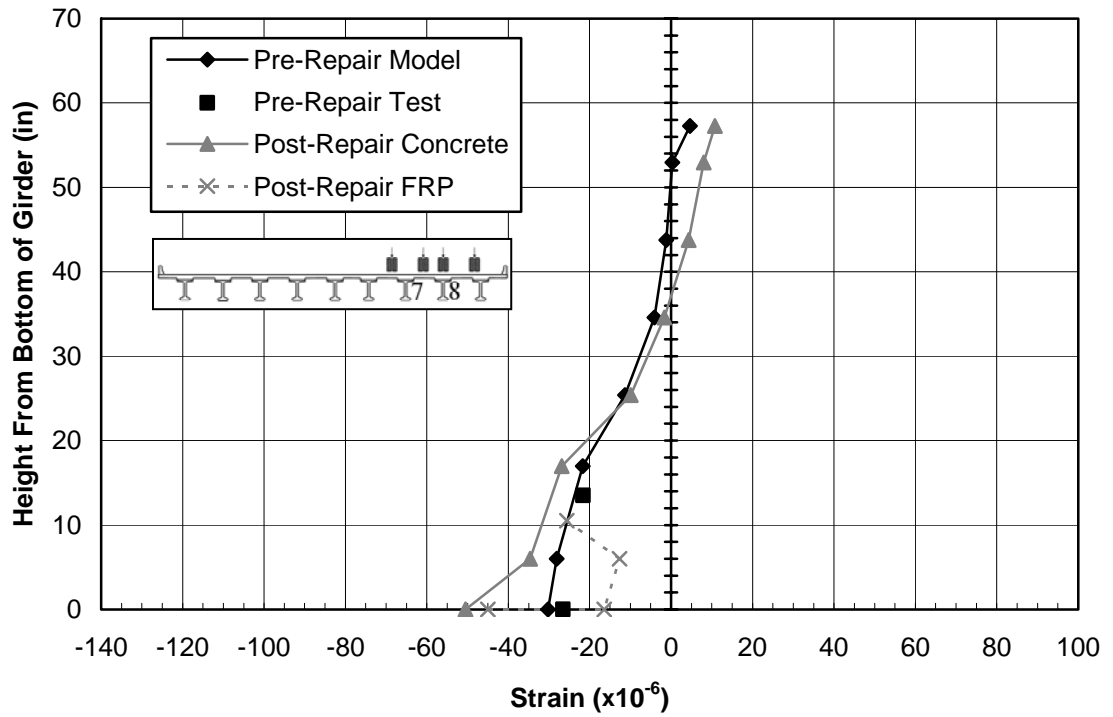
Figure G.16 Strain Profile—Load Position C9, Section 4, Girder 8, West Face
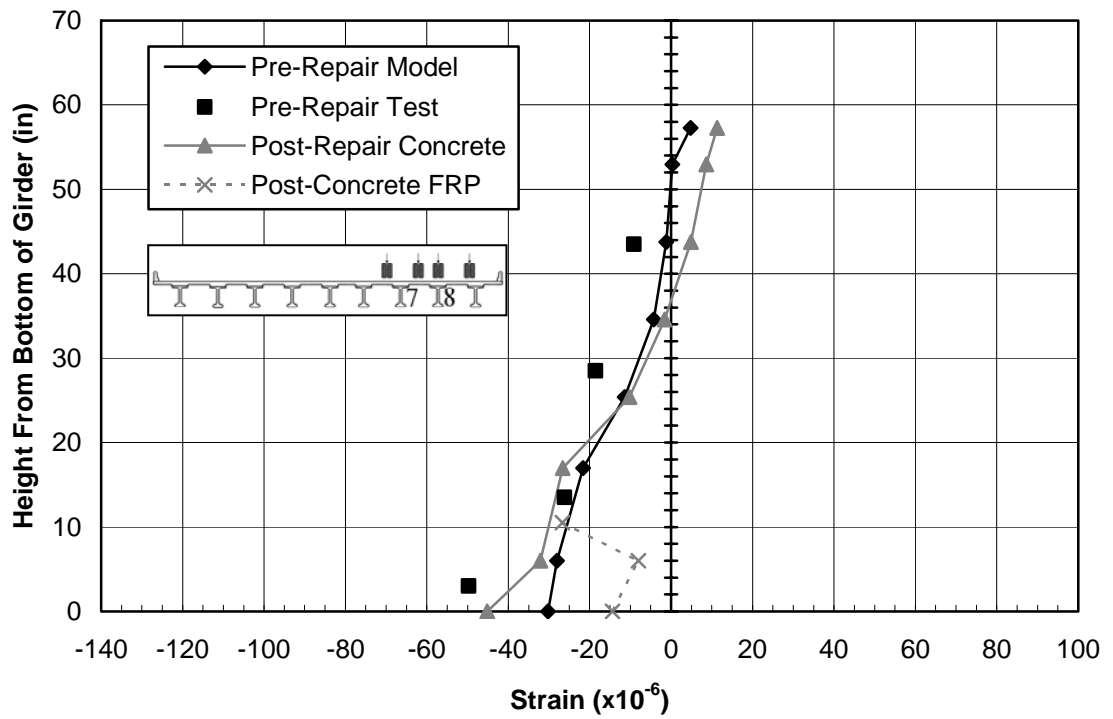
Figure G.17 Strain Profile—Load Position C9, Section 4, Girder 8, East Face

214

APPENDIX H: LOAD TEST DATA

As explained in Chapter 4, tests before and after FRP application needed to be

conducted in order to test the efficacy of FRP repair. The pre-FRP load testing occurred

on the mornings of June 1 and 2, 2005. This summary focuses on the second day of

testing, which occurred on the morning of June 2, 2005. There were nine longitudinal

stop positions and three distinct patterns of transverse positions, making a total of

twenty-seven different load positions. Appendix A further explains the load testing

which resulted in the experimental results presented in Tables H.1–H.3.

Table H.1 Pre-FRP Repair Load Test Data for Transverse Position A

		Ht. of gauge from girder base (in.)	Dist.[a] from center of cont. dia. (in.)	Units	A1	A2	A3	A4
					Outlier Eliminated			
					Widely Varying Data			
					Strains Between 1 and -1 με			
Deflectometers	Girder 7	n/a	-8	in	-0.31	-0.18	-0.10	-0.05
		n/a	-8	in	-0.20	-0.17	-0.10	-0.05
		n/a	8	in	0.03	0.02	0.00	-0.01
		n/a	8	in	0.05	0.04	0.01	-0.01
		n/a	8	in	0.06	0.04	0.02	-0.01
		n/a	8	in	0.06	0.04	0.02	-0.01
	Girder 8	n/a	-8	in	-0.24	-0.14	-0.08	-0.04
		n/a	-8	in	-0.16	-0.12	-0.07	-0.04
		n/a	8	in	0.03	0.02	0.01	-0.01
		n/a	8	in	0.05	0.03	0.01	-0.01
		n/a	8	in	0.05	0.04	0.02	0.00
		n/a	8	in	0.05	0.04	0.02	0.00
Crack Gauges[b]		13.5	-40.00	mm	-0.009	-0.007	-0.005	-0.003
		13.5	56.00	mm	-0.007	-0.006	-0.003	-0.003
		13.5	-49.50	mm	-0.017	-0.003	0.007	0.021
		13.5	47.75	mm	-0.022	-0.020	-0.010	-0.008
Bottom-fiber Strains	Girder 7	0.0	104	με	-27	-22	-8	-2
		0.0	272	με	-24	-19	-8	2
		0.0	440	με	-18	-14	-7	0
		0.0	608	με	-11	-8	-4	-1
	Girder 8	0.0	104	με	-25	-19	-8	-2
		0.0	272	με	-19	-15	-7	0
		0.0	440	με	-14	-11	-5	1
		0.0	608	με	-6	-5	1	11

[a] (-) distance from center of dia. is on Span 10, (+) distance from center of dia. is on Span 11

[b] The first two crack gauges are on Girder 8 and the second two are on Girder 7

| Outlier Eliminated |
| Widely Varying Data |
| Strains Between 1 and -1 με |

		Ht. of gauge from girder base (in.)	Dist. from center of cont. dia. (in.)[a]	Units	A5	A6	A7	A8	A9
Deflectometers	Girder 7	n/a	-8	in	-0.02	0.01	0.02	0.05	0.05
		n/a	-8	in	-0.02	0.01	0.02	0.04	0.05
		n/a	8	in	-0.02	-0.04	-0.06	-0.10	-0.09
		n/a	8	in	-0.03	-0.06	-0.10	-0.18	-0.20
		n/a	8	in	-0.03	-0.06	-0.10	-0.20	-0.27
		n/a	8	in	-0.02	-0.06	-0.09	-0.20	-0.30
	Girder 8	n/a	-8	in	-0.01	0.01	0.02	0.05	0.05
		n/a	-8	in	-0.02	0.01	0.02	0.04	0.04
		n/a	8	in	-0.01	-0.03	-0.05	-0.07	-0.08
		n/a	8	in	-0.02	-0.04	-0.07	-0.13	-0.15
		n/a	8	in	-0.02	-0.05	-0.08	-0.16	-0.21
		n/a	8	in	-0.02	-0.05	-0.07	-0.16	-0.23
Crack Gauges[b]		13.5	-40.00	mm	-0.001	-0.003	-0.005	-0.008	-0.009
		13.5	56.00	mm	-0.002	0.002	0.004	-0.004	-0.007
		13.5	-49.50	mm	0.014	-0.005	-0.010	-0.019	-0.020
		13.5	47.75	mm	-0.006	0.012	0.019	-0.010	-0.021
Bottom-fiber Strains	Girder 7	0.0	104	με	0	13	25	0	-18
		0.0	272	με	11	27	36	75	25
		0.0	440	με	6	19	31	67	71
		0.0	608	με	4	12	21	53	110
	Girder 8	0.0	104	με	0	8	16	0	-13
		0.0	272	με	8	19	24	48	18
		0.0	440	με	5	14	23	48	54
		0.0	608	με	9	7	17	39	74

[a] (-) distance from center of dia. is on Span 10, (+) distance from center of dia. is on Span 11

[b] The first two crack gauges are on Girder 8 and the second two are on Girder 7

Table H.1 cont'd Pre-FRP Repair Load Test Data for Transverse Position A

	Ht. of gauge from girder base (in.)	Dist.[a] from center of cont. dia. (in.)	Units	A1	A2	A3	A4
					Outlier Eliminated	Widely Varying Data	Strains Between 1 and -1 με
Bottom-fiber Strains — Girder 7 Cross Section 1	13.5	-75.25	με	-14	-1	5	11
	0.0	-75.25	με	-17	-2	4	9
	3.0	-75.25	με	-21	1	10	20
	13.5	-75.25	με	-23	-3	6	12
	28.5	-75.25	με	-12	-3	1	7
	43.5	-75.25	με	-10	-11	-15	-6
Girder 8 Cross Section 1	13.5	-75.25	με	-17	-5	0	6
	0.0	-75.25	με	-18	-2	3	11
	3.0	-75.25	με	-13	-2	0	3
	13.5	-75.25	με	-14	-5	0	3
	28.5	-75.25	με	-9	-4	-1	0
	43.5	-75.25	με	-6	-6	-8	-4
Girder 7 Cross Section 2	13.5	-12.75	με	5	3	3	0
	3.0	-12.75	με	-39	-30	-20	-14
	3.0	-12.75	με	-117	-101	-77	-57
	13.5	-12.75	με	-8	-4	-2	-1
	28.5	-12.75	με	2	3	3	3
	43.5	-12.75	με	-1	-4	-3	-5
Girder 8 Cross Section 2	13.5	-12.75	με	-3	0	2	2
	3.0	-12.75	με	-33	-25	-16	-8
	3.0	-12.75	με	-16	-9	-7	-6
	13.5	-12.75	με	0	3	3	3
	28.5	-12.75	με	1	2	2	2
	43.5	-12.75	με	-2	-3	-3	-3

[a] (-) distance from center of dia. is on Span 10, (+) distance from center of dia. is on Span 11

Table H.1 cont'd Pre-FRP Repair Load Test Data for Transverse Position A

| Outlier Eliminated |
| Widely Varying Data |
| Strains Between 1 and -1 με |

		Ht. of gage from girder base (in.)	Dist. [a] from center of cont. dia. (in.)	Units	A5	A6	A7	A8	A9
Bottom-fiber Strains	Girder 7 Cross Section 1	13.5	-75.25	με	6	-5	-8	-17	-17
		0.0	-75.25	με	5	-6	-9	-19	-20
		3.0	-75.25	με	11	-8	-14	-26	-26
		13.5	-75.25	με	6	-9	-15	-27	-28
		28.5	-75.25	με	5	-3	-5	-11	-12
		43.5	-75.25	με	4	0	0	-1	-1
	Girder 8 Cross Section 1	13.5	-75.25	με	4	-5	-9	-16	-18
		0.0	-75.25	με	6	-6	-11	-20	-21
		3.0	-75.25	με	0	-6	-10	-19	-20
		13.5	-75.25	με	1	-6	-9	-16	-17
		28.5	-75.25	με	0	-2	-4	-8	-9
		43.5	-75.25	με	0	0	0	0	0
	Girder 7 Cross Section 2	13.5	-12.75	με	1	3	1	-2	-3
		3.0	-12.75	με	-10	-13	-16	-26	-22
		3.0	-12.75	με	-35	-44	-63	-96	-93
		13.5	-12.75	με	-1	-3	-7	-15	-16
		28.5	-12.75	με	4	0	-1	-3	-4
		43.5	-12.75	με	-1	1	-1	-4	-4
	Girder 8 Cross Section 2	13.5	-12.75	με	4	0	-4	-10	-13
		3.0	-12.75	με	-3	-4	-8	-13	-14
		3.0	-12.75	με	-4	-9	-14	-22	-22
		13.5	-12.75	με	3	-2	-6	-14	-16
		28.5	-12.75	με	2	0	-1	-3	-3
		43.5	-12.75	με	-2	-1	-2	-2	-2

[a] (-) distance from center of dia. is on Span 10, (+) distance from center of dia. is on Span 11

Table H.1 cont'd Pre-FRP Repair Load Test Data for Transverse Position A

		Ht. of gauge from girder base (in.)	Dist.[a] from center of cont. dia. (in.)	Units	A1	A2	A3	A4
					Outlier Eliminated			
					Widely Varying Data			
					Strains Between 1 and -1 με			
Bottom-fiber Strains	Girder 7 Cross Section 3	13.5	-12.75	με	-24	-16	-6	0
		0.0	-12.75	με	-23	-20	-14	-11
		3.0	-12.75	με	-28	-22	-14	-9
		13.5	-12.75	με	-27	-20	-8	-3
		28.5	-12.75	με	-7	-4	-2	0
		43.5	-12.75	με	-3	-3	-1	-1
	Girder 8 Cross Section 3	13.5	-12.75	με	-59	-46	-23	-15
		0.0	-12.75	με	-12	-10	-8	-7
		3.0	-12.75	με	-23	-18	-11	-7
		13.5	-12.75	με	-25	-16	-9	-3
		28.5	-12.75	με	-28	-22	-14	-11
		43.5	-12.75	με	-1	0	0	0
	Girder 7 Cross Section 4	13.5	-75.25	με	-19	-16	-6	-4
		3.0	-75.25	με	-28	-23	-8	-6
		3.0	-75.25	με	-28	-23	-10	-6
		13.5	-75.25	με	-19	-15	-6	-4
		28.5	-75.25	με	-11	-9	-3	-3
		43.5	-75.25	με	-1	0	2	-2
	Girder 8 Cross Section 4	13.5	-75.25	με	-16	-14	-5	-4
		3.0	-75.25	με	-27	-22	-9	-4
		3.0	-75.25	με	-43	-34	-18	-11
		13.5	-75.25	με	-22	-17	-8	-5
		28.5	-75.25	με	-8	-7	-3	-3
		43.5	-75.25	με	-1	-1	2	-2

[a] (-) distance from center of dia. is on Span 10, (+) distance from center of dia. is on Span 11

220

Table H.1 cont'd Pre-FRP Repair Load Test Data for Transverse Position A

		Ht. of gauge from girder base (in.)	Dist. [a] from center of cont. dia. (in.)	Units	A5	A6	A7	A8	A9
					Outlier Eliminated				
					Widely Varying Data				
					Strains Between 1 and -1 με				
Bottom-fiber Strains	Girder 7 Cross Section 3	13.5	-12.75	με	5	7	1	-5	-7
		0.0	-12.75	με	-6	-6	-10	-22	-21
		3.0	-12.75	με	-5	-4	-9	-22	-22
		13.5	-12.75	με	4	11	7	-4	-10
		28.5	-12.75	με	2	3	0	0	0
		43.5	-12.75	με	0	4	3	0	-2
	Girder 8 Cross Section 3	13.5	-12.75	με	-6	9	6	-21	-35
		0.0	-12.75	με	-5	-9	-17	-27	-26
		3.0	-12.75	με	-3	0	-1	-8	-12
		13.5	-12.75	με	1	2	-2	-6	-8
		28.5	-12.75	με	-6	-3	-3	-10	-15
		43.5	-12.75	με	0	0	-1	0	0
	Girder 7 Cross Section 4	13.5	-75.25	με	-2	5	5	-8	-15
		3.0	-75.25	με	-3	11	17	-10	-25
		3.0	-75.25	με	-3	8	12	-11	-25
		13.5	-75.25	με	-1	5	5	-8	-15
		28.5	-75.25	με	-1	3	-1	-8	-10
		43.5	-75.25	με	-2	2	-4	-8	-4
	Girder 8 Cross Section 4	13.5	-75.25	με	-1	4	3	-7	-11
		3.0	-75.25	με	-1	11	20	-2	-14
		3.0	-75.25	με	-5	4	6	-9	-28
		13.5	-75.25	με	-3	3	3	-9	-17
		28.5	-75.25	με	-3	-2	-9	-15	-12
		43.5	-75.25	με	-2	3	-1	-10	-7

[a] (-) distance from center of dia. is on Span 10, (+) distance from center of dia. is on Span 11

Table H.2 Pre-FRP Repair Load Test Data for Transverse Position B

		Ht. of gauge from girder base (in.)	Dist.[a] from center of cont. dia. (in.)	Units	B1	B2	B3	B4
					Outlier Eliminated			
					Widely Varying Data			
					Strains Between 1 and -1 με			
Deflectometers	Girder 7	n/a	-8	in	-0.31	-0.18	-0.10	-0.05
		n/a	-8	in	-0.20	-0.17	-0.10	-0.05
		n/a	8	in	0.03	0.02	0.00	-0.01
		n/a	8	in	0.05	0.04	0.01	-0.01
		n/a	8	in	0.06	0.05	0.02	-0.01
		n/a	8	in	0.07	0.05	0.02	-0.01
	Girder 8	n/a	-8	in	-0.29	-0.17	-0.09	-0.04
		n/a	-8	in	-0.19	-0.15	-0.09	-0.05
		n/a	8	in	0.04	0.03	0.01	-0.01
		n/a	8	in	0.05	0.04	0.02	-0.01
		n/a	8	in	0.06	0.05	0.02	-0.01
		n/a	8	in	0.06	0.05	0.02	0.00
Crack Gauges [b]		13.5	-40.00	mm	-0.010	-0.009	-0.007	-0.003
		13.5	56.00	mm	-0.009	-0.008	-0.005	-0.003
		13.5	-49.50	mm	-0.016	-0.002	0.008	0.021
		13.5	47.75	mm	-0.022	-0.021	-0.012	-0.009
Bottom-fiber Strains	Girder 7	0.0	104	με	-27	-23	-9	-3
		0.0	272	με	-24	-20	-8	1
		0.0	440	με	-18	-15	-7	0
		0.0	608	με	-14	-10	-5	1
	Girder 8	0.0	104	με	-31	-26	-10	-3
		0.0	272	με	-23	-19	-8	2
		0.0	440	με	-17	-13	-6	1
		0.0	608	με	-4	4	4	5

[a] (-) distance from center of dia. is on Span 10, (+) distance from center of dia. is on Span 11

[b] The first two crack gauges are on Girder 8 and the second two are on Girder 7

Table H.2 cont'd Pre-FRP Repair Load Test Data for Transverse Position B

		Ht. of gauge from girder base (in.)	Dist. [a] from center of cont. dia. (in.)	Units	B5	B6	B7	B8	B9
Deflectometers	Girder 7	n/a	-8	in	-0.02	0.01	0.03	0.05	0.05
		n/a	-8	in	-0.02	0.01	0.02	0.04	0.05
		n/a	8	in	-0.02	-0.04	-0.06	-0.10	-0.09
		n/a	8	in	-0.03	-0.06	-0.10	-0.18	-0.20
		n/a	8	in	-0.03	-0.06	-0.10	-0.20	-0.26
		n/a	8	in	-0.02	-0.06	-0.09	-0.20	-0.30
	Girder 8	n/a	-8	in	-0.01	0.02	0.03	0.05	0.06
		n/a	-8	in	-0.02	0.01	0.02	0.04	0.05
		n/a	8	in	-0.02	-0.04	-0.06	-0.09	-0.09
		n/a	8	in	-0.02	-0.06	-0.09	-0.16	-0.18
		n/a	8	in	-0.02	-0.06	-0.10	-0.20	-0.26
		n/a	8	in	-0.02	-0.06	-0.09	-0.19	-0.29
Crack Gauges [b]		13.5	-40.00	mm	-0.001	-0.005	-0.007	-0.010	-0.010
		13.5	56.00	mm	-0.002	0.003	0.007	-0.003	-0.008
		13.5	-49.50	mm	0.013	-0.006	-0.011	-0.019	-0.020
		13.5	47.75	mm	-0.006	0.013	0.021	-0.007	-0.020
Bottom-fiber Strains	Girder 7	0.0	104	µε	-1	14	26	1	-18
		0.0	272	µε	11	27	36	76	25
		0.0	440	µε	6	19	31	66	71
		0.0	608	µε	5	13	23	54	112
	Girder 8	0.0	104	µε	0	12	23	0	-19
		0.0	272	µε	11	25	33	68	22
		0.0	440	µε	7	18	30	63	68
		0.0	608	µε	12	18	25	53	101

Legend:
- Outlier Eliminated
- Widely Varying Data
- Strains Between 1 and -1 µε

[a] (-) distance from center of dia. is on Span 10, (+) distance from center of dia. is on Span 11

[b] The first two crack gauges are on Girder 8 and the second two are on Girder 7

223

Table H.2 cont'd Pre-FRP Repair Load Test Data for Transverse Position B

		Ht. of gauge from girder base (in.)	Dist.[a] from center of cont. dia. (in.)	Units	B1	B2	B3	B4
						Outlier Eliminated		
						Widely Varying Data		
						Strains Between 1 and -1 με		
Bottom-fiber Strains	Girder 7 Cross Section 1	13.5	-75.25	με	-14	-1	5	10
		0.0	-75.25	με	-15	-1	6	11
		3.0	-75.25	με	-21	1	11	21
		13.5	-75.25	με	-23	-2	8	16
		28.5	-75.25	με	-12	-3	1	7
		43.5	-75.25	με	-10	-11	-16	-6
	Girder 8 Cross Section 1	13.5	-75.25	με	-22	-7	0	7
		0.0	-75.25	με	-23	-3	6	16
		3.0	-75.25	με	-19	-3	3	11
		13.5	-75.25	με	-19	-4	0	7
		28.5	-75.25	με	-12	-5	-2	2
		43.5	-75.25	με	-7	-7	-10	-5
	Girder 7 Cross Section 2	13.5	-12.75	με	5	3	2	-1
		3.0	-12.75	με	-30	-22	-16	-11
		3.0	-12.75	με	-126	-115	-88	-63
		13.5	-12.75	με	-8	-3	-2	-2
		28.5	-12.75	με	1	3	3	3
		43.5	-12.75	με	-1	-4	-4	-6
	Girder 8 Cross Section 2	13.5	-12.75	με	-3	2	3	4
		3.0	-12.75	με	-35	-28	-16	-8
		3.0	-12.75	με	-26	-19	-15	-11
		13.5	-12.75	με	-2	2	2	3
		28.5	-12.75	με	1	2	2	2
		43.5	-12.75	με	-3	-5	-4	-5

[a] (-) distance from center of dia. is on Span 10, (+) distance from center of dia. is on Span 11

Table H.2 cont'd Pre-FRP Repair Load Test Data for Transverse Position B

	Ht. of gauge from girder base (in.)	Dist.[a] from center of cont. dia. (in.)	Units	B5	B6	B7	B8	B9
					Outlier Eliminated			
					Widely Varying Data			
					Strains Between 1 and -1 µε			
Bottom-fiber Strains / Girder 7 Cross Section 1	13.5	-75.25	µε	6	-4	-9	-16	-17
	0.0	-75.25	µε	6	-6	-10	-19	-20
	3.0	-75.25	µε	10	-8	-14	-26	-26
	13.5	-75.25	µε	8	-9	-15	-27	-28
	28.5	-75.25	µε	5	-3	-6	-11	-12
	43.5	-75.25	µε	3	0	0	-1	-2
Girder 8 Cross Section 1	13.5	-75.25	µε	5	-7	-13	-22	-23
	0.0	-75.25	µε	9	-9	-15	-27	-28
	3.0	-75.25	µε	5	-9	-15	-25	-26
	13.5	-75.25	µε	3	-8	-13	-21	-23
	28.5	-75.25	µε	3	-4	-6	-11	-12
	43.5	-75.25	µε	1	0	0	0	0
Girder 7 Cross Section 2	13.5	-12.75	µε	1	3	1	-1	-2
	3.0	-12.75	µε	-8	-12	-16	-26	-23
	3.0	-12.75	µε	-35	-41	-62	-92	-90
	13.5	-12.75	µε	0	-3	-7	-15	-16
	28.5	-12.75	µε	4	0	-1	-3	-4
	43.5	-12.75	µε	-1	0	-1	-4	-4
Girder 8 Cross Section 2	13.5	-12.75	µε	5	-1	-6	-15	-17
	3.0	-12.75	µε	-3	-7	-13	-22	-22
	3.0	-12.75	µε	-6	-12	-19	-29	-26
	13.5	-12.75	µε	5	-3	-8	-18	-20
	28.5	-12.75	µε	2	-1	-2	-4	-4
	43.5	-12.75	µε	-2	-2	-2	-3	-3

[a] (-) distance from center of dia. is on Span 10, (+) distance from center of dia. is on Span 11

Table H.2 cont'd Pre-FRP Repair Load Test Data for Transverse Position B

		Ht. of gauge from girder base (in.)	Dist. [a] from center of cont. dia. (in.)	Units	B1	B2	B3	B4
						Outlier Eliminated		
						Widely Varying Data		
						Strains Between 1 and -1 με		
Bottom-fiber Strains	Girder 7 Cross Section 3	13.5	-12.75	με	-24	-17	-7	-1
		0.0	-12.75	με	-24	-22	-13	-9
		3.0	-12.75	με	-25	-21	-14	-11
		13.5	-12.75	με	-26	-21	-9	-4
		28.5	-12.75	με	-6	-3	-2	0
		43.5	-12.75	με	-1	-1	-1	0
	Girder 8 Cross Section 3	13.5	-12.75	με	-75	-61	-33	-21
		0.0	-12.75	με	-17	-14	-11	-8
		3.0	-12.75	με	-27	-24	-17	-12
		13.5	-12.75	με	-31	-22	-13	-6
		28.5	-12.75	με	-37	-31	-21	-15
		43.5	-12.75	με	-2	-2	-2	-1
	Girder 7 Cross Section 4	13.5	-75.25	με	-18	-15	-6	-4
		3.0	-75.25	με	-27	-23	-8	-6
		3.0	-75.25	με	-29	-24	-9	-6
		13.5	-75.25	με	-19	-16	-7	-4
		28.5	-75.25	με	-12	-10	-3	-3
		43.5	-75.25	με	-1	0	2	-2
	Girder 8 Cross Section 4	13.5	-75.25	με	-21	-17	-9	-7
		3.0	-75.25	με	-33	-27	-12	-6
		3.0	-75.25	με	-54	-46	-21	-13
		13.5	-75.25	με	-28	-24	-12	-8
		28.5	-75.25	με	-12	-10	-6	-8
		43.5	-75.25	με	-2	-1	1	-4

[a] (-) distance from center of dia. is on Span 10, (+) distance from center of dia. is on Span 11

Table H.2 cont'd Pre-FRP Repair Load Test Data for Transverse Position B

		Ht. of gauge from girder base (in.)	Dist. [a] from center of cont. dia. (in.)	Units	B5	B6	B7	B8	B9
					Outlier Eliminated				
					Widely Varying Data				
					Strains Between 1 and -1 µε				
Bottom-fiber Strains	Girder 7 Cross Section 3	13.5	-12.75	µε	5	7	2	-4	-6
		0.0	-12.75	µε	-6	-3	-6	-15	-15
		3.0	-12.75	µε	-5	-6	-13	-28	-28
		13.5	-12.75	µε	3	11	6	-6	-11
		28.5	-12.75	µε	3	3	-1	-1	0
		43.5	-12.75	µε	-1	5	2	-1	-2
	Girder 8 Cross Section 3	13.5	-12.75	µε	-8	13	10	-25	-45
		0.0	-12.75	µε	-5	-9	-17	-30	-28
		3.0	-12.75	µε	-6	-3	-9	-19	-23
		13.5	-12.75	µε	2	2	-6	-11	-12
		28.5	-12.75	µε	-9	0	-3	-14	-20
		43.5	-12.75	µε	0	-1	-3	-1	0
	Girder 7 Cross Section 4	13.5	-75.25	µε	-2	5	5	-8	-16
		3.0	-75.25	µε	-3	12	19	-10	-25
		3.0	-75.25	µε	-3	10	15	-12	-26
		13.5	-75.25	µε	-1	6	6	-8	-14
		28.5	-75.25	µε	-1	3	0	-7	-10
		43.5	-75.25	µε	-1	3	-4	-8	-3
	Girder 8 Cross Section 4	13.5	-75.25	µε	-4	3	1	-12	-17
		3.0	-75.25	µε	-1	16	27	-2	-21
		3.0	-75.25	µε	-7	16	28	-14	-40
		13.5	-75.25	µε	-3	5	6	-13	-23
		28.5	-75.25	µε	-5	-3	-11	-20	-16
		43.5	-75.25	µε	-2	2	-4	-13	-9

[a] (-) distance from center of dia. is on Span 10, (+) distance from center of dia. is on Span 11

Table H.3 Pre-FRP Repair Load Test Data for Transverse Position C

		Ht. of gauge from girder base (in.)	Dist.[a] from center of cont. dia. (in.)	Units	C1	C2	C3	C4
						Outlier Eliminated		
						Widely Varying Data		
						Strains Between 1 and -1 με		
Deflectometers	Girder 7	n/a	-8	in	-0.28	-0.17	-0.09	-0.05
		n/a	-8	in	-0.19	-0.15	-0.09	-0.05
		n/a	8	in	0.03	0.02	0.00	-0.01
		n/a	8	in	0.05	0.04	0.01	-0.01
		n/a	8	in	0.06	0.05	0.02	0.00
		n/a	8	in	0.06	0.04	0.02	0.00
	Girder 8	n/a	-8	in	-0.33	-0.19	-0.10	-0.05
		n/a	-8	in	-0.21	-0.17	-0.10	-0.06
		n/a	8	in	0.04	0.03	0.01	-0.01
		n/a	8	in	0.06	0.05	0.02	-0.01
		n/a	8	in	0.07	0.05	0.02	-0.01
		n/a	8	in	0.07	0.05	0.02	0.00
Crack Gauges[b]		13.5	-40.00	mm	-0.011	-0.010	-0.008	-0.004
		13.5	56.00	mm	-0.010	-0.009	-0.006	-0.004
		13.5	-49.50	mm	-0.011	0.001	0.009	0.019
		13.5	47.75	mm	-0.020	-0.019	-0.011	-0.008
Bottom-fiber Strains	Girder 7	0.0	104	με	-25	-21	-8	-3
		0.0	272	με	-22	-18	-8	1
		0.0	440	με	-17	-13	-6	0
		0.0	608	με	-12	-9	-3	0
	Girder 8	0.0	104	με	-36	-30	-12	-4
		0.0	272	με	-27	-22	-10	2
		0.0	440	με	-19	-15	-7	1
		0.0	608	με	-14	-10	0	7

[a] (-) distance from center of dia. is on Span 10, (+) distance from center of dia. is on Span 11

[b] The first two crack gauges are on Girder 8 and the second two are on Girder 7

228

Table H.3 cont'd Pre-FRP Repair Load Test Data for Transverse Position C

		Ht. of gauge from girder base (in.)	Dist. from center of cont. dia. (in.)	Units	C5	C6	C7	C8	C9
Deflectometers	Girder 7	n/a	-8	in	-0.02	0.01	0.02	0.05	0.05
		n/a	-8	in	-0.02	0.01	0.02	0.04	0.05
		n/a	8	in	-0.02	-0.04	-0.06	-0.09	-0.09
		n/a	8	in	-0.02	-0.06	-0.08	-0.16	-0.18
		n/a	8	in	-0.02	-0.06	-0.09	-0.18	-0.24
		n/a	8	in	-0.02	-0.05	-0.08	-0.18	-0.27
	Girder 8	n/a	-8	in	-0.02	0.02	0.03	0.06	0.06
		n/a	-8	in	-0.02	0.01	0.02	0.05	0.05
		n/a	8	in	-0.02	-0.04	-0.07	-0.11	-0.10
		n/a	8	in	-0.03	-0.06	-0.10	-0.18	-0.21
		n/a	8	in	-0.03	-0.07	-0.11	-0.22	-0.29
		n/a	8	in	-0.02	-0.06	-0.10	-0.21	-0.32
Crack Gauges [b]		13.5	-40.00	mm	-0.001	-0.005	-0.008	-0.011	-0.011
		13.5	56.00	mm	-0.003	0.005	0.010	-0.003	-0.008
		13.5	-49.50	mm	0.012	-0.005	-0.010	-0.018	-0.019
		13.5	47.75	mm	-0.006	0.012	0.020	-0.004	-0.016
Bottom-fiber Strains	Girder 7	0.0	104	µε	-1	12	23	1	-16
		0.0	272	µε	9	22	31	68	23
		0.0	440	µε	5	17	27	58	64
		0.0	608	µε	5	12	21	48	101
	Girder 8	0.0	104	µε	-1	14	27	-1	-23
		0.0	272	µε	12	29	38	79	25
		0.0	440	µε	7	20	33	72	77
		0.0	608	µε	11	9	20	54	111

Legend: Outlier Eliminated / Widely Varying Data / Strains Between 1 and -1 µε

[a] (-) distance from center of dia. is on Span 10, (+) distance from center of dia. is on Span 11

[b] The first two crack gauges are on Girder 8 and the second two are on Girder 7

Table H.3 cont'd Pre-FRP Repair Load Test Data for Transverse Position C

	Ht. of gauge from girder base (in.)	Dist. [a] from center of cont. dia. (in.)	Units	C1	C2	C3	C4
				Outlier Eliminated			
				Widely Varying Data			
				Strains Between 1 and -1 με			
Girder 7 Cross Section 1	13.5	-75.25	με	-11	-2	5	9
	0.0	-75.25	με	-14	-2	5	9
	3.0	-75.25	με	-16	0	10	19
	13.5	-75.25	με	-20	-3	7	14
	28.5	-75.25	με	-10	-3	1	6
	43.5	-75.25	με	-8	-9	-14	-7
Girder 8 Cross Section 1	13.5	-75.25	με	-24	-8	0	9
	0.0	-75.25	με	-25	-2	7	19
	3.0	-75.25	με	-24	-5	4	11
	13.5	-75.25	με	-23	-8	0	7
	28.5	-75.25	με	-14	-7	-3	2
	43.5	-75.25	με	-8	-8	-12	-5
Girder 7 Cross Section 2	13.5	-12.75	με	4	2	1	-1
	3.0	-12.75	με	-16	-11	-9	-7
	3.0	-12.75	με	-119	-107	-79	-54
	13.5	-12.75	με	-7	-3	-2	-1
	28.5	-12.75	με	1	2	2	2
	43.5	-12.75	με	-1	-4	-4	-5
Girder 8 Cross Section 2	13.5	-12.75	με	-2	2	3	4
	3.0	-12.75	με	-29	-23	-15	-7
	3.0	-12.75	με	-41	-28	-19	-12
	13.5	-12.75	με	-5	0	2	4
	28.5	-12.75	με	1	3	3	3
	43.5	-12.75	με	-3	-5	-5	-6

Bottom-fiber Strains

[a] (-) distance from center of dia. is on Span 10, (+) distance from center of dia. is on Span 11

230

Table H.3 cont'd Pre-FRP Repair Load Test Data for Transverse Position C

| Outlier Eliminated |
| Widely Varying Data |
| Strains Between 1 and -1 με |

	Ht. of gauge from girder base (in.)	Dist. a from center of cont. dia. (in.)	Units	C5	C6	C7	C8	C9
Girder 7 Cross Section 1	13.5	-75.25	με	6	-5	-8	-14	-16
	0.0	-75.25	με	5	-6	-9	-18	-18
	3.0	-75.25	με	9	-7	-12	-23	-23
	13.5	-75.25	με	6	-8	-14	-25	-26
	28.5	-75.25	με	5	-2	-5	-10	-10
	43.5	-75.25	με	3	0	0	-1	-1
Girder 8 Cross Section 1	13.5	-75.25	με	6	-8	-15	-26	-26
	0.0	-75.25	με	11	-10	-18	-31	-32
	3.0	-75.25	με	5	-10	-17	-29	-29
	13.5	-75.25	με	4	-8	-14	-24	-25
	28.5	-75.25	με	2	-4	-8	-13	-14
	43.5	-75.25	με	2	-1	-1	-1	-1
Girder 7 Cross Section 2	13.5	-12.75	με	0	2	1	-1	-2
	3.0	-12.75	με	-5	-10	-13	-23	-21
	3.0	-12.75	με	-28	-31	-48	-76	-76
	13.5	-12.75	με	0	-3	-7	-13	-14
	28.5	-12.75	με	3	0	-1	-3	-4
	43.5	-12.75	με	-2	0	-1	-3	-4
Girder 8 Cross Section 2	13.5	-12.75	με	6	-1	-7	-19	-21
	3.0	-12.75	με	-2	-7	-16	-29	-29
	3.0	-12.75	με	-7	-12	-19	-29	-27
	13.5	-12.75	με	5	-3	-9	-20	-22
	28.5	-12.75	με	3	-1	-2	-5	-5
	43.5	-12.75	με	-1	-2	-3	-4	-4

Bottom-fiber Strains

a (-) distance from center of dia. is on Span 10, (+) distance from center of dia. is on Span 11

Table H.3 cont'd Pre-FRP Repair Load Test Data for Transverse Position C

		Ht. of gauge from girder base (in.)	Dist. [a] from center of cont. dia. (in.)	Units	C1	C2	C3	C4
					Outlier Eliminated			
					Widely Varying Data			
					Strains Between 1 and -1 με			
Bottom-fiber Strains	Girder 7 Cross Section 3	13.5	-12.75	με	-21	-14	-6	-1
		0.0	-12.75	με	-22	-19	-11	-7
		3.0	-12.75	με	-18	-15	-11	-8
		13.5	-12.75	με	-24	-18	-7	-4
		28.5	-12.75	με	-6	-4	-2	0
		43.5	-12.75	με	-2	-1	-1	0
	Girder 8 Cross Section 3	13.5	-12.75	με	-87	-73	-40	-27
		0.0	-12.75	με	-21	-18	-13	-10
		3.0	-12.75	με	-28	-24	-17	-13
		13.5	-12.75	με	-35	-25	-15	-7
		28.5	-12.75	με	-43	-36	-24	-18
		43.5	-12.75	με	-1	-1	-1	-1
	Girder 7 Cross Section 4	13.5	-75.25	με	-15	-13	-6	-5
		3.0	-75.25	με	-24	-20	-9	-6
		3.0	-75.25	με	-26	-22	-11	-7
		13.5	-75.25	με	-17	-14	-7	-4
		28.5	-75.25	με	-10	-8	-3	-3
		43.5	-75.25	με	0	0	1	-2
	Girder 8 Cross Section 4	13.5	-75.25	με	-23	-20	-10	-8
		3.0	-75.25	με	-38	-32	-13	-7
		3.0	-75.25	με	-61	-54	-28	-17
		13.5	-75.25	με	-31	-27	-13	-8
		28.5	-75.25	με	-14	-11	-6	-8
		43.5	-75.25	με	-2	-2	2	-4

[a] (-) distance from center of dia. is on Span 10, (+) distance from center of dia. is on Span 11

| Outlier Eliminated |
| Widely Varying Data |
| Strains Between 1 and -1 με |

	Ht. of gauge from girder base (in.)	Dist. [a] from center of cont. dia. (in.)	Units	C5	C6	C7	C8	C9
Bottom-fiber Strains / **Girder 7 Cross Section 3**	13.5	-75.25	με	5	7	1	-2	-4
	0.0	-75.25	με	-3	0	-3	-7	-8
	3.0	-75.25	με	-4	-5	-12	-30	-29
	13.5	-75.25	με	3	7	4	-7	-11
	28.5	-75.25	με	1	2	-1	-1	0
	43.5	-75.25	με	-1	3	1	-2	-3
Girder 8 Cross Section 3	13.5	-75.25	με	-10	15	12	-27	-49
	0.0	-75.25	με	-5	-8	-17	-28	-25
	3.0	-75.25	με	-6	-4	-11	-29	-34
	13.5	-75.25	με	2	2	-7	-15	-15
	28.5	-75.25	με	-11	0	-4	-17	-25
	43.5	-75.25	με	0	0	-3	-2	0
Girder 7 Cross Section 4	13.5	-12.75	με	-2	4	4	-7	-13
	3.0	-12.75	με	-3	10	17	-8	-21
	3.0	-12.75	με	-3	8	13	-11	-24
	13.5	-12.75	με	-2	5	5	-6	-12
	28.5	-12.75	με	-1	3	0	-5	-8
	43.5	-12.75	με	-1	3	-3	-6	-2
Girder 8 Cross Section 4	13.5	-12.75	με	-4	3	1	-15	-22
	3.0	-12.75	με	-3	18	33	-4	-27
	3.0	-12.75	με	-8	17	28	-18	-50
	13.5	-12.75	με	-4	7	8	-15	-26
	28.5	-12.75	με	-4	-2	-13	-22	-19
	43.5	-12.75	με	-3	4	-4	-15	-9

[a] (-) distance from center of dia. is on Span 10, (+) distance from center of dia. is on Span 11

APPENDIX I: NOTATION AND ABBREVIATIONS

A	area
AASHTO	American Association of State Highway and Transportation Officials
ACI	American Concrete Institute
AE	acoustic emissions
ALDOT	Alabama Department of Transportation
BT	bulb-tee
C3D4	4-node tetrahedral element
C3D8	8-node brick element
C3D8R	8-node brick element with reduced integration
DOF	degree of freedom
E or E_c	modulus of elasticity
E_{ft}	modulus of elasticity of the fiber in the direction that is transverse to the fiber longitudinal axis
EI	stiffness
ERSG	electrical-resistance strain gauge
f	fiber property
FEM	finite-element modeling
FRP	fiber-reinforced polymer
G	shear modulus
GFRP	glass fiber-reinforced polymer
h	height
I	moment of inertia
L	crack width, length
l	longitudinal direction
LRFD	load and resistance factor design
m	matrix property

p	direction perpendicular to the plane
P_{cr}	critical load
PCI	Precast/Prestressed Concrete Institute
r^2	radius of gyration
RC	reinforced concrete
S	section modulus
S4	4-node shell element
S4R	4-node shell element with reduced integration
T	tension
t	transverse direction
V	volume fraction
y_t	distance from neutral axis to the top of the flange
ν (nu)	Poisson's ratio